

FINAL TECHNICAL REPORT

Hawaii Energy and Environmental Technologies (HEET) Initiative

Office of Naval Research

Grant Number N00014-06-1-0086

For the period October 17, 2005 to September 30, 2007

Hawaii Natural Energy Institute



**School of Ocean and Earth Science and Technology
University of Hawaii at Manoa**

November 2007

TECHNICAL REPORT

20080522038

Hawaii Energy and Environmental Technologies (HEET) Initiative

Office of Naval Research

Grant Number N00014-06-1-0086

For the period October 17, 2005 to September 30, 2007

Hawaii Natural Energy Institute



**School of Ocean and Earth Science and Technology
University of Hawaii at Manoa**

November 2007

REPORT DOCUMENTATION PAGE					Form Approved OMB No. 0704-0188	
<p>The public reporting burden for this collection of information is estimated to average 1 hour per response, including the time for reviewing instructions, searching existing data sources, gathering and maintaining the data needed, and completing and reviewing the collection of information. Send comments regarding this burden estimate or any other aspect of this collection of information, including suggestions for reducing the burden, to Department of Defense, Washington Headquarters Services, Directorate for Information Operations and Reports (0704-0188), 1215 Jefferson Davis Highway, Suite 1204, Arlington, VA 22202-4302. Respondents should be aware that notwithstanding any other provision of law, no person shall be subject to any penalty for failing to comply with a collection of information if it does not display a currently valid OMB control number.</p> <p>PLEASE DO NOT RETURN YOUR FORM TO THE ABOVE ADDRESS.</p>						
1. REPORT DATE (DD-MM-YYYY) 30-11-2007		2. REPORT TYPE Final Technical Report		3. DATES COVERED (From - To) 17-10-2005 to 30-09-2007		
4. TITLE AND SUBTITLE Hawaii Energy and Environmental Technologies (HEET) Initiative				5a. CONTRACT NUMBER		
				5b. GRANT NUMBER N00014-06-1-0086		
				5c. PROGRAM ELEMENT NUMBER		
6. AUTHOR(S) Rocheleau, Richard E. Moore, Robert M. Turn, Scott Q. Antal, Michael J., Jr. Cooney, Michael J. Liaw, Bor Yann Masutani, Stephen M.				5d. PROJECT NUMBER 07PR08492-00		
				5e. TASK NUMBER		
				5f. WORK UNIT NUMBER		
7. PERFORMING ORGANIZATION NAME(S) AND ADDRESS(ES) University of Hawaii 2530 Dole Street, Sakamaki D200 Honolulu, HI 96822				8. PERFORMING ORGANIZATION REPORT NUMBER		
9. SPONSORING/MONITORING AGENCY NAME(S) AND ADDRESS(ES) Office of Naval Research Regional Office Seattle 1107 NE 45th Street, Suite 350 Seattle, WA 98105-4631				10. SPONSOR/MONITOR'S ACRONYM(S) ONR		
				11. SPONSOR/MONITOR'S REPORT NUMBER(S)		
12. DISTRIBUTION/AVAILABILITY STATEMENT Approved for public release; distribution is unlimited.						
13. SUPPLEMENTARY NOTES In addition to the primary text of the Final Technical Report (106 pages), the report has three Appendices with 80 pages total.						
14. ABSTRACT This report covers efforts by the Hawaii Natural Energy Institute of the University of Hawaii under the ONR-funded HEET Initiative that addresses critical technology needs for exploration/utilization of seabed methane hydrates and development/testing of advanced fuel cells and fuel cell systems. Methane hydrates work included: laboratory and analytical investigations of hydrate destabilization phenomena; characterization of the microbial community in marine hydrate beds; development of models to predict the fate of methane released from the seafloor into the water column; and the promotion of international R&D partnerships. In the fuel cell area, accomplishments included: addition of two fuel cell test cells to the Hawaii Fuel Cell Test Facility; improved capabilities for fuel/oxidizer impurity testing; and improved performance of the dynamic HiL test stand. Under the hydrogen production area, efforts were focused on sulfur removal from fuel gas and construction of a reformer system for seafloor methane work. Further work was also carried out with novel fuel cell concepts including biocarbons and bio-fuel cells.						
15. SUBJECT TERMS Fuel Cells, Fuel Cell Testing, Fuel Processing and Gas Conditioning for Hydrogen Production, Fuels Purity, Methane Hydrates, Biocarbons, Bio-Fuel Cells						
16. SECURITY CLASSIFICATION OF:			17. LIMITATION OF ABSTRACT UU	18. NUMBER OF PAGES 186	19a. NAME OF RESPONSIBLE PERSON Yaa-Yin Fong, Director of Research Services	
a. REPORT U	b. ABSTRACT U	c. THIS PAGE U			19b. TELEPHONE NUMBER (Include area code) (808) 956-9081	

Table of Contents

<u>Section No.</u>	<u>Section Title</u>	<u>Page</u>
1	Executive Summary	1
2	Introduction	5
3	Fuel Cell Systems	7
3.1	Objectives	7
3.2	PEM Fuel Cell Testing and Component Development	7
3.2.1	Test stands/Infrastructure Upgrades	7
3.2.2	Cell and Component Testing	10
3.2.3	MEA Fabrication Laboratory	13
3.2.4	Papers and Presentations Resulting from Efforts	14
3.3	Fuel Cell Hardware-in-Loop and System Simulation Development	15
3.3.1	Scope of Work and Approach	15
3.3.2	Technical Accomplishments	16
3.3.3	Papers and Presentations Resulting from Efforts	18
3.4	Fuel Processing and Gas Conditioning for Hydrogen Production	21
3.4.1	Sulfur Removal from Fuel Gas Using Low Temperature Sorbents	21
3.4.1.1	Scope of Work and Approach	21
3.4.1.2	Experimental	22
3.4.1.3	Technical Accomplishments	24
3.4.1.4	References	29
3.4.1.5	Papers and Presentations Resulting from Efforts	30
3.4.2	Reforming of Seafloor Methane for Use in Remote Autonomous Underwater Fuel Cells	30
3.4.2.1	Scope of Work and Approach	30
3.4.2.2	Experimental	30
3.4.2.3	Technical Accomplishments	34
3.4.2.4	Papers Resulting from Efforts	45
3.4.3	Plasma Reforming of Diesel Fuel and Reformate Purification	45
3.5	Novel Fuel Cell and Component Development	47
3.5.1	Biocarbons for Use in Fuel Cells	47
3.5.1.1	Objectives	47
3.5.1.2	Scope of Work and Approach	47
3.5.1.3	Technical Accomplishments	48
3.5.1.4	Papers and Presentations Resulting from Efforts	48
3.5.2	Enzymatic Bio-Fuel Cells	49
3.5.2.1	Objectives	49
3.5.2.2	Scope of Work and Approach	50
3.5.2.3	Technical Accomplishments	50
3.5.2.4	References	53
3.5.2.5	Papers and Presentations Resulting from Efforts	54

4 Methane Hydrates	57
4.1 Objectives	57
4.2 Scope of Work and Approach	58
4.2.1 Hydrate Thermochemistry and Kinetics	58
4.2.2 Environmental Impacts of Methane Release from Seafloor Hydrates	58
4.2.3 Hydrate Microbiology	58
4.2.4 International Collaborative R&D	58
4.3 Technical Accomplishments	58
4.3.1 Methane Hydrate Destabilization	59
4.3.2 Environmental Impacts of Methane Release from Seafloor Hydrates	78
4.3.3 Hydrate Microbiology	96
4.3.4 International Collaborative R&D	101
4.4 Papers Resulting from Efforts	102
4.5 References	102
Appendix A Plasma Reforming of Diesel Fuel and Reformate Purification	107
Appendix B Near-field Characterization of Hydrothermal Vents along the Endeavour Segment of the Juan de Fuca Ridge	123
Appendix C Vertical Mixing above a Steady Circular Hydrothermal Vent	129
Addenda	following page 131
Addendum A Plasma Diesel Processing Final Report Report contents	A-1 to A-30
Addendum B Selective Membrane Purification of Hydrogen for Fuel Cells Article contents	B-1 to B-31
Addendum C Design of Integrated Plasma Reformer Design Report contents	C-i C-1 to C-4

**Technical Report for the
Hawaii Energy and Environmental Technologies (HEET) Initiative
Grant Number N00014-06-1-0086
(October 17, 2005 to September 30, 2007)**

1. Executive Summary

This report summarizes work conducted under Grant Number N00014-06-1-0086, the Hawaii Energy and Environmental Technologies (HEET) Initiative, funded through the Office of Naval Research to the Hawaii Natural Energy Institute (HNEI) of the University of Hawaii. The work reported here under this initiative continued the focus on critical technology needs associated with the development and testing of advanced fuel cells and fuel cell systems, and the exploration and utilization of seabed methane hydrates, and represents the third award of this title.

Major accomplishments under the first award, Grant Number N00014-01-1-0928, included the planning, design and construction of the Hawaii Fuel Cell Test Facility (HFCTF), which opened in May 2003 with three full-size test stands for PEM fuel cells. Under the first award, HNEI, in partnership with industry, established test protocols and conducted a variety of long-term durability studies. The methane hydrates activities under the first agreement initiated studies to characterize hydrate thermochemistry and kinetics, hydrate microbiology and development of international collaborations.

Under the second award (N00014-04-1-0682), HNEI expanded its test capabilities with the addition of three new fuel cell test stands at the HFCTF. Two of these stands, designed for sub-scale fuel cells (e.g., 50 cm²), were used for fuels purity studies which included initial characterization of the effects of trace amounts of benzene, toluene and carbon monoxide in the hydrogen fuel. The third stand was designed for high speed dynamic testing for use in Hardware-in-Loop (HiL) work which included testing of a 100 cm² single cell via a fuel cell vehicle simulation program. Modeling and simulation of a fuel cell energy/power system for use in an unmanned underwater vehicle (UUV) was also completed. Initial experiments with the HiL test stand revealed that the vendor-supplied control system had limitations in dynamic response. HNEI initiated design of a new control system for faster response. In addition to the test work, HNEI also developed an MEA fabrication laboratory to support the existing fuel cell assembly laboratory. Novel fuel cell component research was continued in the areas of using biocarbons in fuel cell bipolar plates and developing enzymatic bio-fuel cells. Alternative fuel research was continued via efforts in fuel processing and gas conditioning for hydrogen production. HNEI's activities in the area of methane hydrates included hydrate destabilization phenomena, with shakedown testing being performed with the HNEI destabilization facility and a major accomplishment being the design and fabrication of a novel fiberoptic probe to be used to identify sample aspects within the calorimeter sample cell using Raman spectroscopy. Molecular biological studies of hydrate sediments were continued and push core samples from the Gulf of Mexico and offshore New Zealand were collected for analysis. Re-analysis of our existing microbial fuel cell data and new calculations indicate that an alternative electrolyte system of seawater and Nafion membrane could greatly reduce inter-electrode resistance and improve performance. Reactors testing this seawater/Nafion electrode system were being fabricated. HNEI sponsored and manned the organizing committee of the 4th International

Workshop on Methane Hydrates that took place in Victoria, British Columbia, Canada on 9-11 May 2005.

During the present reporting period (under award N00014-06-1-0086), we continued to expand the capacity of the HFCTF and made improvements to the infrastructure in support of this expanded capability. Two Fuel Cell Technologies single-cell test stands were added, increasing the total number of test stands to eight. Several of the existing test stands were modified for increased performance. This included modification of the original large-area test stands to allow testing of subscale fuel cells and pressurized operation. A segmented fuel cell system was designed and validated. Diagnostic equipment, including gas analysis equipment, continued to be developed and improved. New diagnostic and analysis algorithms that permit immediate determination of fuel or oxidizer impurity impacts were developed, allowing characterization of impurity impacts even under widely varying cell operating conditions and different materials. In the course of the work under this agreement, the MEA (membrane electrode assembly) Fabrication Laboratory, established under the prior award, was used successfully to produce MEA's that were subsequently used in testing. Hot presses originally purchased for MEA fabrication were upgraded with non-corrosive platens.

Fuel cell HiL development activities focused on improvements to the existing dynamic HiL test stand which previously gave unsatisfactory dynamic performance with the vendor-supplied control system. Improvements included replacement of the control architecture supplied by the original vendor with a new HNEI-designed system. The result was enhanced dynamic capabilities plus improved operating flexibility, safety, and test stand reliability. Simulation work yielded creation of a simulation tool capable of evaluating and screening fuel cell systems for propulsion of a UUV. Further simulation efforts identified an alternative simulation environment, Modelica, for use in modeling fuel cells, and this led to the building of a fuel cell simulation library.

In the area of alternative fuel supplies, HNEI continued research on fuel processing and gas conditioning for hydrogen production. This included examination of sulfur removal from fuel gas using activated-carbon-based sorbents, and reforming seafloor methane for use in underwater fuel cells. Sulfur-removal capability was tested for a variety of individual activated-carbon sorbents and this led to testing of composite sorbents, designed to optimize adsorption of selected sulfur compounds. For the seafloor methane work, a high pressure reformer system was constructed and initial testing was completed. Several different performance optimization criteria are being considered to assist in determining appropriate operating conditions for the reformer.

Work was also conducted in the development of novel fuel cells and components, specifically in the area of biocarbons for fuel cell use and development of enzymatic bio-fuel cells. In the area of biocarbons for use in fuel cells, a variety of charcoals and carbonized charcoals were prepared and characterized in comparison with graphite. Through this effort, HNEI is assisting several industrial companies in their DoD-sponsored development of direct carbon fuel cells. Development of enzymatic bio-fuel cells included enzyme immobilization efforts utilizing macroporous chitosan polymer composites that support both mediator-based and direct-electron-transfer mechanisms. Improved surface characterization protocols utilizing imaging ellipsometry have also advanced the use of polymerized methylene green as the electron transfer mediator used in mediator-based electron-transfer mechanisms.

HNEI's activities in the area of methane hydrates comprised four primary components: laboratory and analytical investigations of hydrate destabilization phenomena; characterization of the microbial community in marine hydrate beds that modulate methane levels in the seafloor sediments and leakage into the water column; development of models to predict the fate of methane released from the seafloor into the water column; and the promotion of international R&D partnerships.

Hydrate destabilization activities included additional analysis of experiments conducted under previous awards. Modeling indicates that the data from these reagent-destabilization experiments are represented better by equilibrium kinetics employing a time-varying convective heat transfer coefficient than by other published kinetic models. A more detailed investigation of the fundamental mechanism of reagent (e.g., alcohols) induced decomposition of methane hydrates was initiated utilizing a novel instrument that combines spectroscopy and calorimetry. The instrument employs a high-pressure fiberoptic probe coupled to a spectrometer that is employed to perform Raman measurements inside the sample cell of a Calvet-Tien differential scanning calorimeter (DSC). The Raman signatures allow us to identify specific phase or chemical transitions associated with the thermal signals measured with the DSC. This system currently is being applied in experiments where alcohol solutions are injected isothermally to destabilize methane hydrates. Preliminary Raman data indicate that an alcohol-water complex forms that disrupts the dynamic equilibrium between hydrate formation and decomposition that occurs at the liquid film on the surface of the solid hydrate phase.

The impact of seafloor methane from hydrates on the marine environment is being explored via experiments and modeling. Biological processes (mostly microbial) in the sediment and the water column are believed to play a major role in determining methane levels throughout the marine environment. The underlying metabolic pathways and the factors that affect these processes are not well understood and have been a focus area of the HNEI methane hydrate task. During the present phase of the HEET initiative, we continued our analysis of sediment samples collected from methane hydrate beds in the Gulf of Mexico and the Hikurangi margin off New Zealand. The microbiology of these samples included *Bacteria* and *Archaea* communities that were investigated by use of molecular DNA cloning. The clones were DNA sequenced and phylogenetic trees were constructed for each of these communities. The initial characterization of sediments indicates that these geologically-distinct hydrate bearing sediments contain many unidentified species of *Archaea* and *Bacteria*. Although clones were not obtained that definitively identify specific methanogenic and sulfate-reducing bacteria (SRBs), the potential for the unknown clones to play a role in the methane cycling in this environment does, however, exist.

Model development was pursued to investigate the fate of methane released from the seafloor into the water column, e.g., as a result of inadvertent or purposeful hydrate destabilization. Simple far-field models of the evolution of methane concentration, isotopic composition and methanotroph-carbon concentration throughout a lateral methane plume were explored. The goal of such models is to better parameterize aerobic oxidation by testing simple formalisms against data sets. Since, currently, there is limited information on hydrate-generated methane plumes in the ocean, hydrothermal seafloor vents were used as a proxy. Hydrothermal vents have been the subject of intense study and data sets are available in the technical literature. Data collected from the Juan de Fuca Ridge provided boundary conditions, key parameters and validation

targets for the models. Progress was made in identifying the approximate order of magnitude for the methane oxidation rate constant, and for the amount of carbon held by methane-oxidizing bacteria.

As part of our goal to promote international collaborative R&D on methane hydrates, HNEI technical personnel participated in a multi-national research cruise off New Zealand in June and July 2006. Samples collected during that cruise have been analyzed at UH. HNEI also participated in the 5th International Workshop on Methane Hydrates that was held in Edinburgh, Scotland in October 2006 and will be a co-organizer and sponsor of the 6th Workshop scheduled for May 2008 in Bergen, Norway.

2. Introduction

The Hawaii Energy and Environmental Technologies (HEET) Initiative, funded to the Hawaii Natural Energy Institute (HNEI) of the University of Hawaii through the Office of Naval Research (ONR), was initiated in the summer of 2001 under Grant Number N00014-01-1-0928 to address critical technology needs associated with the exploration and utilization of seabed methane hydrates and the development and testing of advanced fuel cells and fuel cell systems. During the first three years of operation, the focal point of our activity was development of the Hawaii Fuel Cell Test Facility (HFCTF) which houses dual facilities for fuel cell testing and for the synthesis and characterization of methane hydrates. This program ended March 31, 2005.

Subsequently, a second program funded by the HEET Initiative began under Grant Number N00014-04-1-0682 on June 15, 2005, with an end date of June 30, 2006. The efforts covered in this phase were for specific subtasks specified under the areas of fuel cell systems and methane hydrates.

The third program funded by HEET, which is the subject of this report, is covered under Grant Number N00014-06-1-0086, for the period October 17, 2005 to September 30, 2007. Once again, the efforts are organized into subtasks in the main areas of fuel cell systems and methane hydrates. Within fuel cell systems HNEI conducted four major subtasks: PEM fuel cell testing and component development; fuel cell Hardware-in-Loop (HiL) and system simulation development; fuel processing and gas conditioning for hydrogen production; and novel fuel cell and component development. The area of methane hydrates also included four major subtasks: investigations of hydrate destabilization phenomena, characterization of the microbial community in marine hydrate beds, development of models to predict the fate of methane released from the seafloor, and the promotion of international R&D partnerships.

The remaining two sections of this report focus on each of the major areas covered within the HEET initiative. Section 3 is on fuel cell systems, with subsections for each of the associated subtasks for this area. Section 4 covers methane hydrates, including subsections for the subtasks of this area.

This page is intentional blank

3. Fuel Cell Systems

3.1 Introduction

This task area is organized into four major subtasks: PEM fuel cell testing and component development; fuel cell Hardware-in-Loop (HiL) and system simulation development; fuels processing and gas conditioning for hydrogen production; and novel fuel cell and component development. Under this Grant, HNEI expanded the testing and research capabilities of the Hawaii Fuel Cell Test Facility (HFCTF), including additional gas infrastructure to allow accelerated life testing of PEM fuel cells under H_2/O_2 operating conditions and additional infrastructure and diagnostics to allow characterization of the effects of trace impurities. There were new advances in the area of novel fuel cells; development of HiL capabilities for evaluating fuel cells under simulated real-world operating conditions; and continuing work on fuel processing and gas conditioning research.

Details for the activities conducted under each of these subtasks are given below.

3.2 PEM Fuel Cell Testing and Component Development

Primary activities in this area included the installation and validation of a segmented fuel cell system, modification of the existing UTC XT-800 test stands for testing of sub-scale pressurized cells and small stacks, optimization of the existing Greenlight GLP 50 test stands for characterization of the effects of trace impurities on the performance of PEM fuel cells, and purchasing of additional testing equipment and necessary infrastructure improvements to operate this equipment.

3.2.1 Test Stands/Infrastructure Upgrades

During the past year improvements were implemented on several test stands and diagnostic instruments. With continuing high demand for subscale fuel cell testing, we found it valuable to modify another of the UTC XT-800 test stands to allow subscale (50 to 100 cm^2) testing. Modifications included installation of a parallel lower-capacity humidifier compatible with reduced gas flows, and an automated back-pressure regulation system to allow operation from ambient up to 60 psig.

Careful evaluation of all facility, test station, gas sampling, and analysis systems allowed us to improve our accuracy for performing low-level impurity experiments. Using a new high temperature chilled-mirror dew-point sensor, the control strategy of the humidification system was refined to allow very stable adjustment of fuel and oxidant humidification of up to a relative humidity of 100% at 80 °C. Gas sample lines were upgraded with membrane-based water knock-out systems in each sample line for the existing two Greenlight GLP 50 Fuel Cell Test Stands. The purification control of the facility air supply was optimized to reduce CO_2 concentrations from periodic swings of up to ~ 400 ppm CO_2 to less than 1.5 ppm CO_2 .

Upgrades to HNEI's Varian gas chromatograph now allows consistent low-level impurity measurements. The CO/CO_2 -to-methane conversion efficiency of the methanization system at levels less than 5 ppm was stabilized by injecting a small amount of oxygen at the start of each analysis to oxidize any residual carbon build up on the methanization catalyst. GC data analysis showed that the instrument was operating well within its specifications of peak area

reproducibility (<2%), calibration reproducibility (<±3%) and reduction catalyst efficiency (>95%). Below 65 °C the molar flow balance of carbon, even with CO injection concentrations less than 5 ppm, was reproducibly closed within ±2%, indicating very high data accuracy. However, the small-volume water traps used to remove water from the gas sample sent to the GC did not provide complete drying when the humidifier temperature was above 65 °C. In these cases, water diluted the gas sample stream as shown in Figure 3.2-1, resulting in systematic reduced estimate of the molar fraction of trace contaminants. Experiments were conducted to identify corrective measures for humidifier temperatures above 65 °C. The study delivered correction terms for the gas sample streams taken at the fuel cell inlets. Furthermore, non-saturated gas sample streams entering the fuel cell took up water inside of the fuel cell, resulting in water in the gas sample streams at the fuel exits. Sample streams taken at the exit of the fuel cell anode or cathode thus required individual correction terms which depended on humidifier temperature, operating temperature, fuel cell current and stoichiometric gas flows.

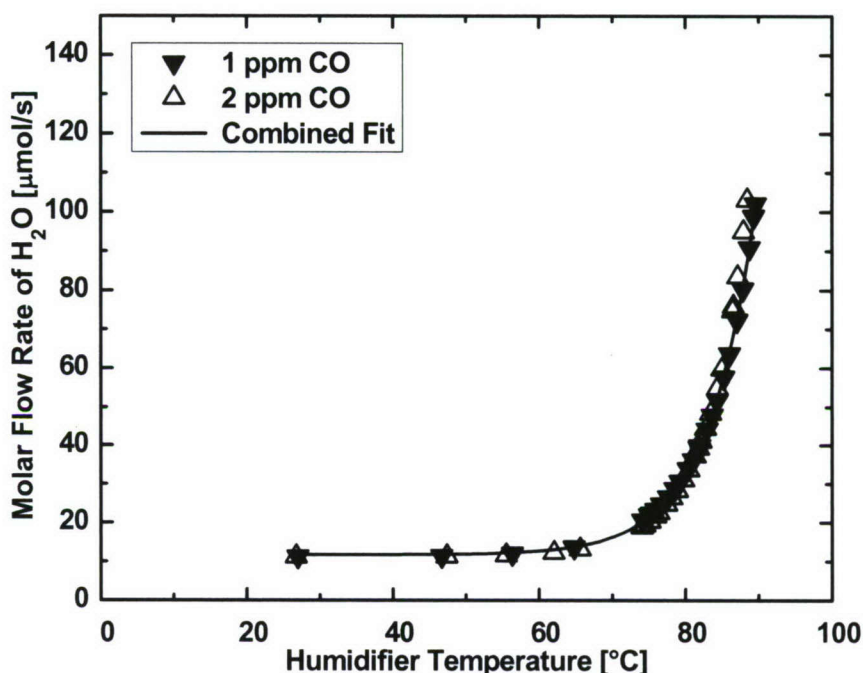


Figure 3.2-1. The measured and calculated molar flow rate of water vapor into the GC as a function of Humidifier temperature for CO injection of 1 and 2 ppm CO.

The resulting detection limits for the various GC detectors are listed in Table 3.2-1. The improvements allowed for reproducible impurity experiments and analysis of low-level impurity injections, e.g., CO impurity levels down to 1 ppm CO. Long-term experiments involving over 200 hours of operation were performed and exhibited consistently high data accuracy.

The available suite of diagnostic techniques at the HFCTF was expanded by purchasing additional equipment. A Solartron 1260 frequency response analyzer (FRA) and Solartron 1287 galvanostat/potentiostat were purchased from Ametek. The FRA allows AC impedance spectroscopy on small- to full-scale fuel cell systems and can, together with the

Table 3.2-1. Detection limits of gas analysis system

Impurity	Detector	Detection Limit
S	PFPD	50 ppb
CO	PDID	100 ppb
CO ₂	FID	100 ppb
C ₃ H ₈	FID	500 ppb
C ₆ H ₆	FID	500 ppb
C ₇ H ₈	FID	500 ppb
O ₂	PDID	10 ppm
N ₂	PDID	10 ppm
H ₂	TCD	100 ppm

galvanostat/potentiostat, be operated as a self-standing diagnostic instrument for analysis of electrochemical processes. The galvanostat/potentiostat can also be utilized for cyclic voltammetry and linear-voltage-sweep experiments which are routinely performed at the HFCTF during impurity testing.

High demands for small-scale testing performed at the HFCTF led to the purchase of a dual test station manufactured by Fuel Cell Technologies. This station was purchased used from Hoku Scientific, a local fuel cell membrane company, that is undergoing redirection of their business interests. This test station is being adapted to match the existing operating fuel cell test stations in their specifications for current, gas flows, humidification, pressure, and temperature, and to allow automated 24/7 operation. Additional gas lines and electrical lines were installed in the facility to supply the additional test stands with gas, water and electrical power.

A segmented cell system was designed and built in house as a diagnostic tool for characterization of impurity effects. This diagnostic system consists of segmented cell hardware, an in-house custom-built current transducer system, and a National Instrument PXI data acquisition instrument. The segmented cell system can be operated with any of the existing test stations at the Hawaii Fuel Cell Test Facility.

The segmented cell hardware was based on the existing HNEI 100 cm² cell design, which consists of a six-channel serpentine flow-field and offers three different heating options: (i) heating pads, (ii) heating cartridge, and (iii) heating/cooling liquid. The segmented flow-field consists of ten cell segments following, consecutively, the path of the six-channel serpentine flow-field. Each segment has an area of 7.6 cm² and consists of its own distinct current collection, and, if desired, distinct gas diffusion layer (GDL) and catalyst area. The cell hardware and electrode segmentation can be applied to either the anode or the cathode.

The data acquisition system allows interrogation of up to 32 current and 32 voltage channels, and is not limited to the existing HNEI 100 cm² cell hardware. The limitation of the individual current sensor for each segment, i.e., 15A, can be increased by using a countercurrent option. This allows for flexibility in cell design and higher accuracy during AC impedance experiments. Figure 3.2-2 shows the current distribution of an Ion Power membrane electrode assembly

(MEA), operated at HNEI's standard conditions of 80 °C temperature, 7/7 psig backpressure, 2/2 stoichiometric flow rates, and 100/50% relative humidity. The cell performed strongest at the cell inlet and showed continuously decreasing performance along the flow-field.

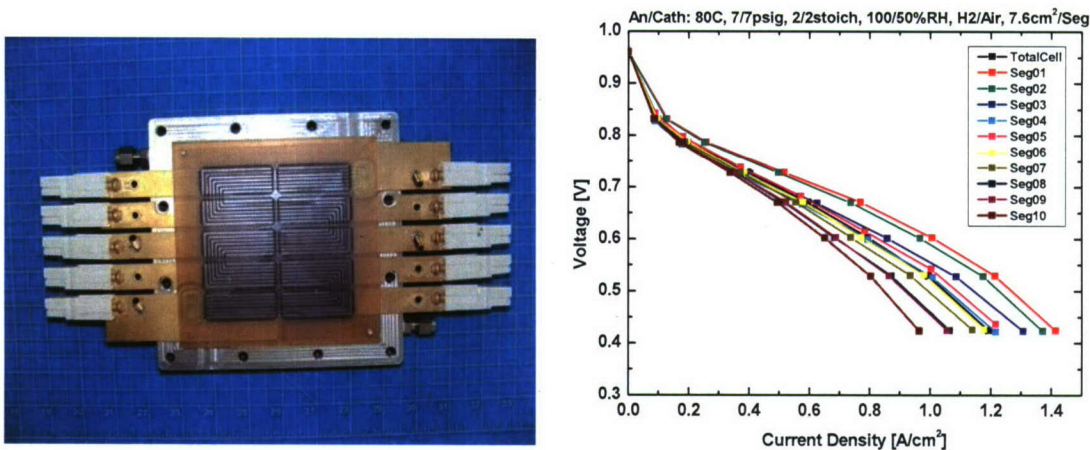


Figure 3.2-2. Left: HNEI's segmented cell hardware. Right: Current distribution of segmented cell.

3.2.2 Cell and Component Testing

New diagnostic and analysis algorithms were developed to allow us to more accurately determine the impact of impurities on cell performance. This method decouples the performance degradation due to impurities from that due to daily decay and aging processes. It employs a polynomial baseline fit of the cell performance prior to impurity exposure which accurately predicts the performance decay due to aging for the entire measurement duration. With this method, the impact of impurities on the electrode overpotential can be exactly determined and compared, even for different operating conditions and fuel cell materials such as MEAs and GDLs. Figure 3.2-3 shows an example of this fitting methodology for 1 ppm CO at 80 °C, anode/cathode operating conditions of H₂/Air flows, 2/2 stoichiometric flow rates, 7/7 psig backpressure, and 80/50% relative humidity.

Changes of the anode overpotential were determined and analyzed for CO partial pressures of 1, 2, and 10 ppm CO. The results are plotted in Figure 3.2-4 in such a way that impurity injection for all measurements occurred after exactly 10 hours of operation. With increasing CO partial pressure, the overpotential increased and the poisoning period (until equilibration was reached) was accelerated. GC analysis during impurity experiments allowed closure of the molar flow balance of carbon to typically $\pm 2\%$. This accuracy allows accurate analysis of CO adsorption and conversion processes over the entire course of the experiment.

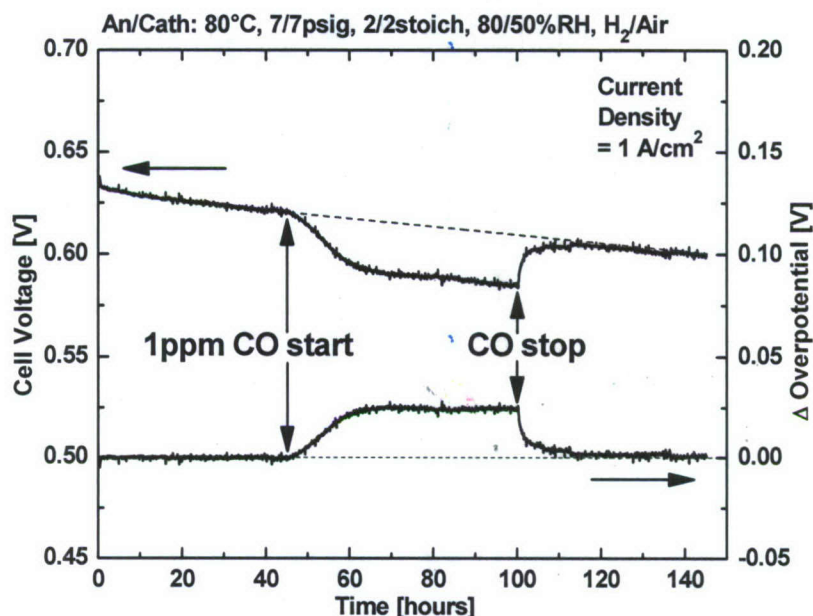


Figure 3.2-3. Top: 1 ppm CO impurity measurement with baseline fit. Bottom: Overpotential change due to 1 ppm CO in anode feed stream.

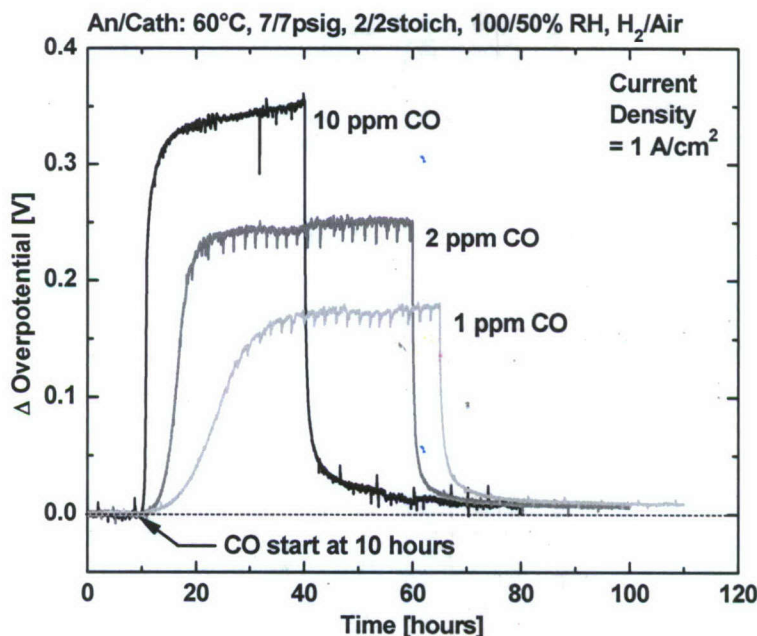


Figure 3.2-4. Overpotential change of the fuel cell due to 1, 2, and 10 ppm CO injected into the anode feed stream at 60 °C and 1 A/cm²

Air contaminant experiments have been performed using sulfur dioxide (SO₂) as oxidant impurity at a constant operating voltage of 0.6 V as shown in Figure 3.2-5. The same total quantity of SO₂ was injected into the fuel cell by adding 1, 2, and 10 ppm SO₂ to the cathode air

feed over 50, 25, and 5 hours, respectively. Slight variations in performance required normalization of the current density for comparison of the results. The normalized cell response is shown in Figure 3.2-5. Normalization was performed to the average current density of the last hour before impurity injection, i.e., starting at 24 hours and ending at 25 hours of operation.

Cell current densities dropped to 11.0, 9.8, and 7.4% of the initial performance with respect to 1, 2, and 10 ppm SO₂. Cell recovery was performed by switching off the SO₂ and recording the current density over a time period of 35 hours. For all three MEAs, recovery was incomplete. The normalized current density recovered to very similar values ranging from 22.1 to 23.6%.

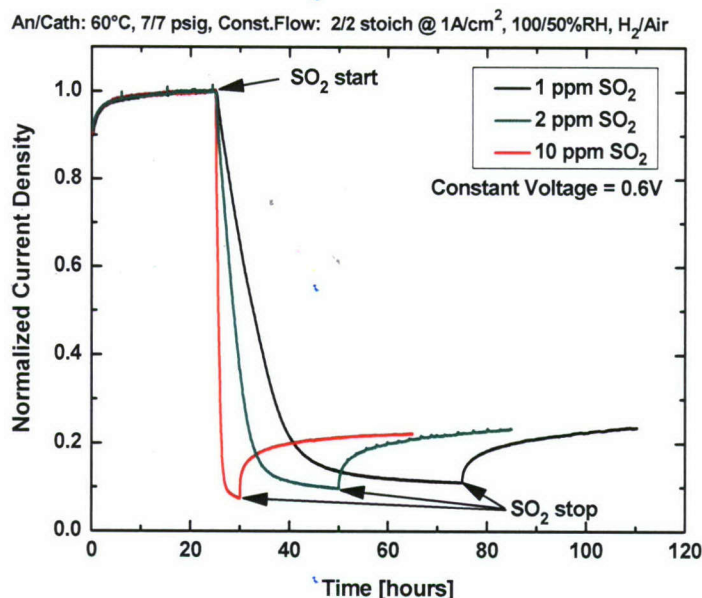


Figure 3.2-5. Normalized current density response due to 1, 2, and 10 ppm SO₂ injected into the cathode feed stream at 60 °C and 0.6 V

Figure 3.2-6 shows cyclic voltammetry (CV) experiments performed at the cathode electrode of the MEA which was used for the 1 ppm SO₂ experiment. These CV experiments were part of the developed protocols for standardized testing and routinely accompany the impurity experiments as part of the beginning of test (BOT) and end of test (EOT) diagnostics. The data indicated shifting peak potentials for hydrogen oxidation and reduction as well as for platinum oxide formation and removal. These results have to be further analyzed to increase understanding of the processes related to exposure of the fuel cell cathode to SO₂.

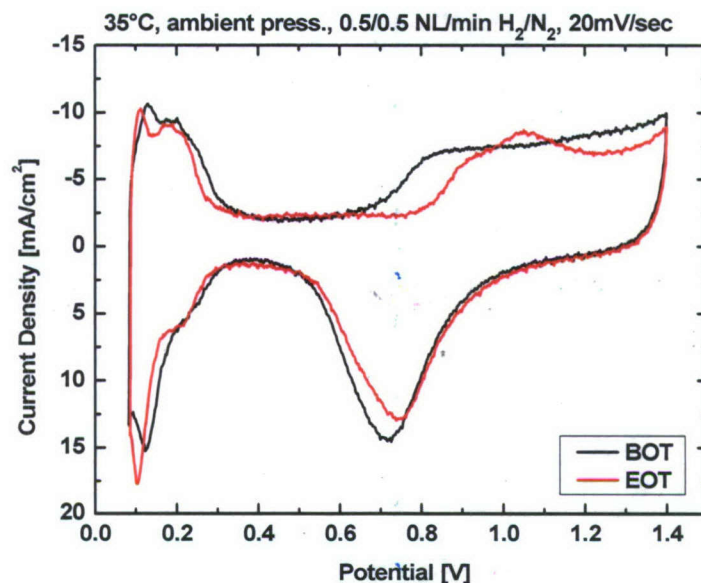


Figure 3.2-6. Beginning of test (BOT) and end of test (EOT) cyclic voltammetry experiments of fuel cell cathode exposed to 1 ppm SO₂ for 50 hours

3.2.3 MEA Fabrication Laboratory

The MEA fabrication laboratory was established during the previous award under the HEET Initiative. During this award period, HNEI successfully produced and tested MEAs using the previously described technique. To prevent loss of platen parallelism, the existing platens of both hot presses were exchanged with non-corrosive material. Figure 3.2-7 shows polarization experiments of an HNEI MEA with 20% Pt/C catalyst and 0.2/0.2 mg Pt/cm² loading tested at ambient and 2 bar gauge pressure. MEA performance was within the expected range at the given operating conditions, catalyst and catalyst loadings.

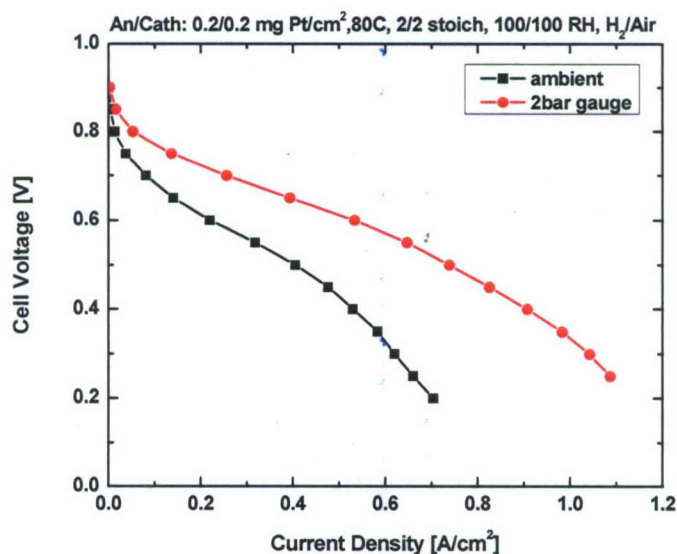


Figure 3.2-7. Polarization curves of an HNEI-fabricated MEA at ambient and 2 bar gauge pressure

3.2.4 Papers and Presentations Resulting from Efforts

PAPERS

G. Bender, M. Angelo, K. Bethune, S. Dorn, R. Rocheleau, "Low Level Impurity Testing for Direct Hydrogen Polymer Electrolyte Fuel Cells", in preparation for submission to Journal of Power Sources, 2007.

G. Bender, M. Angelo, K. Bethune, S. Dorn, R. Rocheleau, "The Carbon Monoxide Balance Of A Direct Hydrogen Polymer Electrolyte Fuel Cell During Exposure To Low Level Carbon Monoxide", in preparation for submission to Journal of the Electrochemical Society, 2007.

PRESENTATIONS

G. Bender, K. Bethune, M. Angelo, S. Dorn, D. Wheeler, R. Rocheleau, "The Impact of Low Level CO Impurities on Cell Degradation", poster presentation at Fuel Cell Seminar, October 15-19, 2007, San Antonio, Texas.

G. Bender, K. Bethune, M. Angelo, S. Dorn, R. Rocheleau, "The Anode Overpotential Dependence on Oxygen Permeation During PEMFC Operation with CO", presented at 212th Electrochemical Society Meeting, Washington DC, October 7-12, 2007.

G. Bender, M. Angelo, K. Bethune, S. Dorn, R. Rocheleau, "Impurity Testing at HNEI, University of Hawaii", Modeling Workshop, Argonne National Laboratory, August 30, 2007.

G. Bender, K. Bethune, D. Wheeler, R. Rocheleau, "Impurity Testing at HNEI", DOE Hydrogen Fuel Quality Meeting, Washington DC, February 14-15, 2007.

3.3 Fuel Cell Hardware-in-Loop and System Simulation Development

The objectives of this subtask were divided between two major activities: a) enhancement of existing Hardware-in-Loop (HiL) testing capabilities, and b) development of fuel cell system simulation tools. The HiL capability and simulation tools are intended to contribute towards providing a Rapid Prototyping System (RPS) for Naval application of fuel cell systems. Both of these topics will be discussed in the following paragraphs.

3.3.1 Scope of Work and Approach

HiL Development

The HNEI fuel cell Hardware-in-Loop (HiL) dynamic test station has been developed and is in operation evaluating Polymer Electrolyte Membrane Fuel Cells (PEMFCs) under dynamic application conditions. HiL methodology is well established in the automotive industry, where the technique is applied to develop and debug control algorithms for automotive drive systems. Figure 3.3-1 shows HNEI's HiL concept layout.

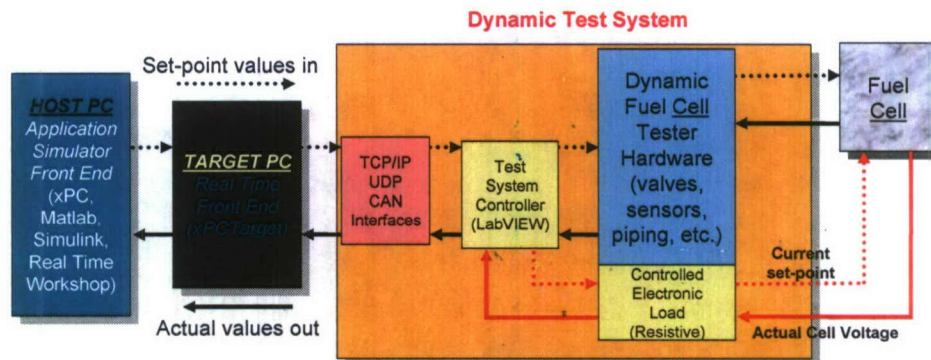


Figure 3.3-1. HNEI fuel cell Hardware-in-Loop concept

HNEI's fuel cell HiL process is capable of developing optimal control strategies and algorithms for a fuel cell system and its associate components using a real-time simulation for a desired fuel cell application under a dynamic load profile. The de-coupling of parameters, combined with high-end instrumentation allows distinguishing of the impact and allocation of weak spots, the performance degradation, and the ageing effects of the cell or stack. The process allows the evaluation of both the performance and durability of a specific fuel cell or stack design (geometry, materials, flow fields, etc.) under dynamic test conditions that mimic the actual conditions that a cell or stack will experience when placed in a realistic environment.

The plan at the beginning of this reporting period was to improve the dynamic response of our HiL fuel cell test stand. In order to make this improvement, it was decided that the vendor-supplied control architecture for the test stand should be replaced. This was accomplished with a controller configuration designed at HNEI. The details of this configuration are discussed in the Technical Accomplishments section on the next page.

With the new control/communication architecture designed, installed, and tested, we experienced an overall controller response time of less than one second as compared to greater than one

second overall response time with the original configuration. The new control/communication architecture allows us to demonstrate the HiL proof-of-concept for the dynamic capabilities of the test stand by running a real-time computer simulation (e.g., FCVSim: Fuel Cell Vehicle simulation) and having the test stand respond quickly enough to produce meaningful results. We could not get valid results using this simulation with the original test stand architecture and its slower response times.

The overall response time improvement also means that we see an increase in the pure data transfer rate of at least a factor of 18-20 over the data rate experienced with the vendor-supplied controller. Besides the improvement in data-rate transfer, we benefited from enhanced operational flexibility, safety, and reliability of the test stand. The control redesign not only allowed us to achieve measurable improvements in performance, as just mentioned, but we see the benefit of improved simulation software integration, too. These improvements now permit HiL evaluation and validating of high-performance Fuel Cell Energy Power System (FCEPS) designs and fuel cell components when applied to an unmanned underwater vehicle (UUV) and other naval applications.

Simulation Tool Development

Since there is an interest in applying fuel cells to UUVs, our group created a simulation tool called UUVSim. Interest in fuel cell technology is based on the assumption that it has the potential to increase the energy storage in a given UUV as compared to other Air-Independent Propulsion systems utilizing energy storage devices such as batteries. This increased energy storage could potentially enable a UUV to achieve greater mission duration and/or range of operation. UUVSim could provide an initial evaluation and technology screening for the application of an FCEPS for the propulsion of a UUV.

When developing the UUVSim simulation program to run in the HiL test station at the Hawaii Fuel Cell Test Facility, efforts were made to find an alternative simulation environment to the one initially investigated. That alternative simulation environment turned out to be Modelica, an object-oriented, physical modeling language. Research efforts were then redirected to model a PEMFC using Modelica. The creation of the *PEMFCSim* library was the result.

3.3.2 Technical Accomplishments

HiL Development

The HiL project involves the development of the real-time simulation system using a commercially available host-target environment program. This project consists of running a fuel cell system simulation with a real cell, or fuel cell stack, using our dynamic-response test stand. During the reporting period in question, the following main objectives were achieved:

Upgrade of HiL#1.0 to HiL#1.9 was achieved. The HiL#1.9 upgrade has the capability of achieving dynamic response in the 50-100 millisecond (ms) range (see Figure 3.3-2), as compared to HiL#1.0's ≥ 800 ms response time (see Figure 3.3-3). This capability enabled us to test the fuel cell under realistic dynamic conditions equivalent to what a cell or stack would experience when operated under dynamic transient conditions.

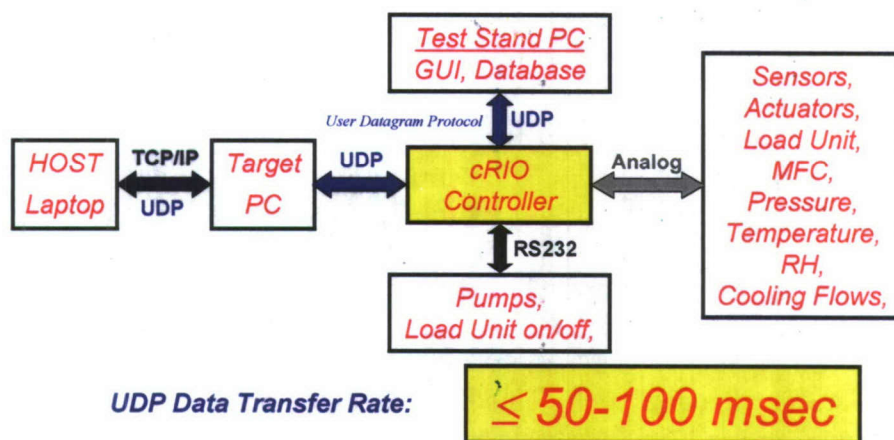


Figure 3.3-2. New controller/communication configuration

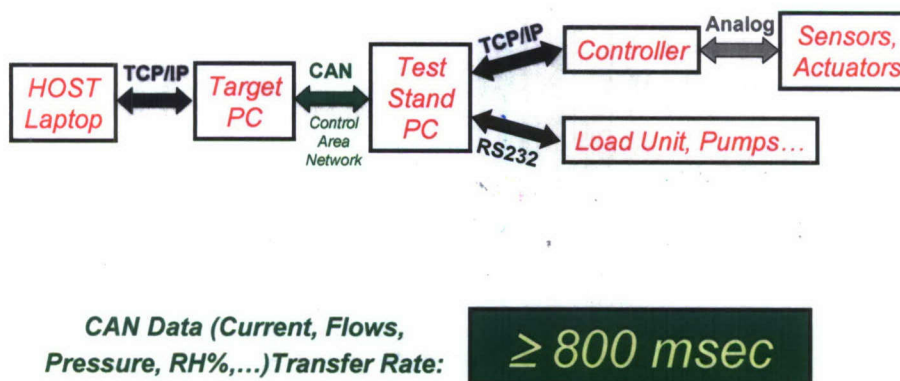


Figure 3.3-3. Original controller/communication configuration

The proof-of-concept demonstration of the capability of HiL#1.9 was demonstrated to visitors during the November 2006 Fuel Cell Seminar held in Honolulu, Hawaii. Office of Naval Research personnel were in attendance. The demonstration included the real-time running of two configurations of the hybrid FCVSim (Battery and PEMFC) on HiL#1.9, using 100 cm² PEMFC hardware.

Installation and testing of an external cooling system for the HiL test station was accomplished. This made it possible to maintain a constant operating temperature of the cell, facilitating the empirical modeling and validation process using our simulation tools with the test stand. Installation and testing of fuel cell exhaust heaters were also carried out.

Empirical modeling/validation of a fuel cell model using three different fuel cells:

Lynntech 100 cm² PEMFC with Lynntech endplates and MEA.

HNEI 100 cm² PEMFC with HNEI hardware (endplates & flow fields) and MEA.

HNEI 100 cm² PEMFC with HNEI hardware and commercial MEA (Ion Power).

For each PEMFC noted above, measurements were made under specific conditions to determine certain parameters which were then used in a model developed at HNEI to predict the

performance of the cell at various operating conditions. Once the model's results were validated, the resultant data was implemented in our simulation models UUVSim and FCVSim.

Simulation Tool Development

The *PEMFCSim* library, which is a simulation structure designed to facilitate the simulation of PEM fuel cells, was completed during this reporting period. *PEMFCSim* uses methods that are physical, dynamic, and component-based. It is written in Modelica. The library, as currently implemented, offers one-dimensional and quasi-two-dimensional fuel cell simulations and is based on existing models from the literature. The Modelica object-oriented modeling approach allows the *PEMFCSim* library simulations to use intuitive and physically-representative component boundaries and connections. This flexibility makes the *PEMFCSim* library ideal for collaboration among researchers focusing on different aspects of fuel cell modeling and simulation.

PEMFCSim library can be integrated with and run within HNEI's existing Simulink-based fuel cell system and fuel cell vehicle models currently being investigated in HNEI's HiL project.

3.3.3 Papers and Presentations Resulting from Efforts

PAPERS

M.B.V. Virji, P.L. Adcock, R.M. Moore, J.B. Lakeman, "Modelling and Simulation of an Indirect Diesel Proton Exchange Membrane Fuel Cell (PEMFC) System for a Marine Application," Fuel Cell Science and Technology, (in press, scheduled publication date November 2007).

R.M. Moore, G. Randolph, M. Virji, and K.-H. Hauer, "Fuel Cell Hardware-in-Loop for PEM Fuel Cell Systems", Electrochemical Society Transactions – 30th Fuel Cell Seminar, Vol. 5, Issue 1, pp. 309-319, March 2007.

R.M. Moore, K.H. Hauer, G. Randolph, and M. Virji, "Fuel cell evaluation for dynamic applications", Electrochemical Society Transactions, v. 3, Issue 1, pp. 923-930, October-November 2006.

R.M. Moore, S. Ramaswamy, J.M. Cunningham, and K.H. Hauer, "A Dynamic Simulation Tool for the Battery-Hybrid Hydrogen Fuel Cell Vehicle," Fuel Cells—From Fundamentals to Systems, n. 5, pp. 387-402, October 2006.

R.M. Moore, K.H. Hauer, and S. Ramaswamy, "Energy Utilization and Efficiency Analysis for Hydrogen Fuel Cell Vehicles," Journal of Power Sources, Vol. 159, Issue 2, 22 September 2006, pp. 1214-1230.

R.M. Moore, K.H. Hauer, G. Randolph, M. Virji, "Fuel Cell Hardware-in-Loop," Journal of Power Sources, Vol. 162, pp. 302-308, August 2006.

G. Randolph, R.M. Moore, "Test System Design for Hardware-in-Loop Evaluation of PEM Fuel Cells and Auxiliaries," Journal of Power Sources, Vol. 158, n. 1, pp. 392-396, July 2006.

K.L. Davies, R.M. Moore, "Unmanned Underwater Vehicle Fuel Cell Energy/Power System Technology Assessment," IEEE Oceanic Engineering Society, (in press, accepted 22 June 2006).

PRESENTATIONS

R.M. Moore, G. Randolph, M. Virji, K.H. Hauer, "Fuel Cell Based Hardware-in-Loop for PEMFC Systems", 2006 Fuel Cell Seminar, Honolulu, Hawaii, 13-17 November 2006.

R.M. Moore, K.H. Hauer, G. Randolph, M. Virji, "Fuel Cell Evaluation for Dynamic Application," Presentation for the Oral Presentation in Section B (Fuel Cell Systems, Cell Stack and Component Hardware) of the "Proton Exchange Membrane Fuel Cells 6" Seminar at ECS 210, 29 October – 3 November 2006, Cancun, Mexico.

This page is intentional blank

3.4 Fuel Processing and Gas Conditioning for Hydrogen Production

Subtask 3.4.1: Sulfur Removal from Fuel Gas using Low Temperature Sorbents

The primary objective for this subtask is to design low temperature sorbents for sulfur removal from fuel gas.

3.4.1.1 Scope of Work and Approach

Due to the lack of naturally occurring hydrogen (H_2), successful fuel cell implementation will require H_2 production based on highly efficient fuel processing in which fuels are converted to H_2 , and contaminants and pollutants are removed. Sulfur is a contaminant of particular interest due to the deactivation it causes in catalyst and electrode materials. This subtask focused on the removal of sulfur compounds from fuel gas using ambient temperature sorbent materials.

Pipeline gases, such as natural gas (NG) and synthetic natural gas (SNG), are composed of methane (CH_4), nitrogen (N_2), carbon monoxide (CO), carbon dioxide (CO_2), water vapor (H_2O), trace amounts of higher hydrocarbons, and sulfur compounds. Due to their developed infrastructure and relatively abundant supply, NG and SNG will be preferred, near-term fuels for fuel cells in residential applications. The sulfur compounds, which are either naturally present or added intentionally as odorants for leak detection, include sulfides, mercaptans, disulfides and thiophenes. Typical sulfur odorants are tetrahydrothiophene (THT), tertiary butyl mercaptan (TBM), ethyl mercaptan (EM), and dimethyl sulfide (DMS). These sulfur compounds are strong poisons for reformer and fuel cell catalysts. Therefore, the removal of sulfur compounds from pipeline gas is a key component for fuel cell applications.

There are different sulfur tolerances reported in the literature for the catalysts used in the reformer and fuel cells anodes. If fuel gas contains 5 ppm of THT, it would produce reformat containing approximately 1 to 2 ppm of H_2S . The resulting sulfur content is high enough to adversely affect the performance of a PEM (proton exchange membrane) fuel cell; negative effect has been verified at H_2S concentration of as low as 0.2 ppm [1]. More strict limitations, sulfur concentrations of less than 10 ppb or 20 ppb, have been reported [2, 3]. In general, sulfur compounds should be removed to the lowest possible level prior to fuel processor and fuel cell use.

Fuel desulfurization is typically carried out using the following competing technologies: adsorption, selective catalytic oxidation (SCO) [4-6] and hydrodesulfurization (HDS). Compared with SCO and HDS technologies, adsorption can achieve sulfur removal at ambient pressures and temperatures, while SCO requires air addition and elevated temperature (150 to 280 °C), and HDS requires hydrogen addition/recycle and elevated pressure and temperature (300 to 400 °C). Therefore, the adsorption approach is attractive and practical to apply in a small-scale fuel cell system, e.g., in residential applications or a transportation system.

Activated carbons are porous sorbents that can be utilized in removing sulfur compounds [7, 8], but offer relatively low sulfur-adsorption capacity at ambient temperature. The adsorption capacity of activated carbons is determined by their physical or porous structure, but is also strongly influenced by their chemical structure. To improve the sorbent performance, surface modification by oxidation [9] or metal impregnation [10] has been applied and verified. These methods can create large amounts of acid groups and more adsorption sites on the surface of

activated carbon [9, 11, 12], which can increase sulfur capacity. It has been pointed out in the literature that modification by oxidation leads to the fixation of weakly acidic functional groups [13]. HNO_3 oxidation can produce a large number of acid surface groups, mainly carboxylic acid, anhydrides, lactones and phenol groups [9, 11]. H_2O_2 oxidation usually generates less acidic groups than the HNO_3 treatment [14]. The use of inorganic metals in carbon modification can form catalytically active metals on the carbon surface that serve as adsorption active points. These different functional groups and metal ions on the carbon surface play important roles in the adsorption/oxidation of sulfur compounds, such as H_2S to sulfuric acid [15, 16], and mercaptans to disulfides [12, 17, 18].

The purpose of the present work is to identify effective methods to modify activated carbons and improve their capacity to adsorb sulfur compounds present in SNG. This work focused on the effects of modification methods, either by oxidizer or impregnates, on sulfur adsorptive capacity of carbons. The effects of modification methods on the individual sulfur compound removal were also investigated. The results of this work were used to design a composite sorbent that improves the adsorptive selectivity for individual sulfur compounds while minimizing material requirements.

3.4.1.2 Experimental

3.4.1.2.1 Sorbent preparation and characteristics

A coconut shell activated carbon (OLC Plus 12x30, Calgon Carbon Corporation) was used as the parent material for all samples modified by impregnation or oxidation.

Impregnation. The selected metal impurities were from the Zn group ($\text{Zn}(\text{NO}_3)_2$ and ZnAc_2), Cu group ($\text{Cu}(\text{NO}_3)_2$ and CuSO_4), Fe group (FeCl_3), K group (KCl , KOH and K_2CO_3), and Na group (NaOH and NaCO_3). The virgin carbon was impregnated by immersing 40 g in a 0.1N solution of the selected metal at 70-80 °C for 6 hours. The modified carbons were then dried at 115 °C overnight. The loaded amount was around 0.4 mmol metal per gram of virgin activated carbon.

Oxidation. Sorbent was prepared by mixing 40 g of the virgin activated carbon with 70 ml of 68-70% HNO_3 or 100 ml of 50% H_2O_2 at room temperature until there was no further gas evolution. The sample was washed with distilled water until no further change in pH was detected (around pH = 5), and then dried overnight in an oven at 115 °C.

Testing procedure and apparatus. A stainless steel pipe 45.7 cm in length and 2.43 cm in inner diameter was used as the sorbent column. All of the components including the sorbent column and gas delivery lines were treated with a Sulfinert® coating or were made from Teflon to prevent sulfur compounds from being adsorbed on the working surfaces of the system. A Teflon insert with an inner diameter of 1.2 cm was packed with sorbent and placed in the column. A 4 g mass of sorbent was tested in all cases. The sorbent bed was about 8 cm long with the major axis oriented vertically. To distribute the flow evenly, 3 mm glass beads were packed into the container below and above the sorbent. SNG was supplied from a laboratory gas-service valve to the sorbent column at a flow rate of 4.0-4.5 l/min using a pump. After the SNG passed through the sorbent, it was analyzed with a gas chromatograph (GC).

The concentrations of sulfur species were measured with a Shimadzu 2041 GC equipped with a capillary column (Rtx-1, 60m-0.53-7 μm , Restek Corporation) and sulfur chemiluminescent

detector (SCD) (Sievers Model 355). Helium (He) served as carrier gas and a six-port sampling valve was used to make automatic injections of samples from the gas exiting the sorbent bed.

In each analysis, the GC column temperature was held at 50 °C for 1 min, ramped to 125 °C at 20 °C/min, ramped to 180 °C at 10 °C/min, held at 180 °C for 1 min, and finally cooled to 50 °C at 100 °C/min. Thus, effluent gas was sampled and analyzed with a cycle time of 13 min. Before and after the sorption test, SNG was analyzed for sulfur compounds from a gas line that bypassed the sorbent bed. Tests typically lasted 10 hours.

The SCD is an equimolar response detector for sulfur independent of the host sulfur compound. Thus, a permeation tube device (Model 355, Kin-Tek Laboratories) loaded with THT was used for sulfur calibration.

3.4.1.2.2 Evaluation of sorbents performance

The sulfur sorption capacity of candidate sorbents was determined by breakthrough testing. Because of the different concentrations with varied sulfur compounds in the SNG, the breakthrough is defined as the first detection of sulfur compounds at different critical points, which is 0.2 ppm for THT and 0.02 ppm for the other S compounds, as shown in Fig. 3.4-1, and 0.5 ppm is the value for the total sulfur in the outlet gas.

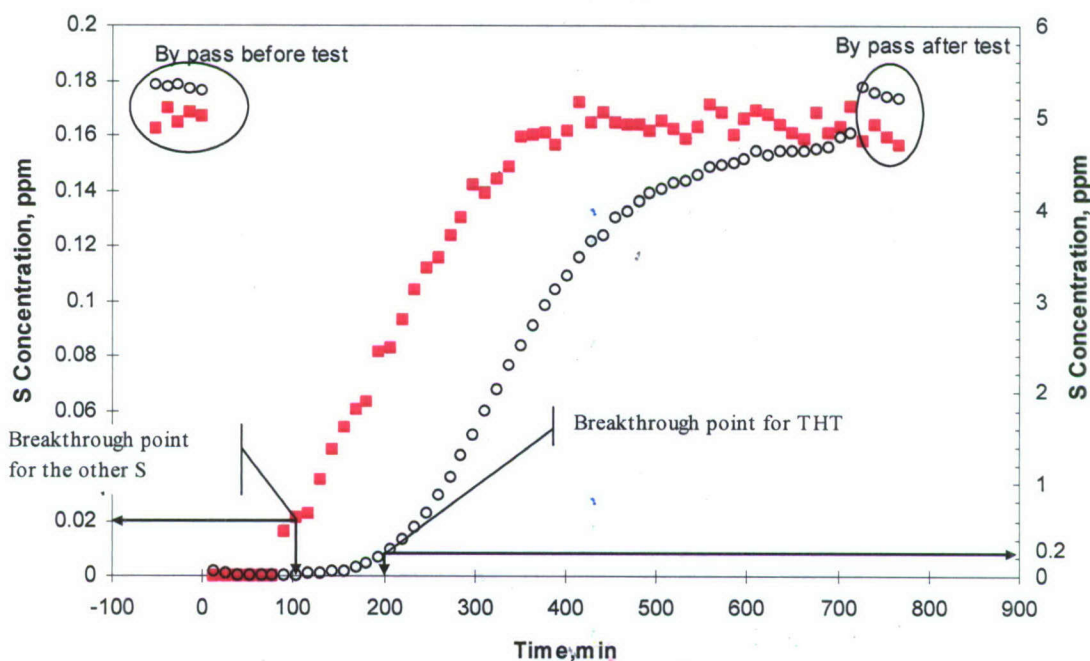


Figure 3.4-1. Determination of breakthrough points for THT and the other sulfur compounds

The sulfur capacity was calculated by using the following equation:

$$S_{cap} (mg / g) = \frac{Q (l / min) \times t (min) \times S_{conc} (ppm) \times 32000 (mg / mol)}{22.4 (l / mol) \times m_{sorb} (g) \times 10^6} \quad (1)$$

where, S_{cap} (mg/g) is the sulfur capacity in milligram elemental sulfur per gram of sorbent; Q (l/min) is the SNG flow rate; t (min) is the breakthrough time; S_{conc} (ppm) is the total sulfur

concentration in the SNG; m_{sorb} (g) is the mass of sorbent tested; and 32,000 (mg/mol), 22.4 (l/mol), and 10^6 are sulfur molar weight, molar volume of ideal gas, and unit conversion from ppm to molar concentration, respectively.

3.4.1.3 Technical Accomplishments

3.4.1.3.1 Sulfur compounds in SNG

Figure 3.4-2 is a typical chromatogram of sulfur compounds in SNG. Eight sulfur compounds were detectable as shown in the figure, including H₂S, methyl mercaptan (MM), EM, DMS, dimethyl disulfide (DMDS), THT, ethyl disulfide (EDS) and one unknown compound, hereafter referred to as UN1. Among these sulfur compounds, THT is added as an odorant and is present in the highest concentration. The concentrations of these various sulfur compounds are presented in Table 3.4-1.

3.4.1.3.2 Evaluation of the sorbents performance

The performance of each sorbent was evaluated by breakthrough testing. Figure 3.4-3 shows the breakthrough curves of each detectable sulfur compound in SNG, using virgin coconut shell activated carbon as sorbent. Different breakthrough points indicate that the carbon surface has different selectivity for each of the sulfur compounds. To compare the capacities of the various sulfur compounds among the tested sorbent, Equation 1 was used to calculate the uptake capacity of virgin and modified activated carbons. Table 3.4-2 presents the calculated results based on elemental S (mg) per gram of activated carbon for individual and total sulfur contents

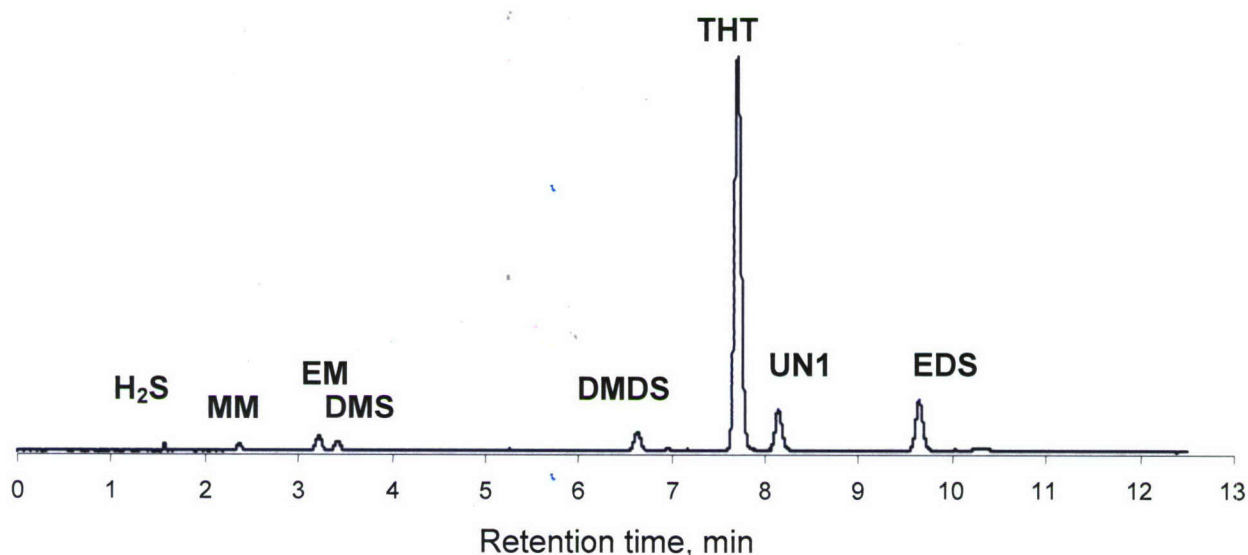


Figure 3.4-2. Chromatogram plot of sulfur compounds in SNG

Table 3.4-1. Sulfur compounds and measured concentrations in Honolulu SNG pipeline gas

Sulfur Compounds	H ₂ S	MM	EM	DMS	DMDS	THT	UN1	EDS	Total
Conc (ppm)	0.06-0.15	0.05-0.13	0.1-0.4	0.06-0.22	0.07-0.23	4.2-7.8	0.3-1.0	0.13-0.18	5.3-9.9

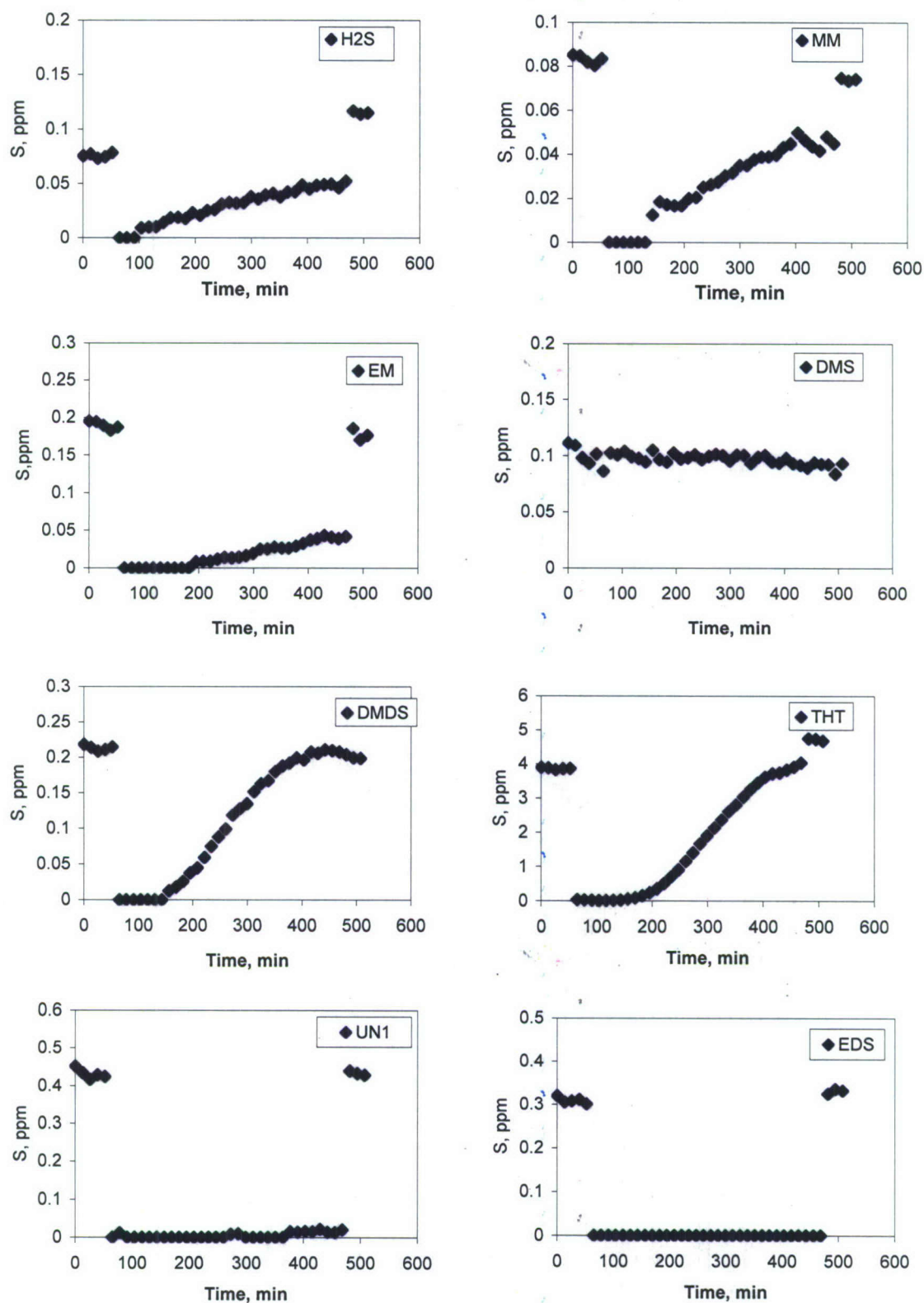


Figure 3.4-3. Breakthrough curves of each sulfur compound for virgin activated carbon

Table 3.4-2. Sulfur compounds uptake capacity in virgin and modified activated carbon based on ~ 10-hour sorbent tests (mg S /g activated carbon)

Sulfur compounds	H ₂ S	MM	EM	DMS	DMDS	THT	UN1	EDS	Total
Virgin AC	0.02	0.02	0.07	0.00	0.03	0.91	0.28	>0.17	1.32
<i>Treated with oxidizer</i>									
AC-HNO ₃	0.03	>0.09	>0.23	0.00	0.29	3.43	>0.43	>0.26	4.80
AC-H ₂ O ₂	0.04	>0.06	>0.16	0.00	0.13	2.05	>0.33	>0.15	2.90
<i>Impregnated with Cu</i>									
AC-CuSO ₄	>0.17	>0.15	>0.33	0.00	0.11	1.55	0.37	>0.36	2.10
AC-Cu(NO ₃) ₂	>0.14	>0.06	>0.12	0.00	0.05	1.76	0.24	>0.33	2.30
<i>Impregnated with Zn</i>									
AC-ZnAc ₂	>0.10	>0.13	>0.36	0.00	0.07	0.52	0.25	>0.33	0.86
AC-Zn(NO ₃) ₂	>0.08	>0.09	>0.22	0.00	0.11	2.14	0.42	>0.27	2.68
<i>Impregnated with Fe</i>									
AC-FeCl ₃	0.02	>0.15	>0.45	0.03	0.29	2.40	>1.06	>0.75	3.50
<i>Impregnated with Alkaline</i>									
AC-NaOH	0.04	0.03	0.09	0.00	0.07	1.24	>0.25	>0.20	1.77
AC-NaCO ₃	0.03	0.03	0.12	0.00	0.13	1.58	>0.42	>0.31	2.25
AC-KOH	0.11	0.05	0.13	0.00	0.09	1.08	0.28	>0.35	1.70
AC-K ₂ CO ₃	0.04	0.05	0.20	0.00	0.11	0.83	0.30	>0.46	1.43
AC-KCl	0.07	0.05	0.12	0.00	0.07	0.89	0.25	>0.22	1.15

H₂S. Virgin carbon had the lowest capacity for H₂S (0.02 mg/g) out of all the sorbents tested. Both oxidization and alkaline impregnation improved sorption capacity up to 5.5 times greater than that of virgin carbon. Sorbents impregnated with Cu or Zn, however, didn't experience breakthrough during the more than 10-hour test, showing that they have much greater H₂S uptake capacity.

MM and EM. Virgin carbon also had the lowest capacity for MM (0.02 mg/g) and EM (0.07 mg/g). Sorbents impregnated with alkaline had a capacity up to 2.5 times greater for MM and nearly 3 times greater for EM when compared with virgin carbon. Breakthrough was not detected for the other sorbents indicating that oxidation and impregnation of Cu, Zn and Fe increased the AC sulfur adsorption capacity by at least 2 to 3 times for MM and EM, respectively. Moreover, MM is likely to be oxidized [7] on the carbon surface to DMDS that remains strongly adsorbed in the pore system, due to its larger size and higher boiling point.

DMS. DMS is regarded as the most difficult compound to remove [19] from pipeline gas. Breakthrough of DMS always occurred first, most sorbents having little or no uptake capacity. AC-FeCl₃ was the only sorbent which had any measurable uptake capacity (0.03 mg/g) under the test conditions.

DMDS. Virgin carbon had the lowest DMDS capacity (0.03 mg/g). The highest capacity was observed by the sorbents oxidized with HNO₃ or impregnated by FeCl₃, both showing nearly 10 times greater capacity. All other sorbents' uptake capacity for DMDS was improved 2-4 times. It was also found that virgin carbon and the sorbents impregnated with alkali had a higher capacity for DMDS than for MM, indicating that DMDS is more easily adsorbed than MM.

THT. Virgin carbon had an uptake capacity of 0.91 mg/g of THT. As was the case for DMDS, AC-HNO₃ and AC-FeCl₃ had the highest THT capacities with 3.43 mg/g and 2.4 mg/g, respectively. Three sorbents, AC-K₂CO₃, AC-KCl, and AC-ZnAc₂, had THT capacities less than that of virgin carbon. All other sorbents had increased capacity; however, some only marginally so.

Unknown, UN1. This sulfur compound has not been identified. Virgin carbon had an uptake capacity of 0.28 mg/g. Cu, Zn and K impregnated sorbent reached breakthrough with a capacity similar to that of virgin carbon. Sorbents oxidized with HNO₃ and H₂O₂ or impregnated with NaOH, Na₂CO₃ and FeCl₃ did not experience breakthrough during the testing time, which likely indicates higher capacity for this unknown sulfur compound.

EDS. This is the easiest sulfur compound to capture. None of the sorbents, including virgin carbon, experienced breakthrough during the testing period.

Total sulfur. AC-HNO₃ had the highest total sulfur capacity of all tested sorbents, but also had poor uptake capacity for H₂S and DMS. AC-FeCl₃, while having the second highest total uptake capacity, had a higher DMS capacity than AC-HNO₃. AC-Zn(NO₃)₂ had the third highest total sulfur capacity and an enhanced H₂S capacity. All other sorbents, except AC-ZnAc₂ and AC-KCl, were also improved by surface modification.

3.4.1.3.3 Evaluation and optimization of the composite sorbents

The evaluation of modified carbons indicates that competitive or selective adsorption of sulfur species occurred on the carbon surface. Sorbent beds using only one type of modified carbon would first exhibit breakthrough for the most recalcitrant sulfur compound, even though the sorbent had underutilized capacity for the other sulfur components. Due to the stringent requirements for fuel processing and fuel cell catalyst materials, early breakthrough of recalcitrant S compounds, even at low concentrations, could impact system performance. A composite sorbent for the removal of a suite of targeted sulfur compounds could be designed based on the sulfur removal capability of individual modified carbons.

Two modified carbons were used to prepare a composite sorbent consisting of 50% AC-Cu(NO₃)₂ and 50% AC-FeCl₃. AC-Cu(NO₃)₂ has a larger capacity for H₂S and a lower capacity of DMS, DMDS, and UN1 than AC-FeCl₃. The composite sorbent was expected to provide better performance, i.e., improved selectivity and capacity for the sulfur compounds identified in the SNG. The test results were shown in Table 3.4-3. As expected, the composite sorbent was improved in H₂S, DMS, DMDS and UN1 capacities.

Table 3.4-3. Sulfur capacities for the composite sorbent of 50% AC-Cu(NO₃)₂ and 50% AC-FeCl₃

Sulfur Compounds	H ₂ S	MM	EM	DMS	DMDS	THT	UN1	EDS	Total
mg S /g sorbent	>0.08	>0.17	>0.57	0.07	0.42	2.31	>1.85	>1.31	3.70

A mathematical (linear programming) model was formulated to optimize the design of the composite sorbent. Let x_i represent the mass of sorbent i in the composite and let c_{ij} represent the

sulfur capacity of sorbent i for sulfur compound j . Thus, x_i 's are the decision variables for the model and the objective is to choose their values so as to minimize sorbent mass:

$$\text{Minimize } Z = \sum_{i=1}^n x_i, \quad (2)$$

subject to the constraints that sufficient sorbent capacity be included for the removal of each individual S compound present in the SNG. Let Y_j represent the target mass (mg) of sulfur compound j to be adsorbed over the life of the composite sorbent bed, then the constraint equations are:

$$\sum_{i=1}^n x_i c_{ij} \geq Y_j \quad \text{for } j = 1 \text{ to } m. \quad (3)$$

Because x_i cannot be negative, it is necessary to restrict the decision variables to be positive:

$$x_i \geq 0 \quad \text{for } i = 1 \text{ to } n. \quad (4)$$

To apply the above mathematical model, two types of sorbents, AC-Zn(NO₃)₂ and AC-FeCl₃ were selected for sulfur removal from SNG in a 1 kW fuel cell application using SNG as fuel for H₂ generation. The composite sorbent bed would be required to remove sulfur from approximately 2500 m³ of SNG (the fuel utilization efficiency is assumed as 75%), the amount required over one year of operation. Table 3.4-4 presents the assumed concentrations for sulfur species present in the SNG and the total amounts of sulfur species to be removed from the SNG during one year of operation. The sulfur capacity of each compound is listed in Table 3.4-4. In cases where no breakthrough occurred during a test, the sulfur capacity is shown as being greater than the amount of sulfur absorbed by the bed over the test duration. This value was used in the linear programming exercise.

Table 3.4-4. Assumed sulfur concentration in the SNG and target sulfur removal per year, based on a 1 kW fuel cell system consumed by 2500 m³ SNG

Sulfur Compounds	H ₂ S	MM	EM	DMS	DMDS	THT	UN1	EDS
S concentration in SNG (ppm)	0.1	0.08	0.2	0.1	0.2	5.0	0.3	0.5
S removal target (mg)	357	285	714	357	714	17,857	1,071	1,785

According to the mathematical model, the following formulation is provided as an objective function:

$$\text{Minimize } Z = x_1 + x_2, \quad (5)$$

subject to the following constraints:

$$H_2S: \quad 0.14x_1 + 0.02x_2 \geq 357.1; \quad (6)$$

$$MM: \quad 0.06x_1 + 0.15x_2 \geq 285.7; \quad (7)$$

$$EM : \quad 0.12x_1 + 0.45x_2 \geq 714.3 ; \quad (8)$$

$$DMS : \quad 0.00x_1 + 0.03x_2 \geq 357.1 ; \quad (9)$$

$$DMDS : \quad 0.05x_1 + 0.29x_2 \geq 714.3 ; \quad (10)$$

$$THT : \quad 1.76x_1 + 2.40x_2 \geq 17,857.1 ; \quad (11)$$

$$UN1 : \quad 0.24x_1 + 1.06x_2 \geq 1,071.4 ; \quad (12)$$

$$EDS : \quad 0.33x_1 + 0.75x_2 \geq 1,785.7 ; \quad (13)$$

$$x_1 \geq 0; \text{ and} \quad (14)$$

$$x_2 \geq 0 ; \quad (15)$$

where x_1 and x_2 represent the weights (g) of AC-Zn(NO₃)₂ and AC-FeCl₃, respectively.

The model was solved using MATLAB[®] software to yield:

$$x_1 = 850 \text{ g}; \quad (16)$$

$$x_2 = 11,903 \text{ g}; \text{ and} \quad (17)$$

$$Z = 12,753 \text{ g}. \quad (18)$$

The calculated results indicate that a sorbent composed of a mixture of 850 g of AC-Zn(NO₃)₂ and 11,903 g of AC-FeCl₃ would be sufficient to remove all sulfur compounds from SNG in a 1 kW fuel cell system. Using AC-FeCl₃ as a single sorbent to treat the same quantity of SNG would require 17,857 g of sorbent, 50% more material than the composite. It would not be possible to use AC-Zn(NO₃)₂ as a single sorbent because it has no capability to remove DMS.

3.4.1.4 References

1. P. J. de Wild, R. G. Nyqvist, F. A. de Bruijn, E. R. Stobbe, *Journal of Power Sources* 159 (2006) 995.
2. H. Topsoe, in *Handbook of Fuel Cells-Fundamentals, Technology and Applications* W. Vielstich, Ed. (John Wiley & Sons, Ltd, 2003), vol. 3, pp. 177-189.
3. I. EG&G Technical Services, "Fuel cell handbook" (Nov, 2004).
4. T. H. Gardner, D. A. Berry, K. David Lyons, S. K. Beer, A. D. Freed, *Fuel* 81 (2002) 2157.
5. X. Wu, V. Schwartz, S. H. Overbury, T. R. Armstrong, *Energy & Fuels* 19 (2005) 1774.
6. X. Wu, A. K. Kercher, V. Schwartz, S. H. Overbury, T. R. Armstrong, *Carbon* 43 (2005) 1087.
7. A. Bagreev, S. Bashkova, T. J. Bandosz, *Langmuir* 18 (2002) 8553.
8. T. Bandosz *et al.*, *Water Science and Technology* 42 (2000) 399.
9. J. L. Figueiredo, M. F. R. Pereira, M. M. A. Freitas, J. J. M. Orfao, *Carbon* 37 (1999) 1379.
10. H.-L. Chiang, J.-H. Tsai, D.-H. Chang, F.-T. Jeng, *Chemosphere* 41 (2000) 1227.
11. Y. Otake, R. G. Jenkins, *Carbon* 31 (1993) 109.
12. S. Bashkova, A. Bagreev, T. J. Bandosz, *Catalysis Today* 99 (2005) 323.
13. P. Chingombe, B. Saha, R. J. Wakeman, *Carbon* 43 (2005) 3132.
14. C. Moreno-Castilla, M. V. Lopez-Ramon, F. Carrasco-Marin, *Carbon* 38 (2000) 1995.

15. T. J. Bandoz, *Journal of Colloid and Interface Science* 246 (2002) 1.
16. R. Yan *et al.*, *Environmental Science and Technology* 38 (2004) 316.
17. A. K. Dalai, E. L. Tollefson, A. Yang, E. Sasaoka, *Industrial & Engineering Chemistry Research* 36 (1997) 4726.
18. H. Tamai, H. Nagoya, T. Shiono, *Journal of Colloid and Interface Science* 300 (2006) 814.
19. G. Israelson, *Journal of Materials Engineering and Performance* 13 (2004) 282.

3.4.1.5 Papers and Presentations Resulting from Efforts

Cui, H., M.A. Reese, and S.Q. Turn. Removal of sulfur compounds from utility pipelined synthetic natural gas using modified activated carbons. *Catalysis Today*. In review.

Cui, H., M. Reese, and S. Turn. 2007. Removal of sulfur compounds from synthetic natural gas using modified activated carbon. Presented at the 234th American Chemical Society National Meeting. Boston, MA. August 20-24, 2007.

Fuel Processing and Gas Conditioning for Hydrogen Production (continued)

Subtask 3.4.2: Reforming of Seafloor Methane for Use in Remote Autonomous Underwater Fuel Cells

This subtask investigates reforming of methane from seeps or hydrates on the seafloor for use in powering remote autonomous underwater fuel cells. The following outlines the desired outcomes of this research.

1. Optimize the performance of conventional autothermal reforming at three representative pressures (3, 30, and 60 bar) using water and gas-phase oxygen.
2. Rerun a fraction of the above conditions using H₂O₂ for comparison and possible validation of H₂O₂ use as oxidizer in an autothermal reactor (ATR).
3. Develop and validate a numeric model that correctly predicts trends in a conventional ATR.

3.4.2.1 Scope of Work and Approach

Naturally occurring methane hydrate seeps on the ocean floor are possible sites for remote recharging stations for autonomous underwater vehicles. The recharging station would consist of a fuel collection system, reformer, fuel cell and ancillary equipment. Whereas in other environments fuel economy is of primary importance, under these conditions the availability and judicious use of oxygen and clean water are of greater concern. Pressures at these depths are also elevated and present unique design challenges. The second project under this task explores methane reforming under conditions representative of the seafloor from both modeling and experimental approaches.

A high pressure reforming system has been constructed and tested. System specifications and data collection/analysis techniques will be presented in the next section.

3.4.2.2 Experimental

3.4.2.2.1 System description

A schematic of the completed high pressure reforming system is shown in Figure 3.4-4.

The reformer is a lab-scale, fixed-bed, catalytic reactor which is 61.0 cm in length and has a 1.1 cm inner diameter. This reformer tube is constructed from schedule XXS 3/4" stainless steel pipe and has suitable geometry and material properties to withstand both high temperature and high pressure; namely 900 °C and 80 bar, respectively.

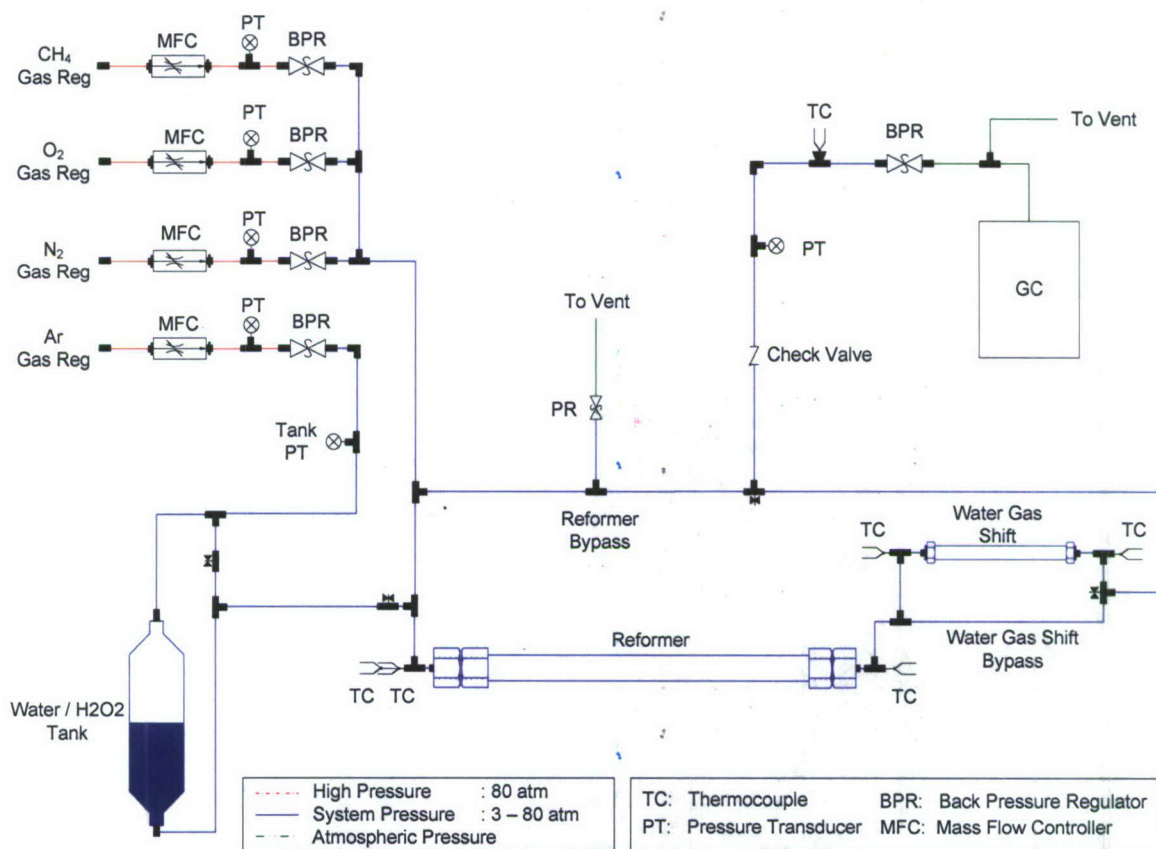


Figure 3.4-4. Schematic diagram of high pressure methane reforming test facility v.1

The reactor is heated by an electric tube furnace with a heating length of 30.5 cm. A nickel-based steam reforming catalyst, GW-91 EW from Süd-Chemie, is crushed to produce a particle size in the range of 1.4 - 4.75 mm. Between 15 and 20 g of catalyst is placed into the center 20 cm section of the reforming tube. Temperatures in the reactor are measured both immediately before and after the catalyst bed.

Methane (Grade 5.0), oxygen and nitrogen are supplied to the reactor from gas bottles and metered using mass flow controllers. Water or hydrogen peroxide is supplied to the reactor from a high pressure reservoir. Argon from a gas cylinder flows through a mass controller into the head space of the reservoir, pushing the liquid out through an injector into the gas stream at the desired flow rate. Resistance element heat tracing, which is applied to the transfer lines between the reservoir and the reactor, preheats the liquid. Pressure in the reactor is set and controlled with a back-pressure regulator. Flow rates are controlled and recorded along with temperatures and pressures via LabView®.

Downstream of the reactor, water vapor is largely removed in a condenser and then dried further using a coalescing filter. The dry effluent gas is analyzed with a Shimadzu 14A gas chromatograph (GC) equipped with a thermal conductivity detector (TCD) and CarboxenTM 1000 column (45/60, SUPELCO). Helium with 8% hydrogen serves as the carrier gas. In each analysis, the temperature is held at 45 °C for 1 minute, increased for 9 minutes to 225 °C, held at 225 °C for 2 minutes, and then decreased for 10 minutes back to 45 °C. The GC system is equipped with a six-port valve which automatically injects a dried sample from the reactor into the GC every 22 minutes. The concentrations of stable gas species – H₂, N₂, CO, CH₄, and CO₂ – are determined along with higher hydrocarbons such as C₂H₄, C₂H₆, C₃H₆, and C₃H₈, when present. ASTM standard D1946-2006 outlines the procedure for determining chemical compositions of reformed gases and gaseous mixtures containing hydrogen, oxygen, nitrogen, carbon monoxide, carbon dioxide, methane, ethane and ethylene. A photograph of the reforming system is shown below in Figure 3.4-5.

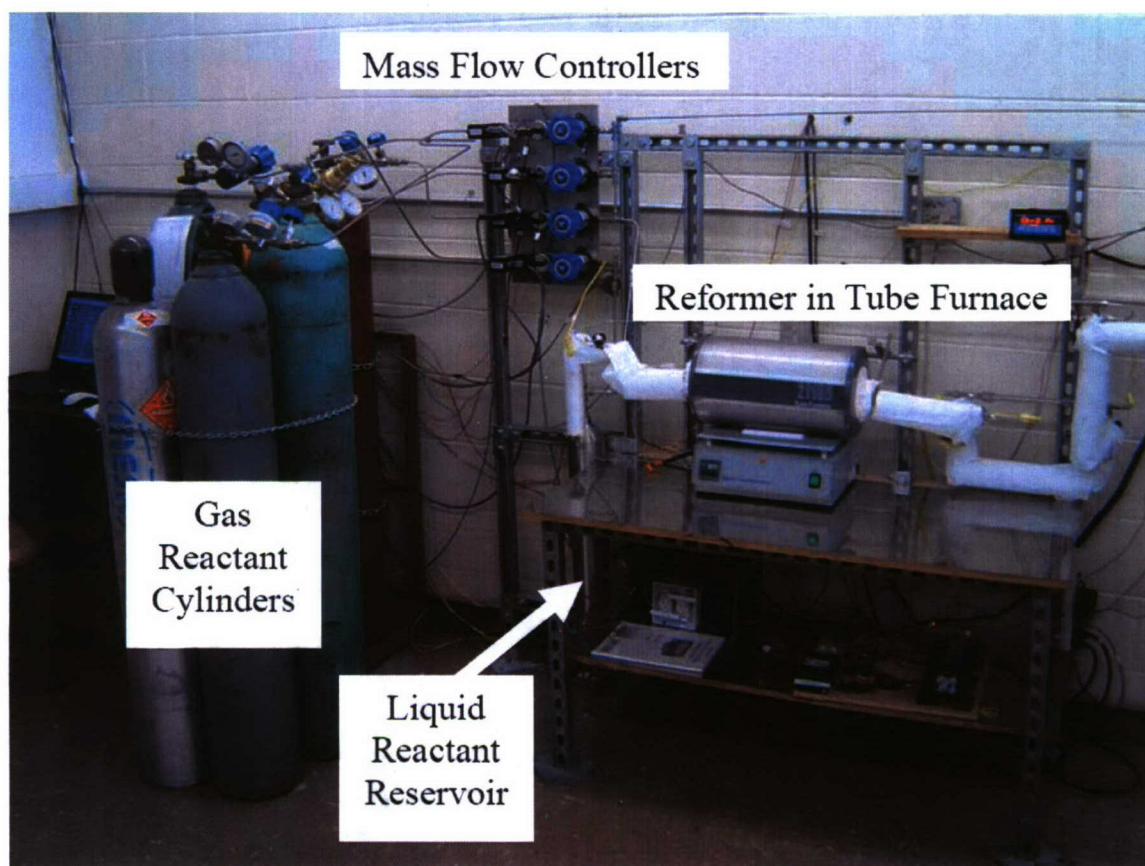


Figure 3.4-5. Photograph of the laboratory-scale reforming test bed designed to operate at pressures up to 80 bar

After several preliminary tests were completed, it became clear that the method for delivering water and hydrogen peroxide to the reformer was less than ideal. System pressure fluctuations of any size would cause the liquid reactant delivery, which was dependent on pressure, to become unstable. To correct this, a high pressure liquid chromatography pump was purchased. The

The schematic diagram illustrates the gas supply system for the CO synthesis reactor. It features three inlet streams at the top left: CH₄, O₂, and N₂. Each stream passes through a Gas Regulator (Reg), a Mass Flow Controller (MFC), a Pressure Transducer (PT), and a Back Pressure Regulator (BPR) before entering a vertical manifold. A Water / H₂O₂ Tank at the bottom left feeds into the same manifold via an HPLC Pump. The manifold leads to a horizontal line containing a Reformer Bypass valve and a Pressure Reducing Valve (PR). This line then splits into two parallel paths: one passing through a Reformer unit and another through a WGS Bypass valve. Both paths converge and pass through a Water Gas Shift unit. The final output line includes a Thermocouple (TC) and a Back Pressure Regulator (BPR) before venting to the atmosphere. A GC (Gas Chromatograph) is connected to the system via a dashed line labeled 'To Vent'. The legend specifies: High Pressure (red dashed line) : 80 atm; System Pressure (blue solid line) : 3 – 80 atm; Atmospheric Pressure (black dashed line).

3.4.2.2.2 Operating Procedure

Startup

After the reactor is connected in the reforming test bed, a pressure test using nitrogen is conducted. Once the system integrity is verified, the calibration procedure can be carried out.

Calibration of the reforming system is critical. The MFCs (mass flow controllers), high pressure water pump and GC are the most sensitive instruments needing calibration. The accuracy of the pressure transducers and temperature sensors are provided from the manufacturer and are viewed as acceptable within the stated accuracy.

Flow controllers

All three MFCs are tested and calibrated prior to starting the experimental phase. In addition, before each day's experimental runs, all MFCs are flow tested and, if needed, adjusted to ensure the desired flow is the actual flow. For flows less than 300 cc/min of O₂ or N₂, a TCD-based flow meter with real-time flow metering is used. For calibration of higher flow rates, regardless of gas species, a bubble flow meter is used. The flows are considered acceptable once the actual flow stabilizes to within 2% of the desired flow. The actual flow is considered stable when three consecutive readings for the bubble flow meter are equal or when the TCD flow meter reads a steady flow for 1 minute.

The high pressure water pump is flow tested before each day's run to insure accurate water delivery. Flow is tested by pumping water into a beaker sitting on a lab scale. After 5 minutes of flow, the difference in beaker weight will be recorded and the actual flow rate determined. If the actual flow is within 2% of the desired flow, it will be considered acceptable; otherwise, the pump flow rate will be adjusted and the flow rate retested.

Gas chromatograph

The gas chromatograph provides area counts for each gas species being analyzed. The area counts are directly related to the concentration of the respective gas species present in the reformat sample. Concentrations for all gas species should therefore add to 100% if the GC is properly calibrated and all peaks are identified.

Calibration of the GC will be conducted before and after each day's experimental run. A two-point calibration with gas species concentrations above and below those of the general reformat gas is performed. This will minimize effects of the GC sensor drift over time.

3.4.2.3 Technical Accomplishments

Initial testing of the experimental set up has already been completed. This section will describe the test conditions and results for the experiments that have been conducted to date.

3.4.2.3.1 Conventional ATR Reforming

Conventional ATR reforming refers to ATR reforming that feeds separate water and O₂ streams to the reformer with the fuel. Preliminary tests were conducted using reactor pressure as the primary variable ranging from 7 to 58 bar. Test conditions are shown in Table 3.4-5. It should be noted that the tests completed were not true ATR tests. While both water and O₂ were fed into the reactor, additional heat was also supplied to the reactor from a surrounding furnace.

Table 3.4-5. Reformer test conditions

Test Test No.	No. of Samples	Feed rate, ml/min				Ratio		Pressure (atm)	Temp. °C	GHSV (hr ⁻¹)
		CH ₄	O ₂	H ₂ O _(g)	N ₂	S/C	O ₂ /C			
1	4	500	80	1.8	500	4.5	0.16	7	800	5888
2	4	500	80	1.8	500	4.5	0.16	28	800	1472
3	4	500	80	1.8	500	4.5	0.16	46	800	896
4	4	500	80	1.8	500	4.5	0.16	58	800	711

Increasing pressure resulted in a decreasing gas-hourly-space velocity (GHSV) from nearly 6000 to 700 hr^{-1} . GHSV is defined as the reactant flow rate, at reactor conditions, divided by the catalyst volume. Equilibrium calculations for the reactant mixtures and reforming conditions shown in the table were performed using the software package FACTSageTM 5.1. Products included CH_4 , H_2 , H_2O , CO and CO_2 . Figure 3.4-7 compares the results of the equilibrium calculations with experimental results. Experimental values are averages of at least four measurements of gas composition. From the error bars shown on the graph, it is clear that experimental conditions were very stable, in terms of both reactor pressure and gas composition. H_2 concentration in the gas decreased from ~75 to 68% over the range of experimental conditions. Gas phase CO concentration also declined from 10 to 7%. CO_2 concentration was relatively unaffected by pressure ranging from 12.5 to 14.5% over the test range. Note that the concentration of unreacted methane increased from 1 to 9.5% as pressure increased from 7 to 58 bar. Reduced methane conversion also resulted in reduced gas yield. Results in Table 3.4-6 show a decline in gas yield from 4.8 to 3.3 liters gas per liter of CH_4 entering the reformer, over the test pressure range. Experimental results are in close agreement with results of the equilibrium calculations over the range of pressures, indicating that at these operating conditions, kinetic limitations to methane reforming do not exist. Elevated pressure can induce carbon formation and coking of the catalyst, but none was observed. Longer-term tests should be conducted for verification. In general, these experiments confirm that methane can be reformed at pressures typical of depths where hydrothermal vents or methane hydrates exist on the sea floor.

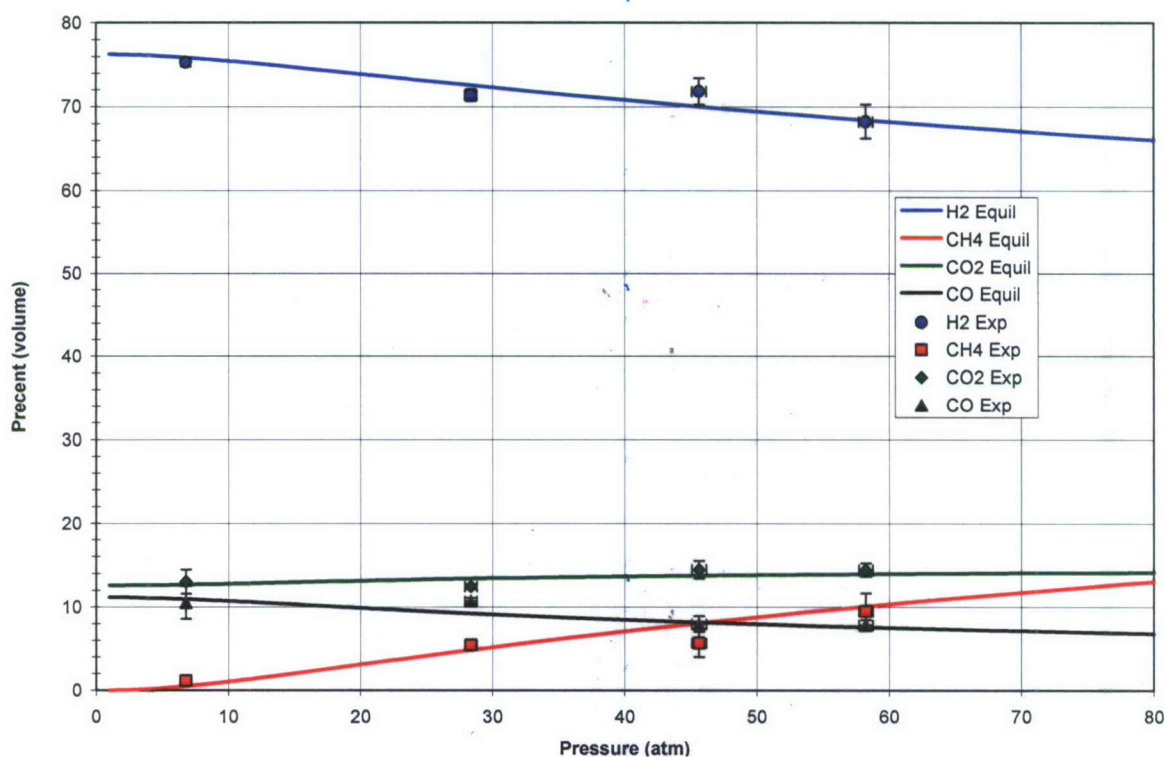


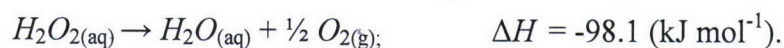
Figure 3.4-7. Comparison of methane reforming results as a function of pressure at $\text{O}_2/\text{C} = 0.16$, $\text{S}/\text{C} = 4.5$, $T_{\text{Reactor}} = 800\text{ }^\circ\text{C}$ and 15 g of G91-EW, a Ni based catalyst (Equi = chemical equilibrium calculation, Exp = experimental result)

Table 3.4-6. Variation of inert free gas yield as a function of pressure

Pressure (atm)	Inert Free Gas Yield mole/mole CH ₄
6.8	4.8 ± 0.3
28.4	3.8 ± 0.1
45.6	3.8 ± 0.3
58.2	3.3 ± 0.3

3.4.2.3.2 H₂O₂-Based Reforming

As mentioned earlier, a major limitation for operating a reformer on the sea floor is having oxygen available at usable concentrations. The experiments described above utilized O₂ from a high pressure gas cylinder. A second set of experiments was performed to evaluate the use of a second oxidizer, hydrogen peroxide, a liquid at ambient conditions that can be decomposed, either catalytically or thermally, to water and oxygen according to the following reaction:



Like the previous reforming tests, the liquid reactants were metered into the reformer from a high pressure tank. Prior to conducting the H₂O₂ tests, the tank and transfer lines were passivated with dilute nitric acid. Based on a 0.5 lpm CH₄ flow rate to the reformer and the decomposition reaction shown in the equation above, a mixture of 9% H₂O₂ in deionized water at a flow rate of 1.8 ml/min was calculated to provide desired oxygen to carbon (0.15) and steam to carbon (4.4) ratios. These match the reactant ratios that were used in the experiments described above.

To calibrate the H₂O₂ delivery system, a mixture of 9% H₂O₂ and 91% deionized water was placed in the liquid reactant reservoir and metered into the empty reformer at a rate of 1.8 ml/min. The reactor was maintained at a temperature of 800 °C using the tube furnace, and the pressure was set to 8.8 bar. CO₂ was introduced into the reformer at a flow rate of 1.0 lpm to simulate the reactant gas flow expected during experiments and to act as a sweep gas that could easily be separated from the O₂ by GC. After analyzing several samples of the outlet gas, the flow of H₂O₂/H₂O mixture was stopped and replaced with a flow of O₂ from a gas cylinder. The flow was varied from 31 to 107 ml/min to provide a series of O₂ concentrations to the GC. The calibration curve is shown in Figure 3.4-8 with an accompanying regression equation. Using this equation, the GC area counts from the earlier analysis of gas from the 9% H₂O₂ and 91% deionized water liquid flow were converted to O₂ concentrations as shown in Table 3.4-7. Eight samples were analyzed with an average O₂ concentration of 6.2% and a standard deviation of 1.9% (absolute).

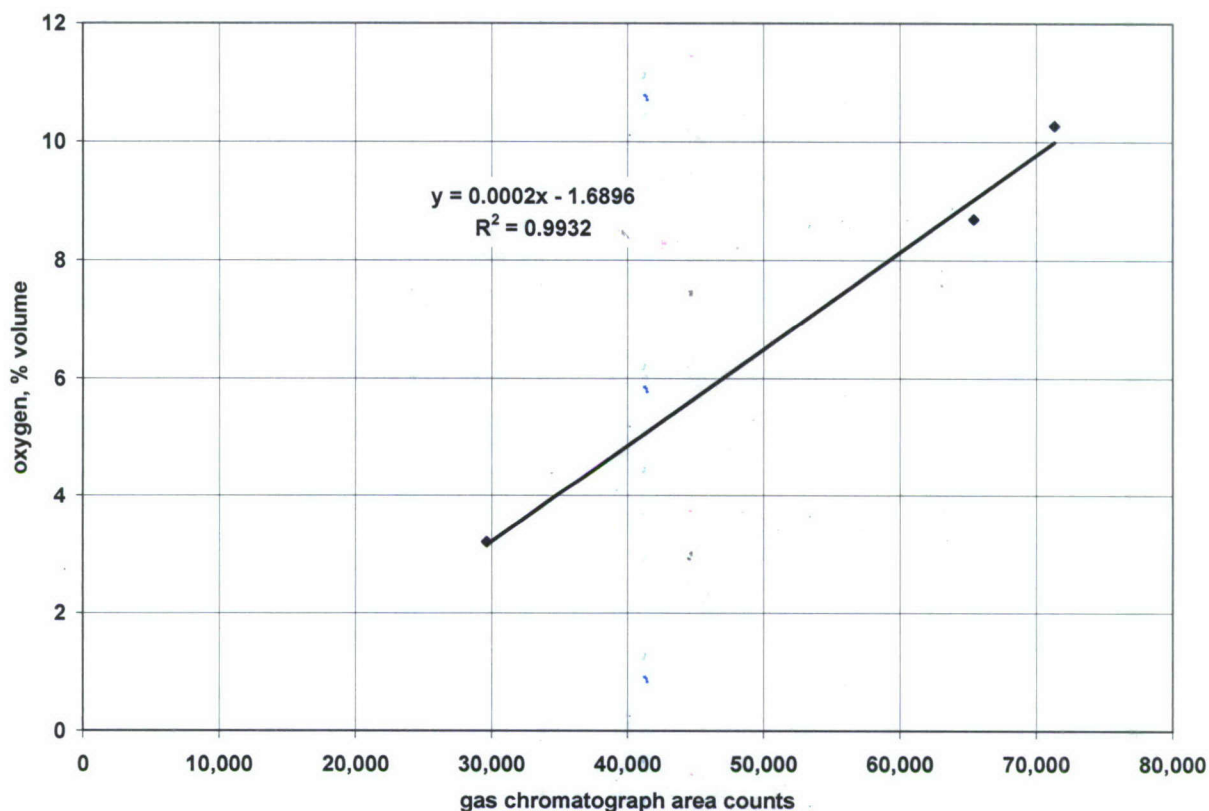


Figure 3.4-8. O₂ calibration curve for the GC, based on concentrations mixed with mass flow controllers

Table 3.4-7. Variability of concentration of O₂ produced from thermally decomposing H₂O₂ in an empty reformer at 800 °C, 8.8 bar

Sample No.	Area Counts	% O ₂
1	46,816	6.0
2	29,700	3.2
3	40,000	4.9
4	51,000	6.7
5	44,929	5.7
6	44,030	5.5
7	72,268	10.1
8	55,960	7.5
Average	48,088	6.2
Standard Dev.	11,655	1.9

Results of the reforming experiments using 9% H₂O₂ and 91% deionized water are shown in Table 3.4-8. Product composition predicted by chemical equilibrium is presented for comparison. As with the earlier experiments using O₂ from gas cylinders, agreement between experiment and equilibrium is quite good. Differences in gas concentration for all species were <2% (absolute). These results provided preliminary validation for the use of H₂O₂ as a liquid

oxygen carrier for reforming applications. Additional verification testing should be conducted across a range of pressures and oxygen to carbon ratios.

Table 3.4-8. Comparison of gas composition from catalytic methane reforming experiments using 9% H₂O₂ / 91% H₂O at 8 bar, 800 °C with composition predicted by chemical equilibrium at the same conditions

Gas	Equilibrium	Experimental
	(% volume)	
H ₂	75.7	77.75
CH ₄	0.71	1.03
CO	10.88	10.04
CO ₂	12.71	11.18

3.4.2.3.3 Reactor Model

Using a software package, COMSOL Multiphysics®, several models to represent the reforming process have been constructed. The model will be used to predict temperature and concentration of gas species within the reactor.

A two-dimensional pseudo-homogenous model was first selected to represent the reactor. This approach allowed the prediction of relatively detailed temperature and conversion results inside the reactor, taking radial variations into account; the radial flux being super-imposed over the convection transport, which is of the plug-flow type.

The model was set up with rotational symmetry about the z-axis, allowing the three-dimensional geometry to be modeled in two dimensions. Below is a schematic layout of the 2-D reactor.

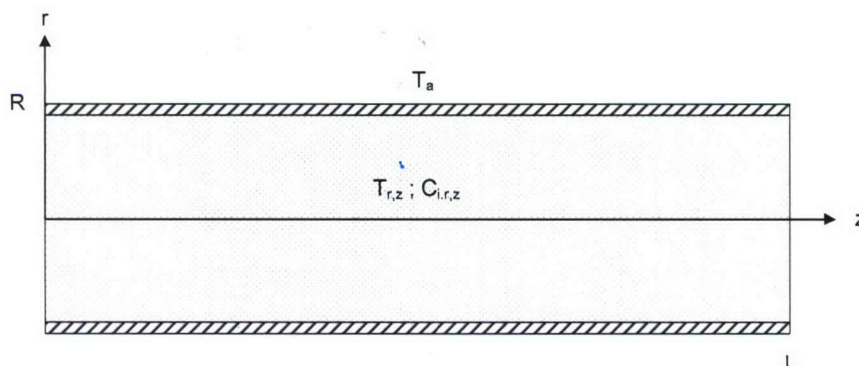


Figure 3.4-9. Schematic layout of the 2-D reactor, where R is the radius of the reactor in the radial direction, r; L is the length of the reactor in the axial direction, z; T_a is the ambient temperature; T_{r,z} is the reactor temperature at location (r, z); and C_{i,r,z} is the concentration of the ith species in the reactor at location (r, z)

The three governing equations describing the model are listed below.

$$\frac{\partial C_i}{\partial t} = D_{pi} \left(\frac{\partial^2 C_i}{\partial r^2} + \frac{1}{r} \frac{\partial C_i}{\partial r} \right) - u \frac{\partial C_i}{\partial z} + \rho_{cat} r_i; \quad (1)$$

$$\rho_{cat} c_{p cat} \frac{\partial T_s}{\partial t} = \lambda \left(\frac{\partial^2 T}{\partial r^2} + \frac{1}{r} \frac{\partial T}{\partial r} + \frac{\partial^2 T}{\partial z^2} \right) + \rho_{cat} \sum_{j=1}^4 (-\Delta H_j) R_j + S_h h (T - T_s); \text{ and} \quad (2)$$

$$\varepsilon \rho_g c_{pg} \frac{\partial T}{\partial t} = -u \rho_g c_{pg} \frac{\partial T}{\partial z} + S_h h (T_s - T); \quad (3)$$

where

i	gas species (H ₂ , O ₂ , CO, CO ₂ , H ₂ O, CH ₄)
j	reaction index (1-4)
t	time (s)
r, z	cylindrical coordinates (m)
C_i	concentration of gas species i (mol m ⁻³)
D_{dpi}	dispersion coefficient of gas species i
u	superficial gas velocity (m s ⁻¹)
ρ_{cat}	density of catalyst bed (kg m ⁻³)
ρ_g	average gas density (kg m ⁻³)
ε	void fraction of the catalyst bed
c_{pg}	average specific heat of gas (J kg ⁻¹ K ⁻¹)
h	heat transfer coefficient between catalyst bed and gas phase (W m ⁻³ K)
S_h	heat transfer area per unit volume of catalyst bed (m ⁻² m ⁻³)
T	temperature of gas phase (K)
T_s	temperature of solid phase (K)
λ	effective thermal conductivity of catalyst bed (W m ⁻¹ K ⁻¹)
r_i	reaction rate of gas species i (mol kg ⁻¹ s ⁻¹)
ΔH_j	heat of reaction j (mol kg ⁻¹ s ⁻¹)
R_j	reaction rate of reaction j (mol kg ⁻¹ s ⁻¹)

$$D_{dpi} = \varepsilon \left(\frac{D_i}{\tau_{bed}} + 0.5 d_p u \right) \quad (4)$$

where

D_i	gas diffusivity of species i (m ² s ⁻¹)
τ_{bed}	tortuosity of the bed
d_p	pellet diameter (m)
and	
$\tau_{bed} = \frac{1}{\sqrt{\varepsilon}}$	

(5)

$$D_i = 1 \times 10^6 \cdot T^{1.75} \cdot \frac{\left(\frac{1}{m_{ave}} + \frac{1}{m_i} \right)^{\frac{1}{2}}}{P \left((20.1)^{\frac{1}{3}} + (p_i \cdot 20.1)^{\frac{1}{3}} \right)^2} \quad (6)$$

where

m_{ave} average molar mass of gas into which gas species i is diffusing (g mol⁻¹)
 m_i mass of gas species i (g mol⁻¹)
 P system pressure (bar)
 p_i partial pressure of gas species I (bar).

Subject to the boundary conditions:

$$t = 0 : T = T_0 \quad (7)$$

$$z = 0 : T = T_g^{in} ; C_i = C_i^{in} \quad (8)$$

$$z = L : \frac{\partial C_i}{\partial z} = 0 ; \frac{\partial T}{\partial z} = 0 \quad (9)$$

$$r = 0 : \frac{\partial C_i}{\partial r} = 0 ; \frac{\partial T}{\partial r} = 0 \quad (10)$$

$$r = R : \frac{\partial C_i}{\partial r} = 0 ; \lambda \frac{\partial T}{\partial r} = \alpha (T - T_a) \quad (11)$$

where

T_g^{in} gas inlet temperature (K)
 C_i^{in} concentration of inlet gas species i (mol m⁻³)
 α overall heat transfer coefficient through the reactor wall (W m⁻²)
 T_a ambient temperature (K).

Equations (1)-(3) are: the mass balance for the gas phase, the energy balance for the solid phase and the energy balance for the gas phase, respectively.

Since the actual reformer has a large aspect ratio, having a catalyst bed length of approximately 0.20 m and an inner diameter of 0.011 m, the model equations were scaled to avoid having to generate a large numbers of needless nodes and elements. Each term in the energy and mass balance equations is multiplied by scaling factors for the radial (r) and longitudinal (z) directions, 'scaler' and 'scalez', respectively, that are the same order as the order of derivative in the term. For example, diffusion, being a second-order derivative, is scaled to r/scaler² and z/scalez², while convection, being a first-order derivative term, is scaled by r/scaler, etc.

After generating some initial results from the 2-D pseudo-homogenous model, it was found that both temperature and gas concentration had negligible radial variations. To take advantage of

this situation, the model was reduced to a 1-D pseudo-homogenous model. Additionally, a heterogeneous 1-D model was developed to include temperature differences and heat transfer between the gas and solid phases. As more experimental data become available and are compared against model results, the model and model parameters will be refined to improve agreement with reforming results.

3.4.2.3.4 Experimental Design

A well laid-out design of experiments is critical to obtain meaningful results and conclusions. Again, the thrust of this research is to study the performance of ATR reforming at pressure, using H_2O and O_2 to form a basis of comparison against results obtained when H_2O_2 is used as the oxidant. Therefore, the experimental design will be based primarily around an H_2O and O_2 ATR, with the occasional performance comparison to H_2O_2 ATR reforming. The independent variables controlled in the research are shown below in Table 3.4-9.

Table 3.4-9. Independent variables

Variable		
Name	#	Unit
S/C	1	-
O_2/C	2	-

The variables, although continuous, do have defined ranges, due to physical limitations of the reforming process. Note that temperature, while an extremely important factor in the reforming process, is a dependant variable in autothermal reforming.

Factorial approach

Typically parametric studies are completed by observing the desired response when changing one independent variable at a time. For this study, however, a 2^2 factorial design approach will be used. The two-level factorial design allows multiple independent variables to be changed at the same time and to isolate the effects of the independent variables and the effects of the interactions between independent variables. Among other advantages, this method has the potential to reduce the number of experimental runs needed to find an optimum condition.

Operating pressure for a subsea power generating station located on the ocean floor is determined by operating depth. It follows then, that the focus of these experiments will be to determine the optimal operating conditions for a given pressure. This approach will be carried out at multiple pressures from 3 bar to 60 bar, representing depths between 30 m and 600 m below sea level. A two-level factorial design for this study is shown below in Table 3.4-10, the column headings correlate to the variable numbers in Table 3.4-9.

Table 3.4-10. Variable levels for factorial experimental design

Order	Treatment	1	2	12
2	1	-1	-1	1
4	2	1	-1	-1
3	3	-1	1	-1
1	4	1	1	1

As shown in Table 3.4-10, each variable has a high (+1) and low (-1) value at which experiments will be conducted.

Optimization

Clear criteria must be set forth in order to optimize any process. For the experiments at hand, several possible optimization criteria exist, and selecting one depends on what outcome is most desirable for a particular application. A list of potential optimization criteria are listed below:

- maximize the mole fraction of H_2 in the output gas stream;
- maximize the moles of H_2 produced per mole of CH_4 in the feed gas;
- minimize the mole fraction of CO in the output gas stream while keeping the H_2 mole fraction above a given threshold;
- minimize the mole fraction of CO in the output gas stream while keeping the CH_4 conversion above a given threshold; and
- maximize the moles of H_2 produced per mole of O_2 in the feed gas.

Obviously there is no end to possible criteria and yet, in some cases, different criteria could in fact lead to the same optimum condition.

For the application at hand, the methane supply from gas vents will be considered unlimited. Oxygen, however, must be stored onboard the system, likely in the form of H_2O_2 as previously stated. Minimizing the consumption of O_2 is thus directly related to the size and, potentially, cost of the system. Additionally, PEMFCs do not require pure hydrogen on the anode side, provided that CO concentration is less than 10 ppm. Other gases, such as CO_2 , will only have a dilution effect on the cell performance. It is, therefore, proposed that the optimization criteria for the application at hand be the following: to maximize the moles of H_2 produced per mole of O_2 consumed. Using Factsage 5.1 to predict equilibrium gas composition, Figures 3.4-11 to 3.4-13 show the moles of H_2 produced per mole of O_2 fed into the reactor at 3, 30 and 60 bar respectively. For comparison, Figures 3.4-14 to 3.4-16 show the moles of H_2 produced per mole of CH_4 fed into the reactor, for 3, 30 and 60, respectively. This parameter is a more common performance index.

From the equilibrium results, it is clear that optimizing for moles of H_2 produced per mole of O_2 in the fed gas does, in fact, lead to different optimum operating conditions than optimizing for moles of H_2 produced per mole of CH_4 in the fed gas does.

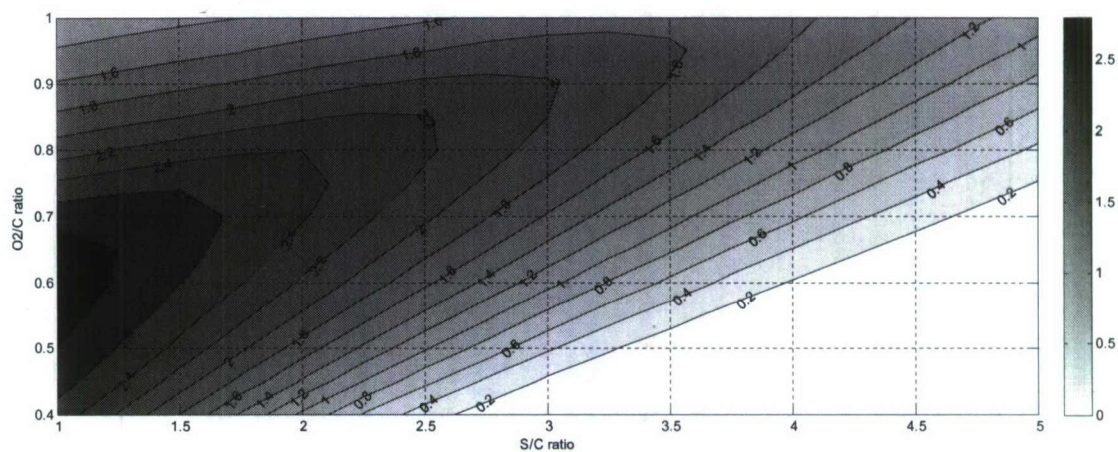


Figure 3.4-11. Mole of H_2 produced/mole of O_2 fed into the reactor (equilibrium values, 3 bar, no heat loss)

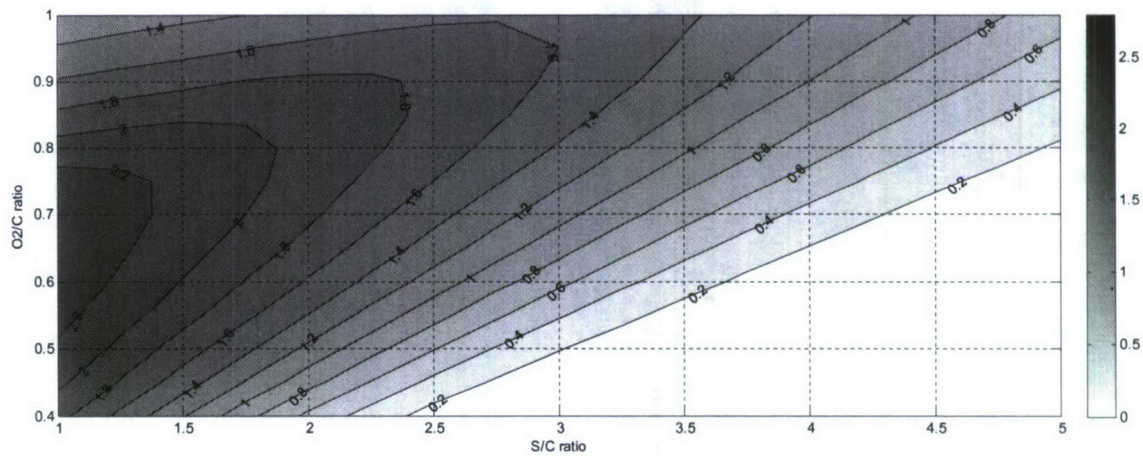


Figure 3.4-12. Mole of H_2 produced/mole of O_2 fed into the reactor (equilibrium values, 30 bar, no heat loss)

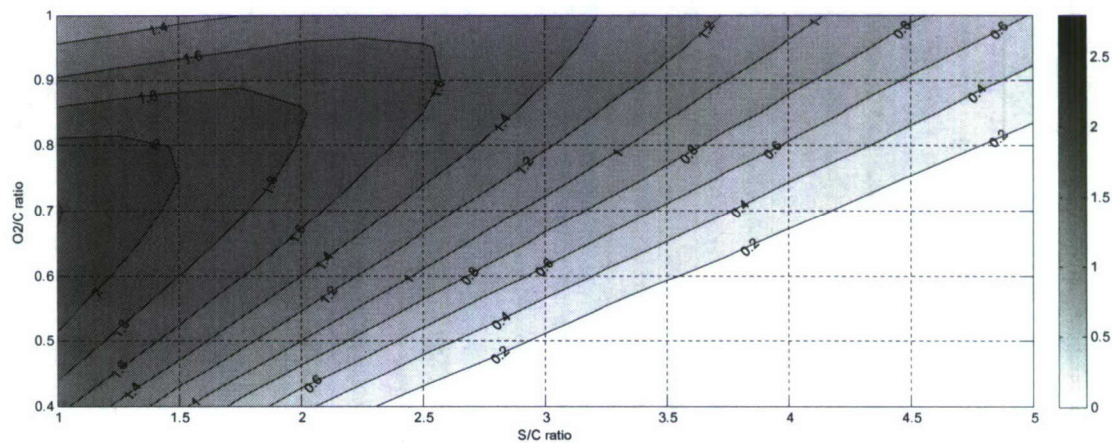


Figure 3.4-13. Mole of H_2 produced/mole of O_2 fed into the reactor (equilibrium values, 60 bar, no heat loss)

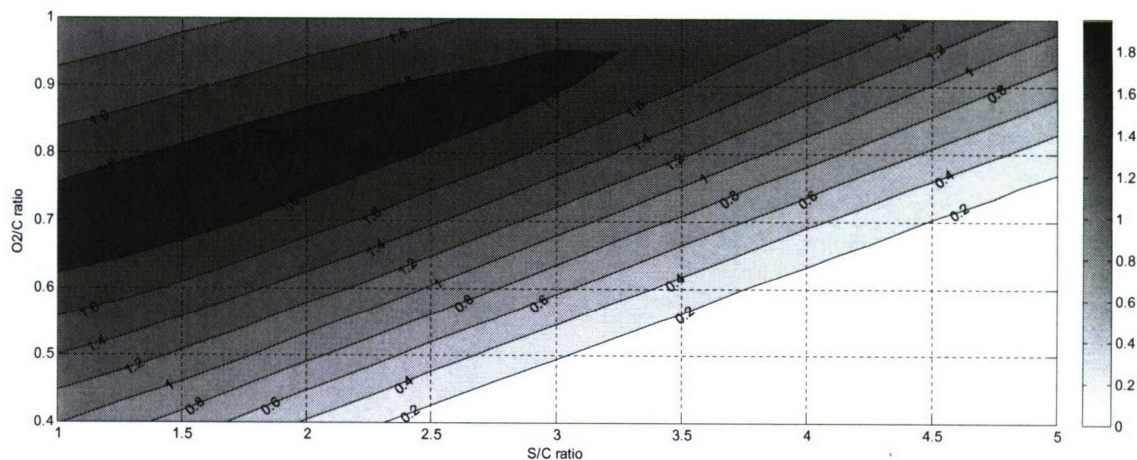


Figure 3.4-14. Mole of H₂ produced/mole of CH₄ fed into the reactor (equilibrium values, 3 bar, no heat loss)

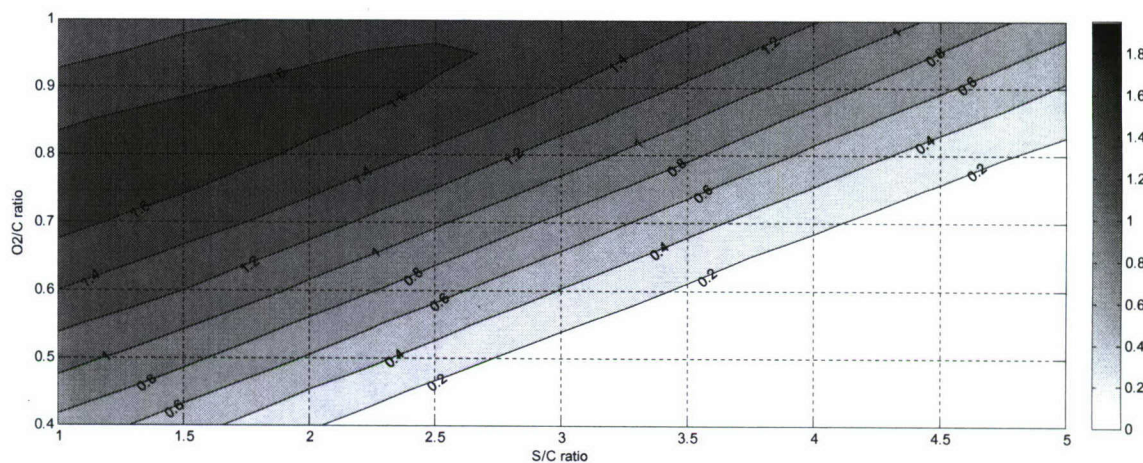


Figure 3.4-15. Mole of H₂ produced/mole of CH₄ fed into the reactor (equilibrium values, 30 bar, no heat loss)

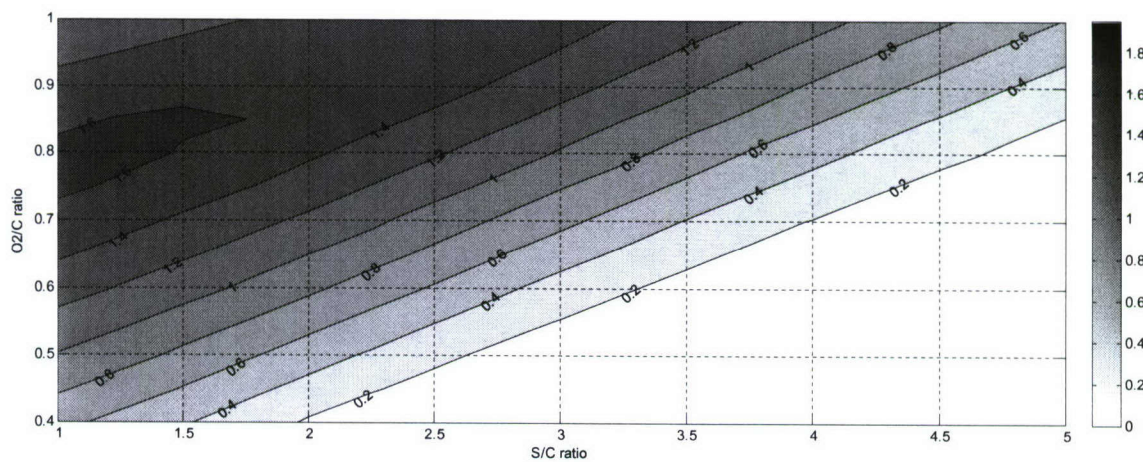


Figure 3.4-16. Mole of H₂ produced/mole of CH₄ fed into the reactor (equilibrium values, 60 bar, no heat loss)

During the experimental runs, when an optimum condition appears to have been reached for a given pressure, the GHSV of the system will be increased until significant changes in gas concentration are noticed. At that point, conclusions will be drawn about the maximum GHSV the system can handle. The optimization process will then be restarted for a second and third pressure.

3.4.2.3.5 Initial Test Conditions

The initial high and low values for each variable have been selected and are shown in Table 3.4-11. Selection was made based on review of the literature, results from previous tests, and equilibrium calculations.

Table 3.4-11. Initial operating conditions for low pressure (3 bar) experiments.

#	Variable Name	Unit	Value	
			+	-
S/C	1	/	1.5	1
O ₂ /C	2	/	0.75	0.5

Additionally, two runs will also be conducted at the center point of the conditions listed in Table 3.4-11: namely, a S/C ratio of 1.25 and an O₂/C ratio of 0.625. Upon completing the first set of experiments, the data will be analyzed and surface response methodology will be used to change the independent variables and move closer to an optimum condition.

3.4.2.4 Papers Resulting from Efforts

Douette, A., S.Q. Turn, W. Wang, and V. Keffer. An experimental investigation of hydrogen production from glycerin reforming. *Energy & Fuels*. In press, 2007.

Wang, W., S.Q. Turn, V. Keffer, and A. Douette. 2007. Study of process data in autothermal reforming of LPG using multivariate data analysis. *Chemical Engineering Journal*. 129, pp. 11-19.

Fuel Processing and Gas Conditioning for Hydrogen Production (continued)

Subtask 3.4.3: Plasma Reforming of Diesel Fuel and Reformate Purification

Under this subtask, DJW Technologies, under contract to HNEI, investigated plasma reforming of commercial diesel fuel and membrane purification of reformat. A low-temperature plasma reformer from Advanced Hydrogen Technologies, Inc. was used to successfully reform high-sulfur diesel fuel (315 ppm S) with high carbon conversion at reduced temperatures. Reformate containing 50 ppm H₂S and 1% CO was converted by selective membrane purification to yield an enriched hydrogen stream (~97%) with H₂S reduced to <10 ppb and CO reduced to <10 ppm. The final report presenting detailed results of this work is included in Appendix A.

This page is intentional blank

3.5 Novel Fuel Cell and Component Development

The effort to develop novel fuel cell components included two major activities: 1) biocarbons for use in fuel cells, and 2) enzymatic bio-fuel cells. Each of these topics is addressed in the following paragraphs.

3.5.1 Biocarbons for use in fuel cells

3.5.1.1 Objectives

Graphite is an important component of the bipolar plate assembly that is employed in many fuel cells. Graphite also plays a critical role in many batteries and capacitors. Graphite is desired for these applications because it is an excellent conductor of electricity and it is inert. Unfortunately, because it is inert it is not a good support for catalysts. Likewise, it has a very low porosity and surface area. High surface areas can be desirable for some catalytic applications.

The electrical conductivity of many biocarbons (carbonized charcoal produced from biomass) approaches that of graphite. These biocarbons can be inert. Unlike graphite, biocarbons can possess very high surface areas and easily can be loaded with catalysts. In spite of these attractive features, virtually no attention has been given to the use of biocarbons as replacements for graphite in fuel cell bipolar plates, capacitors, and batteries.

The objective of this work was to characterize the electrical and physical properties of a wide range of biocarbons in order to facilitate their use in improved fuel cells, capacitors, and batteries.

3.5.1.2 Scope of Work and Approach

Because the USA has the largest reserves of coal in the world, and because biomass can be converted into biocarbons quickly and efficiently, there is growing interest in the efficient use of solid carbon fuels. Also, battlefield refuse can be quickly and efficiently converted into carbon.

A recent EPRI study indicates that "direct" carbon fuel cells have the potential to convert coal or charcoal into electrical power at a system level efficiency of about 60%, which is over 20% higher than the efficiencies realized by current state-of-the-art integrated gasification combined cycle (IGCC) or advanced pulverized coal power generation systems.

The following companies are engaged in the commercial development of direct carbon fuel cells: SRI International, SARA, Contained Energy Corp. (representing the Lawrence Livermore National Laboratory -- LLNL), Direct Carbon Technologies LLC (representing Stanford University), and CellTech Power. The most promising direct carbon fuel cell results (published by LLNL) were obtained using a biocarbon (charcoal) fuel. The SRI research also emphasizes biocarbon (charcoal) fuel. Much of this work has been supported by DARPA or the DoD.

HNEI has developed and patented a quick and efficient ("Flash CarbonizationTM") process for the conversion of biomass and wastes into biocarbons. The patents have been licensed to the Kingsford Products Co. and Carbon Diversion Corp. In addition to this, with ONR support, HNEI has been a leader in characterizing the properties of biocarbons (see section 3.5.1.4 below). Because of this activity, EPRI has requested HNEI to supply corn cob biocarbons to two direct carbon fuel cell research projects (SRI International and CellTech Power) for testing. Also, HNEI

has supplied biocarbons to Contained Energy Corp. (representing the LLNL) for testing. The SRI research is supported by DARPA, and the Contained Energy Corp. research is supported by the DoD.

3.5.1.3 Technical Accomplishments

Highlights of our recent accomplishments include the preparation of charcoals and carbonized charcoals ("biocarbons") from a wide variety of biomass substrates. Model biocarbons were synthesized from sucrose, glucose, fructose, Inulin, and Kraft lignin. Commercial biocarbons were synthesized from oak wood, corncob, and demineralized corncob. Biocarbons doped with boron and phosphorous were also prepared. These biocarbons were characterized by XRD, NMR, ICP-MS, SEM, MALDI-TOF MS and TG-MS; and their properties were compared to those of graphite. These analyses (especially the MALDI-TOF MS results) enabled the development of a new model for the molecular structure of biocarbons that represents many of their unusual properties. This work comprised the MS thesis research of Jared Bourke who earned his degree at the University of Waikato (NZ) following a year of research with ONR support at UH. The University of Waikato Chemistry faculty awarded Jared's thesis an A+ with First Class Honors in recognition of the importance of his findings.

As mentioned above, with ONR support we are assisting EPRI, SRI International, Contained Energy Corp., and CellTech Power with their development of direct carbon fuel cells. Much of the direct carbon fuel cell research is sponsored by DARPA and the DoD.

The Consortium on Plant Biotechnology Research is sponsoring a project at HNEI entitled "Flash-CarbonizationTM Catalytic Afterburner Development" that is enabling us to scale-up the UH Flash CarbonizationTM process and thereby enabling us to produce larger quantities of biocarbon for testing and use in DARPA- and DoD-sponsored direct carbon fuel cell research.

3.5.1.4 Papers and Presentations Resulting from Efforts

PAPERS

Antal, Jr., M.J., Nihous, G.C. "Thermodynamics of an aqueous-alkaline/carbonate carbon fuel cell" submitted to *Ind. Eng. Chem. Res.*, 2007.

Antal, Jr., M.J., Bourke, J., Manley-Harris, M., Fushimi, C., Dowaki, K., and Nunoura, T. "A Model of the Chemical Structure of Carbonized Charcoal" *Ind. Eng. Chem. Res.*, Vol. 46, 2007, pp. 5954-5967.

Antal, Jr., M.J., Meszaros, E., Varhegyi, G., Jakab, E.; Bourke, J., Manley-Harris, M.; and Nunoura, T. "Do all carbonized charcoals have the same chemical structure? Implications of TG-MS measurements." *Ind. Eng. Chem. Res.*, Vol. 46, 2007, pp. 5943-5953.

Antal, Jr., M.J., Varhegyi, G., Meszaros, E., Bourke, J., and Jakab, E. "Combustion Kinetics of Corncob Charcoal and Partially Demineralized Corncob Charcoal in the Kinetic Regime." *Ind. Eng. Chem. Res.*, Vol. 45, 2006, pp. 4962-4970.

Antal, Jr., M.J., Wade, S.R., and Nunoura, T. "Studies of the Flash Carbonization Process. 2. Violent Ignition Behavior of Pressurized Packed Beds of Biomass: A Factorial Study." *Ind. Eng. Chem. Res.*, Vol. 45, 2006, pp. 3512-3519.

PRESENTATIONS by Michael J. Antal, Jr.

Organized and will chair two topical sessions concerning chemical engineering for novel fuel cell applications and biomass conversion during the *AIChE Annual Meeting* in Salt Lake City from 4 – 9 November, 2007.

Presented invited seminars on the carbon fuel cell at Eindhoven University (7 February 2006), the University of Missouri at Columbia (10 November 2006), the University of Massachusetts at Boston (16 February 2007), the University of Hawaii at Manoa (25 September 2007), and the Hungarian Academy of Sciences (25 October, 2007).

Organized and chaired three topical sessions concerning chemical engineering for novel fuel cell applications and biomass conversion during the *AIChE Annual Meeting* in San Francisco from 13 – 17 November, 2006. Presented two talks: “Optimization of Flash CarbonizationTM Conditions for Charcoal Production from Sunflower Shells”, and “Performance of a First-Generation Aqueous-Alkaline Biocarbon Fuel Cell” in these sessions.

On 28, 29 August 2006, attended a “by-invitation-only” meeting at EPRI Headquarters in Palo Alto and delivered a lecture entitled: “Performance of a First-Generation Aqueous-Alkaline Biocarbon Fuel Cell”.

3.5.2 Enzymatic Bio-Fuel Cells

3.5.2.1 Objectives

As stated in our previous reports, enzymatic bio-fuel cells (EBFCs) use enzymatic biocatalysts to convert chemical energy directly to electricity as power sources. They are promising alternatives to complement conventional fuel cell technologies that rely on transitional metal oxides or noble metals as catalysts for conversion of chemical energy, typically stored in hydrogen, to useful electrical energy. An EBFC exhibits some promising technical merits as follows:

- Selectivity – Enzyme catalysts are fuel specific and capable of handling complex fuels in the liquid phase, which can simplify fuel logistics and cell design.
- Abundance in supply – Unlike conventional Pt-based catalysts, enzymatic catalysts can be produced via biological or chemical methods, thus promising a potentially low-cost mass production and unlimited supply.
- Wider range of operation – Due to their selectivity, enzymes are generally more adaptive to extreme conditions and tolerant to contaminants.
- Reformulation – If the gene coding for the enzyme is obtained, a suite of directed evolution techniques exist to create mutants that are more effective in catalysis.
- Self-assembly – Unique in biological systems, to simplify fabrication processes for micro-devices *in situ*.

The continuation of support has enabled us to focus on fundamental studies that elucidate charge transfer limitations in enzyme-catalyzed electrodes, so we can transfer this knowledge into engineering designs of practical *bio-fuel cells*. The following long-term objectives have and continue to be pursued:

- Establish an array of quantitative *in situ* characterization techniques, test cells, and modeling capabilities to determine limitations to bioelectrocatalysis [1-4], and to construct a test bed that will allow us to refine such techniques in microbial- or enzyme-based bioelectrocatalysis operation [5]; and

- To develop a technology base with know-how to improve performance (e.g., catalyst lifetime, current density) with respect to important process variables such as choice of catalyst, choice of mediators, immobilization matrix, and mode of immobilization (e.g., covalent attachment versus physical entrapment of enzyme).

3.5.2.2 Scope of Work and Approach

Over the course of this project, three major tasks in the EBFC work have emerged:

- 1) Develop platform fabrication technology to control the resulting multidirectional pore structure of three-dimensional electrodes;
- 2) Develop qualitative and quantitative fluorescence as a characterization technique for enzyme fuel cells; and
- 3) Fabricate and test full bio-fuel cells.

For this specific funding period, we were funded to pursue:

- 1) Casting of three-dimensional carbon nanotube (CNT)/polymer composite films mixtures onto glassy carbon electrodes, and characterizing their performance in terms of electrochemical oxidation of NADH (the reduced form of nicotinamide adenine dinucleotide), high-resolution surface imaging, porosity measurements, and fluorescence microscopy. We will also use a simplified diffusion model to estimate, *in situ*, the total electrode activity in the absence of mass transfer effects [2], as well as a lumped diffusion term.
- 2) Reviewing of the potential of fluorescent probes, to define the optimum conditions which bind them to the enzyme without loss of activity, to verify the enzyme/probe binding ratio, as well as purifying the tagged enzyme. We also proposed to investigate the effect of probe charge on enzyme distribution within polymer films as well as the effect of the film chemical nature on the distribution of tagged enzyme within the film.
- 3) Demonstrating a working bio-fuel cell using alcohol dehydrogenase to catalyze partial ethanol oxidation at the anode and a home-made air cathode using Pt catalyst with a Nafion membrane as the separator. Power generation at low rate was measured with a stack cell configuration.

3.5.2.3 Technical Accomplishments

Summary of work from previous project periods. In past reports, we have presented several prototype cells constructed to deliver gas (e.g., H₂) fuels. A final working hydrogenase enzymatic bio-fuel cell was constructed and tested (Figure 3.5-1). The design considerations and test applications were described in the June 2005 Final Technical Report. Complete details on this work have been published [1]. From this work we determined, and reported previously, that the use of gaseous fuels is limited by the solubility of the gaseous fuel in the aqueous buffer that is required to maintain enzyme activity.

In past reports we have commented on the development of a suite of characterization techniques through the complementation of methods utilized, including potentiostatic DC polarization, dynamic potentiometry, and electrochemical impedance spectroscopy (EIS) combined with spectrophotometric detection of enzyme activity

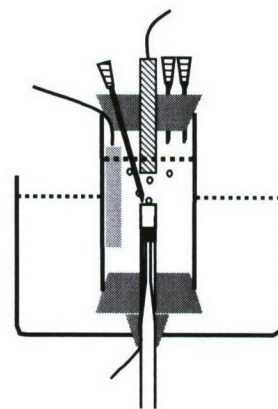


Figure 3.5-1.
Hydrogenase enzyme

in order to characterize electrode performance, and to differentiate between the relative contributions towards charge transfer efficiency. Among the results of our efforts, in particular, we believe we were one of the first groups to report charge transfer efficiency for bound enzyme [1] and to report a mass transport modeling effort that can be combined with DC-polarization data to yield information valuable for future electrode development [2]. A detailed description of the technique application, data and results can be found in the literature. A summary can also be found in a book chapter that was published in 2007 [6].

We have pursued the technique of fluorescence in order to characterize the distribution of enzymes within polymer films used to immobilize them. The polymer films, and the immobilization process, are part electrode fabrication methodologies that inherently assume that the immobilized enzymes are homogeneously distributed. Our work, which has tagged ethanol-oxidizing enzymes with various fluorescent probes and then used laser scanning confocal microscopy to image the spatial distribution of the enzyme within the film [3], has clearly demonstrated that this is not necessarily the case, and that the tagged enzymes may not be homogeneously distributed within polymer films (Figure 3.5-2).

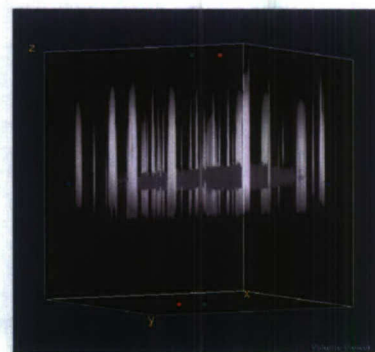


Figure 3.5-2. 3D distribution of tagged enzyme within polymer

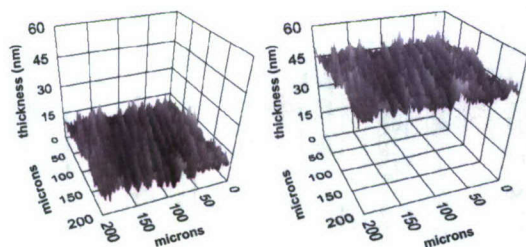


Figure 3.5-3. Film thickness of poly(methylene green films)

To evaluate film thickness during electrochemical deposition of electrode immobilization matrix or mediator film on electrode surface, we have combined the technique of imaging ellipsometry with the cyclic voltammetric deposition technique to track the thickness of the deposited film with cycle number. This very valuable technique has contributed new information regarding the fundamental reaction kinetics and mechanisms underlying the electrochemical deposition of conductive films onto electrode surfaces (see Figure 3.5-3). The initial work has been published [4].

These outcomes were used to leverage two extramurally funded projects. The first one is a grant from the Director of the Central Intelligence Postdoctoral Fellow Research Program to support development of bio-fuel cells for micro-power source applications (B.Y. Liaw, PI). The second is a sub-award from the AFOSR Multi-disciplinary University Research Initiative (MURI) program (M. Cooney, PI) awarded to the lead institution, the University of New Mexico (P. Atanassov, PI). Both awards have lent national recognition of this EBFC program.

Summary of accomplishments for this reporting period. In support of 1) we have begun an effort exploring chitosan and chitosan-composite scaffolds as a material for the fabrication of macroporous electrodes that can support both mediator-based and direct electron transfer (Figure 3.5-4). Work accomplished during the period has included the development of protocols for the fabrication of chitosan scaffolds immobilizing NADH-dependent glucose oxidase. Our work, in collaboration with Dr. Shelley Minter, has shown that the scaffold design (all other variables

variables remaining constant) can significantly increase power density for mediator-based systems. This work has currently led to the submission of one paper to the Journal of Materials Chemistry; which, after receiving encouraging reviews, is in the process of being revised [7]. Future work will look at improving our knowledge of the scaffold fabrication process and its application to direct electron transfer processes.

In support of 2) we have studied how the charge-charge interaction between the enzyme and the polymer affect the immobilization process; we have also studied the steady state and dynamic polarization of fluorescent probes when placed in solution with charged polymers. We are also measuring the steady state and dynamic polarization of tagged enzymes with polymers. We are hoping to submit a manuscript of this work to the journal of Materials Chemistry by the end of this year.

The support of 3) has resulted in the promise of future collaborations with national and international premier research institutions to expand the scope and level of competency in this field. In response, we developed a liquid-phase prototype Bio-fuel Test Cell. This prototype, which we term the modular stack cell, in development for over two years, was tested during this funding period for its capacity as a characterization tool. Specifically, we sent duplicate models of the modular stack cell (Figure 3.5-5) to three cooperating labs in the U.S. that also specialize in enzyme fuel cell development. Each lab (Dr. Shelley Minter at St. Louis University, Dr. Plamen Atanassov at the University of New Mexico, and Dr. Scott Barton at Michigan State University) were given the same protocol to execute (i.e., to develop a poly(methylene green) electrode film that oxidizes NADH), and the electrochemical data from all labs were consolidated and statistically analyzed for reproducibility. The results, which demonstrated the modular stack cell provides a framework for comparative analysis of systems, are now in the form of a final manuscript that will shortly be submitted to the Journal of Electroanalysis [8].

With this confidence, we fabricated a full ethanol-based bio-fuel cell based on this design (Figure 3.5-6). Although we have achieved full operation (see power curves in Figure 3.5-6)

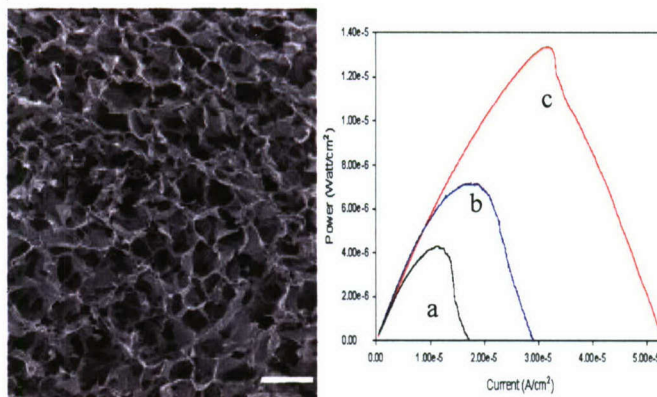


Figure 3.5-4. SEM image of chitosan scaffold (Left) and power curves from chitosan film (a) and scaffolds (b, c)

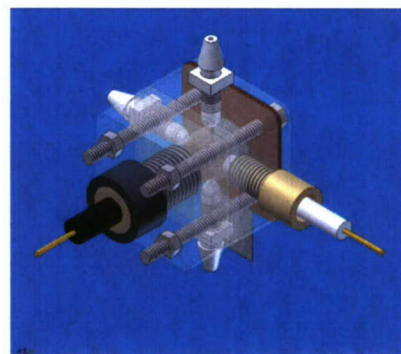


Figure 3.5-5. The modular stack cell

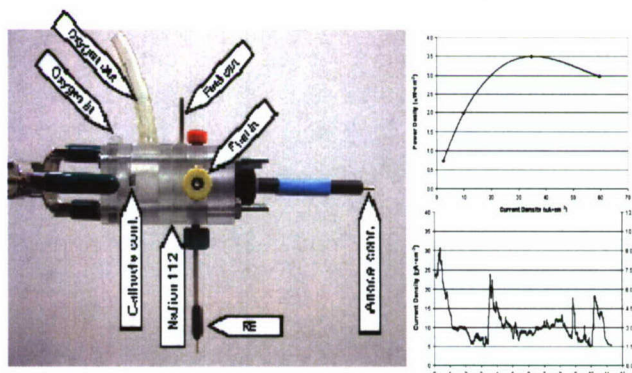


Figure 3.5-6. Operation biofuel cell, based on modular stack cell design.

with an air-breathing cathode, this work is still in development.

Summary of additional work accomplished during this period. In addition to these accomplishments, we also initiated an enzyme immobilization effort to establish a common platform for apo-enzyme reconstitution. The prosthetic group pyrroloquinoline quinine (PQQ) and PQQ-dependent glucose dehydrogenase (PQQ-GDH) have been chemically bound to CHIT-CNT films in the presence of EDC (acronym for 1-ethyl-3-(3-dimethylaminopropyl) carbodiimide hydrochloride), respectively. The immobilized PQQ-GDH displayed a quasi-reversible electron transfer with a formal potential $E^{\circ'}$ of -0.110 V, which was found to be independent of the scan rate. The bioactivity of the immobilized PQQ-GDH was retained. Additionally, the enzyme-free bound PQQ exhibits a more facile electron transfer with a glassy carbon electrode (GCE) compared to the immobilized PQQ-GDH, suggesting that PQQ-bound CHIT-CNT films hold promise as a platform for the reconstitution of PQQ-dependent apo-enzymes, with potential application in biosensors and bio-fuel cells.

Evidence of electron transfer between bound PQQ-GDH and the GCE was observed, when PQQ-GDH was coupled with EDC to a CNT-functionalized CHIT film. The experimental results suggest that the presence of CNT in the CHIT film promoted the electron transfer of bound PQQ-GDH to the GC electrode. A quasi-reversible electrochemical reaction, as revealed by a pair of well-defined redox peaks, was observed by cyclic voltammetry. Additional experimental results demonstrated that bioactivity of PQQ-GDH was retained in PQQ-GDH-bound CHIT-CNT/GCE, which permits its use as a platform catalyst combination for a mediated bio-fuel cell anode or amperometric biosensor electrode for glucose detection. It should be noted that PQQ bound to CHIT-CNT film also exhibits an effective charge transfer with GCE, suggesting that it can be used as a promising platform for reconstitution of various PQQ-dependent apo-enzymes. A summary of this work has been submitted to the Journal of the Electrochemical Society and is currently under review [9].

In the NAD-based enzymatic systems, we focused on the mediator systems using polymethylene green as an effective mediator for electron transfer in the NADH oxidation. A unique imaging ellipsometric technique in combination with quartz crystal microbalance (QCM) and electrochemical cyclic voltammetric techniques for surface film deposition and characterization is being developed through this effort. Imaging ellipsometry is capable of measuring surface morphology and film thickness in nanometer scale, providing us a powerful surface characterization technique that is *in situ* and non-invasive. We were able to control the polymer film formation with accurate thickness and morphology control during deposition. This technique also helped us understand the stepwise underlying mechanism in the deposition and provided unprecedented details in the film formation process involving redox reactions. We are currently using this technique to study the redox kinetics involved in the NADH oxidation.

3.5.2.4 References

1. Johnston, W., Cooney, M.J., Liaw, B.Y., Sapra, R., and Adams, M.W.W., *Design and characterization of redox enzyme electrodes: new perspectives on established techniques with application to an extremophilic hydrogenase*. Enzyme and Microbial Technology, 2005. **36**: p. 540 - 549.

2. Johnston, W., Maynard, N., Liaw, B., and Cooney, M.J., *In situ measurement of activity and mass transfer effects in enzyme immobilized electrodes*. Enzyme and Microbial Technology, 2006. **39**: p. 131 - 140.
3. Konash, S., Cooney, M.J., Liaw, B.Y., and Jameson, D., *Characterization of Polymer-Enzyme Interactions using Fluorescence*. Journal of Materials Chemistry, 2006. **DOI: 10.1039/b611686h**.
4. Svoboda, V., Cooney, M.J., Rippolz, C., and Liaw, B.Y., *In-Situ Characterization of Electrochemically Polymerized Methylene Green Films on Platinum and Glassy Carbon Electrodes*. Journal of the Electrochemical Society, 2006. **154**(3): p. D113 - D116.
5. Svoboda, V., Cooney, M.J., Rippolz, C., and Liaw, B.Y., *In situ Characterization of an Enzyme Catalyzed Bio-Fuel Cell*. 2007. **In Preparation**.
6. Cooney, M.J. and Liaw, B.Y., *In Situ Characterization Techniques for Design and Evaluation of Micro and Nano Enzyme-Catalyzed Power Sources*, in *Nano-Scale Sciences & Technology in Biomolecular Catalysis*, P.S. Wang and J.B. Kim, Editors. 2007, American Chemical Society.
7. Cooney, M.J., Windmeisser, M., Liaw, B.Y., Lau, C., Klotzbach, T., and Minteer, S.D., *Design of chitosan gel pore structure: Towards enzyme catalyzed flow-through electrodes*. Submitted to the Journal of Materials Chemistry, 2007.
8. Svoboda, V., Cooney, M.J., Liaw, B.Y., Minteer, S., Piles, E., Lehnert, D., C., B.S., Rincon, R., and Atanassov, P., *Towards standardized characterizations of enzyme bioelectrocatalysis*. Journal of Electroanalysis, 2007. **To be submitted**.
9. Sun, D., Scott, D., Cooney, M.J., and Liaw, B.Y., *A promising reconstitution platform of PQQ-glucose dehydrogenase in chitosan - carbon nanotube matrices*. Journal of the Electrochemical Society, 2007. **Submitted**.

3.5.2.5 Papers and Presentations Resulting from Efforts

PAPERS

- Cooney[✉], M.J., Windmesier, M, Lau, C., Liaw, B.Y., Klotzbach, T. and Minteer[✉], S. Design of Chitosan Gel Pore Structure: Towards Enzyme Catalyzed Flow-Through Electrodes. **Submitted to the Journal of Materials Chemistry**, 2007.
- Minteer[✉], S., Liaw, B.Y., and Cooney, M.J. *Enzyme-Based Biofuel Cells*. Current Opinions in Biotechnology. March 29th. **In Press**, 2007.
- Svoboda, V., Rippolz, C., Cooney[✉], M.J., and Liaw[✉], B.Y. *Characterization of electrochemically polymerized methylene green films on platinum and vitreous carbon supports*. The Journal of Electrochemical Society. 154(3): D113 – D116, 2007.
- Cooney[✉], M.J., and Liaw[✉], B.Y. *In situ characterization techniques for design and evaluation of micro and nano enzyme-catalyzed power sources*. **In Press** (P.S Wang and J. B. Kim Editors), 2006.

- Johnston, W. J., Cooney[✉], M.J., and Liaw[✉], B.Y. In situ measurement of effective diffusion coefficients in enzyme immobilized electrodes. *Enzyme and Microbial Technology*. 39:131 – 140, 2006.
- Konash, A., Cooney[✉], M.J., Liaw[✉], B.Y., and Jameson, D.M. Characterization of enzyme-polymer interactions using fluorescence. *Journal of Materials Chemistry*, 16: 4107 – 4109, 2006, DOI: 10.1039/b611686h.
- Johnston, W. J., Liaw, B.Y., Sapra, R., Adams, M.W.W., and Cooney[✉], M.J. Design and characterization of redox enzyme electrodes: new perspectives on established techniques with application to an extremeophilic hydrogenase. *Journal of Enzyme and Microbial Technology*. 36(4): 540 – 549, 2005.

PRESENTATIONS

- Minteer, S. D., Klotzbach, T., Cooney, M. J., and Liaw, B.Y. *Nanopore Engineering Of Chitosan Polymer For Enzyme Immobilization And Stabilization*. November 4 -9, 2007. Salt Lake City, Utah.
- Cooney, M. J., Liaw, B.Y., Lau, C., and S. D. Minteer. *Application Of Mesopore Engineered Chitosan Polymer For Fabrication Of Multi-Dimensional And Multi-Directional Enzyme Catalyzed Electrodes*. November 4 -9, 2007. Salt Lake City, Utah.
- Scott, D. Liaw, B.Y., and Cooney, M.J. Improved Current Sustainability from the Ammonia, PPy Interaction with H₂O₂-One Step Closer to a Urine Fuel Cell. The 212th ECS Meeting, October 7-12, 2007.
- Liaw, B.Y., Cooney, M.J., Svoboda, V., Konash, A., Jameson, D.M. *In situ characterization of polymer matrices for bio-electrode applications*. 17th International Symposium on Fine Chemistry and Functional Polymers (FCFP-XVII) & 3rd IUPAC International Symposium on Novel materials and their Synthesis (NMS-III), Shanghai, China, October 18th-20th, 2007.
- Svoboda, V., Liaw, B.Y., and Cooney, M.J. *In-situ transient characterization of electrochemical polymerization of methylene green with analysis of stepwise reaction mechanism*. 211th ECS Meeting, Chicago Illinois. May 6-11th, 2007.
- Liaw, B. Y, Svoboda, V., Cooney, M. J., and Minteer, S. *Fabrication of an effective biocatalytic electrode with in situ characterization of electrode and its materials*. 211th ECS Meeting, Chicago Illinois. May 6-11th, 2007.
- Cooney, M. J., Windmeisser, M., Liaw, B.Y., and Minteer, S. *Design of chitosan gel pore structure: towards enzyme catalyzed electrodes*. 211th ECS Meeting, Chicago Illinois. May 6-11th, 2007.
- Konash, A., Cooney, M.J., Liaw, B.Y, and Jameson, D. *Enzyme-polymer interaction study using fluorescence probes*. Symposium on Nano-scale Science and Technology in Biomolecular Catalysis. 232th ACS National Meeting, San Francisco CA, Sept 10 – 14, 2006.
- Svoboda, V., Cooney, M.J., Rippolz, C., and Liaw, B.Y. *Development of an Enzymatic Ethanol Bio-Fuel Cell for Micro-Power Generation*. Fuel Cell Seminar, Honolulu HI, November 13 – 17, 2006.

- Cooney, M.J., Svoboda, V., Rippolz, C., and Liaw, B.Y. *Design considerations and characterization of enzymatic ethanol fuel cells*. 209th ECS Meeting, May 7-12, 2006, Denver, CO.
- Svoboda, V., Cooney, M.J., Rippolz, C. and Liaw, B.Y. *Design Consideration and In-situ Characterization of Bio-Anode for Enzymatic Ethanol Fuel Cell Application*. IBA –HBC 2006, Waikoloa, Hawaii, 9-12 January 2006.
- Cooney, M.J., Svoboda, V., Rippolz, C., and Liaw, B.Y. *Design considerations and characterization of enzymatic ethanol fuel cells*. 209th ECS Meeting, May 7-12, 2006, Denver, CO.
- Liaw, B.Y., Quinlan, F., Cooney, M.J. *Polypyrrole Deposition in Aqueous Solutions: Film Characteristic Dependence on Deposition Conditions*. 208th Meeting of the Electrochemical Society. Los Angeles, California. Oct. 16-21, 2005.
- Liaw, B.Y., Svoboda, V., Cooney, M.J. *Morphological Study of Conducting Polymer via Electrochemical Deposition Using Imaging Ellipsometry and RQCM Technique*. 208th Meeting of the Electrochemical Society. Los Angeles, California. Oct. 16-21, 2005.
- Cooney, M.J., Johnston, W. and Liaw, B.Y. *Modeling the relative contribution of mass transfer limitation on performance in enzyme fuel cells*. 207th Meeting of the Electrochemical Society, Quebec City, Canada. May 15 - May 20, 2005.
- Quinlan, F., Cooney, M.J. and Liaw, B.Y. *Investigation of polypyrrole morphology with different deposition conditions*. 207th Meeting of the Electrochemical Society, Quebec City, Canada. May 15 - May 20.
- Liaw, B.Y., Cooney, M.J., Quinlan, F., Svoboda, V. and Maynard, N. *Engineering Effective Bioelectrocatalysis Electrodes for Power Generation*. Second International Conference on Polymer Batteries and Fuel Cells (Fuel Cells). Las Vegas, Nevada from June 12 - June 17, 2005.
- Johnston, W.A., Cooney, M.J., and Liaw, B.Y. *Evaluating adsorption and charge transfer of redox enzymes bound to carbon support*. The 204th Meeting of the Electrochemical Society, Inc. July, 2003, Orlando, Florida.

4. Methane Hydrates

4.1 Objectives

Methane hydrates in ocean sediments constitute an enormous energy reservoir that is estimated to exceed the energy content of all known coal, oil, and conventional natural gas resources. Located on continental margins throughout the world, methane hydrates offer unique opportunities as an onsite source of fuel for various marine applications and are believed to play a major role in seafloor stability and global climate.

National R&D programs on methane hydrates were initiated in Japan and India in the mid-1990s with the goal of commercial gas production within a 20-year time horizon. The U.S. established its own program in May 2000. The Methane Hydrate Research and Development Act of 2000 (Public Law 106-193) included seven technical areas of focus: (1) identification, exploration, assessment, and development of methane hydrate as a source of energy; (2) technology development for efficient and environmentally-sound recovery of methane from hydrates; (3) transport and storage of methane produced from methane hydrates; (4) education and training related to methane hydrate resource R&D; (5) assessment and mitigation of environmental impacts of natural and purposeful hydrate degassing; (6) development of technologies to reduce the risks of drilling through methane hydrates; and (7) support of exploratory drilling projects. The objectives of the present Methane Hydrates Task, which was initiated in 2001, reflect most of the priorities of P.L. 106-193, but emphasize those areas of particular relevance to the Office of Naval Research (ONR) and which are consistent to the overall goals of the HEET initiative. Specifically, the development of hydrates and related sources of seafloor methane as logistical fuels for Naval applications and related marine environmental issues, have been the principal areas of interest; exploratory drilling projects and seafloor stability/safety have received limited attention. Task objectives were devised to fully leverage hydrate R&D expertise and infrastructure that had been developed at HNEI during previous research programs on CO₂ ocean sequestration and deep oil spills.

During the present reporting period (2005-2007), the goals of the HEET Methane Hydrates Task were:

- Pursue development of means to recover methane gas from hydrates.
- Investigate the microbial processes in sediment that generate and modulate methane levels.
- Investigate the fate of methane leaking into the water column from the seafloor.
- In cooperation with the Naval Research Laboratory (NRL) and ONR Global (previously ONR-IFO), promote international collaborative research on methane hydrates.

Specific technical objectives that were pursued to attain the above goals included:

- Development of laboratory facilities to conduct fundamental studies of hydrate thermochemistry and decomposition kinetics.
- Development of laboratory facilities and protocols to investigate microbial methane generation and consumption in seafloor sediments.
- Development of models of hydrate stability.
- Development of models of methane in the oceanic water column.
- Conduct of laboratory experiments on hydrate destabilization by chemical methods.

- Collaborative field studies of offshore hydrate biogeochemistry with the Naval Research Laboratory.
- Organization of workshops to promote international collaboration on methane hydrate R&D.

4.2 Scope of Work and Approach

Pursuant to the goals and technical objectives identified in the preceding section, work on the Methane Hydrates Task during the present reporting period focused on four primary areas which are described below.

4.2.1 Hydrate Thermochemistry and Kinetics

Testing and characterization of the performance of the novel combined calorimetry and Raman spectroscopy facility that was recently constructed was a major priority of this subtask. That instrument subsequently was applied to investigate the fundamental mechanisms by which various reagents (e.g., methanol solutions, brine) act to destabilize hydrates to release the methane gas. Analysis of chemical reagent and pressure destabilization data collected during earlier experiments also was undertaken.

4.2.2 Environmental Impacts of Methane Release from Seafloor Hydrates

This subtask is a continuation of activities pursued in previous years to: (1) assess the consequences of inadvertent or purposeful releases of methane from seafloor hydrates via the development of a model of methane transport through the ocean water column to the atmosphere; and (2) elucidate the mechanisms by which sediment microbes control free methane gas levels in, and methane leakage from, the seafloor sediment and arctic permafrost.

Hydrothermal vents were investigated as a natural analog of hydrate outgassing from the seafloor to extend our models of transport of methane in the ocean. Data in the literature from surveys of these vents were applied to validate model predictions.

4.2.3 Hydrate Microbiology

Microbial studies during the present reporting period focused on analyses of sediment samples collected during a 2006 oceanographic research cruise on the Hikurangi Margin offshore of the North Island of New Zealand. These microbiological assays were correlated with geochemical data on corresponding profiles of dissolved methane and geophysical records collected by NRL.

4.2.4 International Collaborative R&D

To promote international R&D cooperation on methane hydrates, HNEI is again helping to organize and sponsor the International Fiery Ice Workshop series on methane hydrates. In addition, in June-July 2006, HNEI personnel participated in a collaborative oceanographic research cruise of methane hydrate sites off New Zealand.

4.3 Technical Accomplishments

The principal technical accomplishments of the HEET Methane Hydrates Task for each of the components identified in the previous section are summarized below.

4.3.1 Methane Hydrate Destabilization

During the present reporting period, the primary accomplishments of this subtask were: (1) continuation of the analysis of a preliminary data set on hydrate destabilization arising from the injection of chemical inhibitors; (2) testing of the new instrument to perform simultaneous Raman spectroscopy and calorimetry; and (3) application of this instrument to investigate the formation and dissociation of hydrates with or without chemical inhibitors. Details of these accomplishments are provided below.

Reagent Destabilization of Methane Hydrates

The hydrate destabilization facility and initial shakedown experiments performed with this facility were described in the Final Technical Report for ONR Grant N00014-01-1-0928. During the present reporting period, the analysis of a suite of experiments conducted in an earlier Phase of HEET was pursued. In those tests, synthetic methane hydrate samples were destabilized by injection of warm water or methanol-water solutions, or by depressurization.

Initial modeling efforts showed that equilibrium kinetics (where the decomposing hydrate 'instantly' reaches thermodynamic equilibrium) were somewhat more successful in representing the data than published kinetic models. This analysis was based on a constant convective heat transfer coefficient H at the hydrate-liquid interface. We subsequently decided to investigate using simpler, but relatively more consistent, equilibrium hydrate dissociation kinetics while allowing H to vary with time. This approach was based on the intuitive premise that the more gas is released per unit of dissociation area, the more turbulence occurs in the liquid phase contacting the hydrate surface. Since the rate of gas release per unit area is proportional to the dissociation front velocity dL/dt , the choice of simple functional forms $H = C (dL/dt)^m$ was adopted to be tested in the numerical model, where C is a constant and m a positive exponent. The evolution equation for dL/dt then becomes implicit and must be solved at each time step within the Runge-Kutta scheme of the model.

Figures 4-1 through 4-6 compare selected load-cell and water-level data records with numerical results. One set of calculations, labeled SQRT 1.5E5, corresponds to $m = 0.5$ and C equal to 150,000. The other set was obtained with $m = 0.75$ and values of C increasing from 1.1×10^6 to 2.7×10^6 as the methanol concentration of the injected solution decreases¹. Overall, a decent match between data and calculations was obtained. With the methanol-rich cases of Records # 051003 and 051012, it should be noted that after about 10 minutes, the *real* hydrate sample a few centimeters long is likely to have been consumed, while the numerical sample ($L_0 = 0.5$ m) would continue to dissociate. A single value of C when $m = 0.5$ may be attractive for the sake of formal simplicity, but there is no reason *a priori* to rule against a value of C being different with different methanol concentrations since the physical properties of methanol-water solutions significantly change with composition. In this case, the choice $m = 0.75$ provides a very good fit with the data.

¹ Units for C vary with m and correspond to H and dL/dt expressed in SI units.

Record # 051028

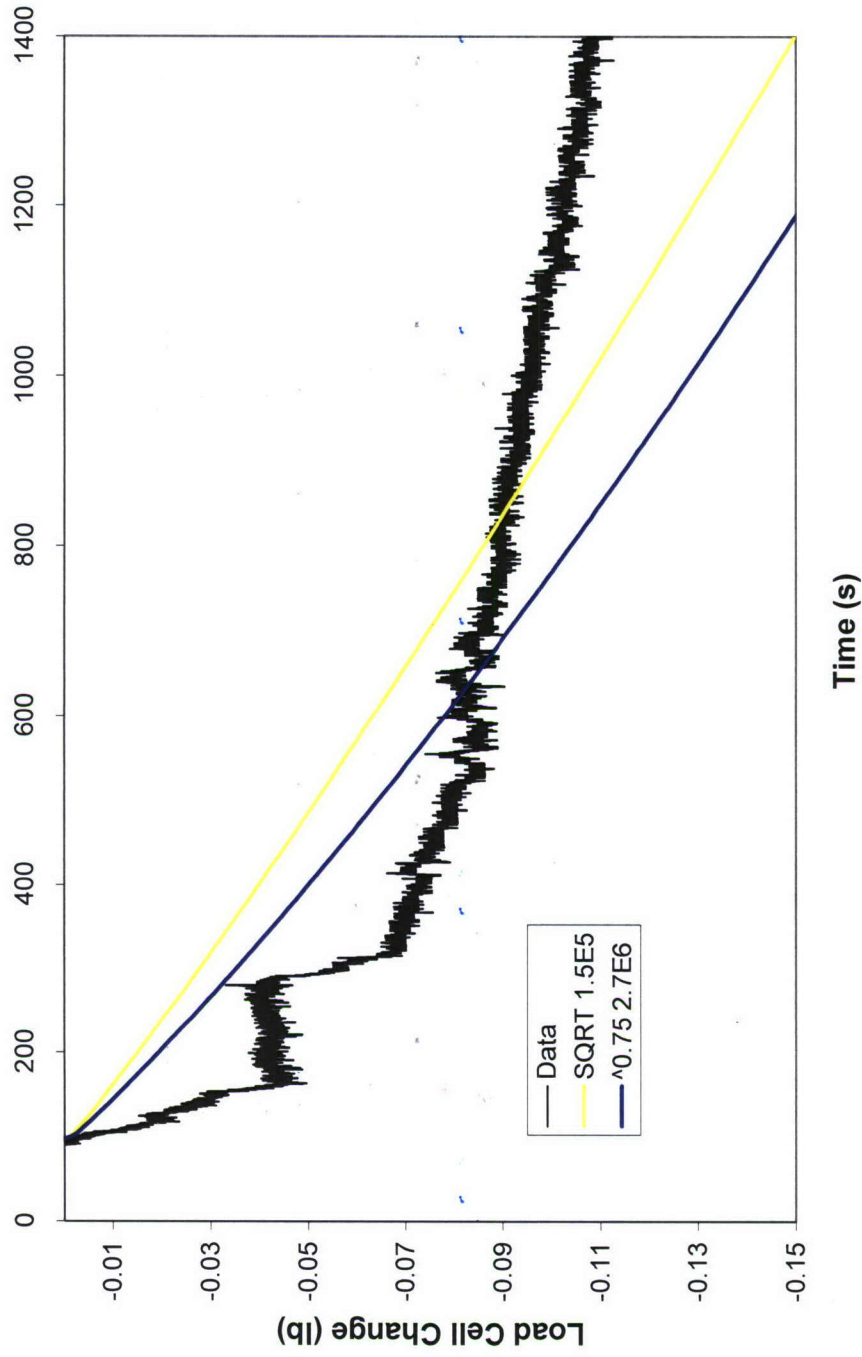


Figure 4-1. Load cell data and calculations with variable heat transfer coefficient for Record # 051028

Record # 050930

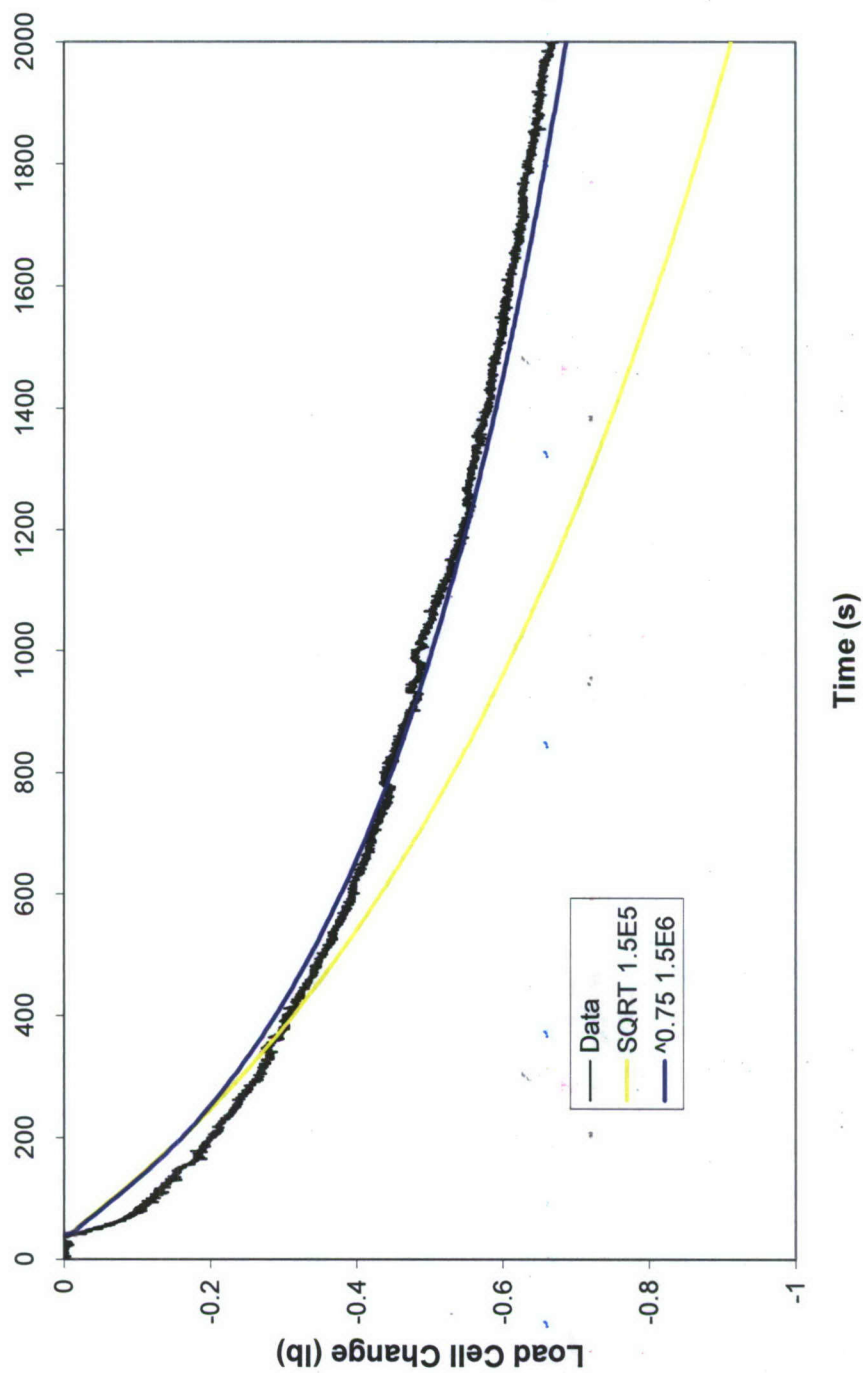


Figure 4-2. Load cell data and calculations with variable heat transfer coefficient for Record # 050930

Record # 051003

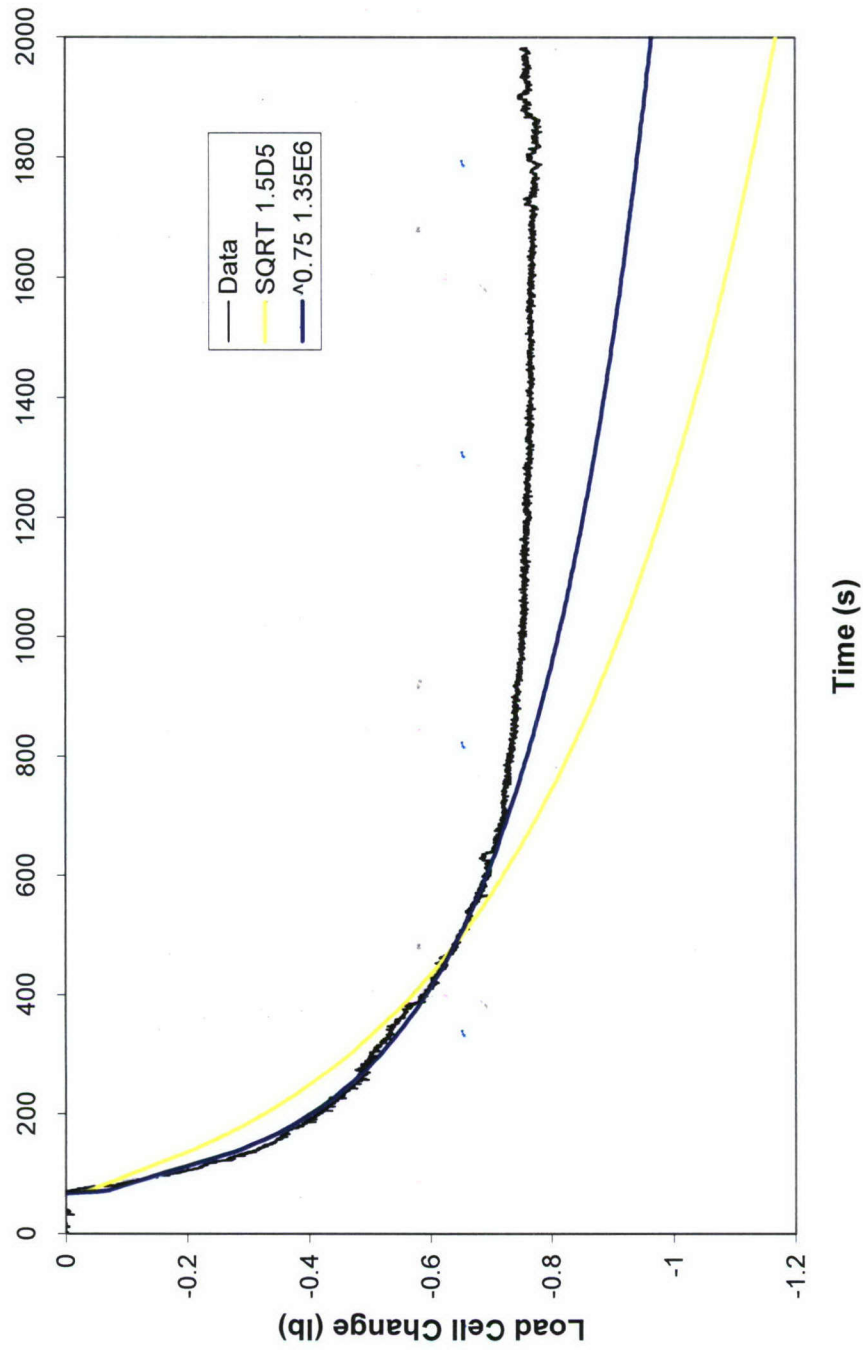


Figure 4-3. Load cell data and calculations with variable heat transfer coefficient for Record # 051003

Record # 051031

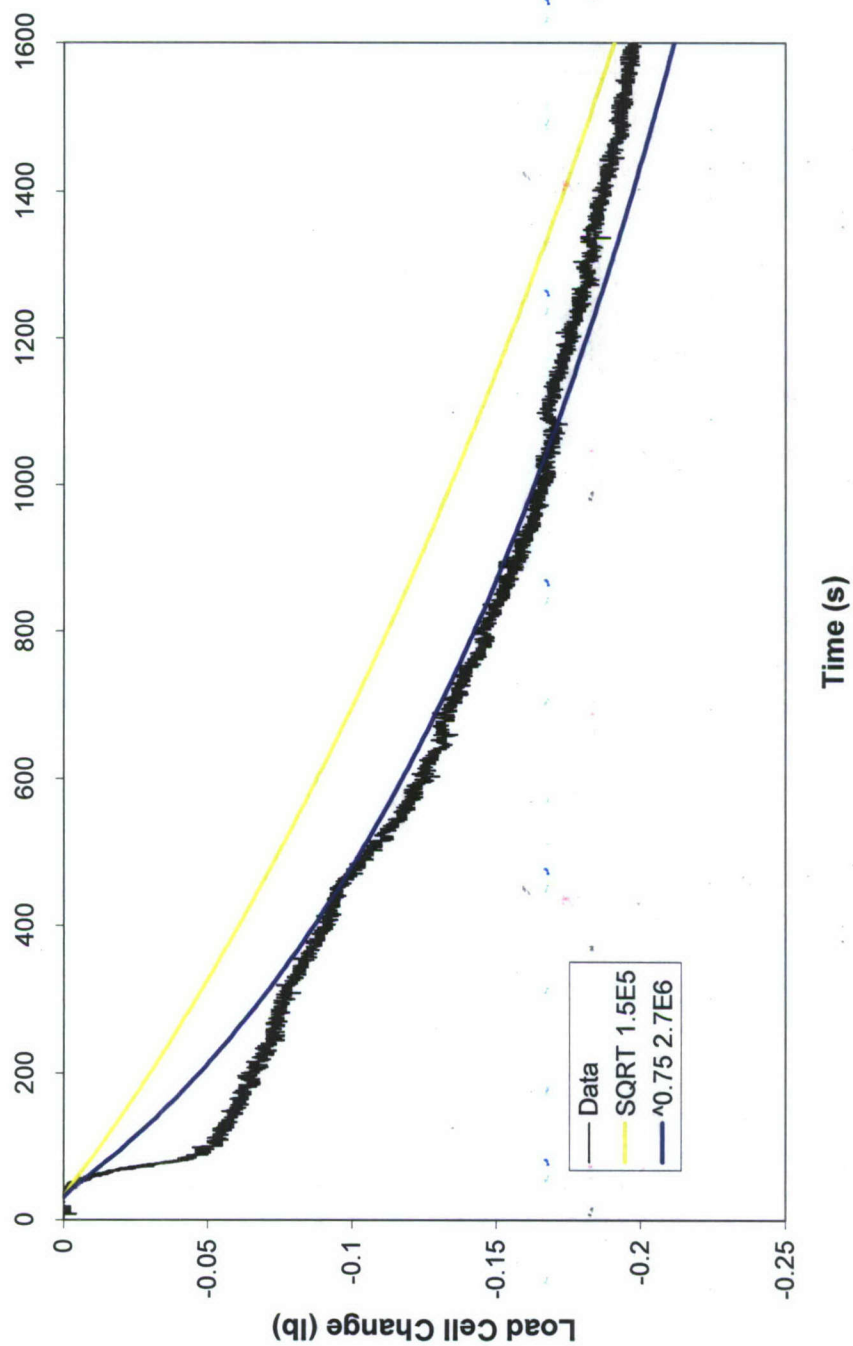


Figure 4-4. Load cell data and calculations with variable heat transfer coefficient for Record # 051031

Record # 051109

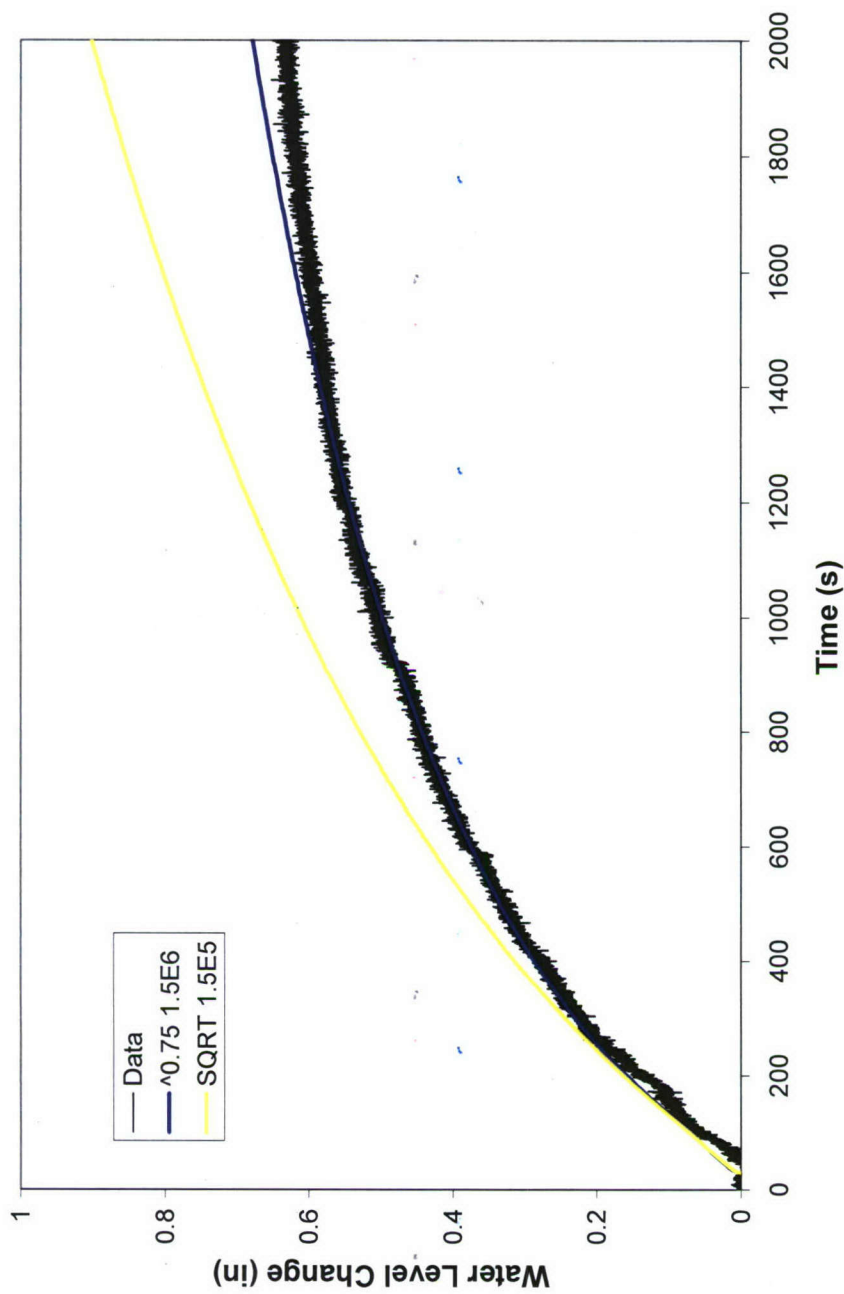


Figure 4-5. Water level data and calculations with variable heat transfer coefficient for Record # 051109

Record # 051012

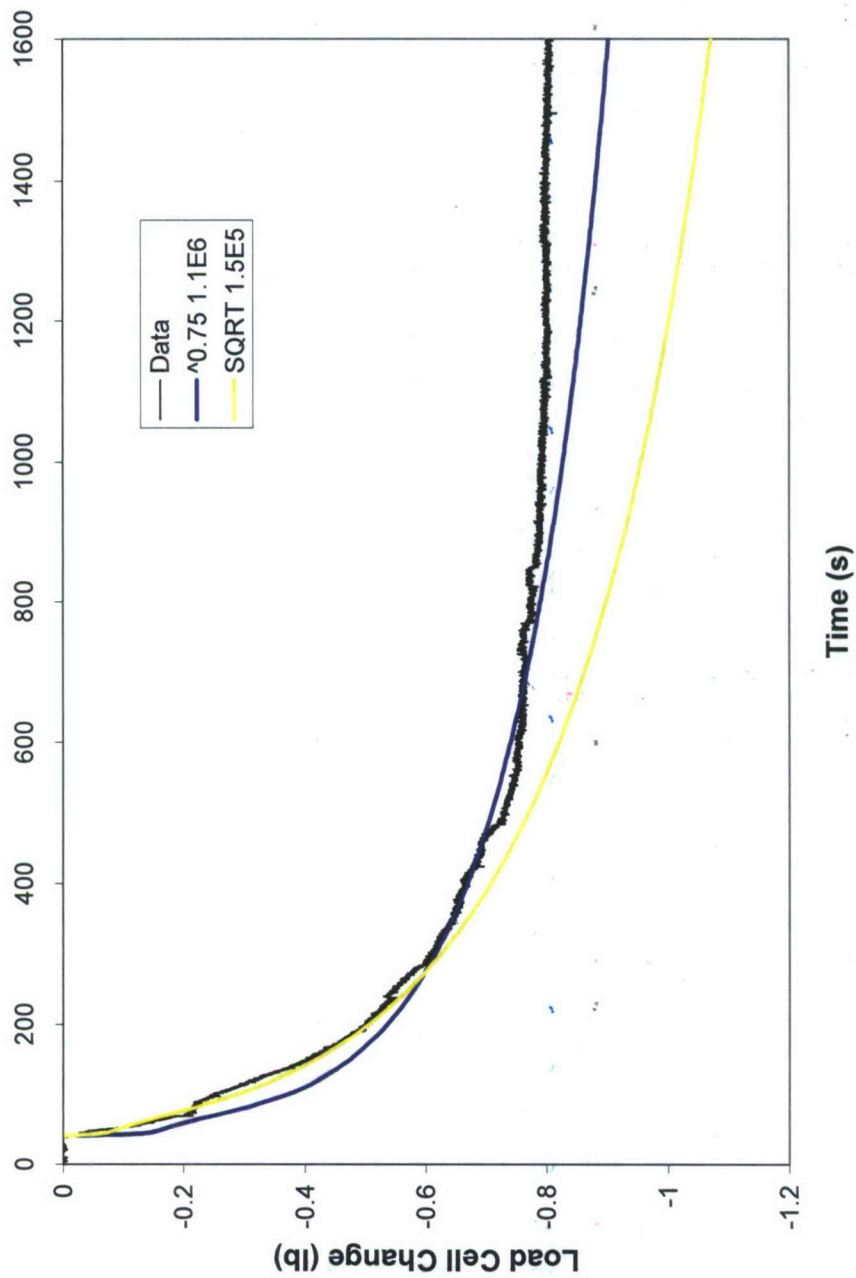


Figure 4-6. Water level data and calculations with variable heat transfer coefficient for Record # 051012

A dimensional analysis of typical convective heat transfer problems results in a relationship between Nusselt, Prandtl and Reynolds numbers. Many empirical relationships, sometimes based on boundary-layer theory, express the Nusselt number as the product of fractional powers of the Reynolds and Prandtl numbers, up to a multiplicative constant (e.g., Kreith and Bohn, 2001). Data on the density, viscosity and thermal conductivity of liquid methanol-water solutions were collected from the literature (Mikhail and Kimmel, 1961; Isdale *et al.*, 1985; Li, 1976) and a linear dependence of specific heat on composition was assumed. Interpreting dL/dt as the velocity in the Reynolds number, we tried to relate the expression selected for H in the numerical algorithm to an equivalent empirical relationship between non-dimensional numbers. Although all physical properties of methanol-water solutions monotonically increase as the methanol content drops, with the exception of viscosity, no satisfactory correlation was found that could explain the variation of C when $m = 0.75$.

Simultaneous Raman Spectroscopy and Calorimetry

The unique Raman spectroscopy and differential scanning calorimetry (DSC) system introduced in the Final Technical Report for ONR Grant N00014-01-1-0928 was completed and tested during the present reporting period. The system comprises three main components: (1) a Setaram BT2.15 DSC; (2) a Raman spectrometer; and (3) a fiber optic probe that is inserted into the DSC sample cell to provide optical access for the Raman measurements. A line diagram of the system is shown in Figure 4-7 and a photograph is provided in Figure 4-8. Also included in the figures is the reagent injection system that is used to study hydrate dissociation. The injection system is described in a following section.

The Raman subsystem consists of an excitation source (100 mW cw diode-pumped solid state laser at 532 nm), spectrograph, and optical detector. Two spectrograph units that feature triple grating turrets with adjustable center wavelengths were procured from Princeton Instruments in order to provide the full range of spectral resolution needed for the anticipated measurements. The SpectraPro-2558i and SpectraPro-2758i have focal lengths of 0.500 and 0.750 m, respectively. They are coupled to a Princeton Instruments PIXIS 2K 7533-0001 CCD camera that employs a 2048 x 512 back-illuminated detector array. This combination provides resolutions of approximately 0.05 nm (2558i) and 0.028 nm (2758i). High resolution is desirable since the Raman shifts of methane gas and hydrate are only separated by about 0.3 nm (8 cm^{-1}). The optical throughput of longer focal length (higher resolution) spectrographs, however, is reduced, which can be a problem at low light levels.

Laser light is brought into the DSC pressurized sample cell and scattered radiation is brought out and guided into the spectrograph with a fiber optic probe. The probe consists of seven 200 μm diameter UV-fused silica fibers potted in epoxy to provide a pressure seal inside a 0.125" o.d. stainless steel tube. A central transmitting fiber (that brings laser radiation into the cell) is surrounded by six receiving fibers. The probe is inserted through a 0.25" o.d. tube connected to the sample cell closure. The tube also encloses a length of 1/16" o.d. PEEK tube which is used to flow gases or liquid reagents into the cell. Gases flow out of the cell through the space between the probe, PEEK tubing and inner surface of the 0.25" tube. A special transition section was designed and fabricated from a block of 316 stainless steel to provide pressure-sealed access for the probe and various tubes. A photograph of the assembled probe and transition section is provided in Figure 4-9.

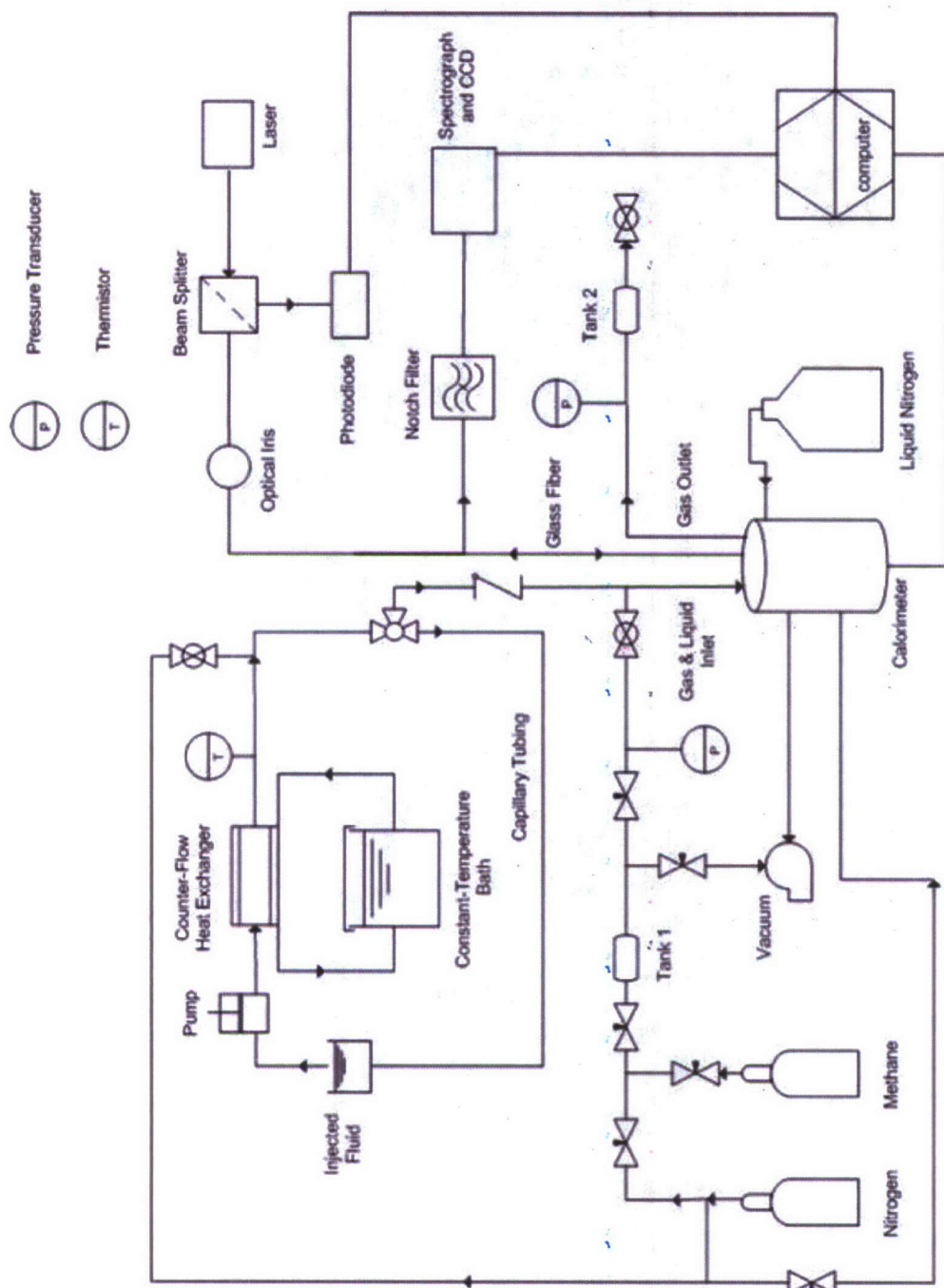


Figure 4-7. Line diagram of combined Raman spectroscopy and Differential Scanning Calorimetry system for the study of gas hydrates

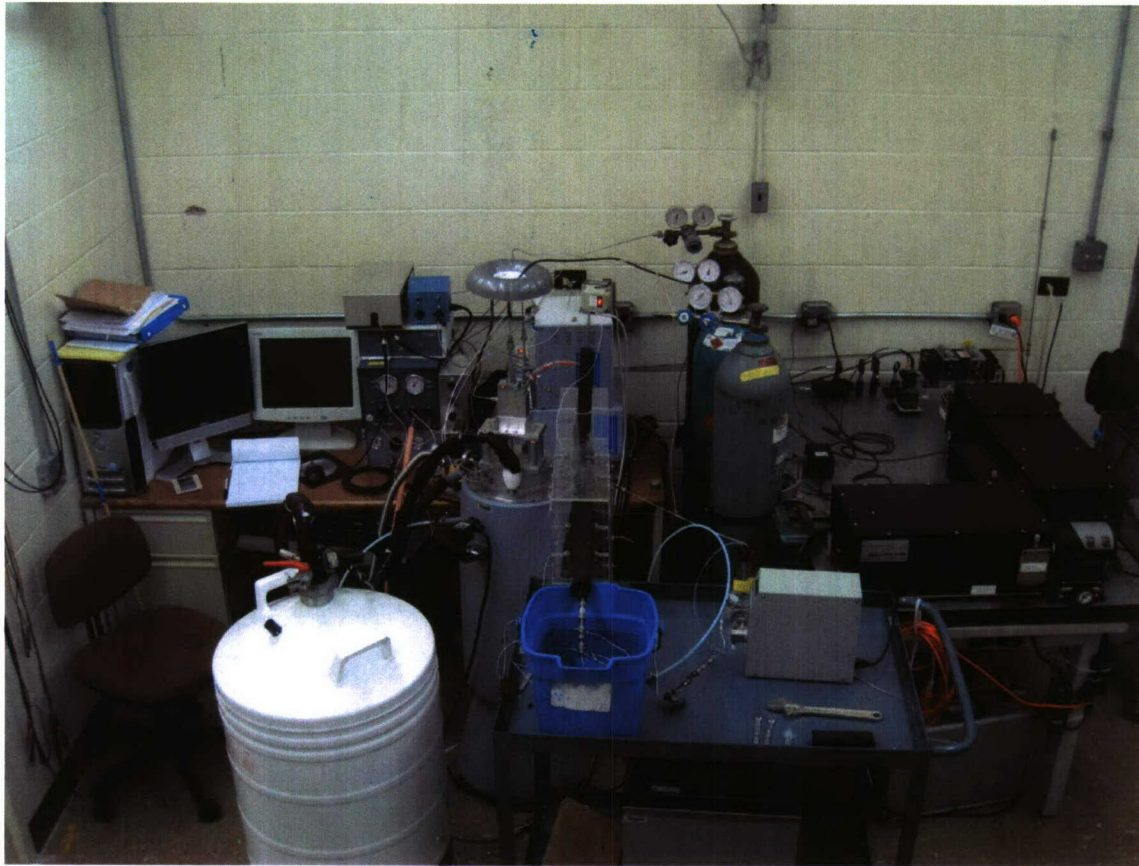


Figure 4-8. Photograph of the Raman spectroscopy/DSC facility

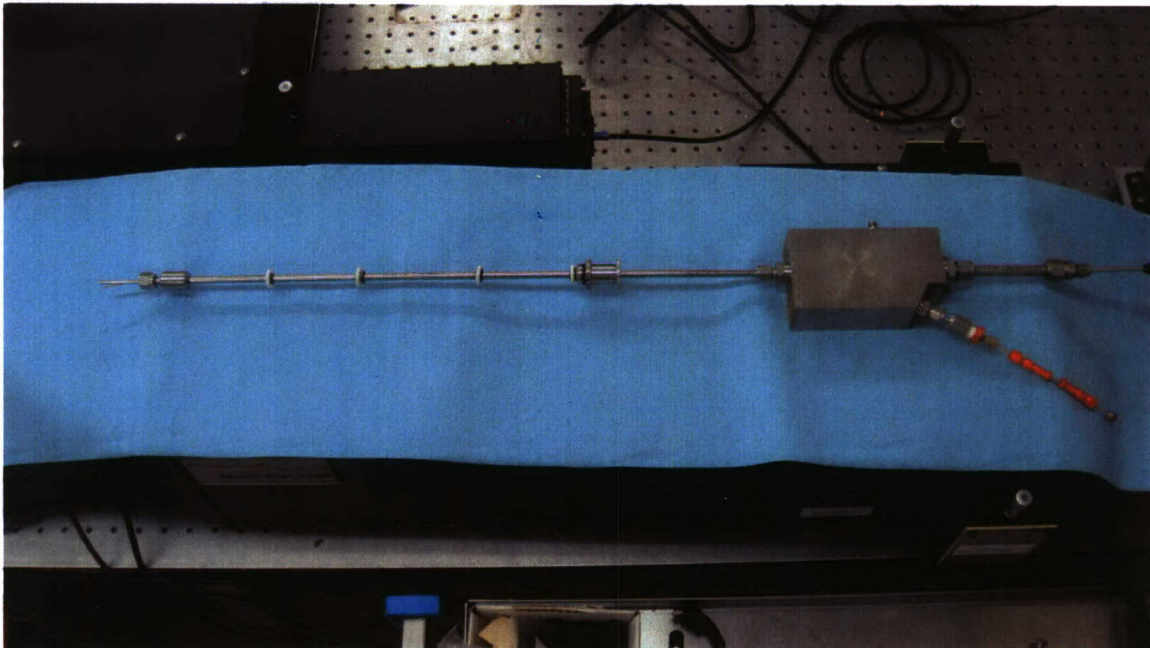


Figure 4-9. Photograph of the fiber optic probe assembly

Radiant energy of the laser is added to the sample cell when Raman measurements are performed. This energy must be deducted from the energy measured by the calorimeter. To account for the added energy, a portion (about 5%) of the laser beam incident on the transmitting fiber is directed through a narrow-band laser line filter onto a photodetector by a pellicle beam splitter. Via calibration, the output of this reference photodetector provides a continuous record of the laser power entering the sample cell.

Figure 4-10 shows the thermogram (power vs. time) measured by the calorimeter with laser radiation entering the empty sample cell. The graph on the right is the laser power exiting the fiber inferred from the calibrated reference detector signal. Both power curves can be integrated to estimate the laser energy added to the sample cell. Values of 1.34 J and 1.25 J are obtained from the thermogram and the photodetector signal, respectively. Note that heat flow out of the calorimeter declines slowly after the laser is turned off, due to the thermal capacitance of the cell and its contents. A portion of the 7% difference between the results can be attributed to light energy leaving the sample cell through the receiving fibers. Although agreement is not perfect, this method is sufficiently accurate to correct for the energy addition by the Raman excitation laser for most of the planned hydrate phase-change experiments. It is being employed in ongoing experiments.

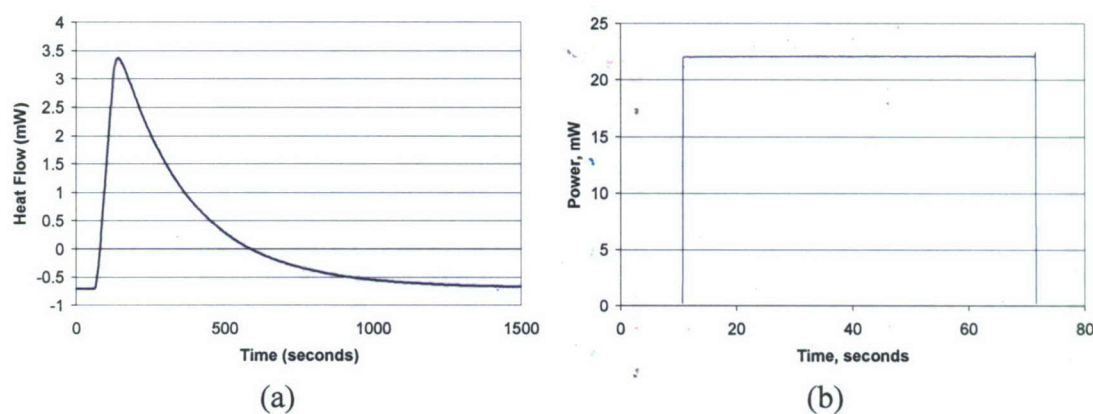


Figure 4-10. (a) Thermogram of laser radiation into the empty calorimeter sample cell and (b) laser power into the sample cell determined from the reference photodetector signal

Once the system was operational, it was applied in experiments in which methane hydrate was formed from ice and then thermally destabilized. The DSC thermogram and five of the collected Raman spectra are shown in Figures 4-11 through 4-16. Raman shifts for methane and methane hydrate have been reported by Subramanian and Sloan (1999), who observed that those peaks occur around 630 nm and are separated by 7-8 cm^{-1} . The thermogram (Figure 4-11) provides a record of heat flow and sample temperature over the duration of the experiment. The points in the process when Raman spectra were collected are also indicated on the thermogram. The first spectra (Figure 4-12) was taken after loading the sample cell with fine ice (crystal size < 200 μm) and pressurizing it with methane gas to 950 psig (6.65 MPa). It indicates the presence of methane gas and ice by their spectral peaks at 629.4 nm and 650 nm, respectively.

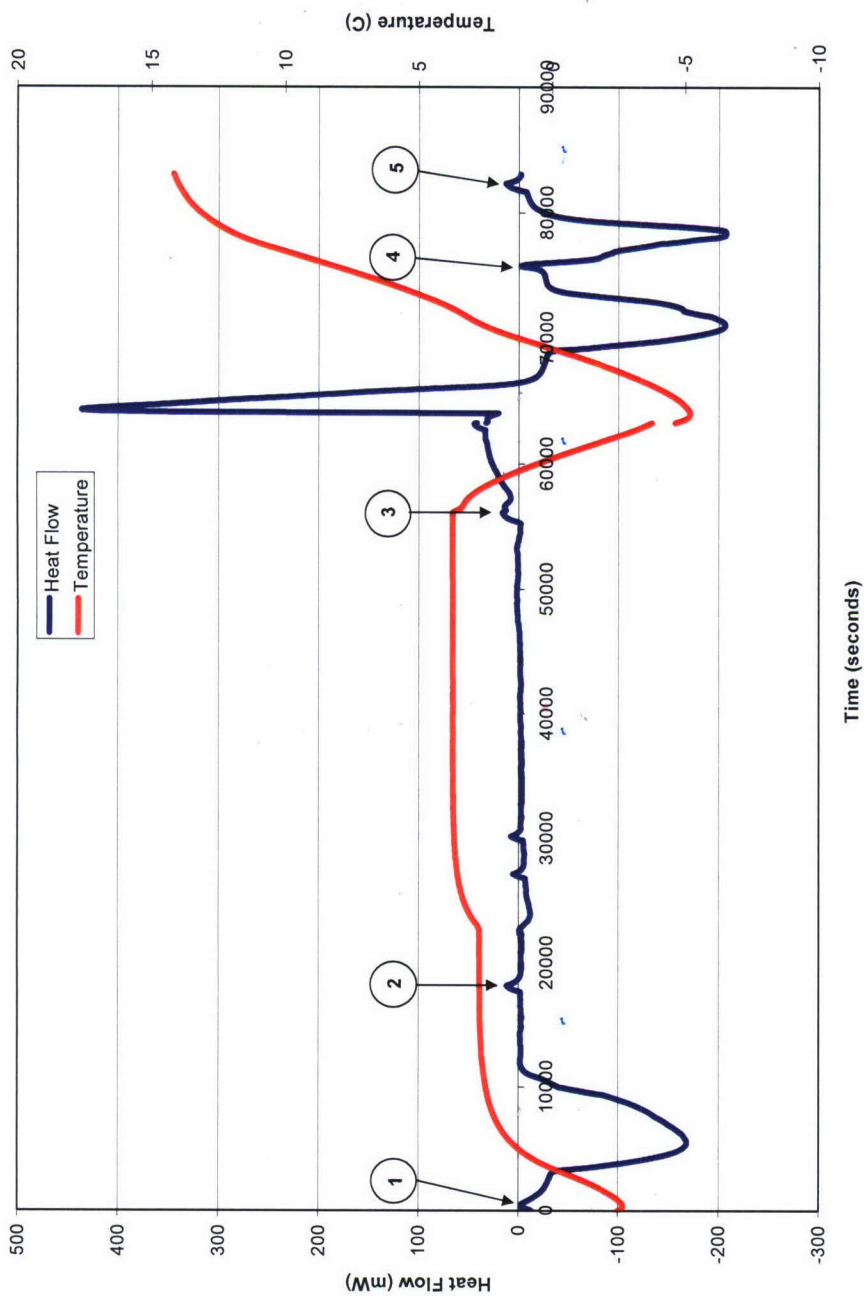


Figure 4-11. Thermogram of hydrate formation from ice and thermal destabilization of methane hydrate. Raman spectra were collected at the five points shown on the figure (see spectra on Figures 4-12 to 4-16).

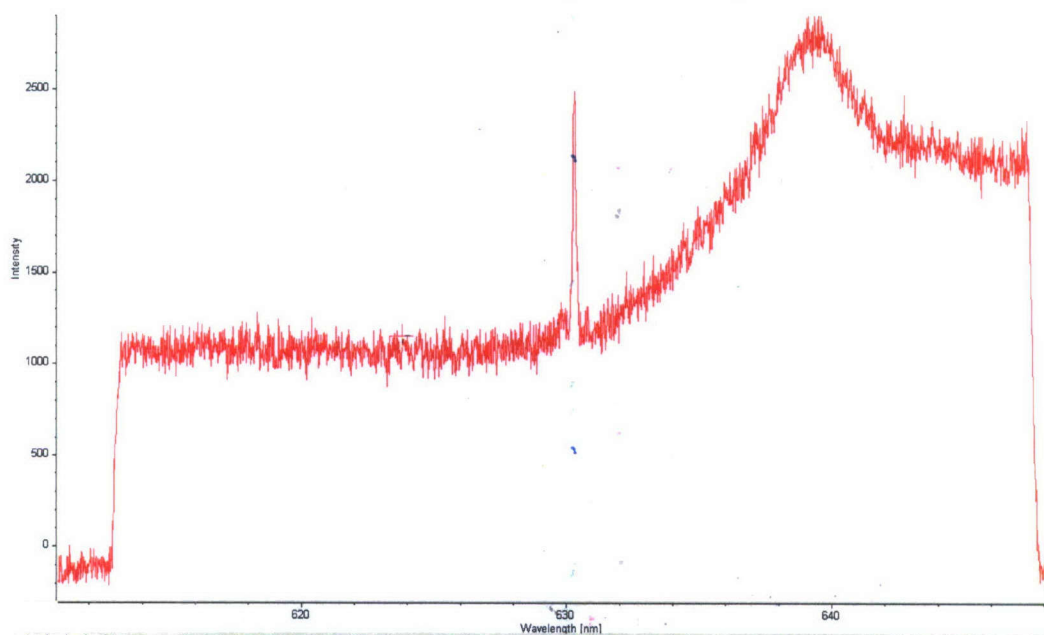


Figure 4-12. Raman spectra of the contents of the calorimeter cell filled with fine ice crystals at -3 °C and pressurized to 950 psig with methane gas

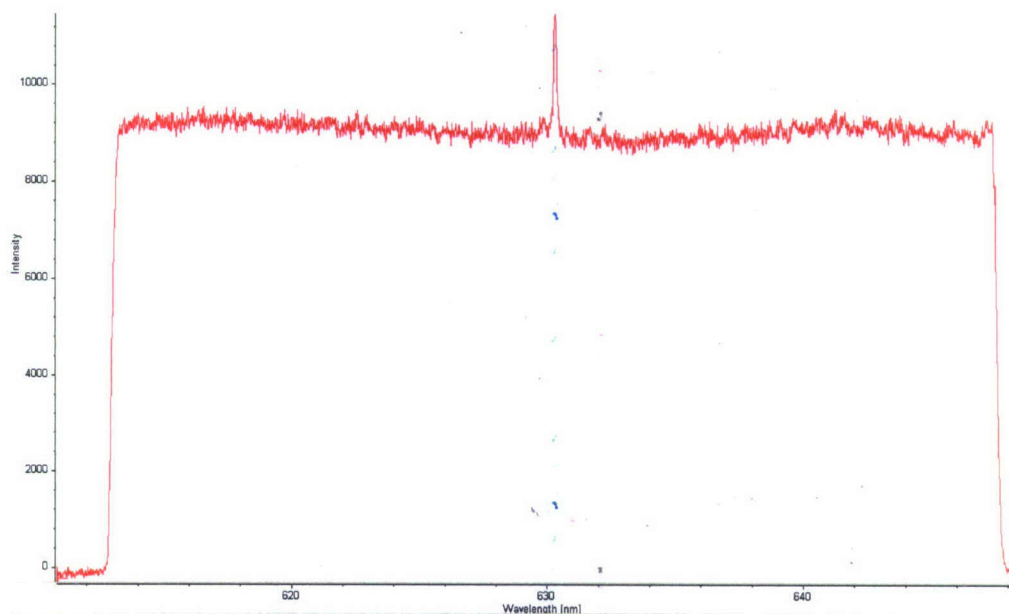


Figure 4-13. Raman spectra of the contents of the calorimeter cell after warming through the ice point to 4 °C

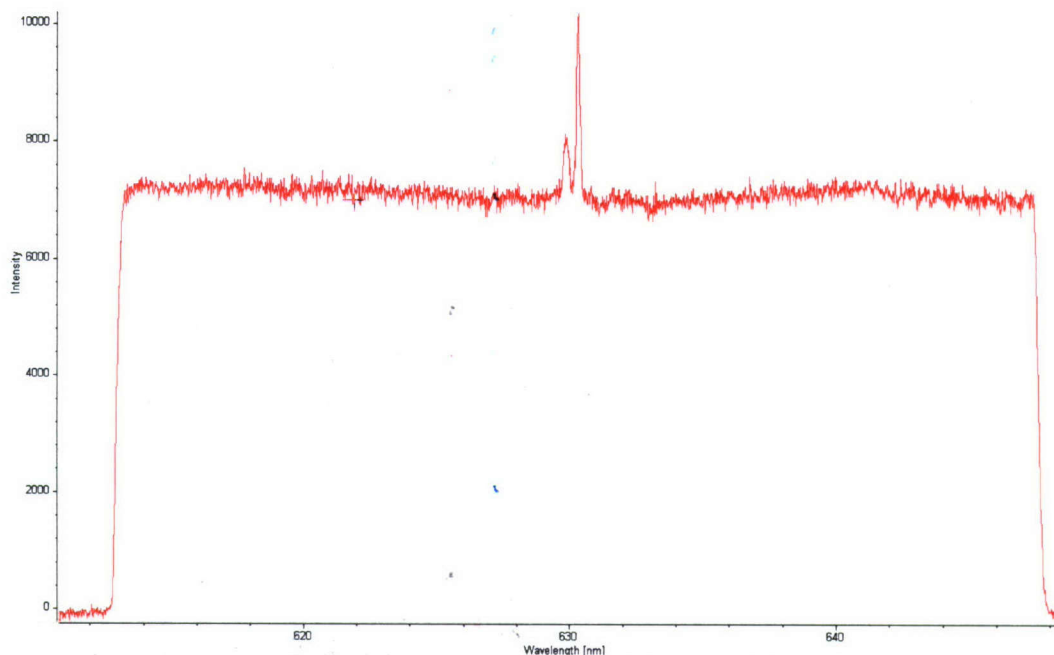


Figure 4-14. Raman spectra of the contents of the calorimeter cell after 12 hours at 4 °C

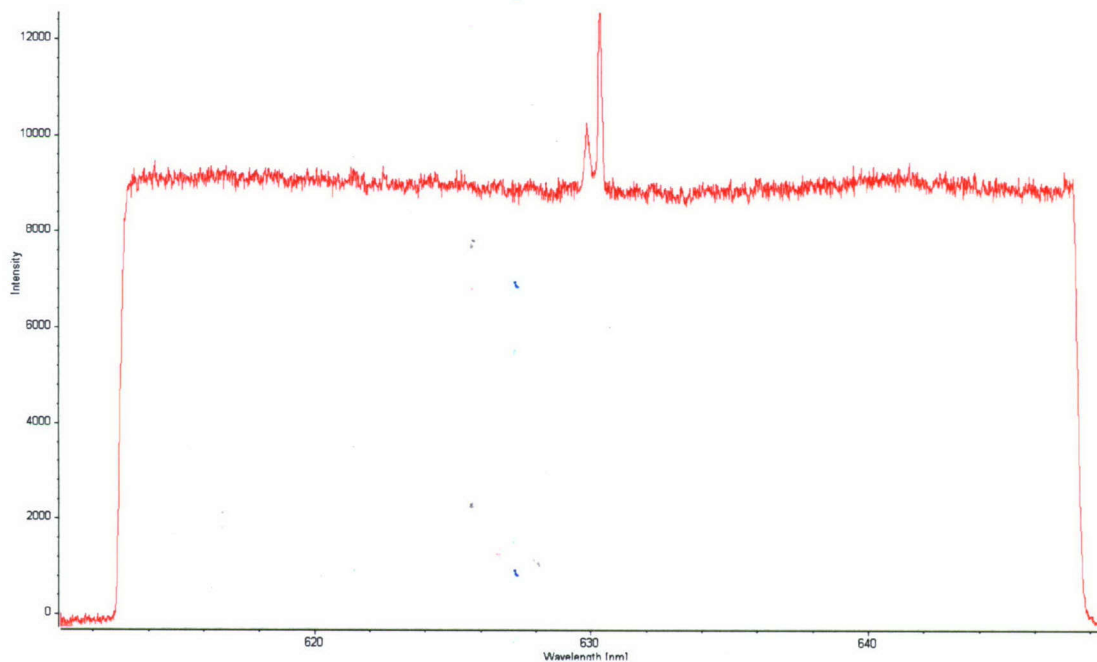


Figure 4-15. Raman spectra of the contents of the calorimeter sample cell after ice formation and melting

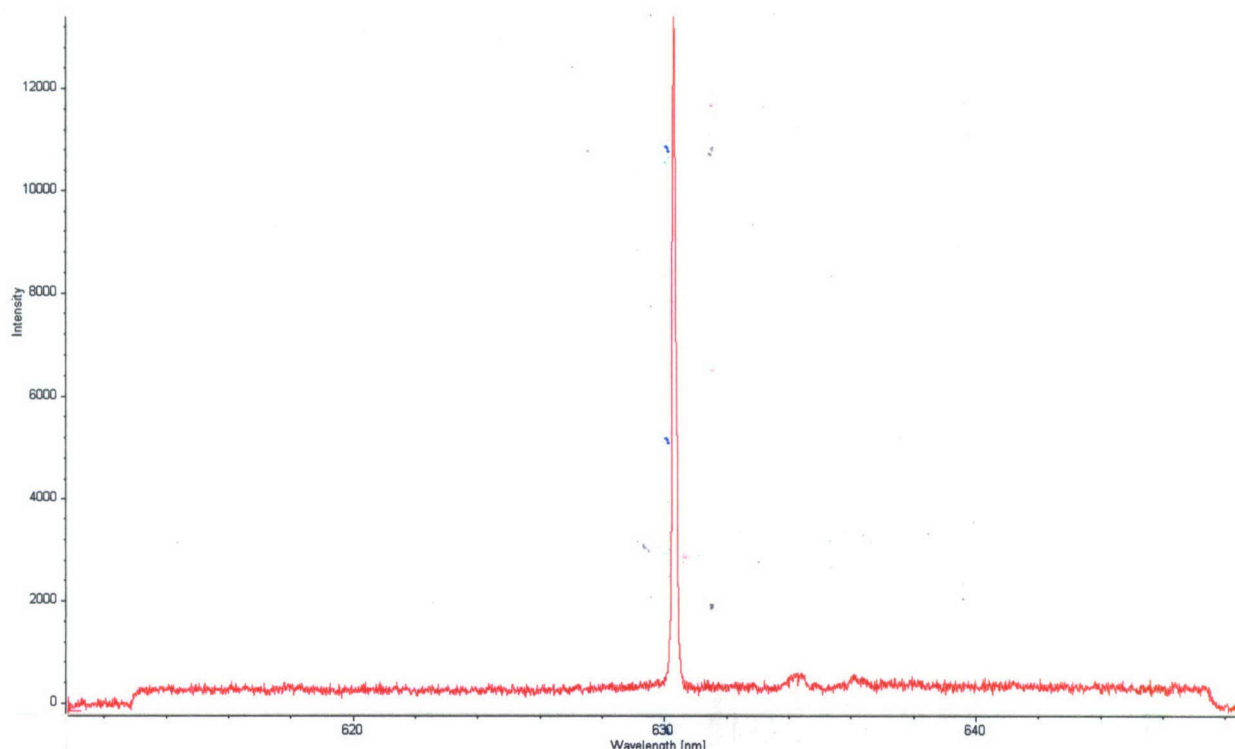


Figure 4-16. Raman spectra of the contents of the calorimeter cell after warming from 8 °C to 14 °C to destabilize the methane hydrate

The second spectra (Figure 4-13) was collected after the ice melted, as shown by the endothermic heat-flow peak on the thermogram, which begins once the temperature reaches 0 °C. The ice peak disappears from the Raman spectra and the methane peak remains at 630 nm. The third spectra (Figure 4-14) corresponds to the point in the process just before the temperature was reduced to -5°C. A gas hydrate peak is observed at 628.9 nm, approximately 12.6 cm^{-1} from the methane gas peak. A fourth spectra (Figure 4-15) was taken after ice formation and melting. Methane gas and hydrate are still detected. Finally, in the last spectra (Figure 4-16), the hydrate has disappeared (as well as the ice); only the methane gas peak remains. The thermogram reveals an endothermic heat-flow peak associated with hydrate dissociation, and the spectra indicates the disappearance of the hydrate phase.

These tests demonstrate the value of combining Raman spectroscopy and DSC to study methane hydrates. Whereas previously, the absence of definitive heat-flow peaks might imply that hydrate had not formed, Raman measurements can conclusively confirm the existence of hydrates – for example, between points 2 and 3 in Figure 4-11. The new instrument provides us with the means clearly to identify the processes and structures associated with the energy signatures measured by the calorimeter.

Application of Simultaneous Raman Spectroscopy and Calorimetry to the Study of Hydrate Dissociation by Alcohols

Three methods have been proposed to destabilize and extract fuel gas from hydrates: heating, depressurization, and chemical reagents. Chemical reagents (thermodynamic inhibitors) also have been employed for decades to avoid hydrate blockages in natural gas pipelines. While there is a substantial amount of information in the literature regarding hydrate decomposition using thermodynamic inhibitors such as alcohols, most studies have been limited to determining the pressure-temperature stability curve of hydrates in the presence of these inhibitors. The mechanism by which alcohols decompose hydrates remains elusive. Knowledge about the fundamental mechanism could help identify more environmentally-benign alternatives (for, say, methane recovery from hydrates in seafloor sediment or permafrost, where the injection of large quantities of methanol is not acceptable).

Since the driving force for hydrate dissociation in the presence of thermodynamic inhibitors is not known, models have been developed based, for example, on a change in partial pressure (Masoudi and Tohidi, 2005) or a change in the activity of water (Javanmardi *et al.*, 2001). There are deficiencies in these approaches which underscore the need to identify the driving force.

Faraday (1859) was the first to propose the existence of a quasi-liquid layer that covered the surface of ice. Since then, numerous studies, including theoretical work of Fletcher (1968), vibrational spectroscopy studies performed by Wei *et al.* (2002), and molecular dynamics simulations by Furukawa and Nada (1997), all have confirmed the existence of this quasi-liquid layer.

The quasi-liquid layer lowers the free energy of ice (Fletcher, 1968). While the onset temperature of the quasi-liquid layer is controversial and varies from one study to another, surface-specific experimental studies have shown the layer at temperatures of 219 K (Lied *et al.*, 1994) and 200 K (Wei *et al.*, 2002) – well below the freezing point of water. We posit that a similar layer exists at the surface of solid hydrate crystals as well.

Experimental studies by Ebukuro *et al.* (1999) and Guo *et al.* (2003) using Raman spectroscopy and X-ray emission spectroscopy, respectively, examined the interaction between methanol and water molecules. It was discovered that methanol molecules formed chains and rings that were six or eight molecules long. When methanol and water molecules were mixed, these studies showed that the water molecules broke apart the methanol chain and ring structures, and formed methanol-water clusters bound by the hydroxyl group.

In consideration of these findings, we propose the hypothesis that alcohols are effective hydrate inhibitors because their hydroxyl group binds to the water molecules and changes the chemical potential in the quasi-liquid layer. This disturbance in the dynamic equilibrium between the water molecules in the hydrate lattice and the water molecules in the quasi-liquid layer drives hydrate dissociation. That is, in the absence of alcohols, there exists a balance between hydrate decomposition and hydrate formation at the solid surface. The alcohols bind up the released

water such that formation is hindered. The new spectroscopy-calorimetry facility is being employed to test our hypothesis.

A liquid injection system was fabricated to add methanol to the pressurized sample cell. Primary components are shown in Figure 4-7. An Eldex Optos 2SMP piston pump was used to inject the methanol into the cell through the 1/16" o.d. PEEK tubing. The flow rate can be adjusted between 0.03 ml/min and 40 ml/min. The maximum discharge pressure is 6000 psig (41.5 MPa). An ethylene glycol circulating temperature bath is used to cool the methanol in a counterflow heat exchanger before it is injected, to minimize thermal effects. In preliminary tests, by proper selection of methanol temperature and injection rate, it was possible to limit the perturbation of sample temperature due to the addition of methanol solutions to less than 0.5 °C.

Experiments were conducted in which methane hydrate was again synthesized from ice. Fine ice crystals ($< 200 \mu\text{m}$) were loaded into the calorimeter sample cell and then pressurized to 950 psig (6.65 MPa). The sample temperature was raised above the melting point of ice and then held for 9 hours at 4 °C, within the hydrate stability zone. The sample was next cooled to temperatures well below the ice point (around -20 °C) before being increased to about -5 °C. Spectra collected at this stage of the process indicated the presence of gas hydrate (Figure 4-17). 2 mL of methanol was then injected into the cell at a rate of 1 mL/min. Spectra taken immediately after injection did not detect gas hydrate (Figure 4-18). The thermogram shown in Figure 4-19 reveals a large endothermic reaction near the end of the process that can be attributed to hydrate destabilization.

Raman measurements also were performed during the injection experiment to investigate the binding of methanol and water. According to experimental studies by Ebukuro *et al.* (1999) as well as Guo *et al.* (2003), the Raman shift of methanol decreases from 1037 cm^{-1} to 1020 cm^{-1} as it binds to water molecules. In our experiment, a decrease in the Raman shift from 1040 cm^{-1} to 1029 cm^{-1} was observed after methanol injection into the sample cell, as seen in Figure 4-20. This suggests that methanol was binding to the water molecules in the quasi-liquid layer since there was no bulk-liquid-water phase.

Measurements performed with the new calorimetry/Raman spectroscopy instrument indicate the existence of a methanol-water complex that coincides with the destabilization of methane hydrate. Future tests will include injecting liquid alkane compounds, which have similar properties to methanol, but without a hydroxyl group. This will further test our hypothesis that alcohols dissolve hydrate by binding water molecules in the quasi-liquid layer and disrupting the dynamic equilibrium between formation and decomposition.

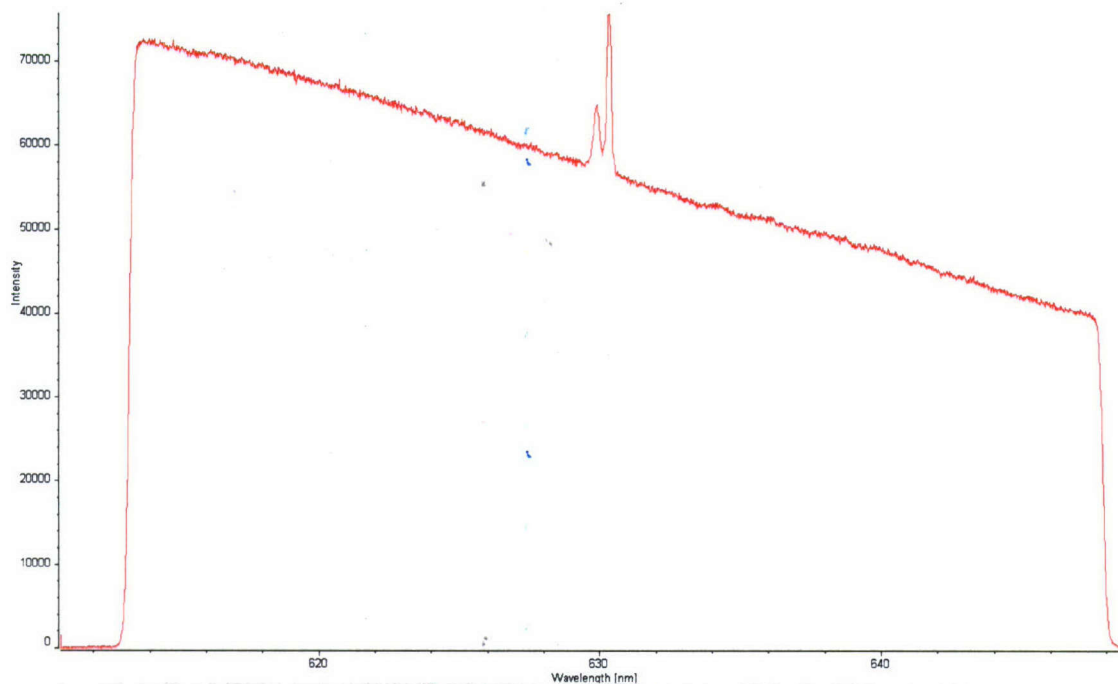


Figure 4-17. Raman spectra showing methane hydrate in sample cell prior to methanol injection

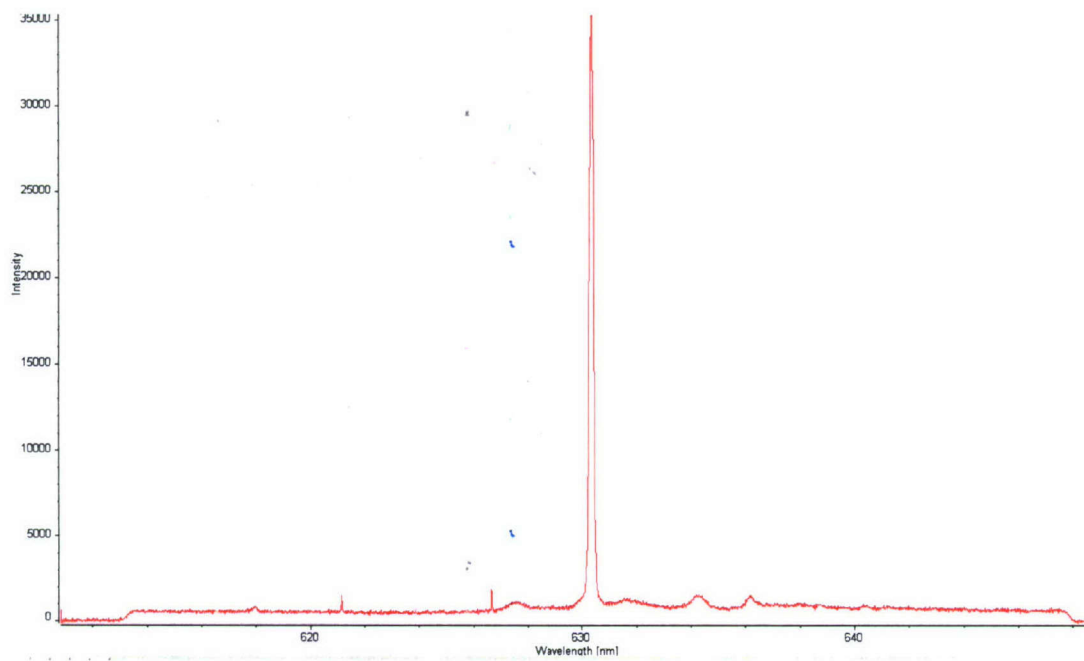


Figure 4-18. Raman spectra of contents of calorimeter cell after methanol injection. The hydrate peak has disappeared.

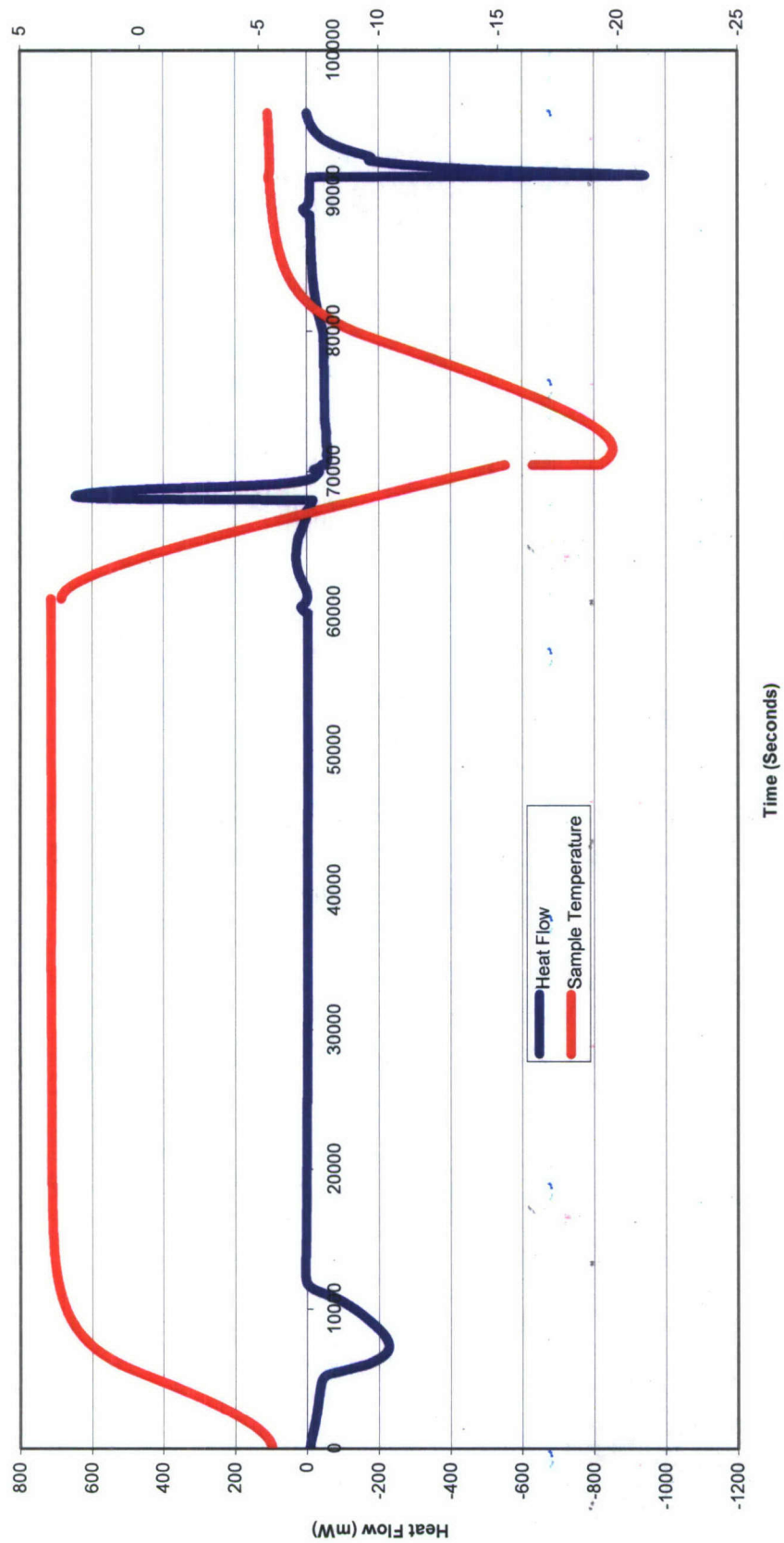


Figure 4-19. Thermogram of the injection (between 80,000 and 90,000 s) of 2 mL of methanol onto solid hydrate at a rate of 1 mL/min

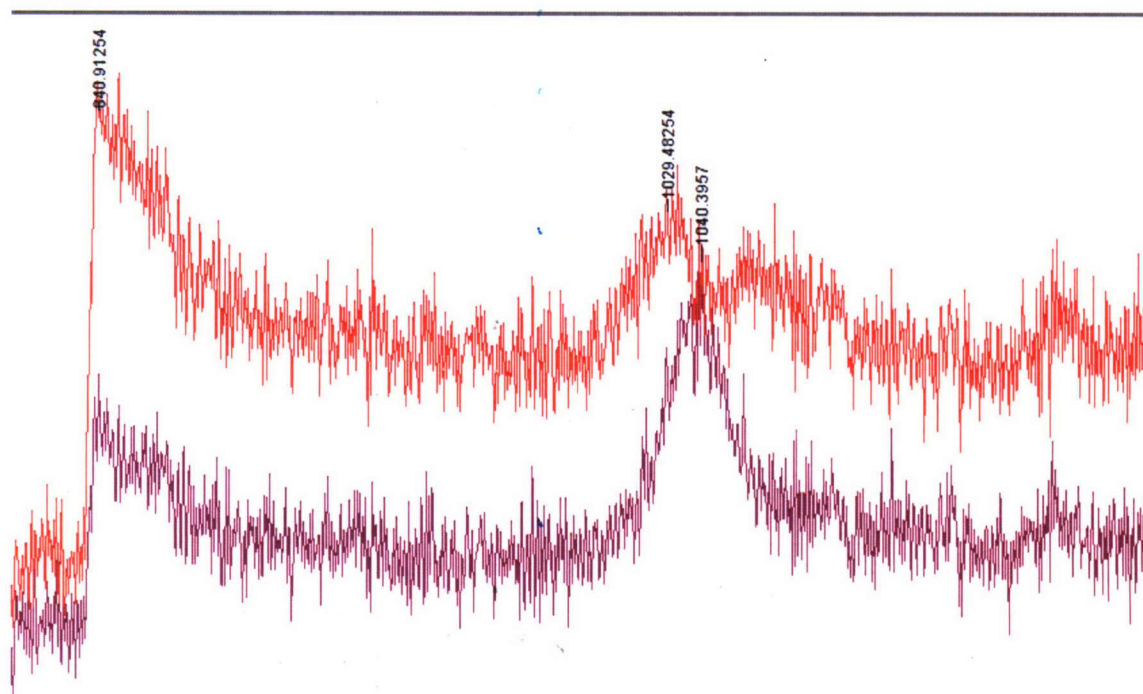


Figure 4-20. Change in Raman shift of pure methanol (purple) to a methanol-water complex (red) after injection into the hydrate sample

4.3.2 Environmental Impacts of Methane Release from Seafloor Hydrates

During the present reporting period, the primary accomplishments of this subtask was the development of a suite of simple models of methane in the vicinity of hydrothermal seafloor vent fields.

Modeling of Methane in Aging Hydrothermal Plumes

Waters in the vicinity of marine fields provide unique opportunities to improve our understanding of aerobic methane oxidation mediated by bacterial assemblages because methane concentrations are much greater than in background waters, while the spatial and temporal scales of the near-field (buoyant) and far-field (neutrally buoyant) plumes are sufficiently small to account for dispersal in relatively simple ways. A site of considerable interest is the Endeavour Segment of the Juan de Fuca Ridge, at about 48°N and 129°W, where many measurements have been made including methane concentration, methane oxidation rate and stable carbon isotopic composition $\delta^{13}C$ (Lupton *et al.*, 1985; de Angelis *et al.*, 1993; Johnson *et al.*, 2000; Cowen *et al.*, 2002). Even though cold seeps such as Hydrate Ridge (Cascadia Oregon Margin) have also been investigated (Grant and Whiticar, 2002), the lack of a temperature anomaly and of appreciable buoyancy in the released fluids represents a relative modeling drawback. Therefore, data collected along the Endeavour Segment of the Juan de Fuca Ridge were used to provide boundary conditions, a few key parameters (e.g., isotopic fractionation) and, more importantly, validation targets for the present effort.

The basic physical characteristics of the buoyant plumes that rise from seafloor hydrothermal vents to a level of neutral buoyancy are discussed in Appendix B. Biological and oxidation processes *per se* are not expected to play any role during the short ascent of these buoyant plumes, but some understanding of volume flux and dilution of the original vent fluids is useful to better characterize boundary conditions for the intrusion layer. The intrusion layer, or lateral plume, slowly spreads over days at a nearly constant level above the seafloor. This far-field plume extends over several kilometers horizontally. In the area of interest, and in spite of considerable dilution of the vent fluid in the near field, the far-field plume exhibits methane concentrations two orders of magnitude greater than in background seawater (de Angelis *et al.*, 1993; Cowen *et al.*, 2002). The time and space scales of the far-field plume combined with high initial substrate (methane) availability lend themselves to significant oxidation. This is evident in: a) the methane oxidation rates measured by de Angelis *et al.* (1993), described as “the highest such rates so far reported for the water column of any marine environment;” and b) in the stable isotopic (^{13}C) composition data of Cowen *et al.* (2002), with $\delta^{13}\text{C}$ values “among the heaviest yet reported from a natural marine environment.” Simple far-field models of the evolution of methane concentration, isotopic composition and methanotroph-carbon concentration throughout the lateral plume are presented below. The goal of such models is to better parameterize aerobic oxidation by testing simple formalisms against data sets.

Far-field model formulation

Three variables of interest are methane concentration x , carbon-13 methane ($^{13}\text{CH}_4$) concentration y and methanotroph carbon concentration z . The isotopic composition of methane is given by $\delta^{13}\text{C}(\text{‰}) = 1000\{y / \{R_{\text{PDB}}(x - y)\} - 1\}$, where R_{PDB} is the isotopic ratio of the PDB standard equal to 0.011237 (Craig, 1957). Vertical transport phenomena are considered negligible through the laterally spreading plumes. The steady-state equations for x , y and z , defined in a horizontal fluid domain of uniform thickness, can be written:

$$\left\{ \begin{array}{l} (\vec{u} \cdot \nabla)x - \nabla \cdot (K \nabla x) = -kxz, \\ (\vec{u} \cdot \nabla)y - \nabla \cdot (K \nabla y) = -\frac{kxyz}{y + \alpha_k(x - y)}, \text{ and} \\ (\vec{u} \cdot \nabla)z - \nabla \cdot (K \nabla z) = \alpha_k xz. \end{array} \right. \quad \begin{array}{l} (1.a) \\ (1.b) \\ (1.c) \end{array}$$

The velocity vector \vec{u} and eddy diffusion coefficient K are functions of the horizontal coordinates X and Y , and the Nabla operator ∇ is equal to $(\partial/\partial X, \partial/\partial Y)$. The right-hand sides of Eq. (1) reflect the non-conservative behavior of methane-related species. In Eq. (1.a), methane oxidation is assumed to be proportional to x and z with a basic rate constant k . This formulation implies that methane concentrations are well below kinetic saturation levels of the order of a few μM (Harrits and Hanson, 1980; Ward, 1987), but much higher than possible low oxidation thresholds of the order of 1 nM (Scranton and Brewer, 1978; Nihous and Masutani, 2006). Eq. (1.b) reflects the preferential uptake of $^{12}\text{CH}_4$ during oxidation and subsequent $^{13}\text{CH}_4$ enrichment of the ambient water; with the fractionation factor α_k slightly larger than one and $x \gg y$, the sink

of $^{13}\text{CH}_4$ can be closely approximated by $-kyz/\alpha_k$. Eq. (1.c) assumes that methane is a limiting substrate for methanotroph growth with an assimilation ratio α , although other nutrients like ammonium are consumed (Jones *et al.*, 1984; Ward, 1987; Cowen *et al.*, 2002). Over characteristic time scales for plume spreading, it is also assumed for lack of better knowledge that any sink balancing methanotroph growth is negligible.

A closed-form solution

Assuming negligible diffusion ($K = 0$) and a uniform current of magnitude U along the X -direction, the transport operator in the left-hand-sides simply is Ud/dX . The resulting system of equations yields closed-form solutions if the $^{13}\text{CH}_4$ sink is approximated by $-kyz/\alpha_k$. Assigning the subscript 0 to quantities at the origin of the lateral plume $X = 0$, we obtain:

$$x = \frac{\left(\frac{\alpha x_0^2}{z_0} + x_0\right) \exp\left\{-\left(\alpha x_0 + z_0\right) \frac{kX}{U}\right\}}{1 + \frac{\alpha x_0}{z_0} \exp\left\{-\left(\alpha x_0 + z_0\right) \frac{kX}{U}\right\}}, \quad (2.a)$$

$$y = \frac{y_0 \left(1 + \frac{\alpha x_0}{z_0}\right)^{\frac{1}{\alpha_k}} \exp\left\{-\left(\alpha x_0 + z_0\right) \frac{kX}{U}\right\}}{\left[1 + \frac{\alpha x_0}{z_0} \exp\left\{-\left(\alpha x_0 + z_0\right) \frac{kX}{U}\right\}\right]^{\frac{1}{\alpha_k}}}, \text{ and} \quad (2.b)$$

$$z = \frac{\alpha x_0 + z_0}{1 + \frac{\alpha x_0}{z_0} \exp\left\{-\left(\alpha x_0 + z_0\right) \frac{kX}{U}\right\}}. \quad (2.c)$$

As expected from the differential equations, the identity $\alpha x + z = \alpha x_0 + z_0$ holds everywhere. In particular, methane is consumed completely and methanotroph carbon concentration reaches the asymptotic value $\alpha x_0 + z_0$ at large downstream distances X . With diffusion, however, z would be expected to reach a maximum instead. This is confirmed by measurements of specific methane oxidation rates $Sp = kz$ and bacterial cell counts as a function of X performed in lateral plumes of the Endeavour Segment (de Angelis *et al.*, 1993); the maxima are reached within 4 km downstream of the vent locations and typically represent a two- to four-fold increase over initial values. If methane oxidation proceeds rapidly enough in the neighborhood of the hydrothermal vents, then a measured peak in specific oxidation rate could be interpreted as the asymptotic value of the zero-diffusion model. The knowledge of α , x_0 and the maximum of $Sp/Sp_0 = z/z_0$ would then yield estimates of z_0 . With $\alpha \approx 0.30$ (de Angelis *et al.*, 1993) to 0.50 (Ward, 1987) and $x_0 \approx 400$ (de Angelis *et al.*, 1993) to 600 nM (Cowen *et al.*, 2002), values of Sp/Sp_0 between two and four imply that $z_0 \approx 100$ nM.

In turn, the rate constant k can be constrained by the ratio Sp_0/z_0 . With measured specific oxidation rates of 0.02 to 0.08 day^{-1} at the origin of the lateral plume $X \approx 0$ (de Angelis *et al.*,

1993), it was inferred that k must be of order 10^{-9} to $10^{-8} \text{ nM}^{-1}\text{-s}^{-1}$. This range is compatible with methanotroph biomass-specific oxidation rates $Spm = kx$ recently published in a study of aerobic methane oxidation in three small temperate lakes (Sundh *et al.*; 2005).

The rise in measured bacterial cell counts, from about $7 \times 10^5 \text{ ml}^{-1}$ to $9 \times 10^5 \text{ ml}^{-1}$ (de Angelis *et al.*, 1993), does not match that in specific oxidation rates, although Sp is by definition proportional to z . A simple explanation is that only a fraction of the bacterial population represents methanotrophs; the data under consideration would suggest that the methanotroph count is of the order of 10^5 ml^{-1} at $X \approx 0$. This corresponds to the proportion of methanotrophs approximately increasing from 1/7 to 1/3 in the initial spreading stage of the lateral plume. Such values are comparable to methanotroph biomass fractions as high as 41% reported by Sundh *et al.* (2005). Dividing $z_0 \approx 100 \text{ nM-C}$ by the estimated cell count at $X \approx 0$ yields a methanotroph carbon content of 12 fg-C/cell . This is close to published values for marine bacterial assemblages (Fukuda *et al.*, 1998; DeLong, 1999; Button *et al.*, 1999) as well as to an estimate derived from Sundh *et al.* (2005).

Using a methanotroph carbon content of 12 fg-C/cell , it is possible to infer a value of k as high as $8 \times 10^{-7} \text{ nM}^{-1}\text{-s}^{-1}$ for the incubation experiments of Ward (1987). This is two orders of magnitude higher than our estimate. Sundh *et al.* (2005) also noted that values of Spm derived from *in situ* data seem much lower than those obtained from laboratory cultures of methanotrophs. One possible factor is temperature since the far field of deep marine hydrothermal plumes as well as the hypolimnion of high-latitude lakes is cold, while laboratory cultures typically are conducted at 'room temperature.' The strong influence of temperature on methanotroph metabolism has been documented (Sieburth *et al.*, 1987; Harrits and Hanson, 1980; Hutton and Zobell, 1949).

The elements of Eq. (2) were considered with $\alpha = 0.30$ (de Angelis *et al.*, 1993), and the following parameters from Cowen *et al.* (2002): $x_0 = 600 \text{ nM}$, $y_0 = 6.357 \text{ nM}$ (or $\delta^{13}\text{C} = -47\text{‰}$ at the origin), $\alpha_k = 1.0075$ and a target value $\delta^{13}\text{C} = -5\text{‰}$ at a distance $X = 15 \text{ km}$. z_0 was varied upward from 50 nM to 260 nM . For this range of initial methanotroph carbon concentrations and with $U = 1 \text{ km/day}$, the target isotopic enrichment is reached for k between 2.4×10^{-8} and $1.1 \times 10^{-8} \text{ nM}^{-1}\text{-s}^{-1}$. The solution is invariant if k and U remain proportional so that a current of 500 m/day would correspond to k between 1.2×10^{-8} and $6.1 \times 10^{-9} \text{ nM}^{-1}\text{-s}^{-1}$. The earlier inference that k should be of order 10^{-9} to $10^{-8} \text{ nM}^{-1}\text{-s}^{-1}$ was not reached using any ^{13}C isotopic measurement. Yet, this range of methane oxidation rate constants successfully reproduces measured $\delta^{13}\text{C}$ values, 15 km away from the vent location.

An axisymmetric model without current

Many black smokers ($n \approx 40$) potentially representative of 'point sources' were identified in the area under consideration (Lupton *et al.*, 1985). With the estimate $Q(h) = 327 \text{ m}^3/\text{s}$ made in Appendix B for each individual buoyant plume, an overall volume flux Q_f of about $1.3 \times 10^4 \text{ m}^3/\text{s}$ would feed the lateral (far-field) plume of thickness $D = 180 \text{ m}$. With negligible currents, at least in an average sense, the lateral plume would be axisymmetric and the far-field Eq. (1) one-dimensional in the radial direction r . Assuming a horizontal eddy diffusivity $K = Pr$ based on the concept of diffusion velocity (Joseph and Sendner, 1958), the advection-diffusion operator in

Eq. (1) can be written $\frac{Q_f}{2\pi Dr} \frac{\partial}{\partial r} - \frac{1}{r} \frac{\partial}{\partial r} (Pr^2 \frac{\partial}{\partial r})$. For any conservative species such as the

temperature anomaly $\delta\theta$, the steady-state equation would consist in setting this operator to zero; the solution is:

$$\delta\theta = \delta\theta|_{r=0} \left\{ 1 - \exp\left(-\frac{Q_f}{2\pi DP r}\right) \right\}. \quad (3)$$

Although the temperature-anomaly data of Cowen *et al.* (2002) is not easy to interpret, it suggests a characteristic length $r_f = Q_f/(2\pi DP)$ of the order of 10 km. With the values of Q_f and D above, this corresponds to $P \sim 1$ mm/s.

Eq. (1) elements for methane-related species and the proposed axisymmetric configuration were solved next in a region extending 60 km radially from the vent location. The same values of α , x_0 , and y_0 as above were selected, as well as a slightly larger isotopic fractionation constant $\alpha_k = 1.0077$, and a baseline value z_0 equal to 100 nM. With a numerical domain considerably larger than the sampled area, Dirichlet conditions were applied at the outside boundary, namely a methane concentration of 2 nM, a ^{13}C -methane concentration based on $\delta^{13}\text{C} = -43\text{‰}$ and a methanotroph carbon concentration corresponding to a background turnover time of 50 years (Rehder *et al.*, 1999; Valentine *et al.*, 2001; Nihous and Masutani, 2006). k , P and Q_f were varied in order to match the following experimental targets as well as possible: the mean values of $\delta^{13}\text{C}$ measured by Cowen *et al.* (2002) at several sampling stations, and the specific methane oxidation rates reported by de Angelis *et al.* (1993).

The parameters k , P and Q_f were swept to identify trends, and manually tuned thereafter. This task was somewhat simplified by the fact that predictions of the isotopic composition and of the specific oxidation rates often responded in opposite ways as a single parameter changed. Parametric variations where r_f or Sp_0 are constrained were also examined; in the latter case, a change in k was adjusted with a different value of z_0 . A combination that yielded good results is $k = 7.5 \times 10^{-9} \text{ nM}^{-1}\text{-s}^{-1}$, $P = 3 \times 10^{-4} \text{ m/s}$ and $Q_f = 3250 \text{ m}^3/\text{s}$; this volume flux is only a quarter of the estimate based on 40 black smokers and the analysis from Appendix B – it corresponds to $r_f \approx 10$ km. A variation, where k increases to $1.0 \times 10^{-8} \text{ nM}^{-1}\text{-s}^{-1}$ while z_0 drops to 50 nM, was considered as well. Finally, a third combination, with $k = 1.0 \times 10^{-8} \text{ nM}^{-1}\text{-s}^{-1}$, $z_0 = 50 \text{ nM}$ and $Q_f = 1625 \text{ m}^3/\text{s}$, was selected.

Predicted methane concentrations shown in Figure 4-21 rapidly drop with distance. This decline is representative of active microbial oxidation. Calculations agree reasonably well with observations given the steepness of the curve and the risk of sampling away from the plume core (17 - 62 nM at $r \sim 3$ km versus 26 nM in Cowen *et al.*, 2002). At greater distances, however, calculated values fall well below observed residual concentrations (0.01 nM at $r \sim 15$ km versus < 5.4 nM in de Angelis *et al.*, 1993, and < 11 nM in Cowen *et al.*, 2002). Figure 4-22 displays predictions of isotopic compositions. The data of Cowen *et al.* (2002) is well reproduced with the two parametric combinations corresponding to the larger flow ($Q_f = 3250 \text{ m}^3/\text{s}$); in those cases, the very strong ^{13}C enrichment about 15 km away from the vent location is predicted as a maximum, although no data collected at greater distances can ascertain that the maximum does not occur further. With the smaller flow, enrichment does not reach high enough levels at great enough distances. Finally, the specific oxidation rates measured by de Angelis *et al.* (2003) were compared to model calculations as shown in Figure 4-23. Here, the lower flow ($Q_f = 1625 \text{ m}^3/\text{s}$) yields oxidation rates that closely represent the upper envelope of the data set; in contrast, the

higher flow leads to overestimated oxidation rates at radial distances beyond about 3 km. This suggests that flow rates may have been lower in the early 1990s than in the early 2000s, e.g., as a result of tectonic events (Johnson *et al.*, 2000). In all cases, maximum oxidation rates occur about 2 to 3 km away from the vent location; such distance corresponds to the time lag during which methanotroph growth outweighs dispersal. $\delta^{13}C$ is defined with a ratio of isotopic species that both undergo dispersal so that the effect of the oxidation process on ^{13}C enrichment extends much further; this is clearly demonstrated by experimental and model results.

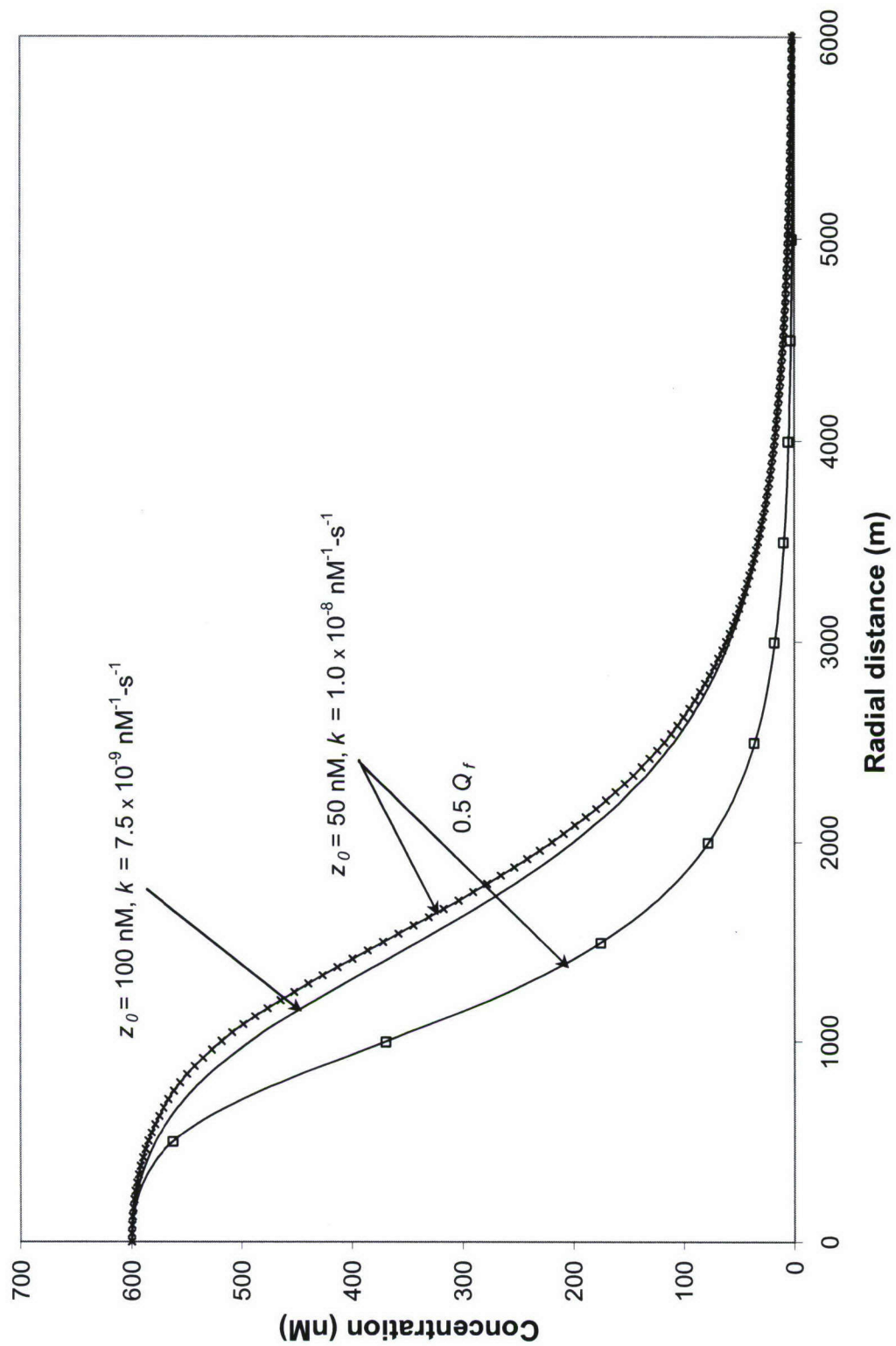


Figure 4-21. Predicted methane concentration (axisymmetric model)

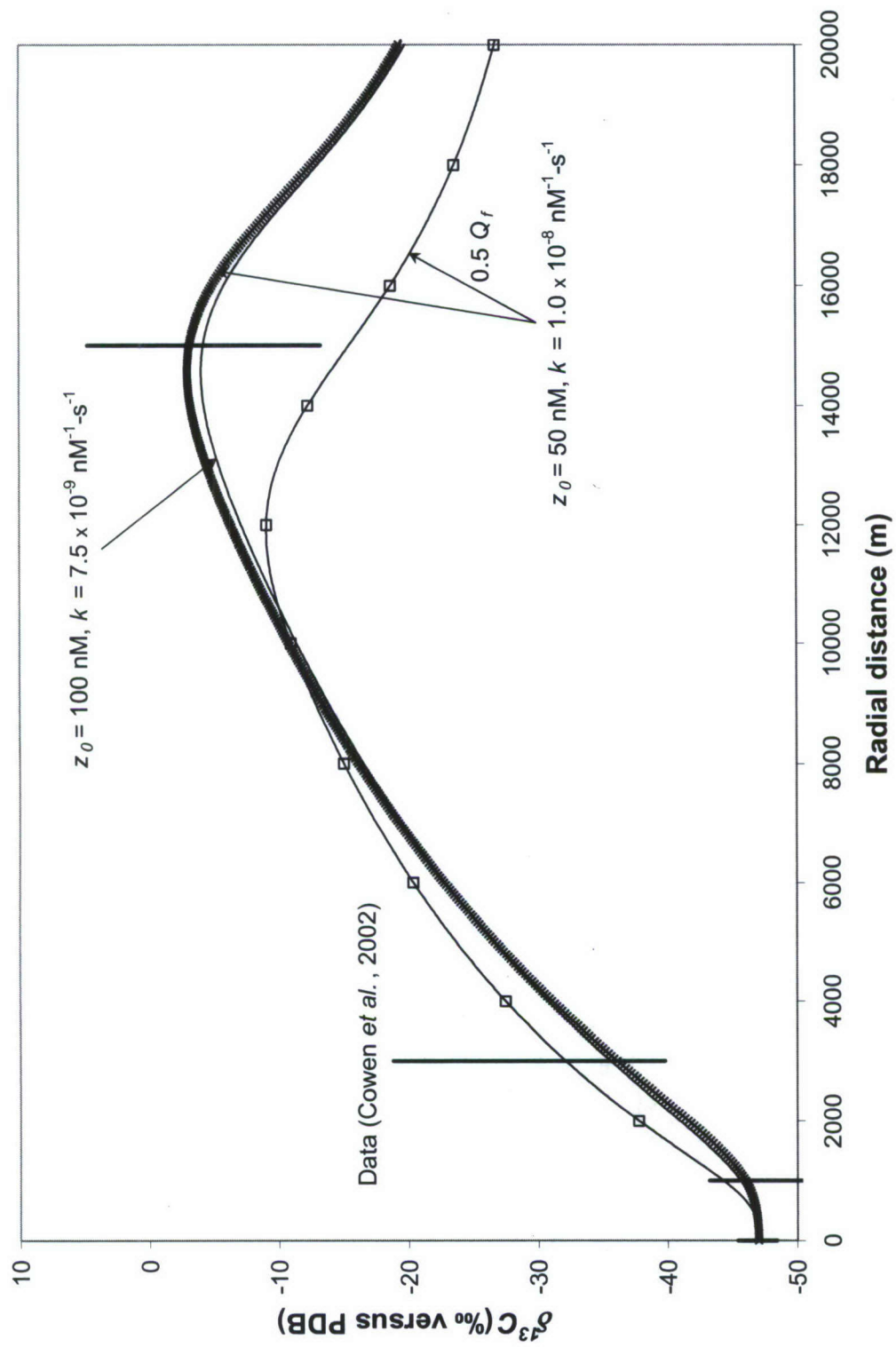


Figure 4-22. Predicted isotopic composition (axisymmetric model) and data of Cowen et al. (2002)

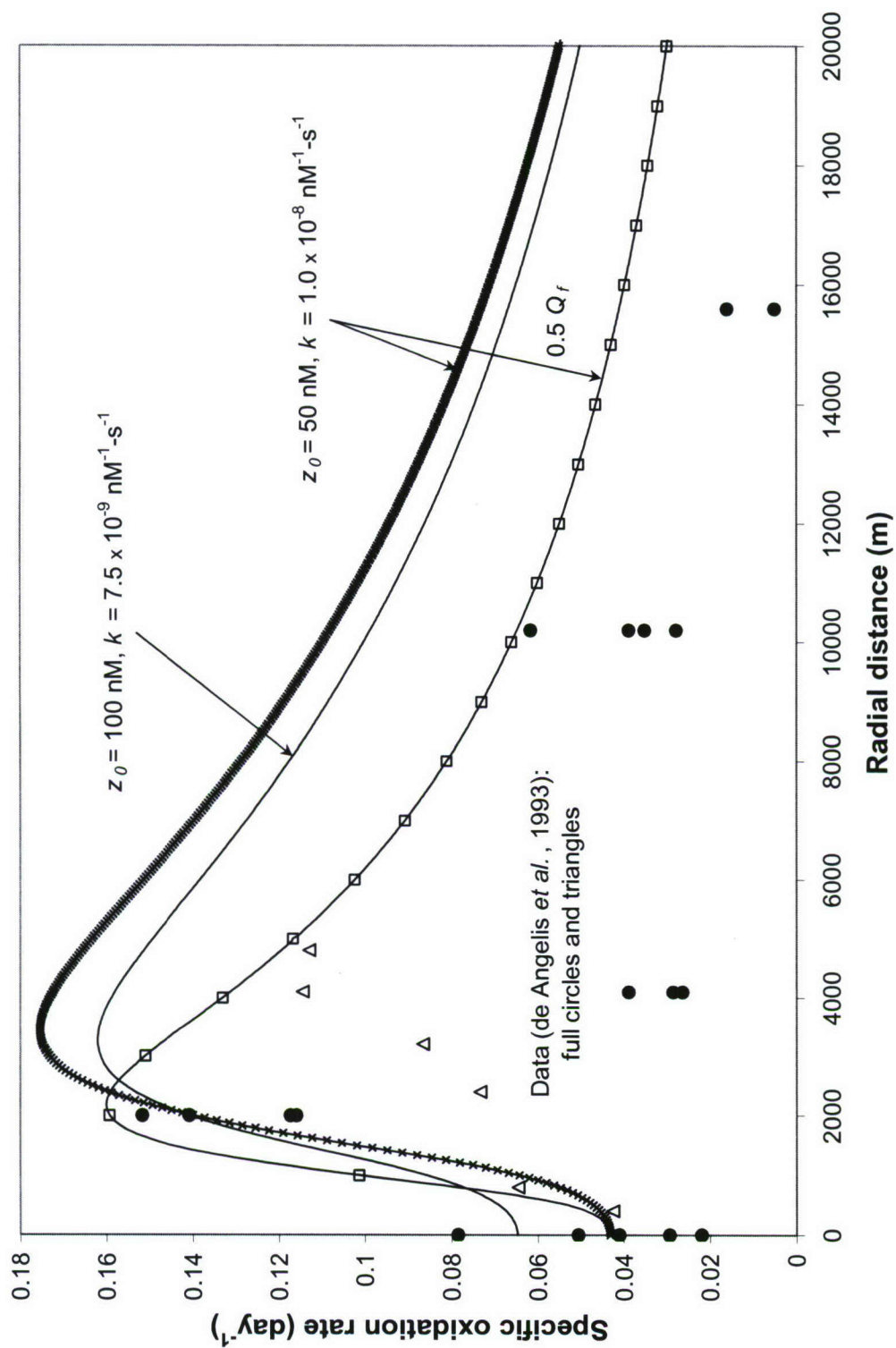


Figure 4-23. Predicted specific methane oxidation rate (axisymmetric model) and data of de Angelis *et al.* (1993)

A two-dimensional model with current

A uniform current U was considered as well as Fickian diffusion (constant diffusion coefficient K). Numerical solutions of Eq. (1) were obtained with a commercial finite-element solver (FEMLAB[®] 3, Version 3.1, COMSOL, Inc., 2003). The numerical domain was represented by a square 60 km by 60 km of implicit thickness D . Ambient concentrations were enforced on all boundaries except for a line of width $Q_f/(DU)$ at $X = 0$, corresponding to the transition from near field to far field, and for the downstream open boundary where convective fluxes (zero gradient) were chosen. Numerical simulations showed that matching the target oxidation rate and isotopic composition data simultaneously would be difficult with constant advection. Relatively good results were obtained with $k = 1.0 \times 10^{-8} \text{ nM}^{-1}\text{-s}^{-1}$, $z_0 = 50 \text{ nM}$, $K = 1 \text{ m}^2\text{-s}^{-1}$ and $U = 250 \text{ m-day}^{-1}$, as shown in Figures 4-24 and 4-25. The width of the near-field-to-far-field transition line was about 8 km as Q_f was taken to be 10 times the value of $Q(h)$ estimated in Appendix B. The full solutions for the temperature anomaly, methane concentration, isotopic composition and specific methane oxidation rate are shown in Figures 4-26 through 4-29. Figure 4-30 displays selected half sections of calculated values of $\delta^{13}\text{C}$ in the cross-current direction; it can be seen that a 2-km off-axis measurement would underestimate the 'true' peak by about 4‰ at $X = 10 \text{ km}$, 8‰ at $X = 15 \text{ km}$, and 11‰ for X between 15 and 30 km.

Summary

Simple models of ^{12}C -methane, ^{13}C -methane and methanotroph-carbon concentrations in neutrally-buoyant plumes generated in the vicinity of hydrothermal seafloor vent fields were developed. Data collected in lateral plumes at the Endeavour Segment of the Juan de Fuca Ridge was used to provide boundary conditions, a few key parameters (e.g., isotopic fractionation) and, more importantly, validation targets for the models. Methane oxidation was defined with a rate constant k as a first-order process with respect to both substrate and methanotroph concentration. This elementary formalism proved sufficient to reproduce salient features of the data: maximum methane turnover times of about a week 2 km from the vent field location and stable carbon isotopic enrichment from -47‰ to values exceeding -5‰ over a distance of 15 km. The modeling process suggested that k is of order $10^{-8} (\text{nM-s})^{-1}$ at local conditions and that the carbon content of methane-oxidizing bacteria is about 12 fg ($12 \times 10^{-15} \text{ g}$) per cell. The rate constant appears to be much smaller than those inferred from laboratory incubation experiments (e.g., Ward, 1987); temperature could play a major role in the apparent discrepancy between *in situ* and laboratory oxidation kinetic parameters, although other factors likely exist. 'Initial' methanotroph carbon concentrations of about 50 to 100 nM above the vent field were inferred as well; this amount allowed predicted values to sharply increase within a couple of kilometers as demonstrated by oxidation rate data (deÁngelis *et al.*, 1993); at its peak, the methanotroph population would represent about a third of the measured overall bacterial cell count. Finally, the tuning of the plume flow rate in the axisymmetric model, with a smaller (half) value to better fit specific oxidation rate data, is consistent with the possibility that tectonic activity in 1999 changed some hydrothermal vent characteristics and increased fluid output (Johnson *et al.*, 2000). Methane oxidation is defined with a rate constant k as a first-order process with respect to both substrate and methanotroph concentration. This elementary formalism coupled with simplified representations of advection and diffusion through the lateral plume is sufficient to reproduce salient features of the data: maximum methane turnover times of about a week 2 km

from the vent field location and stable carbon isotopic enrichment from -47‰ to values exceeding -5‰ over a distance of 15 km. Results suggest that k is of order $10^{-8} \text{ (nM-s)}^{-1}$ at local conditions and that methane-oxidizing bacteria hold about 12 fg of carbon per cell.

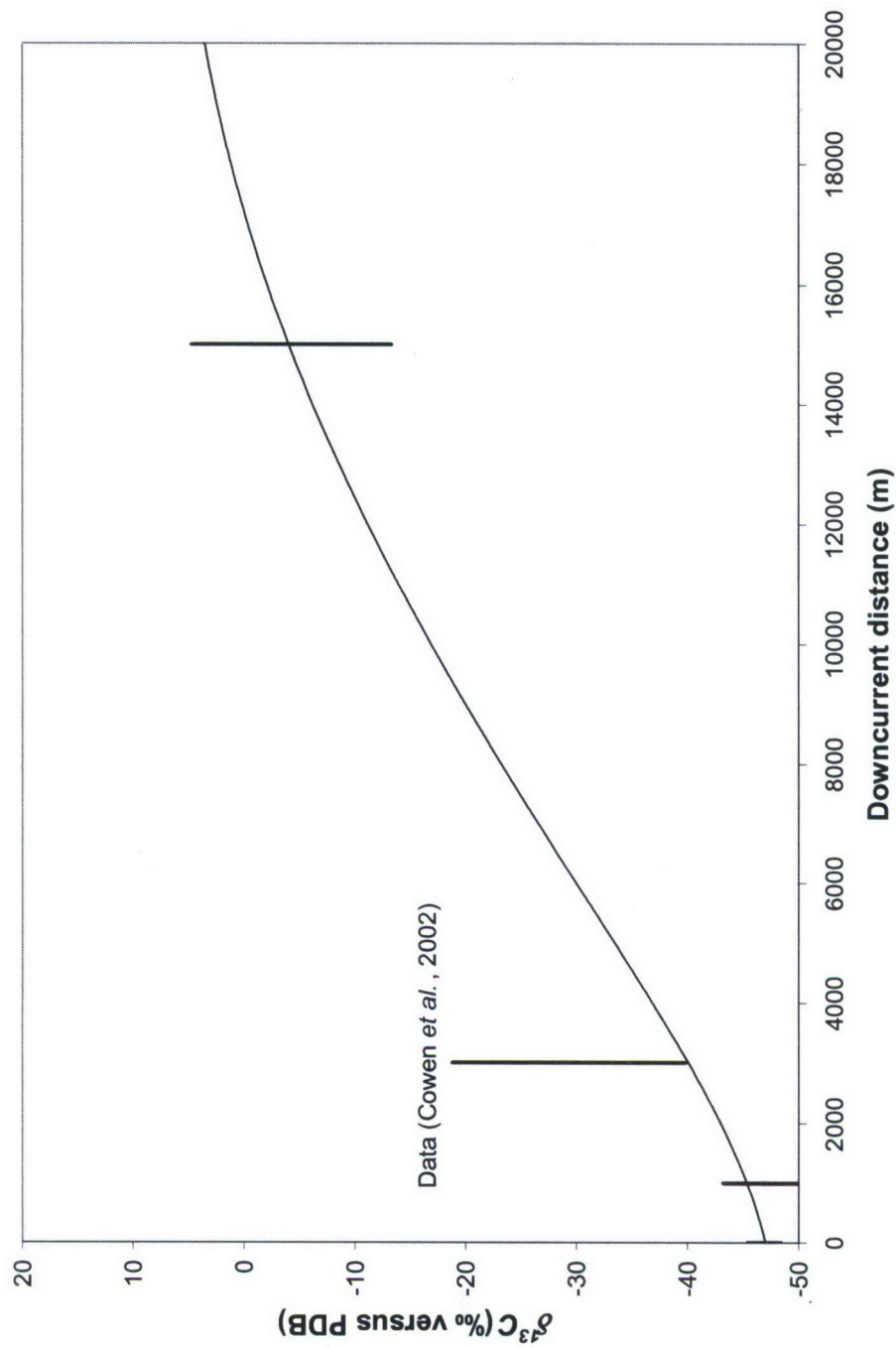


Figure 4-24. Predicted isotopic composition (two-dimensional model, solid line) and data of Cowen et al. (2002)

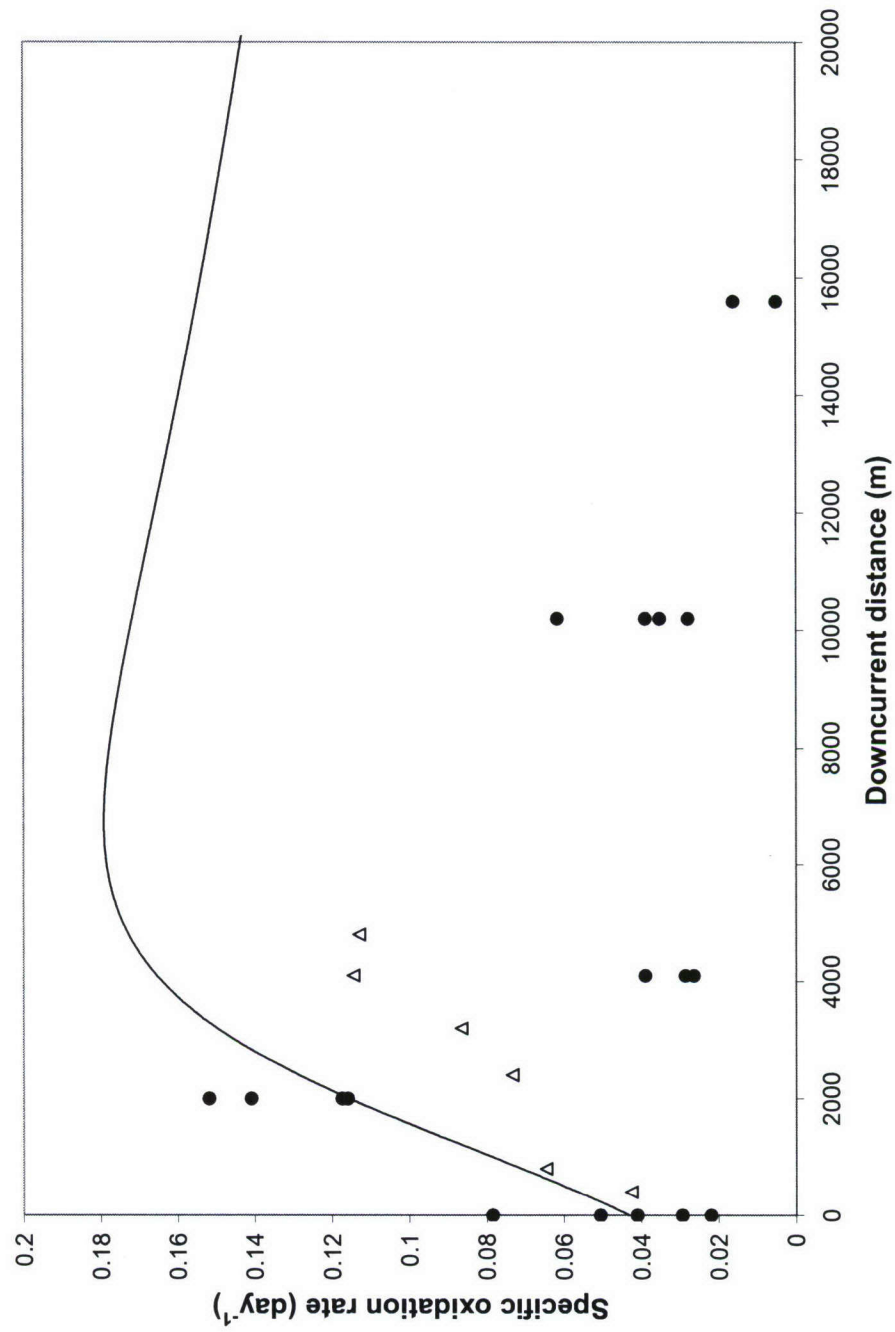


Figure 4-25. Predicted specific methane oxidation rate (two-dimensional model, solid line) and data of de Angelis *et al.* (1993)

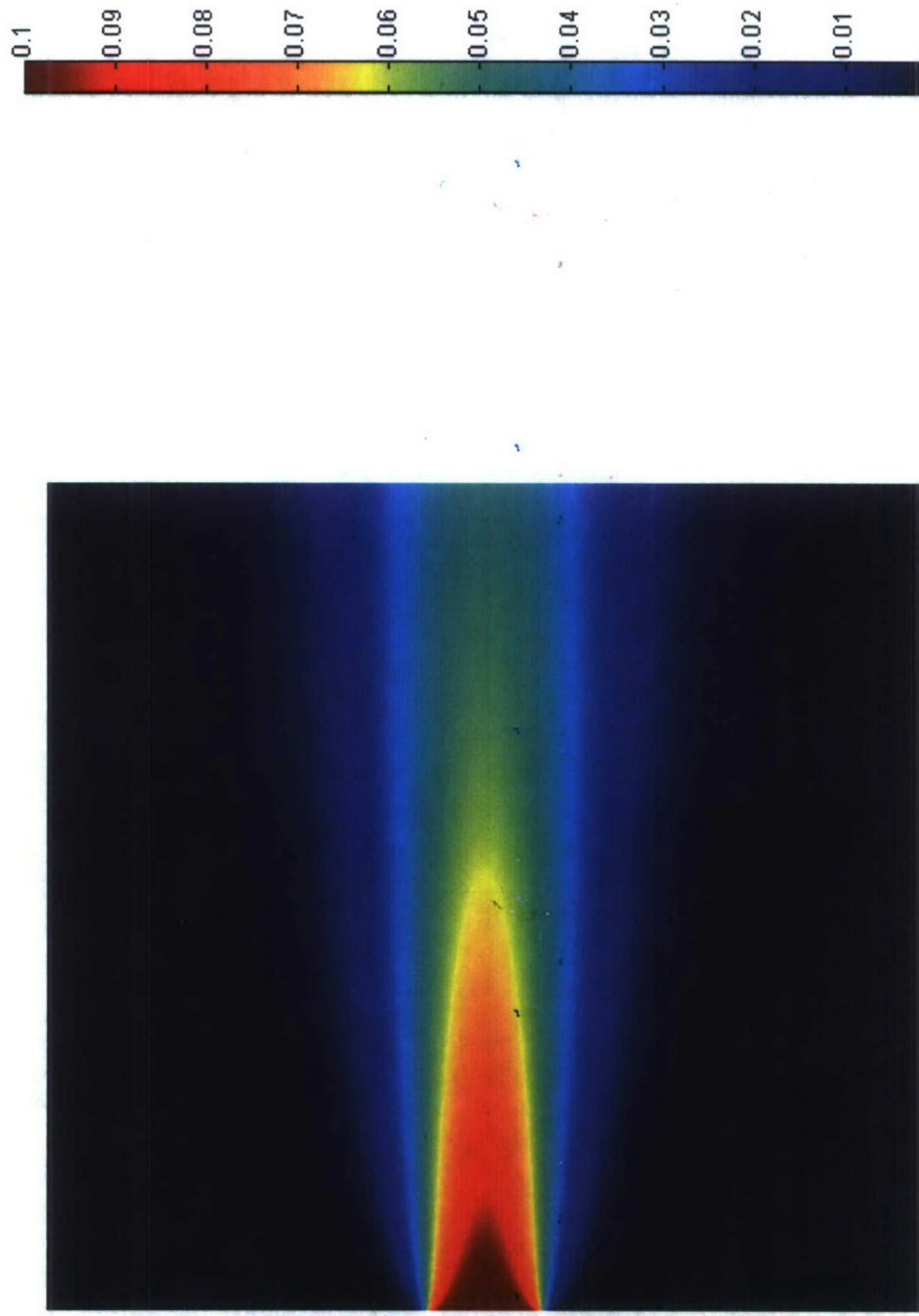


Figure 4-26. Predicted temperature anomaly ($^{\circ}\text{C}$) in a horizontal domain 60 km by 60 km

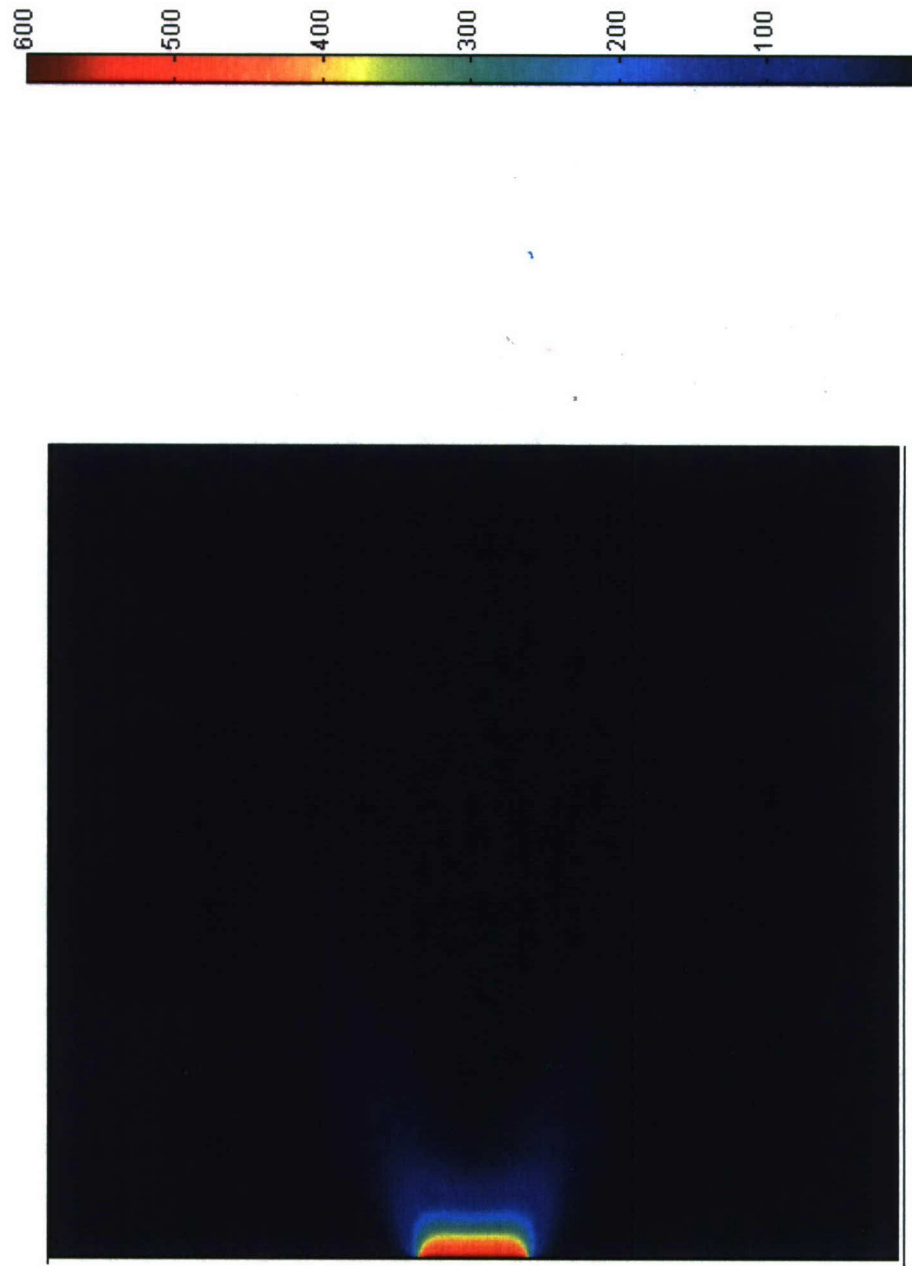


Figure 4-27. Predicted methane concentration (nM) in a horizontal domain 60 km by 60 km

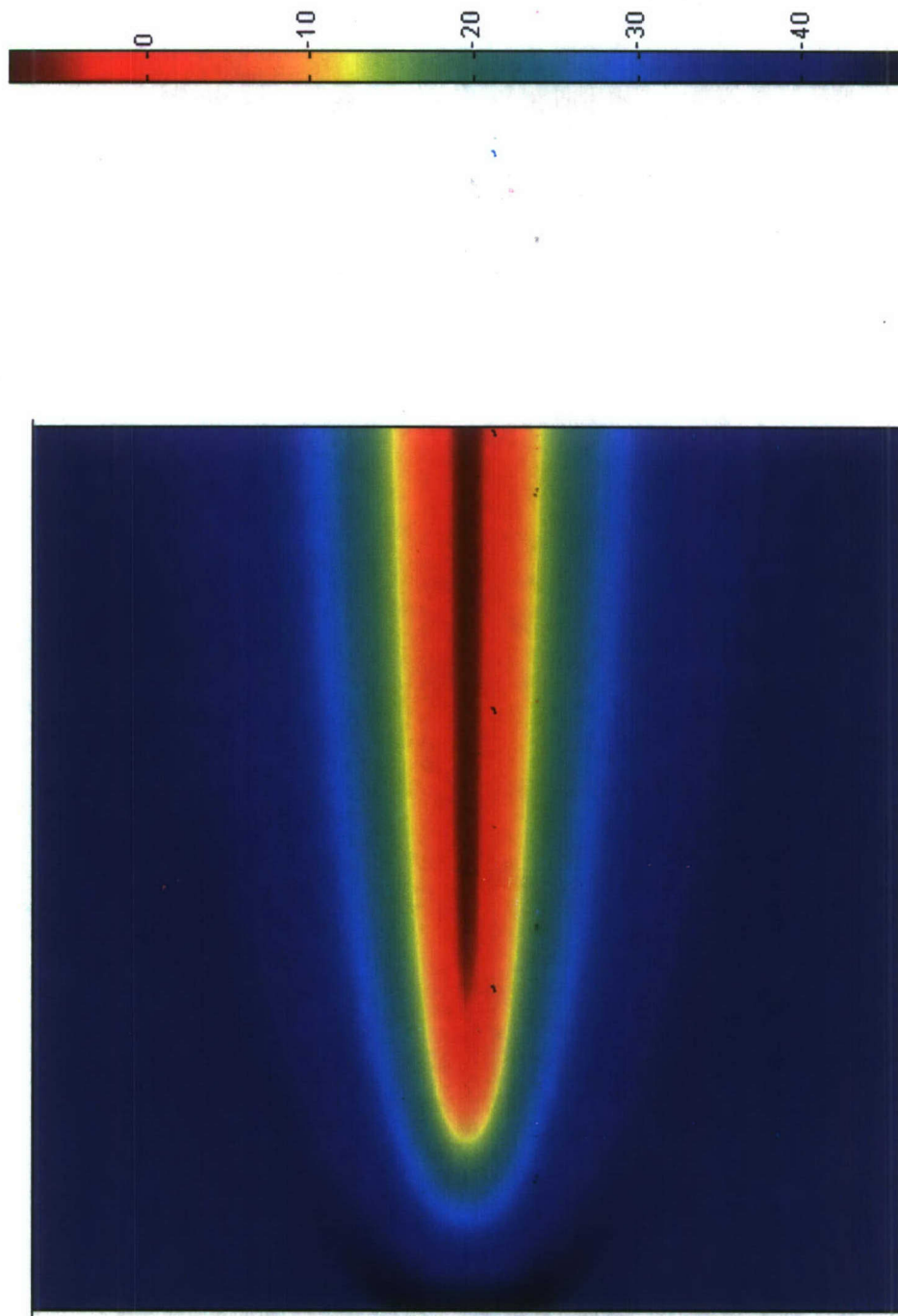


Figure 4-28. Predicted isotopic composition (‰) in a horizontal domain 60 km by 60 km

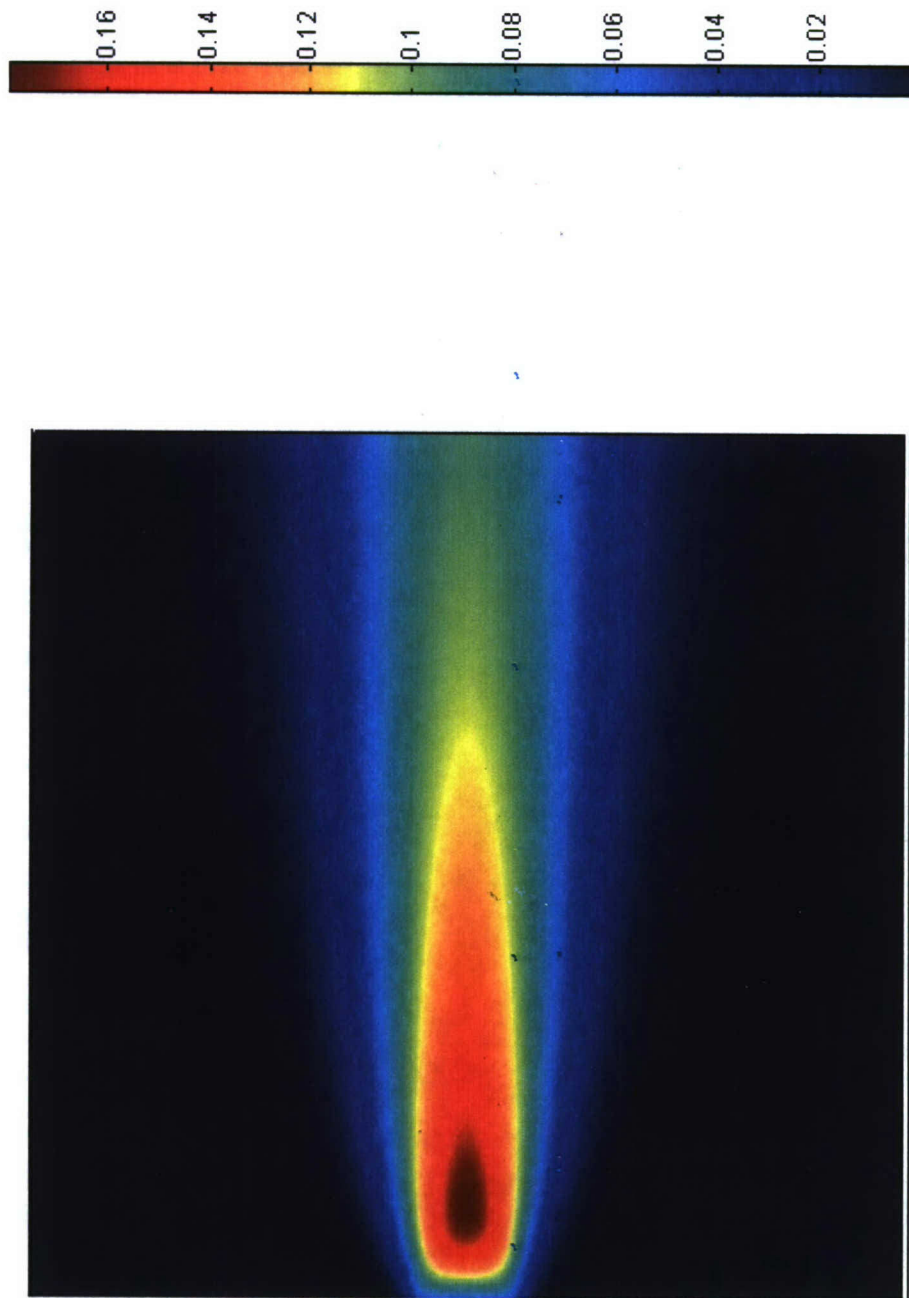


Figure 4-29. Predicted methane oxidation rate (day^{-1}) in a horizontal domain 60 km by 60 km

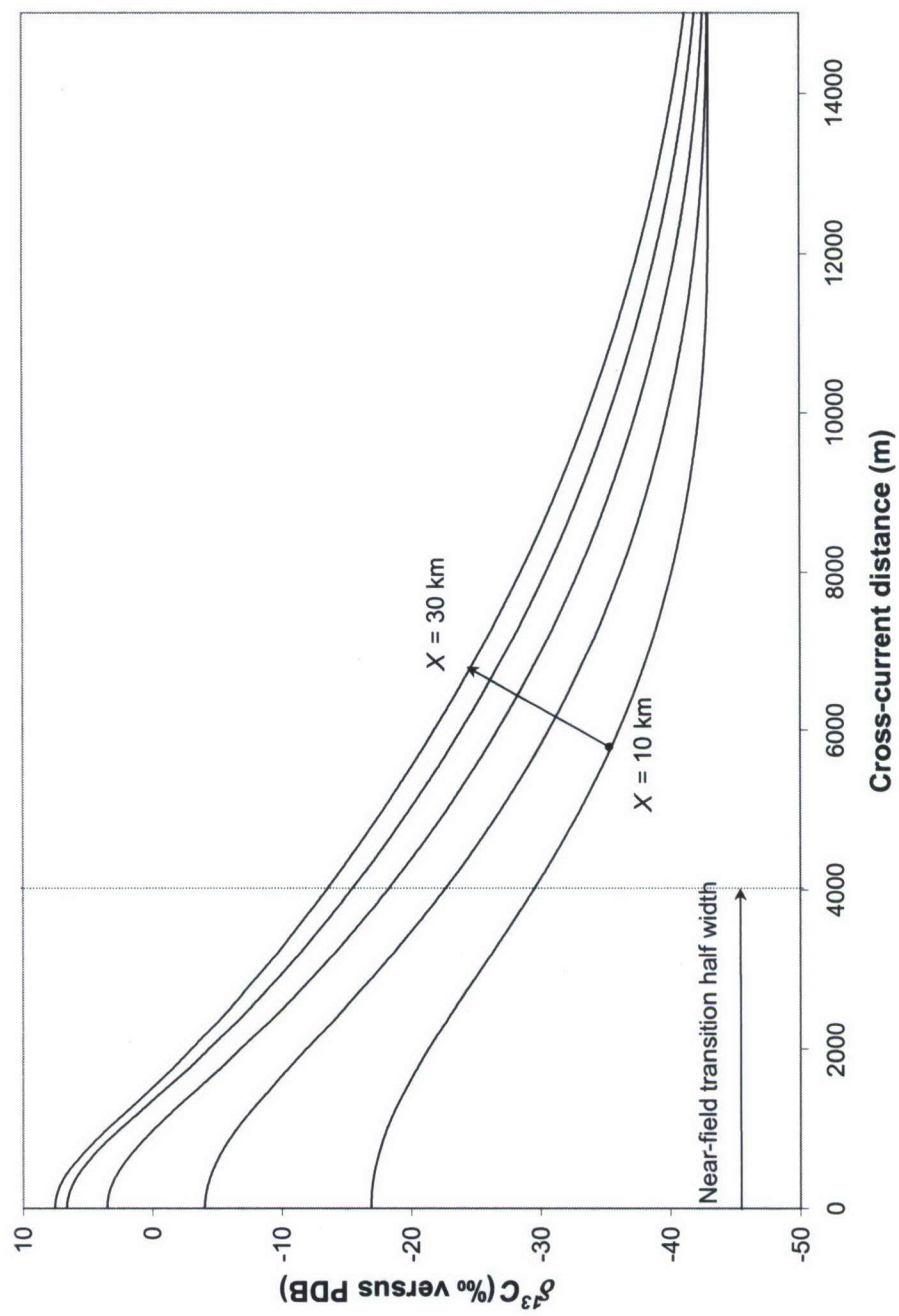


Figure 4-30. Cross-current half profiles of predicted isotopic composition (two-dimensional model)

Notation

D	thickness of plume intrusion layer (m)
h	neutral-buoyancy height of near-field plume above seafloor (m)
k	methane oxidation rate constant ($\text{nM}^{-1}\text{-s}^{-1}$)
K	far-field eddy diffusion coefficient ($\text{m}^2\text{-s}^{-1}$)
n	number of near-field point sources of buoyancy
P	eddy diffusion velocity (m-s^{-1})
Q	plume volume flux ($\text{m}^3\text{-s}^{-1}$)
Q_f	volume flux in lateral (far-field) plume ($\text{m}^3\text{-s}^{-1}$)
r	horizontal radial distance from vent field (m)
r_f	characteristic length for axisymmetric advection-diffusion processes (m)
R_{PDB}	isotopic ratio of PDB standard
Sp	specific methane oxidation rate (s^{-1})
Spm	methanotroph biomass-specific oxidation rate (s^{-1})
\vec{u}	velocity vector (m-s^{-1})
U	current magnitude (m-s^{-1})
x	methane concentration (nM)
X	horizontal coordinate along current direction (m)
Y	horizontal coordinate perpendicular to current direction (m)
y	carbon-13 ($^{13}\text{CH}_4$) methane concentration (nM)
z	methanotroph carbon concentration (nM)

Greek letters

α	carbon assimilation ratio for methanotrophs
α_k	isotopic fractionation for microbial methane oxidation
$\delta^{13}\text{C}$	isotopic composition of methane (‰)
$\delta\theta$	plume temperature anomaly (kg-m^{-3})

Subscript

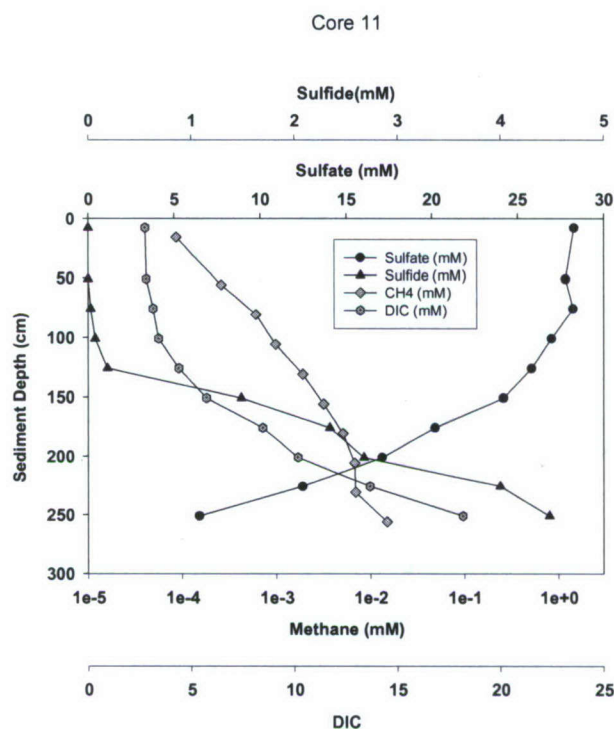
0	far-field origin
---	------------------

4.3.3 Hydrate Microbiology

The widespread presence of gas hydrates offshore of New Zealand has been inferred from bottom-simulating reflections (BSRs) for over two decades (Katz 1981). The Hikurangi Margin, offshore New Zealand's North Island east coast is predicted to contain large quantities of gas hydrates, based on the observation of wide-spread BSRs (Pecher and Henrys 2003). Their first estimates of the resource potential, based on the distribution of BSRs, have resulted in data that narrow the gas hydrate province to an area of about 50,000 km^2 .

The first core samples from sediments containing methane from New Zealand were collected during a joint scientific cruise aboard the RV Tangaroa during the summer of 2006. Twenty two piston cores were collected and geochemical data that includes sulfate, sulfide and dissolved inorganic carbon were immediately analyzed onboard the research vessel during the cruise. Select core sections were immediately placed in a refrigerator and shipped by air with dry ice to the University of Hawaii for further processing.

In-depth molecular genetic analysis based on the amplification of extracted nucleic acids was performed with Core number 11, to provide further insight into the composition and structure of the microbial communities at this location. This core displayed a typical geochemical profile often observed in sediments containing methane hydrates, clearly showing the concurrent depletion of sulfate and methane in the sediment at the sulfate-methane interface (SMI) in Figure 4-31. Specifically, core sections from 10, 65, 90, 115, 165, 190 and 220 centimeters below sea floor (cmbsf) were used for community determination.



Unpublished data property of NRL Biogeochemistry group.

Figure 4-31. Geochemical analysis of pore water from piston core sample number 11 obtained on the Hikurangi Margin, New Zealand

DNA has been extracted for molecular phylogenetic analysis from the core sections employing a method described by Corinaldesi *et al.*, 2005. This particular method was employed to reduce the co-extraction of polymerase-chain-reaction (PCR) inhibiting agents. Analysis of DNA in the samples was still hampered by the co-extraction or co-purification of humic substances (Bachoon *et al.*, 2001). Humic acids are chemically complex and polydisperse mixtures of microbiologically decomposed and transformed organic materials. PCR amplification is sensitive to co-extracted substances such as heavy metals, pigments, and humic acids (Holben *et al.*, 1998, Juniper *et al.*, 2001). Extracted DNA was then PCR amplified using the specific primers given in Table 4-1. Qualitative amplification results showing the distribution of the different groups are presented in Table 4-2. The successful amplifications do not present a readily apparent pattern that correlates with the geochemical data. The most reproducible

amplifications were obtained using the *Archaea* and *Bacteria* specific primers. These PCR results were used to investigate the microbial *Bacteria* and *Archaea* communities by the use of molecular DNA cloning.

Table 4-1. PCR primers used for molecular analysis of DNA extracted from cores collected from the Hikurangi Margin

Target gene	Primers F/R	Product size
<i>Bacteria</i> 16S rDNA (Weisburg <i>et.al.</i> 1991)	27F / 1492R	1.45kb
<i>Archaea</i> 16S rDNA (DeLong 1992)	21F / 958R	950kb
Methanotroph type I 16S rDNA (Wise <i>et.al.</i> 1999)	MethT1dF / MethT1bR	920kb
Methanogen 16S rDNA (Marchesi <i>et.al.</i> 2001)	146F / 1324R	1.2kb
Sulfate Reducing Bacteria, Dissimilatory sulfate reductase (Wagner <i>et.al.</i> 1998)	Dsr1F / Dsr4R	1.5kb

Table 4-2. Extracted DNA were separated into whole cellular components and free extra-cellular DNA. PCR was performed using various primer sets that target specific groups of microorganisms. Positive amplification (X) and negative amplification (O). New Zealand, Hikurangi margin, Core #11.

Core section DNA extracts from cellular fraction (c) and extracellular fraction (ex)							
Primer specificity	220c/ex	190c/ex	165c/ex	115c/ex	90c/ex	65c/ex	10c/ex
<i>Bacteria</i>	X / X	X / X	X / X	X / X	X / X	X / X	X / X
<i>Archaea</i>	O / X	O / X	O / O	O / X	O / O	X / O	O / X
Methanotroph	O / X	O / X	O / X	O / X	O / X	O / X	O / X
Methanogen	O / O	O / X	O / X	O / X	O / X	O / X	O / X
Sulfate reducing bacteria	O / O	O / X	O / X	O / X	O / X	O / X	O / X

The extracellular PCR products for the *Bacteria* and *Archaea* were used for DNA cloning, using the TOPO™ TA® cloning kit and OneShot® TOP10 chemically-competent *E. coli* cells (Invitrogen). The selected clones were then sequenced at the University of Hawaii in an Applied Biosystems 377XL DNA sequencer or an Applied Biosystems BigDye terminator ABI 3730XL capillary-based DNA sequencer. DNA sequences were manually edited and compared with those in the public domain through a BLASTn search (Altschul *et al.*, 1997). Phylogenetic analyses were performed with programs in the PHYLIP 3.63 package (Felsenstein, 1993). Phylogenetic trees (see Figures 4-32 and 4-33) were constructed with jumbled orders of the sequences using the neighbor-joining method (Saitou and Nei, 1987).

The weak PCR amplifications resulted in reduced cloning efficiency. Seventy colonies from the bacterial amplifications were selected (10 clones per core section), 29 samples were sequenced and 19 of them were distinct; however, the majority are closely related to cultured organisms (Figure 4-32). When compared with samples of methane-hydrate-bearing sediments from the Cascadia Margin that have been previously analyzed by other groups, the bacterial species from these sediments were primarily affiliated with the *Proteobacteria* and overall bacterial diversity was relatively low (Marchesi *et al.* 2001). The same is true with our samples as 38% of the clones were grouped with the *Proteobacteria* and diversity also is low. Sulfate-reducing bacteria (SRB) are commonly found in the delta *Proteobacteria*, but no confirmed SRB clones were obtained. Six uncharacterized clones were found in this group and may, however, have the potential for sulfate reduction.

The majority of the *Archaea* clones were included in the phylum *Euryarchaeota* that contain the methanogens; however, distinct methanogenic sequences belonging to the commonly found *Methanosarcinales* and the *Methanobacteriales* orders were not obtained. None of the clones in the *Euryarchaeota* were closely related to any cultured organisms.

Within the water column and in near-surface environments, methanotrophy typically occur under aerobic or microaerophilic conditions. Methanotrophs are aerobic bacteria and successful amplifications within all of the core section were atypical. Further analysis indicated that the successful amplifications were anomalies, most likely due to the weaker specificity of degenerate primer amplifications. Cloning and sequencing of the PCR product indicated that non-specific amplifications were being observed. *Psychromonas profunda*, a psychropiezophilic bacteria isolated from deep Atlantic sediments, was consistently amplified and represented when cloned (Table 4-2).

The enzyme dissimilatory sulfite reductase (DSR) catalyzes the final steps in microbial sulfate reduction and is synthesized by all known SRB (Wagner *et al.* 1998). The ubiquity of DSR and its high sequence conservation has made this enzyme ideal for assessing the biodiversity of SRB (Wagner *et al.* 1998). The obtained results suggest that sample preservation and handling may not have been sufficiently stringent, resulting in significant cell lysis. Sulfate-reducing bacteria are ubiquitously found in a wide range of environments and it would be expected that from all the primers currently used, successful amplifications would be observed with these. Only the extracellular DNA product was amplifiable. Extractions will be performed in future experiments using a homogenate of both DNA pools.

The initial characterization of sediments collected from the Hikurangi Margin indicates that these geologically distinct hydrate-bearing sediments contain many unidentified species of *Archaea* and *Bacteria*. Although clones were not obtained that definitively identify specific methanogenic and sulfate-reducing bacteria, the potential for the unknown clones to play a role in the methane cycling in this environment does, however, exist. Further analysis by cloning will be performed using the PCR products targeting the methanogens and SRBs.

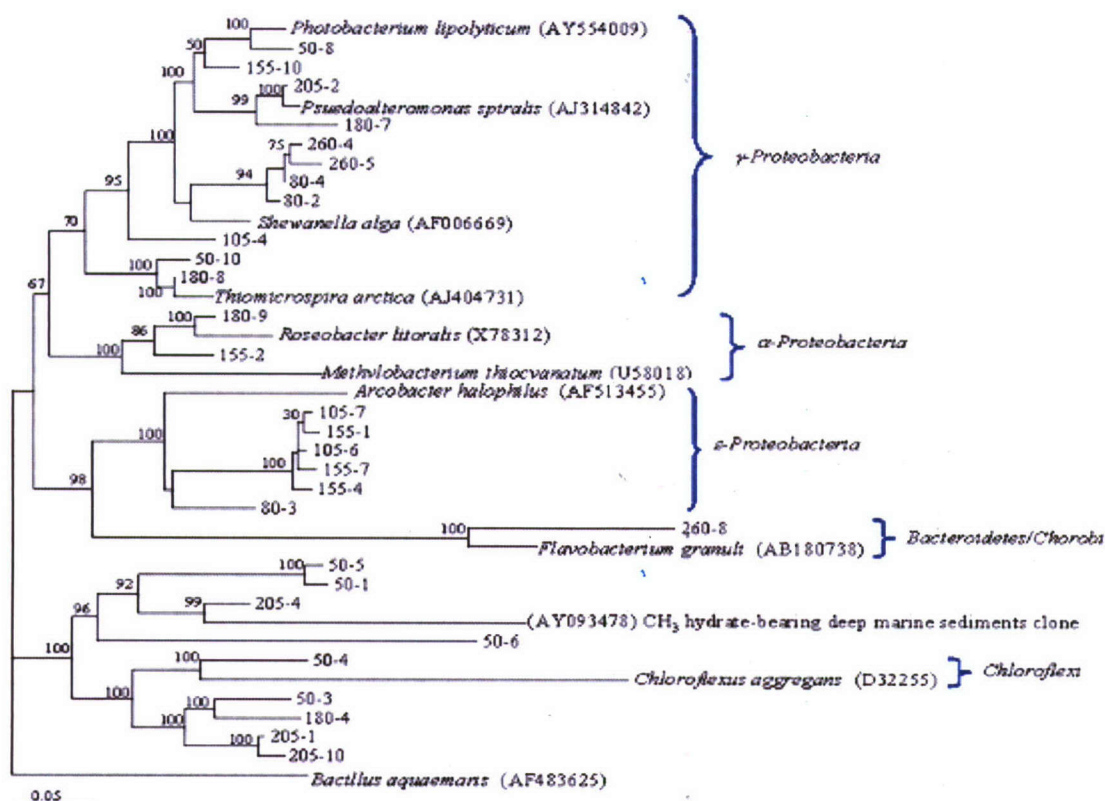


Figure 4-32. A *Bacteria* 16S rDNA phylogenetic tree was constructed based on partial sequences obtained from NZ Hikurangi Margin core #11. The clone library was constructed using 27F / 1492R.

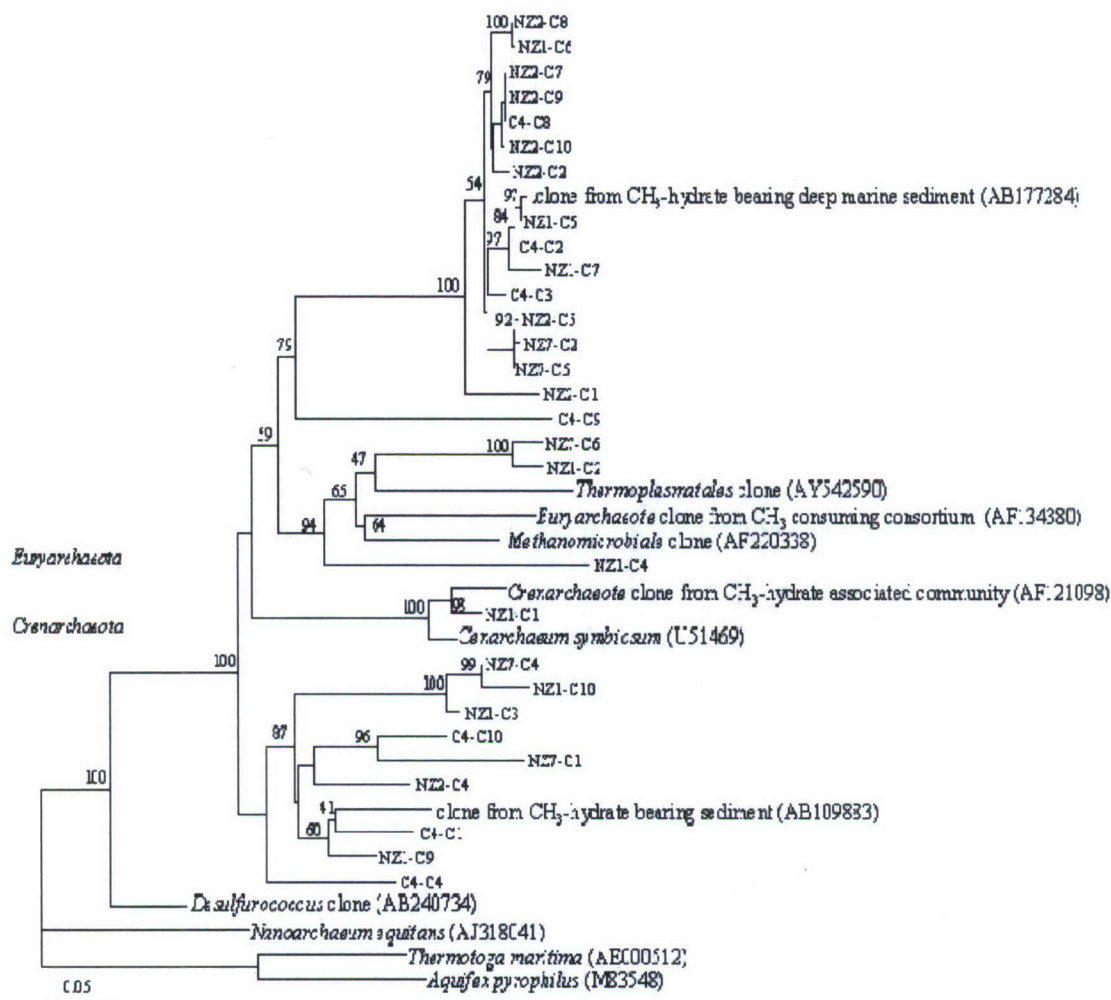


Figure 4-33. A Archaea 16S rDNA phylogenetic tree was constructed based on partial sequences obtained from NZ Hikurangi Margin core #11. The clone library was constructed using 21F / 958R.

4.3.4 International Collaborative R&D

In collaboration with the multi-national oceanographic research cruise of methane hydrate sites off New Zealand, HNEI technical personnel participated and assisted in collection of samples that were subsequently analyzed at the University of Hawaii. These samples included those analyzed under the hydrate microbiology section above.

HNEI was also a participant in the 5th International Workshop on Methane Hydrates that was held in Edinburgh, Scotland in October 2006. Furthermore, HNEI is planning to be a co-organizer, sponsor and participant for the 6th Workshop scheduled for May 2008 in Bergen, Norway.

4.4 Papers Resulting from Efforts

During the present reporting period, R&D conducted as part of the HEET Methane Hydrates Task has produced the following papers.

Nihous, G.C. and S.M. Masutani, "Notes on the modeling of methane in aging hydrothermal vents," accepted for publication in *Journal of Marine Research*, 2007.

Nihous, G.C., C.K. Kinoshita, and S.M. Masutani, "Stress concentration factors for oblique holes in pressurized thick cylinders," accepted for publication in *J. Pressure Vessel Technol.*, 2007.

4.5 References (includes references quoted in Appendices A and B)

Altschul, S. F., T. L. Madden, A. A. Schaffer, J. Zhang, Z. Zhang, W. Miller, D. J. Lipman. 1997. Gapped BLAST and PSI-BLAST: A new generation of protein database search programs. *Nucl. Acids Res.*, 25, 3389-3402.

de Angelis, M. A., M. D. Lilley, E. J. Olson and J. A. Baross. 1993. Methane oxidation in deep-sea hydrothermal plumes of the Endeavour Segment of the Juan de Fuca Ridge. *Deep Sea Res.*, 40, 1169-1186.

Bachoon, D. S., E. Otero, E. and R. E. Hodson. 2001. Effects of humic substances on fluorometric DNA quantification and DNA hybridization. *J. Microbiol. Methods*, 47, 73-82.

Bemis, K. G., P. A. Rona, D. Jackson, C. Jones, D. Silver and K. Mitsuzawa. 2002. A comparison of black smoker hydrothermal plume behavior at Monolith Vent and at Clam Acres Vent Field: Dependence on source configuration. *Marine Geophys. Res.*, 23, 81-96.

Button, D. K. and B. Robertson. 1999. Properties of small free-living aquatic bacteria in Size limits of very small microorganisms – Proceedings of a workshop, The National Academies Press, 164 p.

Cowen, J. P., X. Wen and B. N. Popp. 2002. Methane in aging hydrothermal plumes. *Geochim. Cosmoch. Acta*, 66, 3563-3571.

Craig, H. 1957. Isotopic standards for carbon and oxygen and correction factors for mass spectrometric analysis of carbon dioxide. *Geochim. Cosmochim. Acta*, 12, 133-149.

DeLong E. F. 1992. Archaea in coastal marine environments. *Proc. Natl. Acad. Sci.* 89, 5685-5689.

DeLong, E. F. 1999. Diminutive cells in the ocean – Unanswered questions in Size limits of very small microorganisms – Proceedings of a workshop, The National Academies Press, 164 p.

Ebukuro, T., Takami, A., Oshima, Y. and S. Koda. 1999. Raman Spectroscopic Studies on Hydrogen Bonding in Methanol and Methanol/Water Mixtures Under High Temperature and Pressure. *J. Supercrit. Fluid*, 15, 73-78.

Epstein, M. and J. P. Burelbach. 2001. Vertical mixing above a steady circular source of buoyancy. *Int. J. Heat Mass Trans.*, 44, 525-536.

Faraday, M. 1859. On Regelation, and on the Conservation of Force. *Philos. Mag.*, 17, 162-169.

Felsenstein, J. 1993. Phylogeny Inference Package (PHYLIP). Version 3.5. University of Washington, Seattle.

- Fletcher, N. H. 1968. Surface Structure of Water and Ice II. A Revised Model. *Philos. Mag.*, *18*, 1287-1300.
- Fofonoff, P. and R. C. Millard Jr. 1983. Algorithms for computation of fundamental properties of seawater. UNESCO Tech. Papers in Mar. Sci., *44*, 53 p.
- Fukuda, R., H., T. Ogawa and I. Koike. 1998. Direct determination of carbon and nitrogen contents of natural bacterial assemblages in marine environments. *Appl. Environ. Microbiol.*, *64*, 3352-3358.
- Furukawa, Y. and H. Nada. 1997. Anisotropic Surface Melting of an Ice Crystal and Its Relationship to Growth Forms. *J. Phys. Chem. B.*, *101*, 6167-6170.
- Grant, N. J. and M. J. Whiticar. 2002. Stable carbon isotopic evidence for methane oxidation in plumes above Hydrate Ridge, Cascadia Oregon Margin. *Global Biogeochem. Cy.*, *16*, 13 p.
- Guo, J.-H., Y. Luo, A. Augustsson, S. Kashtanov, J.-E. Rubensson, D. K. Shuh, H. Ågren and J. Nordgren. 2003. Molecular Structure of Alcohol-Water Mixtures. *Phys. Rev. Lett.*, *91*, 157401.
- Harrits, S. M. and R. S. Hanson. 1980. Stratification of aerobic methane-oxidizing organisms in Lake Mendota, Madison, Wisconsin. *Limnol. Oceanograph.*, *25*, 412-421.
- Hewett, T. A., J. A. Fay and D. P. Hoult. 1971. Laboratory experiments of smokestack plumes in a stable atmosphere. *Atm. Env.*, *5*, 767-789.
- Holben, W. E., J. K. Jansson, B. K. Chelm and J. M. Tiedje. 1988. DNA probe method for the detection of specific microorganisms in the soil bacterial community, *Appl. Environ. Microbiol.*, *54*, 703-711.
- Huang, H., R. E. Fergen, J. R. Proni and J. J. Tsai. 1998. Initial dilution equations for buoyancy-dominated jets in current. *ASCE J. Hydr. Eng.*, *124*, 105-108.
- Hutton, W. E. and C. E. Zobell. 1949. The occurrence and characteristics of methane-oxidizing bacteria in marine sediments. *J. Bact.*, *58*, 463-473.
- Isdale, J. D., A. J. Eastal, and L. A. Woolf. 1985. Shear viscosity of methanol and methanol-water mixtures under pressure. *International Journal of Thermophysics*, *6*(5), 439-450.
- Javanmardi, J., M. Moshfeghian and R. Maddox. 2001. An Accurate Model for Prediction of Gas Hydrate Formation Conditions in Mixtures of Aqueous Electrolyte Solutions and Alcohol. *Can. J. Chem. Eng.*, *2001*, 367-373.
- Johnson, H. P., M. Hutnak, R. P. Dziak, C. G. Fox, I. Urcuyo, J. P. Cowen, J. Nabelek and C. Fisher. 2000. Earthquake-induced changes in a hydrothermal system on the Juan de Fuca mid-ocean ridge. *Nature*, *407*, 174-177.
- Jones, R. D., R. Y. Morita and R. P. Griffiths. 1984. Method for estimating *in situ* chemolithotrophic ammonium oxidation using carbon monoxide oxidation. *Mar. Ecol. Prog. Ser.*, *17*, 259-269.
- Joseph, J. and H. Sendner. 1958. The horizontal diffusion in the ocean. *Deutsche Hydrographische Zeitschrift*, *11*, 49-77.
- Juniper, S. K., M. A. Cambron, F. Lesongeur and G. Barbier. 2001. Extraction and purification of DNA from organic rich subsurface sediments (ODP Leg 169S). *Mar. Geol.*, *174*, 241-247.

- Katz, H. R. 1981. Probable gas hydrate in continental slope east of the North Island, New Zealand. *J. Petrol. Geol.*, 3, 315-324.
- Kreith, F., and M. S. Bohn. 2001. Principles of Heat Transfer, 6th edition, Brooks/Cole, 700 p. and appendices.
- Li, C.C. 1976. Thermal conductivity of liquid mixtures. *AIChE Journal*, 22(5), 927-930.
- Lied, A, H. Dosch and J. H. Bilgram. 1994. Surface Melting of Ice Ih Single Crystals Revealed by Glancing Angle X-Ray Scattering. *Phys. Rev. Lett.*, 72, 3554-3557.
- Lupton, J. E., J. R. Delaney, H. P. Johnson and M. K. Tivey. 1985. Entrainment and vertical transport of deep-ocean water by buoyant hydrothermal plumes. *Nature*, 316, 621-623.
- Marchesi, J. R., A. J. Weightman, B. A. Cragg, R. J. Parkes and J. C. Fry. 2001. Methanogen and bacterial diversity and distribution in deep gas hydrate sediments from the Cascadia Margin as revealed by 16S rRNA molecular analysis. *FEMS Microbiol. Ecol.*, 34, 221-228.
- Masoudi, R and B. Tohidi. 2005. Estimating the Hydrate Stability Zone in the Presence of Salts and/or Organic Inhibitors Using Water Partial Pressure. *J. Petrol. Sci. Eng.*, 46, 23-36.
- Mikhail, S. Z. and W. R. Kimel. 1961. Densities and viscosities of methanol-water mixtures. *Journal of Chemical and Engineering Data*, 6, 533-537.
- Morton, B. R., G. I. Taylor and J. S. Turner. 1956. Turbulent gravitational convection from maintained and instantaneous sources. *Proc. Royal Soc. Lond.*, A234, 1-23.
- National Institute of Standards and Technology. 2005. Thermophysical Properties of Fluid Systems. U. S. Dept. of Comm. online data base, <http://webbook.nist.gov/chemistry/fluid/>
- Nihous, G. C. 2006. Near-field evaluation of artificial upwelling concepts for open-ocean oligotrophic conditions," *J. Mar. Env. Eng.*, 8, 225-246.
- Nihous, G. C. and S. M. Masutani. 2006. A model of methane concentration profiles in the open ocean. *J. Mar. Res.*, 64, 629-650.
- Pecher, I. A. and S. A. Henrys. 2003. Potential gas reserves in gas hydrate sweet spots on the Hikurangi Margin, New Zealand, Science Report, Institute of Geological and Nuclear Sciences, Lower Hutt, 32 pp.
- Rehder, G., R. S. Keir and E. Suess. 1999. Methane in the Northern Atlantic controlled by microbial oxidation and atmospheric history. *Geophys. Res. Lett.*, 26, 587-590.
- Roberts, P. J. W., W. H. Snyder and D. J. Baumgartner. 1989. Ocean outfalls: I: Submerged wastefield formation. II: Spatial evolution of submerged wastefield. III: Effect of diffuser design on submerged wastefield. *J. Hydr. Eng.*, 115, 1-70.
- Rona, P. A., K. G. Bemis, D. Silver and C. D. Jones. 2002. Acoustic imaging, visualization, and quantification of buoyant hydrothermal plumes in the ocean. *Marine Geophys. Res.*, 23, 147-168.
- Saitou, N. and M. Nei. 1987. The neighbor joining method: a new method for reconstructing phylogenetic trees. *Mol Biol. Evol.*, 4, 406-425.
- Scranton, M. I. and P. G. Brewer. 1978. Consumption of dissolved methane in the deep ocean. *Limnol. Oceanogr.*, 23, 1207-1213.

- Sieburth, J. McN., P. W. Johnson, M. A. Eberhardt, M. E. Sieracki, M. Lidstrom and D. C. Laux. 1987. The first methane-oxidizing bacterium from the upper mixing layer of the deep ocean: *Methylomonas pelagica* sp. nov. *Current Microbiol.*, *14*, 285-293.
- Sieburth, J. McN., P. W. Johnson, V. N. Church and D. C. Laux. 1993. C₁ bacteria in the water column of Chesapeake Bay, USA. III. Immunologic relationships of the type species of marine monomethylamine- and methane-oxidizing bacteria to wild estuarine and oceanic cultures. *Mar. Ecol. Prog. Ser.*, *95*, 91-102.
- Subramanian, S. and E. D. Sloan Jr. 1999. Molecular Measurements of Methane Hydrate Formation." *Fluid Phase Equilib.*, *158-160*, 813-820.
- Sundh, I., D. Bastviken and L. J. Tranvik. 2005. Abundance, activity, and community structure of pelagic methane-oxidizing bacteria in temperate lakes. *Appl. Environ. Microbiol.*, *71*, 6746-6752.
- Wagner, M., A. J. Roger., J. L. Flax, G. A. Brusseau and D. A. Stahl. 1998. Phylogeny of dissimilatory sulfite reductases supports an early origin of sulfate respiration. *J. Bacteriol.* *180*, 2975-2982.
- Ward, B. B. 1987. Kinetic studies on ammonia and methane oxidation by *Nitrosococcus oceanus*. *Arch. Microbiol.*, *147*, 126-133.
- Wei, X., P. B. Miranda, C. Zhang and Y. R. Shen . 2002. Sum-Frequency Spectroscopic Studies of Ice Interfaces. *Phys. Rev. B*, *66*, 085401.
- Weisburg, W. G., S. M. Barns, D. A. Pelletier and D. J. Lane. 1991. 16S ribosomal DNA amplification for phylogenetic study. *J. Bacteriol.*, *173*, 697-703.
- Wise, M. G., J. V. McArthur and L. J. Shimkets. 1999. Methanotroph diversity in landfill soil: isolation of novel type I and type II methanotrophs whose presence was suggested by culture independent 16S ribosomal DNA analysis. *Appl. Environ. Microbiol.*, *65*, 4887-4897.
- Wright, S. J. 1977. Mean behavior of buoyant jets in a crossflow. *ASCE J. Hydr. Div.*, *103*, 499-513.
- Wright, S. J., D. R. Wong, K. E. Zimmerman and R. B. Wallace. 1982. Outfall diffuser behavior in stratified ambient fluid. *ASCE J. Hydr. Div.*, *108*, 483-501.

This page is intentional blank

APPENDIX A

Plasma Reforming of Diesel Fuel and Reformate Purification

Under this subtask, HNEI contracted with DJW Technologies to investigate plasma reforming of commercial diesel fuel and membrane purification of reformat. In summary, two primary goals were achieved. For the first goal, a low-temperature plasma reformer from Advanced Hydrogen Technologies, Inc. was used to successfully reform high-sulfur diesel fuel (315 ppm S) with high carbon conversion at reduced temperatures. For the second goal, reformat containing 50 ppm H₂S and 1% CO was converted by selective membrane purification to yield an enriched hydrogen stream (~97%) with H₂S reduced to <10 ppb and CO reduced to <10 ppm.

A final report prepared by DJW Technologies was submitted, with detailed results of the above work. The main text of the DJW Technologies report is given on the following pages (pages 109 to 122). This DJW Technologies final report also includes three Addenda which will be provided following presentations of the remaining Appendices (Appendices B and C, given on pages 123 to 131) of this primary HEET report. The three DJW Technologies report Addenda are given following page 131.

This page is intentional blank

MSN Explorer.Ink

DJW TECHNOLOGY, LLC

Final Report

to the

Hawaii Natural Energy Institute

Fuels Processing and Purity Studies

Purchase Order # Z774282

Prepared by
DJW TECHNOLOGY, LLC
June, 2007

TABLE OF CONTENTS

Summary.....	111	
Plasma Reforming.....	112	
Diesel fuel reforming with 315 ppm sulfur impurity.....	112	
Conclusions AH2T plasma reforming of diesel containing high sulfur levels:.....	115	
Hydrogen Enrichment.....	116	
Removal of H ₂ S from syngas.....	116	
Modeling of Hydrogen Enrichment Reactor.....	117	
System Integration.....	119	
Two Stage Purification Concept.....	119	
System Components.....	121	
Conclusions.....	121	
Recommendations.....	122	
 Addendum A: Final Report from AH2T.....	 A-1	
Addendum B: Final Report Selective Membrane Purification of Hydrogen for Fuel Cells; OSU.....	B-1	
Addendum C: Design of Integrated Plasma Reformer.....	C-1	

Final Report Plasma Reforming

Purchase Order #Z774282

Summary

This final report identifies the status of Tasks 1, 2 and 3 identified in the Statement of Work for Purchase Order No. Z774282 issued by the Research Corporation of the University of Hawaii to DJW TECHNOLOGY, LLC, DJWT.

The two major goals for the project were achieved: (1) Reforming by AH2T of high sulfur diesel (315 ppm S) with high carbon conversion and reduced temperatures; and (2) selective membrane purification of reformat containing 50 ppm H₂S and 1% CO to yield enriched hydrogen stream, ~97%. Reduction of H₂S from 50 ppm to <10 ppb H₂S was demonstrated. Reduction of CO from 1% to < 10 ppm CO was demonstrated.

The system integration study identified the balance-of-plant components to integrate the plasma reforming with the selective membrane purification process. Parker Hannifin was contacted and the BOP components are available.

The AH2T low-temperature plasma reformer has two stages in the reforming process: (1) the plasma stage where the electrically generated plasma (100 watts) pre-reforms the fuel and (2) the autothermal reforming stage, ATR, which completes the reforming process. The advantage of the low-temperature plasma stage is to breakdown the large hydrocarbons into smaller hydrocarbons that are more easily and completely reformed in the ATR stage.

AH2T's low-temperature plasma reforming of diesel fuel with 315 ppm achieved 94.6% fuel conversion. Near 100% carbon conversion for iso-octane and kerosene was demonstrated; 97% and 102% respectively. No to little deactivation of the catalyst was observed over the period of the experiments. A reference micro-reactor test demonstrated deactivation of the reformer catalyst by sulfur in the diesel fuel when there was not plasma processing. Both the iso-octane and kerosene values are consider within the error bar for 100% conversion. The operating temperatures used in the ATR stage of the plasma reformer are lower than those reported by other researchers; approximately 100 to 200°C lower. The lower temperature provides an advantage in materials, design and durability of the plasma reformer. The lower temperature reformat exiting the plasma reformer assists the integration of the plasma reformer with the selective membrane purification stage.

The selective membrane purification activities at The Ohio State University demonstrated removal of H₂S from syngas with a reduction from 50 ppm H₂S to 10 ppb H₂S. The reduction of carbon monoxide from 1% to less than 10 ppm was demonstrated. The modeling activity has established critical operating parameters and laboratory experiments using a single cell confirm the results.

The system integration activity has addressed the interfaces between the plasma reformer and the selective membrane purification system. Balance-of-plant components were identified. A system design with two-stage selective purifications was developed: stage 1 for H₂S removal and stage 2 for CO reduction.

Plasma Reforming

A subcontract was executed effective the 7th day of July, 2006, between DJWT and Advanced Hydrogen Technology, Inc., AH2T, and is identified by Contract Number DJWLLC-A2HT-0001. The objective of this contract is to demonstrate plasma reforming on diesel or diesel like fuels containing sulfur impurities.

Plasma reforming of commercial diesel fuel containing 15 ppm sulfur was demonstrated. The sulfur content of the fuel to 315 ppm was increased with the addition of 300 ppm sulfur. Plasma reforming was successfully demonstrated using the high sulfur content diesel fuel. Plasma reforming of the high sulfur diesel was successful at temperatures below 800°C. The lower operating temperature plasma enhanced reforming provides an operating environment that increases the durability of the reformer. The lower operating temperature is an improvement over traditional catalyzed partial oxidation (CPOX) and autothermal reforming (ATR) that need to operate at temperature 100°C to 200°C higher.

Diesel fuel reforming with 315 ppm sulfur impurity

Micro-reactor experiments

The two catalyst used in the plasma reformer evaluations were evaluated in a micro-reactor which did not have plasma reforming enhancement capability: a noble metal-based catalyst on alumina and a monolith used for ATR reforming. The catalysts were not designed for sulfur tolerance. The catalysts were found to be severely poisoned by the 315 ppm sulfur impurity when operating at 720°C as shown in Figure A-1. Raising the temperature to 820° stabilized the catalyst to the sulfur poisoning as shown in Figure A-2.

Plasma reactor experiments

Plasma enhanced reforming of diesel fuel with 15 ppm sulfur was successful. The temperature of the catalyst region did not exceed 710°C. There was a temperature gradient in the reactor from the center at 710° to the outer shell of the reactor at 630°C. The results of the experiment are given in Figure A-3.

The hydrogen yield remained constant over the band 29% to 34% over several days of testing. The experiment was operated with overnight interruptions. The operating procedure included shut down with oxidant (air and steam) flowing but no fuel flow while the operating temperature was decreased. A similar start-up procedure was used, i.e. oxidant flowing without fuel, during the period the reactor was brought up to temperature. Both start-up and shutdown procedures produce operating conditions where the carbon-coke would be removed as CO or CO₂. Removal of sulfur from the catalyst by oxidation would also be possible. This is an experimental problem for AH2T because they do not have the capability to operated uninterrupted for extended periods of time; e.g. 1,000 hours.

Plasma enhanced reforming of diesel fuel with 315 ppm sulfur was successful. AH2T reports 94.6% conversion. The temperature stability of the reactor was very uniform and is shown for selected thermocouples in Figure A-4. The temperature varied from 720°C to 780°C within the reformer.

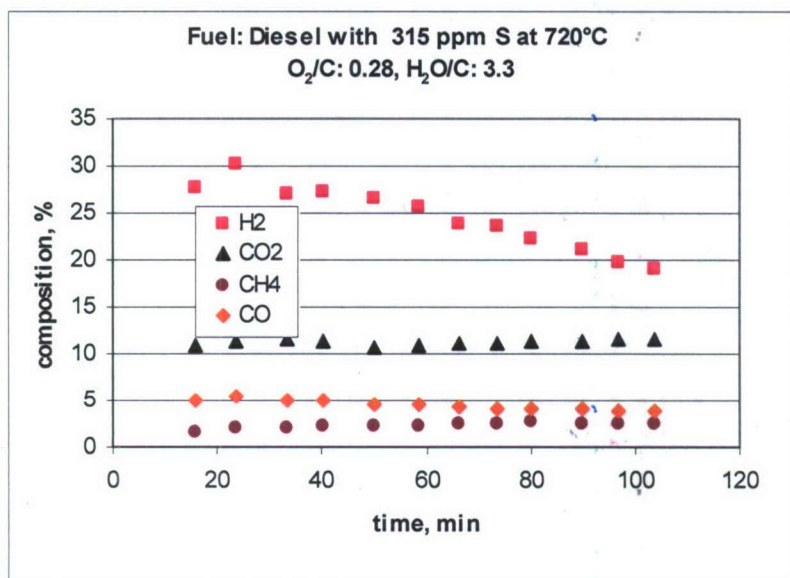


Figure A-1: Micro-reactor experiments: Poisoning of reformer catalyst operating on diesel fuel containing 315 ppm at 720°C.

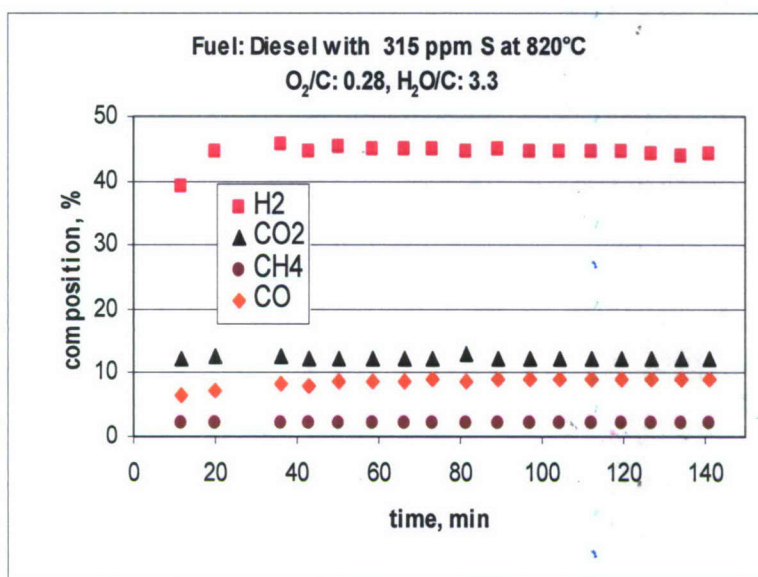


Figure A-2: Micro-reactor experiments: Stability of reforming catalyst operating on diesel fuel containing 315 ppm sulfur at 820° C

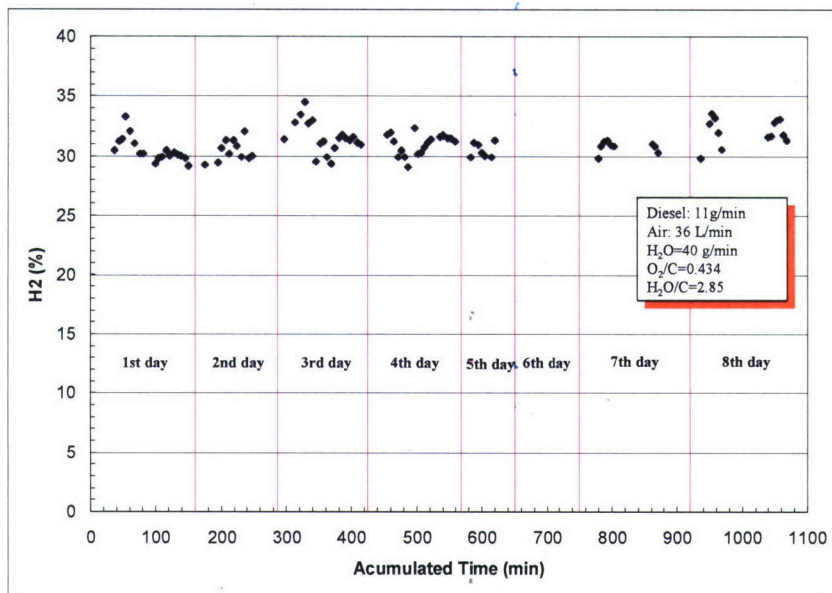


Figure A-3: Plasma reforming of ESSO Diesel with 15 ppm sulfur impurity

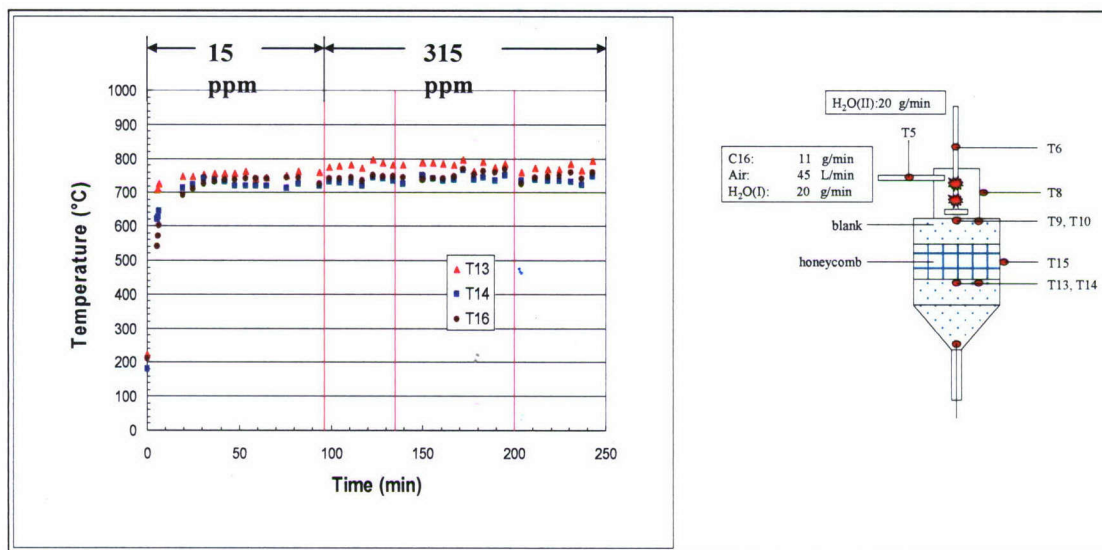


Figure A-4: Plasma reforming ESSO diesel with 315 ppm sulfur impurity temperature within reactor at selected thermocouples

The data in Figure 5 showing a decrease in hydrogen concentration with time during one test period while hydrogen concentration remained constant during two other test periods.

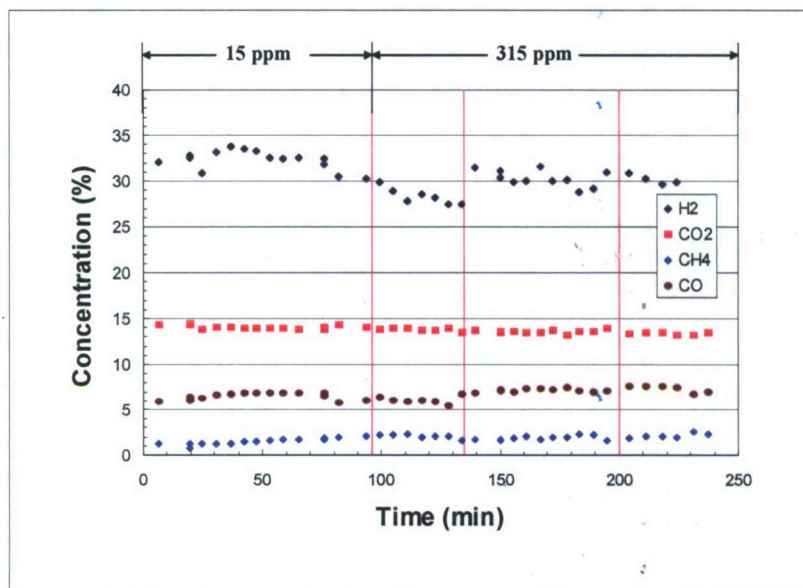


Figure A-5: Plasma reforming of ESSO diesel with 315 ppm S impurity. Reformate compositions

The methane concentration given in Figure A-5 remains relatively constant over the course of the experiments. Reformate methane impurity is recognized as an indicator of inefficiency for the reforming process. The change in hydrogen concentration during the first period of operation on diesel with 315 ppm S shows no corresponding change in the methane concentration. The carbon dioxide concentration also remains constant during the first period of operation on diesel with 315 ppm S; and the carbon monoxide concentration is constant over all three periods of operation on diesel with 315 ppm S. Based on the concentrations of all of the gases in reformate, the catalyst activity appears to be constant.

Experiments conducted by AH2T demonstrated a dependence on the yield of hydrogen based on flow rate of the reactants and operating temperature of the reactor. Increasing the flow rate of reactants (doubling) lowered the carbon conversion from 97.5% to 94.5% carbon conversion. These data are given in Appendix A.

Conclusions AH2T plasma reforming of diesel containing high sulfur levels:

1. Plasma reforming of diesel fuels containing up to 315 ppm sulfur is feasible.
2. Hydrogen yields up to 97.6% have been obtained
3. Catalysts that are poisoned by sulfur in a micro-reactor do not appear to be poisoned during plasma reforming.
4. Long term plasma reforming of diesel fuels containing 315 ppm or greater sulfur need to be demonstrated experimentally.

Hydrogen Enrichment

A subcontract was executed effective the 25th day of July, 2006, between DJW TECHNOLOGY, LLC (DJWT) and The Ohio State University Research Foundation, OSU, and is identified as Agreement Number: DJWTLLC-OSURF-0001. The objective of the work under this contract is to demonstrate selective membrane purification of synthetic reformates fuel with composition based on the effluent from a plasma reformer processing diesel-like fuels.

Removal of hydrogen sulfide impurities from syngas containing up to 50 ppm H₂S to less than 80 ppb was demonstrated using a selective membrane synthesized by The Ohio State University, OSU. The concentration of the exit H₂S is dependent on the flow rate of the feed gas. At 10 cc/minute for a cell 19.8 cm long and with an active area of approximately 340 cm², the concentration was lowered to 80 ppb. The reduction of the H₂S concentration to 10 ppb from an initial concentration of 50 ppm was demonstrated in this cell.

Reduction of the H₂S concentration to less than 5 ppb was demonstrated in cell having an active area of approximately 45 cm² with the initial syngas H₂S concentration at 100 ppb and the flow rate at 10 cc/minute. Argon was used as the sweep gas for simplification of the chemical analysis. The membrane purification system has a high H₂S permeability; greater than 20000 Barrers at 110 - 130°C. The H₂S / H₂ selectivity is high at 600.

Reduction of carbon monoxide to less than 10 ppm from an initial concentration of 1% was demonstrated using the membranes developed by OSU and these data were reported in the interim report¹.

OSU synthesized membranes containing amino groups with high CO₂ permeability and high CO₂/H₂ and CO₂/CO selectivities. The membranes showed a high CO₂ permeability of about 4000 Barrers, a high CO₂/H₂ selectivity of greater than 40, and a high CO₂/CO selectivity of greater than 160 at 100 – 170°C. These membranes could be operated to about 180°C.

Removal of H₂S from syngas:

The reduction of H₂S for syngas having 50 ppm H₂S, 6.5% CO and a CO₂ concentration of 12% is shown in Figure A-6 as a function of the flow rates. The calculated space velocity (GHSV, hr⁻¹) is 2500 hr⁻¹. The operating temperature of the selective membrane purification was 120°C and the pressure was 2.5 atm.

Membranes were synthesized by OSU and the CO₂ and H₂S permeabilities measured as a function of temperature. The permeability of the H₂S is approximately three times that of CO₂ at an operating temperature of 140°C. At lower temperatures (110°C), the permeability of the H₂S is greater than five times that of the CO₂. The data are represented in Figure A-7.

¹ Interim Report (Updated January 4, 2007) to Hawaii Natural Energy Institute, "Fuel Processing and Purity Studies", Purchase Order No. Z774282

The selectivity of H_2S versus H_2 is in the range of 600 to 200 as shown in Figure A-8. The very high selectivity of H_2S and the high permeability of H_2S compared to CO_2 provide the basis for design characteristics for the systems integration.

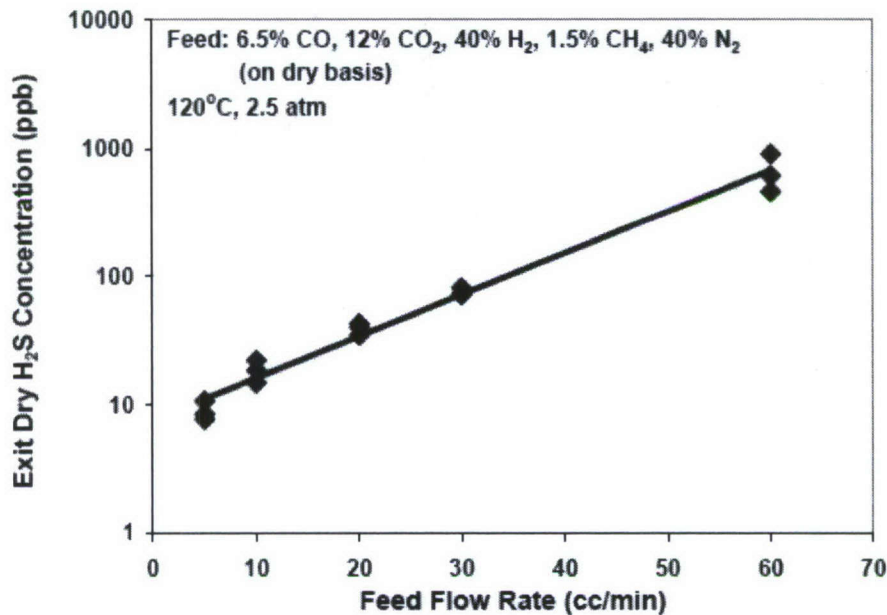


Figure A-6: H_2S in exit hydrogen at various flow rates for syngas feed containing 50 ppm H_2S and 6.5% CO

Modeling of Hydrogen Enrichment Reactor

A one-dimensional non-isothermal model was developed by OSU to predict the performance of the novel water-gas-shift (WGS) membrane reactor. The modeling results have shown that H_2 enhancement via CO_2 removal and CO reduction to 10 ppm or lower are achievable for synthesis gas from the autothermal reforming of gasoline with air.

Based on the modeling study using the membrane data obtained, OSU showed the feasibility of achieving H_2 enhancement via CO_2 removal, CO reduction to ≤ 10 ppm, and high H_2 recovery.

The modeling effort at OSU provided the basis for designing the multi-stage purification system proposed here. Ohio State University has a contract to build a pilot plant for the manufacture of membrane. OSU anticipates the facility will be functional in early 2008. TriSep Corporation was contacted for fabrication of the membrane purification system. In Figure A-9, representative products from TriSep are identified.

H₂S Has Higher Permeability than CO₂

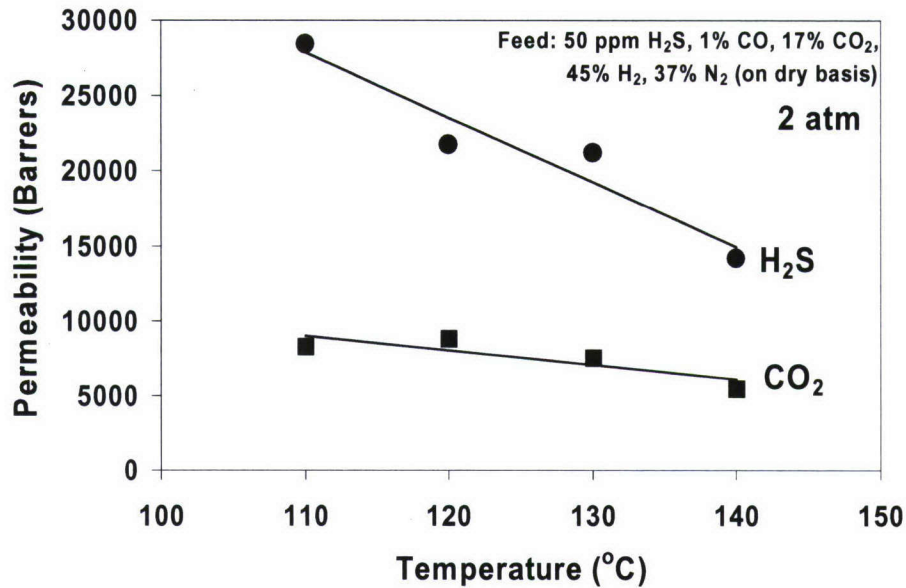


Figure A-7: H₂S permeability as a function of temperature

H₂S/H₂ Selectivity Higher than CO₂/H₂ Selectivity

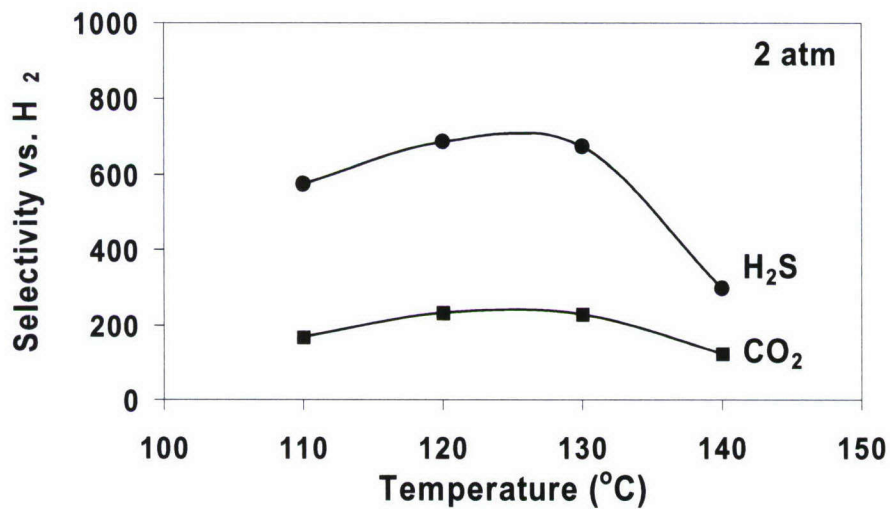


Figure A-8: H₂S has high selectivity versus hydrogen and greater selectivity than CO₂ versus hydrogen

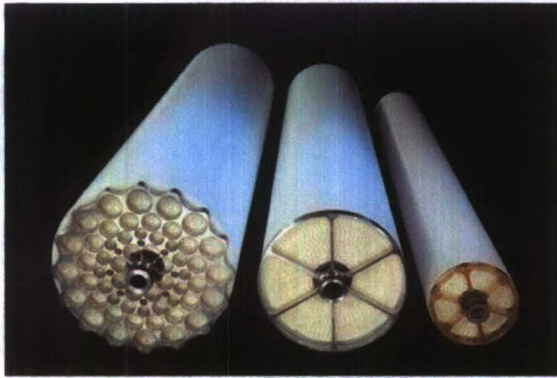


Figure A-9: TriSep membrane cartridges

System Integration

The objective of the systems integration activity is to identify the physical and chemical interfaces between the plasma reformer and the selective membrane purification system. Analysis of the interface requirements will define the balance of plant components for the integrated system.

Two Stage Purification Concept:

The design of a two stage purification unit with the first stage to remove H_2S appears a tractable solution for H_2S and CO_2 reductions. The design may require an initial reduction of the reformat input to the purifier to $120^\circ C$ to eliminate the H_2S . Subsequent heating of the partially purified reformat to $\sim 150^\circ C$ would then permit optimum reduction of the CO_2 . The concept is shown in Figure A-10.

The sweep gas for the selective membrane purification system is considered to be air. A mismatch exists in the temperatures of the exiting reformat and the input requirements for the selective membrane purification system. Preheating of the H_2S scrubbed reformat is required prior to stage 2. Water gas shift catalyst is used in stage 2 to promote the conversion of CO to CO_2 . The enriched hydrogen for the PEM fuel cell exits stage 2. The complete system is schematically given in Figure A-11.

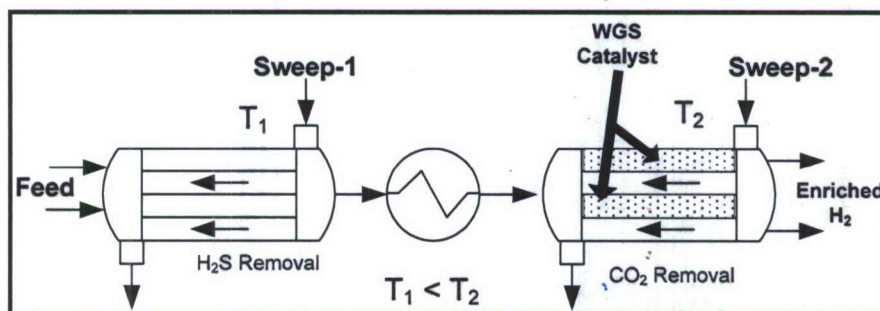


Figure A-10: Two stage hydrogen purification system

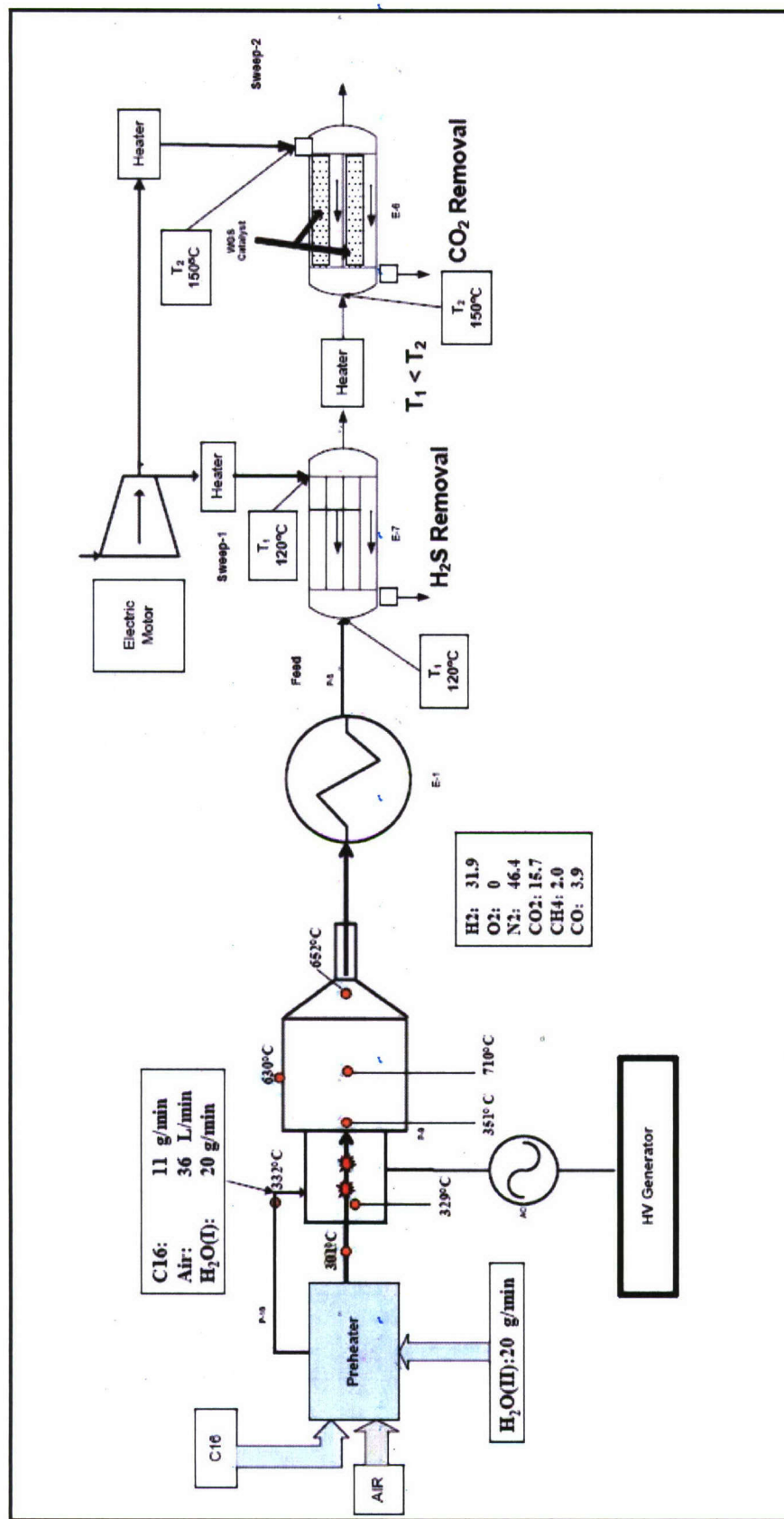


Figure A-11: System diagram for plasma reformer interfaced with selective membrane purification system

System components:

Parker Hannifin was contacted and the availability of balance-of-plant components reviewed. The heat exchangers, gas pre-heaters, and flow control components (not shown in Figure A-11. Parker Hannifin identified that off-the-shelf components could be for the initial system.

Conclusions:

Task 1: Plasma reforming of methane and diesel like fuels was demonstrated. Diesel fuels containing up to 315 ppm sulfur were plasma reformed without deactivation of the catalyst over the time period of the experiments. Typical reforming times were on the order of 100 minutes. Input parameters to the plasma reformer were identified. The temperature distribution of the reformer was identified and the temperatures for reforming were lower, by approximately 100 to 200°C, than temperature reported in the literature. The carbon conversion ranged from 94% to 97% depending on the operating parameters of the plasma reformer.

Task 2: Reformate purification with the reduction of H₂S from 50 ppm to less than 10 ppm was demonstrated using the membrane purification system developed by The Ohio State University. The operating parameters for the H₂S removal system were identified.

Reformate purification with the reduction of CO to less than 10 ppm was demonstrated using the membrane purification system developed by The Ohio State University. The operating parameters for the hydrogen purification system were identified.

A model developed by The Ohio State University under a separate program was used to identify the operating conditions for the reduction of CO and H₂S impurities in reformate using the membrane purification system. The model provided engineering parameters for the design of membrane purification system.

TriSep was contacted to discuss the feasibility of building the membrane purification system.

Task 3: A system integration study of the plasma reformer with the membrane purification system was completed. The balance-of-plant components for integration of the plasma reformer to the membrane purification system were identified.

A two stage membrane purification system was proposed and balance-of-plant components identified. The operating parameters for the two stage membrane purification system were identified and balance-of-plant components identified.

Contacts were made with manufactures were made to identify the availability of balance-of-plant components. Parker Hannifin reports the balance-of-plant components are available and can be considered off the shelf components.

Reports:

An interim report was issued on January 4, 2007 (update).

This document is the final report for the project.

Recommendations:

The development of the integrated plasma reformer – selective membrane purifications system has past the initial stage of proof of concept. In the next stage the following are recommended:

1. Long term continuous testing of the plasma reformer with sulfur containing diesel fuel. These test would eliminate questions regarding the start / stop procedures used by AH2T.
2. Testing of the plasma reformer with very high sulfur containing fuels; sulfur concentrations of 1000 ppm to 3000 ppm.
3. Plasma reforming with varied plasma power inputs to determine the optimum operating conditions of the plasma reformer
4. Construction of the laboratory two stage selective membrane purification system for demonstration of simultaneous H₂S and CO reductions.
5. Construction of an integrated plasma reformer / selective membrane purification system.

APPENDIX B

Near-field Characterization of Hydrothermal Vents along the Endeavour Segment of the Juan de Fuca Ridge

Simple arguments are presented here to characterize the behavior of the buoyant section of plumes generated in the vicinity of hydrothermal vents. This hydrodynamic near field corresponds to the vertical rise of seafloor vent fluid and entrained seawater in a stratified environment until the mixture reaches neutral buoyancy. Characteristics of the near field (flow rate, chemical composition) can be used as an input to subsequently analyze the more expansive lateral spreading of vertically-stabilized plume fluid, or far field. We focus our attention on the example of the Endeavour Segment of the Juan de Fuca Ridge described in Lupton *et al.* (1985). The area of interest is a hydrothermal vent field of about 250 m by 150 m, including about 40 active 'black smokers' at a water depth of about 2200 m.

Lupton *et al.* (1985) reported vent fluid dilutions of the order of 10^4 when the rising plume becomes neutrally buoyant about 200 m above the seafloor. This dilution magnitude was based on the ratio of estimated vent fluid temperature (300 °C) over a measured temperature anomaly $\delta\theta \approx 0.05$ °C in the lateral plume (far field) 4.4 km away from the vent location. The authors' attempt to use plume theory, however, resulted in greater predicted dilutions (3.4×10^4) and a significantly higher neutral-buoyancy level h (370 m). Although the real fluid flow probably is complex and not sufficiently characterized, the lack of agreement with robust plume models warrants attention. Recent studies of hydrothermal plume behavior (Bemis *et al.*, 2002; Rona *et al.*, 2002) using acoustic imaging have generally validated classical plume theory (e.g., Morton *et al.*, 1956) as long as the vents behaved like point sources of buoyancy and that multiple plumes remained sufficiently separated. Other issues that may be raised are the distance where the end-point temperature anomaly was measured and the fact that the entrainment of progressively warmer water in a vertically-stratified environment corresponds to higher dilutions than given by temperature anomaly ratios. In what follows, these ideas are succinctly explored.

Buoyant plume without current

The thickness D of the laterally-spreading plume (far field) was estimated to be 180 m from CTD casts (Lupton *et al.*, 1985). The near equality $D \approx h$ between intrusion layer thickness and buoyant-plume trap height is characteristic of small currents U (Wright *et al.*, 1982; Roberts *et al.*, 1989). We consider here the case when U , perhaps in an average sense, is zero.

Several difficulties are encountered at this juncture. Point-source buoyant plumes entrain surrounding ambient fluid and widen as they rise; the plume radius b is predicted to grow linearly with height Z according to the equation $b = 1.2(6/5)EZ$ (Morton *et al.*, 1956). With b interpreted as an average value (top-hat profiles of plume parameters¹), the entrainment coefficient E typically is 0.12. Considering 40 black smokers assumed to be spread uniformly in an area 250 m by 150 m (Lupton *et al.*, 1985), the plumes produced by individual smokers would merge at a height of 100 m above the seafloor, about half-way from reaching neutral buoyancy.

¹ In the original derivation based on Gaussian profiles, b is the e-folding radius and E is $\sqrt{2}$ smaller.

Moreover, the lateral entrainment of ambient fluid in a rising plume closely surrounded by similar plumes is conceptually problematic since it would be inhibited by reason of symmetry; it is likely that this configuration might be best described as a distributed source of seafloor buoyancy drawing ambient fluid into a mixing boundary layer from which a plume(s) would buoyantly rise. Such a mechanism was experimentally and theoretically analyzed for the distributed injection of freshwater into brine (Epstein and Burelbach, 2001). Although the possible merging of individual plumes and their potential origin from a mixing layer would not permit a straightforward use of classical point-source plume theory, some insight may be gained by invoking this simpler framework as discussed below.

In stratified fluids where the buoyancy frequency $N = [(g/\rho_a)d\rho_a/dZ]^{1/2}$ is constant, Morton *et al.* (1956) derived the following estimate for h :

$$h = 3.79 B(0)^{1/4} N^{-3/4}. \quad (B.1)$$

Here, g is the acceleration of gravity and Z the vertical coordinate measured from the seafloor; the ambient seawater density ρ_a taken as $1000 + \sigma_2$ (potential density at a reference pressure of 2000 dbar) is calculated from Fofonoff and Millard (1983). B is the buoyancy flux defined as $Qg\delta\rho/\rho_{ref}$, where Q is the plume volume flux, $\delta\rho$ the density anomaly between plume and ambient fluids and ρ_{ref} a reference density. With $N^2 = 1.46 \times 10^{-6} \text{ s}^{-2}$ (Lupton *et al.*, 1985) and $h \approx 200 \text{ m}$, Eq. (B.1) implies an initial buoyancy flux of $0.0137 \text{ m}^4/\text{s}^3$, i.e., much less than the value of $0.17 \text{ m}^4/\text{s}^3$ cited by Lupton *et al.* (1985) for a single black smoker. Interestingly, the estimation of buoyancy fluxes from hot hydrothermal vents appears to be flawed (and skewed toward low values) in the technical literature (e.g., Bemis *et al.*, 2002). The buoyancy deficit term $\delta\rho/\rho_{ref}$ usually is obtained by multiplying the temperature difference between seawater and vent fluids, $\theta_0 - \theta_a(0)$, by the local thermal expansion coefficient for seawater $\alpha \approx 1.5 \times 10^{-4} \text{ }^\circ\text{C}^{-1}$. With $\theta_0 - \theta_a(0)$ of the order of $300 \text{ }^\circ\text{C}$, however, the linearity of water density with temperature breaks down as shown in Figure B.1 (freshwater data at a constant pressure of 20.101325 MPa from NIST, 2005); the substantial variation of density over the temperature range of interest also suggests that the Boussinesq approximation may not be acceptable for fluid models as in Epstein and Burelbach (2001). Our estimate of $B(0)$ corresponds to a buoyant rise time of about half an hour deemed typical of hydrothermal vent environments (Rona *et al.*, 2002).

We define the reference density as $\rho_{ref} = \rho_a(0) = 1000 + \sigma_2(1.80 \text{ }^\circ\text{C}, 34.6 \text{ ppt}) = 1036.9 \text{ kg/m}^3$. Ambient and vent fluids appear to have similar salinities s at the release point (Lupton *et al.*, 1985). The density ρ_0 of $300 \text{ }^\circ\text{C}$ hydrothermal vent fluid is estimated to be 756.9 kg/m^3 by applying a salinity correction of 0.64 s (Epstein and Burelbach, 2001) to the freshwater data. With our estimate of $B(0)$, this would correspond to $Q(0) = 5.17 \times 10^{-3} \text{ m}^3/\text{s}$. Note that $Q(0)$ usually is assessed from field observation. Formulas for the volume flux of buoyant plumes in unstratified fluids are for the most part applicable in slightly stratified environments (Nihous, 2006). With top-hat profiles in the absence of currents, the following equation can be used (Wright, 1977; Huang *et al.*, 1998):

$$Q = 0.2 B(0)^{1/3} Z^{5/3}. \quad (B.2)$$

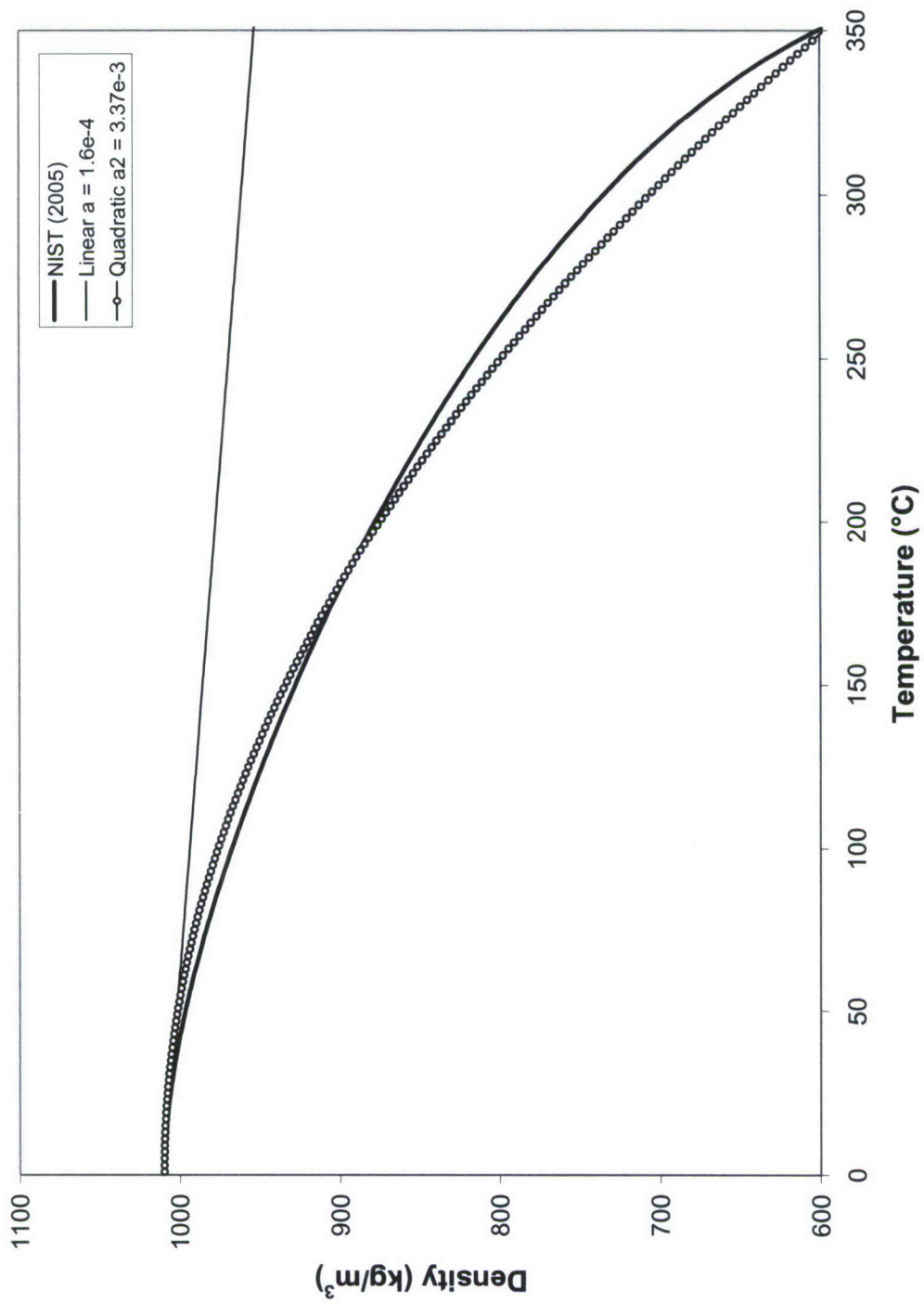


Figure B.1. Density of fresh water at constant pressure (20.101325 MPa)

With $Q(h) = 327 \text{ m}^3/\text{s}$, the dilution $Q(h)/Q(0)$ would be of the order of 6.3×10^4 . Thus, a derivation where h constrains $B(0)$ via Eq. (B.1) and where the hydrothermal vent fluid temperature θ_0 defines the initial density deficit yields much greater dilution than was observed. An alternative approach is to consider $\theta(0)$ to be unknown as long as the heat input from a typical single black smoker $H(0) \approx Q(0)\rho(0)c_p(0)\theta(0)$ is given (e.g., 10^7 cal/s in Lupton *et al.*, 1985). Both density ρ and specific enthalpy c_p depend on temperature. If $B(0)$ also is available, then an implicit equation in $\theta(0)$ can be obtained by eliminating $Q(0)$:

$$\theta(0)c_p(0) \left\{ \frac{\rho_{ref}}{\rho(0)} - 1 \right\}^{-1} = \frac{gH(0)}{B(0)\rho_{ref}}. \quad (\text{B.3})$$

The right-hand side being known, a solution of Eq. (B.3) yields $\theta(0) \approx 11 \text{ }^\circ\text{C}$. Such a low value could suggest the existence of a seafloor mixing layer formed by a distributed vent source where a dilution of the vent fluid of the order of 30 would take place. This idea is explored in some details in Appendix C. It can be shown that a circular source about 1.4 m in diameter releasing $300 \text{ }^\circ\text{C}$ hot vent fluid at 2 cm/s would yield such a value of $\theta(0)$ less than a meter above the seafloor. Visual observations of vents typically yield high release velocities ($\sim 1 \text{ m/s}$) over small areas (effective diameter $\sim 3 \text{ cm}$) instead (Rona *et al.*, 2002). While simple models and scant observations are not likely to offer definitive answers, the mixing-layer paradigm may support the notion expressed in Lupton *et al.* (1985) that “although black smokers are the most visible type of discharge...a large fraction of the [plume] effluent layer may be the result of diffuse hydrothermal flows...”

From solving Eq. (B.3), we also find that $Q(0) = 0.92 \text{ m}^3/\text{s}$ so that within the rising plume, an additional dilution of 355 takes place. This corresponds to an overall volume dilution of 1.1×10^4 , in much better agreement with observations. With the product ρc_p nearly constant at $4.14 \times 10^6 \text{ J-m}^{-3}\text{-K}^{-1}$ and using Eq. (B.2), the ‘temperature flux’ $Q\theta$ satisfies the following approximate equation:

$$\frac{d(Q\theta)}{dZ} = \frac{1}{3} B(0)^{1/3} Z^{5/3} \theta_a(Z). \quad (\text{B.4})$$

Linearizing the ambient temperature profile as $\theta_a(Z) = 1.8 + 6.5 \times 10^{-4}Z$ (Lupton *et al.*, 1985) makes the integration of Eq. (B.4) between 0 and h straightforward. As the plume reaches neutral buoyancy, the temperature anomaly $\delta\theta = \theta_a(h) - \theta(h)$ can be derived to be $0.0814 \text{ }^\circ\text{C}$ from the solution. This value is in good agreement with observations (Lupton *et al.*, 1985; Cowen *et al.*, 2002); it also shows that the ‘dilution of temperature anomaly’ ($298.2/0.0814 \approx 3700$) invoked by Lupton *et al.* (1985) to assess mixing is only about one third of volume dilution. Their potential underestimation of near-field entrainment likely was offset by using a value $\delta\theta \approx 0.05 \text{ }^\circ\text{C}$ measured 4.4 km away from the vent field location.

Buoyant plume in current

de Angelis *et al.* (1993) reported typical horizontal currents of the order of 1 km per day in the area of interest. This value of U is rather small, but could alter the dynamics of the buoyant

hydrothermal plumes. Here, we simply retrace the steps of the simple analysis presented when $U = 0$. An equivalent of Eq. (B.1) is given by Hewett *et al.* (1971):

$$h = 1.7 B(0)^{1/3} U^{1/3} N^{-2/3}. \quad (\text{B.5})$$

With $h = 200$ m, the initial buoyancy flux $B(0)$ would be $0.0275 \text{ m}^4/\text{s}^3$. This would correspond to $Q(h) = 413.5 \text{ m}^3/\text{s}$ from Huang *et al.* (1998). Assuming the plume to originate from a 300°C point source results in excessive dilution, of the order of 4×10^4 , as before. Solving Eq. (B.3) instead yields $\theta(0) \approx 43^\circ\text{C}$ and $Q(0) = 0.24 \text{ m}^3/\text{s}$, for an overall volume dilution of 1.2×10^4 . With such values, the mixing-layer model would correspond to a distributed source only about half a meter in diameter with an average release velocity of about 0.2 m/s . Finally, repeating the estimation of the temperature anomaly at neutral buoyancy by integrating Eq. (B.4), we find that $\delta\theta(h) = 0.092^\circ\text{C}$.

Notation

a	thermal expansion coefficient of seawater ($^\circ\text{C}^{-1}$)
b	buoyant plume radius (m)
c_p	specific enthalpy of seawater ($\text{J}\cdot\text{kg}^{-1}\cdot\text{K}^{-1}$)
B	plume buoyancy flux ($\text{m}^4\cdot\text{s}^{-3}$)
D	thickness of plume intrusion layer (m)
E	buoyant plume entrainment coefficient
g	acceleration of gravity ($\text{m}\cdot\text{s}^{-2}$)
h	neutral-buoyancy height of near-field plume above seafloor (m)
H	plume heat flux (W)
N	buoyancy frequency (s^{-1})
Q	plume volume flux ($\text{m}^3\cdot\text{s}^{-1}$)
s	salinity (ppt)
U	current magnitude ($\text{m}\cdot\text{s}^{-1}$)
Z	vertical coordinate (m)

Greek letters

$\delta\rho$	plume density anomaly ($\text{kg}\cdot\text{m}^{-3}$)
$\delta\theta$	plume temperature anomaly ($\text{kg}\cdot\text{m}^{-3}$)
ρ	seawater density ($\text{kg}\cdot\text{m}^{-3}$)
ρ_{ref}	reference density ($\text{kg}\cdot\text{m}^{-3}$)
σ_2	potential density referred to 2000 dbar ($\text{kg}\cdot\text{m}^{-3}$)
θ	temperature ($^\circ\text{C}$)

Subscript

a	ambient seawater (plume model with stratification)
0	vent fluid

References

References for Appendix B are included with the Section 4.5 References in the main body of this report..

This page is intentional blank

APPENDIX C

Vertical Mixing above a Steady Circular Hydrothermal Vent

The mixing boundary-layer model of Epstein and Burelbach (2001) describes the upward injection of buoyant fluid at a velocity v_0 over a circular area of radius R_0 into another fluid of constant properties (subscript ∞). In the process, ambient fluid is drawn radially inward until conditions for the existence of a rising plume are met, at $r = r_p$. Model assumptions and analytical procedures are not discussed here unless they are of special relevance. Additional details can be found in the above reference. In the original analysis, relative buoyancy is generated by releasing fresh water into brine. A hot source into a cold environment would achieve the same result, and these cases can be made undistinguishable by non-dimensionalizing all variables. The Boussinesq approximation whereby fluid density is assumed constant except in the vertical momentum equation is retained even though large density variations may occur in the vicinity of hydrothermal vents.

The radial distance and boundary-layer thickness are non-dimensionalized with R_0 and noted η and δ^* , respectively. The non-dimensional average inward radial velocity \bar{u}^* and volume flux Q^* are referred to v_0 and $\pi R_0^2 v_0$, respectively. The average buoyancy agent $\bar{\theta}$ is replaced by the non-dimensional variable $\sigma = (\bar{\theta} - \theta_\infty)/(\theta_0 - \theta_\infty)$. A densimetric Froude number is defined for this problem as $F = v_0 \{g R_0 (\rho_\infty - \rho_0) / \rho_{ref}\}^{-1/2}$. The linear relationship between density and the buoyancy agent (salinity, temperature) is replaced here with the simple quadratic form $\rho \approx \rho_\infty (1 - a_2 \theta^2)$. This approach allows density to remain within 5% of exact values over a wide high-temperature range, as shown in Figure B.1 of Appendix B with $a_2 = 3.37 \times 10^{-3} \text{ }^\circ\text{C}^{-2}$. Another assumption is that $\theta_\infty = 0 \text{ }^\circ\text{C}$. At this point, the derivation in Epstein and Burelbach (2001) can be followed step by step. The integral form of heat conservation is unchanged and Eq. (19) in Epstein and Burelbach (2001) holds. Hydrostatic pressure is affected, however, by the different functional dependence of density on temperature. Subsequent integration of the horizontal momentum equation yields $\bar{u}^* = (0.3 \delta^*)^{1/2} \sigma / F$ in lieu of Eq. (18) in Epstein and Burelbach (2001). As a result, the following surface boundary condition is obtained:

$$6^2 \beta^2 \sigma^2 \delta^{*1/2} + 3F\sigma = F, \quad (\text{C.1})$$

where β is the mixing-length thickness coefficient. Eq. (C.1) can further be expressed in terms of only one unknown (e.g., σ) after appropriate substitutions, but an implicit equation is obtained. In the practical low-Froude-number limit, where the convective term $3F\sigma$ is neglected in Eq. (C.1), the following explicit solution can be obtained:

$$\delta^* = 6^2 \beta^2 \left(\frac{5}{6}\right)^{1/2} \left(\frac{1 - \eta^2}{\eta}\right), \quad (\text{C.2})$$

$$\bar{u}^* = \frac{1}{2 \cdot 5^{3/8} 6^{1/8} \beta^{1/2} F^{1/2}} \left(\frac{1 - \eta^2}{\eta}\right)^{1/4}, \quad (\text{C.3})$$

$$\sigma = \frac{F^{1/2}}{6^{3/2} \beta^{3/2}} \left(\frac{6}{5}\right)^{1/8} \left(\frac{1-\eta^2}{\eta}\right)^{-1/4}, \text{ and} \quad (\text{C.4})$$

$$Q^* = \frac{6^{3/2} \beta^{3/2}}{F^{1/2}} \left(\frac{5}{6}\right)^{1/8} \eta \left(\frac{1-\eta^2}{\eta}\right)^{5/4}. \quad (\text{C.5})$$

An important identity is $Q^* \sigma + \eta^2 = 1$. As in Epstein and Burelbach (2001), the apparent singularity of σ at $\eta = 1$ is the result of discarding the convective term in Eq. (C.1); the correct value should be $\sigma(1) = 1/3$ (surface temperature of θ_0 at the edge of the source area).

Next, the transition between mixing boundary layer and buoyant plume is considered. Instead of $Q_p^* \approx Q^*(\eta_p)$ and $\sigma_p \approx \sigma(\eta_p)$, i.e., Eq. (25) in Epstein and Burelbach (2001), exact heat and mass balances yield $Q_p^* = Q^*(\eta_p) + \eta_p^2$ and $\sigma_p = \{Q^*(\eta_p) + \eta_p^2\}^{-1}$. Inserting these values into Eq. (43) in Epstein and Burelbach (2001), the following low-Froude-number equation for η_p is obtained:

$$4 \cdot 6^6 \left(\frac{5}{6}\right)^{1/2} E \beta^6 (1 - \eta^2)^5 = \eta^6. \quad (\text{C.6})$$

With β and E about 0.14 and 0.12, respectively, we find that η_p is about 0.55 instead of 0.43 with linear density.

The estimation of vent characteristics from plume initial values $Q(0) = Q_0 Q_p^*$ and $\theta(0) = \theta_0 \sigma_p$, identified here with transition values from mixing layer to plume *per se*, could theoretically be done. Since $Q_p^* \sigma_p = 1$, Q_0 can be obtained as $Q(0)\theta(0)/\theta_0$. The knowledge of Q_p^* with Eq. (C.5) then yields F (which should be small). Expressing the definitions of Q_0 and F , the radius R_0 and velocity v_0 can be determined straightforwardly.

Notation

a_2	quadratic thermal expansion coefficient of seawater ($^{\circ}\text{C}^{-2}$)
E	buoyant entrainment coefficient
F	densimetric Froude number
g	acceleration of gravity ($\text{m}\cdot\text{s}^{-2}$)
Q	plume volume flux ($\text{m}^3\cdot\text{s}^{-1}$)
Q^*	non-dimensional radial inward volume flux in mixing boundary layer
r	horizontal radial distance (m)
R_0	radius of seafloor source of buoyant fluid (m)
\bar{u}^*	non-dimensional average radial inward velocity in mixing boundary layer
v_0	upward velocity of vent fluid (m)

Greek letters

β	mixing-length thickness coefficient
δ^*	non-dimensional mixing-boundary-layer thickness
η	non-dimensional radial coordinate
ρ	seawater density ($\text{kg}\cdot\text{m}^{-3}$)
ρ_{ref}	reference density ($\text{kg}\cdot\text{m}^{-3}$)
σ	non-dimensional average temperature across the mixing boundary layer

θ temperature (°C)
 $\bar{\theta}$ average temperature across the mixing boundary layer (°C)

Subscript

p properties at transition from mixing boundary layer to buoyant plume
0 vent fluid
 ∞ ambient seawater (mixing-layer model with constant properties)

References

References for Appendix C are included with the Section 4.5 References in the main body of this report.

ADDENDA

For Appendix A of this report

Following this page, three Addenda will be presented that are part of the final report submitted by DJW Technologies under Subtask 3.4.3 of the main body of this report. The primary text of the final report is presented in Appendix A.

Addendum A Plasma Diesel Processing Final Report

Addendum B Selective Membrane Purification of Hydrogen for Fuel Cells

Addendum C Design of Integrated Plasma Reformer



AH2T, Inc

PLASMA DIESEL PROCESSING

FINAL REPORT

DJWLLC-AH2T-0001

225, President Kennedy Avenue
PK 6230
Montreal (Quebec), H2X 3Y8
CANADA

March 2007

Table of Content

Introduction

Prior work

Plasma processing of diesel with sulfur

- Fuel

- Experimental Procedure

- Micro reactor experiments

- Plasma reactor experiments

Conclusions

References

INTRODUCTION

Jet fuel is the most widely used logistics fuel. There is a strong need to process it and extract hydrogen in order to feed fuel cells such as PEMFC and SOFC for various applications.

Jet fuel is very similar to kerosene and consists of a complex mixture of hydrocarbons, additives and a numerous impurities in trace concentrations.

The major problems of processing jet fuel are related to :

- high concentration of sulfur , 2000-4000 ppm by weight.
- high concentration of aromatics, 20-30 %

With 1000 ppm S or more it is impossible to reform it successfully . No known catalyst would last long with this high concentrations of sulfur.

Therefore a desulfurization step has to be introduced between the original fuel and the reformer. The sulfur is mainly in mercaptans.

How deep the desulfurization should be is a decision the system designer has to make. The lower the sulfur content is the better for the reformer but, perhaps, at the cost of larger size and weight and the cost of the catalyst used.

After the reformer a further desulfurization step is required and especially in the case of PEMFC. This is normally done either chemically by means of adsorber/regenerator system, or by using membranes which separate all the impurities from the hydrogen. Sulfur in the reformat is mainly in the form of H₂S and SO₂.

In addition to sulfur, liquid fuels such as jet fuels and diesel present other difficulties related to carbon deposition (coking). Both effects deactivate catalysts and it is thought that carbon deposits enhance poisoning by sulfur. This is why it is difficult to separate the two effects.

PRIOR WORK

Three processing methods have been applied to fuel reforming: CPOX, ATR and SR.

All three processing methods rely heavily on catalysts that are different for each process.

The processes go from the very exothermic (CPOX) to the very endothermic (SR)

The ratio of oxygen to carbon (O/C) is highest for CPOX and zero for SR.

The ratio of steam to carbon is zero (or almost zero) for CPOX and highest for SR.

The temperature in the catalyst region is highest for CPOX and lowest for SR.

The hydrogen concentration in the reformat is highest in SR and lowest in CPOX.

ATR is a process that combines the characteristics of CPOX and SR and avoid some of their disadvantages.

AH2T is developing a new plasma method which is different from the above described methods. This method will be discussed separately in the following Section .

In CPOX, ATR and SR , the designer can chose the ratio of reactants: fuel, oxygen(air) and H2O; he can also chose the temperature, pressure and flow (hence the space velocity). However his choice is limited concerning the catalyst which is the most important factor in the process. The catalyst has to be not only very active but also resistant to sulfur poisoning and carbon deposition in order that its lifetime in the reactor becomes acceptable.

ADDITIONAL A Final Report H2

Confidential Information

Most catalysts, so far, have been formulated for low sulfur concentrations in the fuel, i.e. less than 20 ppm. If current commercial catalysts are used at high concentration of sulfur their lifetime would be much affected. This is why most of the current work on jet fuel processing is concentrated on formulating "sulfur tolerant" catalysts which , hopefully, could also be resistant to carbon deposition.

From the results in the published literature it can be seen that the experiments can be classified according to the concentration of sulfur in the fuel. Refs [1-9].

(a) Zero (or nearly zero) ppm of sulfur in the fuel: The problem here is limited to carbon and several catalysts for different processes have been used with some success.

(b) 15-22 ppm S:

The current ULSD is available with only 15 ppm S. Several experiments have also been performed with fuels containing 22 ppm after desulfurizing.

Certain catalysts gave adequate results.

(c) 50 ppm S :

The deactivation of catalysts used (mostly proprietary) is still a problem but some show improvement compared with non-proprietary catalysts.

(d) 300 ppm S :

The only experiments reported in this range were performed in short contact micro-rectors. The temperatures was more than 1000 C and the deactivation remained strong. The sulfur poisoning is too strong for known catalysts.

ADDENDUM A - Final Report 4/21

Confidential Information

(e) 1000 – 4000 ppm S:

The objective of the very few experiments that have ventured in this range was to simply show that catalysts deactivation in this range is catastrophic and that desulfurization is necessary prior to fuel reforming.

The fuels used in the above experiments were :

- (1) A single molecule type e.g. iso-octane or hexadecane.
- (2) Surrogate fuel with one or more molecular types.
- (3) Standard (commercial) fuels such as desulfurized jet-fuel and ULSD with or without added sulfur.

Only type (3) should be taken as a true representative of a practical situation because standard fuels :

- 1- have a distribution of C_n, some of which are very high, C₂₀ – C₂₆. The latter have strong tendency to deposit more carbon.
- 2- have also various additives, that could cause problems
- 3- have large concentrations of aromatics (20-30 %) or higher. These are known to be more difficult to process and could impact negatively the catalyst activity.

Unfortunately the majority of experiments reported in the literature are of simple molecular type or a surrogate fuels.

It is also important to note here that most of the experiments mentioned above have been conducted in very small volume micro-reactors which consist of small diameter tubes ($1/4$ or $1/2$ in.) and the catalyst occupied only a small section , e.g. total volume of $\sim 10 - 20$ cc.

These experiments are correct for measuring the effect of different catalysts since the temperature is controlled from the outside and is uniform throughout the catalyst and the flow of the reactants is also uniform.

In a real reformer the size brings with it problems and limitations that are imposed on the overall performance. The problems of temperature and flow distribution become more severe as the diameter of the reactor increases. The peripheral regions which constitute larger portion of the reactor volume are precisely the regions where the temperature could be lower by ($50 - 100$ C) by comparison to central regions.

As the sulfur poisoning and carbon deposition are sensitive to temperature (See micro-reactor results) it is clear that $50- 100$ C lower temperature in the peripheral region would make a big difference to catalyst activity and performance.

PLASMA PROCESSING OF DIESEL with various contents of sulfur

AH2T applied its plasma technology to treating liquid fuels (gasoline, kerosene and diesel) with varying contents of sulfur. This technology differs from standard methods (CPOX, ATR, SR) in that it uses an internally generated plasma gas to enhance fuel reforming.

Low power distributed electric discharges produce intense pulses of electrons which, by collisions, break the fuel into smaller molecules, i.e to lower distribution of Cn. See Fig (1). The discharges produce in the main time radicals and ions that are strongly reactive.

The quality of the this active gas depends on the plasma sources distribution and intensity. However the overall temperature of the gas is not appreciably different from that of the input mixture.

The temperature, however, increases in the catalyst region. The control of this temperature affects the performance of the catalyst and its sensitivity to sulfur poisoning and carbon deposition.

A detailed description of the various components of the processor system was given in the Interim Report.

Fuel

Jet fuel was not readily available to our laboratory and in any case a desulfurization would have been necessary to bring sulfur content from ~ 2000 ppm to 300 ppm or lower. Diesel was chosen instead; and since commercially available diesel contains only 15 ppm, additional 300 ppm were added to permit testing of fuel with high sulfur.

Experimental procedure

The fuel and water were evaporated and heated in the Heat Manager to ~ 350 C. The reformat from the plasma reactor was first cooled to condense the steam . The dry reformat was then directed to a gas chromatograph equipped with a TCD and FID detectors to determine the gas composition. The overall dry reformat flow was also measured and was used to calculate the conversion of the fuel. The latter was defined as the ratio of the carbons in the gas (CO, CO2 and CH4) to the total carbons in the initial fuel.

Two types of experiments were performed:

1- Micro-reactor experiments where the volume of the catalyst was small. It is worth noting here that most of the open literature results are from micro-reactor type experiments.

2- Plasma reactor experiments which simulate real operational conditions of a processor and which include the effects of reactants mixing and gas flow and temperature distributions.

Micro-reactor Experiments

Two catalysts were used in these tests, the first was a noble metal-based on an alumina support and the second was a monolith used normally for ATR processing. Neither catalyst was particularly designed to be sulfur tolerant.

Typical results are shown in Figs (2 , 3) for diesel containing 315 ppm of sulfur.

It is clear that the deactivation of the catalyst (from mainly sulfur poisoning but also from carbon deposition) is very temperature sensitive.

A temperature controller kept the temperature constant at a predefined level. Since the volume of the catalyst was small the temperature was uniform throughout the catalyst.

At 720 C H₂ concentration decreased from an initial 30% to 20 % in about 100 min. When the temperature was increased to 820 C little deactivation if any was observed.

Plasma Reactor Experiments

Two sulfur concentrations were examined:

1- Low sulfur content : 15 ppm

The experiment lasted several days with as many stops and restarts. O₂/C was 0.43 and steam/C was 2.85. The stability of the catalyst seems to be satisfactory , Fig(5).

It is important to notice the temperature distribution in the reactor shown in Fig(4).

In the plasma region it is low and does not exceed 350 C while in the catalyst region it increases to 710 C at the center of the reactor and 630 C at the outer radius of the reactor. So effectively most of the catalyst was not exceeding 650 C.

2- High sulfur content : 315 ppm

A series of experiments were conducted on diesel with additional 300 ppm of sulfur bringing the total to 315 ppm.

In the experiment March-15 the O₂/C was 0.54 and steam/C was 2.85. The temperature distributions are given in Fig (7) in the positions indicated in Fig(6). It is clear that the temperature in the majority of the catalyst region was ~ 750 C.

The experiment was started for the first 90 min with 15 ppm S diesel before switching to 315 ppm diesel for the rest of the duration. The results are shown in Fig(8) with interruptions and restarts indicated by the vertical lines.

It can be seen that the activity of the catalyst remained constant. A much longer tests would be performed to confirm these positive results. Fuel conversion was 94.6%. Detailed calculations are shown in Fig (9). The experiments of March-20 and March-21, Figs (10,15), were performed at different flows. In addition to confirming conclusions from March-15 experiment one would see some small differences due to changes in flow distribution and an overall lower temperature in the catalyst region.

CONCLUSIONS

Several laboratories are actively pursuing the development of processing methods for logistics fuels. Since the latter contain high concentrations of sulfur, 1000 – 4000 ppm, the main objective is to process these fuels without a necessity for deep desulfurization which could be a great handicap for portable and transportable applications.

Results published so far show that if processing of fuels with up to ~ 50 ppm S is feasible with "sulfur tolerant" new catalysts, processing of 50 – 300 ppm fuels remain a major problem. The deactivation of the best catalysts available is too strong and their lifetime is too short to be practical. The methods used so far (CPOX, ATR and SR) rely heavily on the use of catalysts, and it seems extremely difficult to find a catalyst that would allow processing a 300 ppm S fuel satisfactorily.

AH2T's method which relies on using plasma enhanced reforming and uses less catalyst has shown from the work done so far promising results for a 315 ppm diesel fuel.

Even better results could be obtained with some short term improvements :

- A new design which would allow higher and more uniform temperature distribution.
- The use of a commercially available catalyst (e.g. Rh- based) which shows some tolerance to sulfur.

Some long term designs would render the reformer more sulfur flexible without having to develop a "sulfur tolerant" catalyst. For instance a compact adsorber/regenerator in one or two zones or cycling fuel flow would allow treating high concentrations of sulfur.

REFERENCES

- 1- M. Fokema
 " Logistic fuel processing for portable power applications"
 6th Annual DoD Logistic Fuel Processing Conference May 2006
- 2- W.E. Rhine et al
 " Sulfur and coke resistant autothermal diesel reforming catalysts"
 Final Report 2004
- 3- I.C. Lee et al
 "JP-8 reforming for fuel cell applications"
- 4- J. J. Krummenacher et al
 J. Cat. 222(2004) 429
- 5- J.J. Krummenacher et al
 J. Cat 215 (2003) 332
- 6- J. R. Budge et al
 " Distillate fuel reformer development for fuel cell applications"
 5th Annual DoD Logistic fuel processing
- 7- C. Song et al
 App. Cat. 41(2003) 207
- 8- Q.Ming et al
 Cat. Today 77 (2002) 51
- 9- P.M. Irving et al.
 "Desulfurization and reforming of JP-8", Logistic Fuel processing 2006
 ADDENDUM A - Final Report AH2T



Example Diesel Fuel and Jet Fuel Composition (GC/MS)

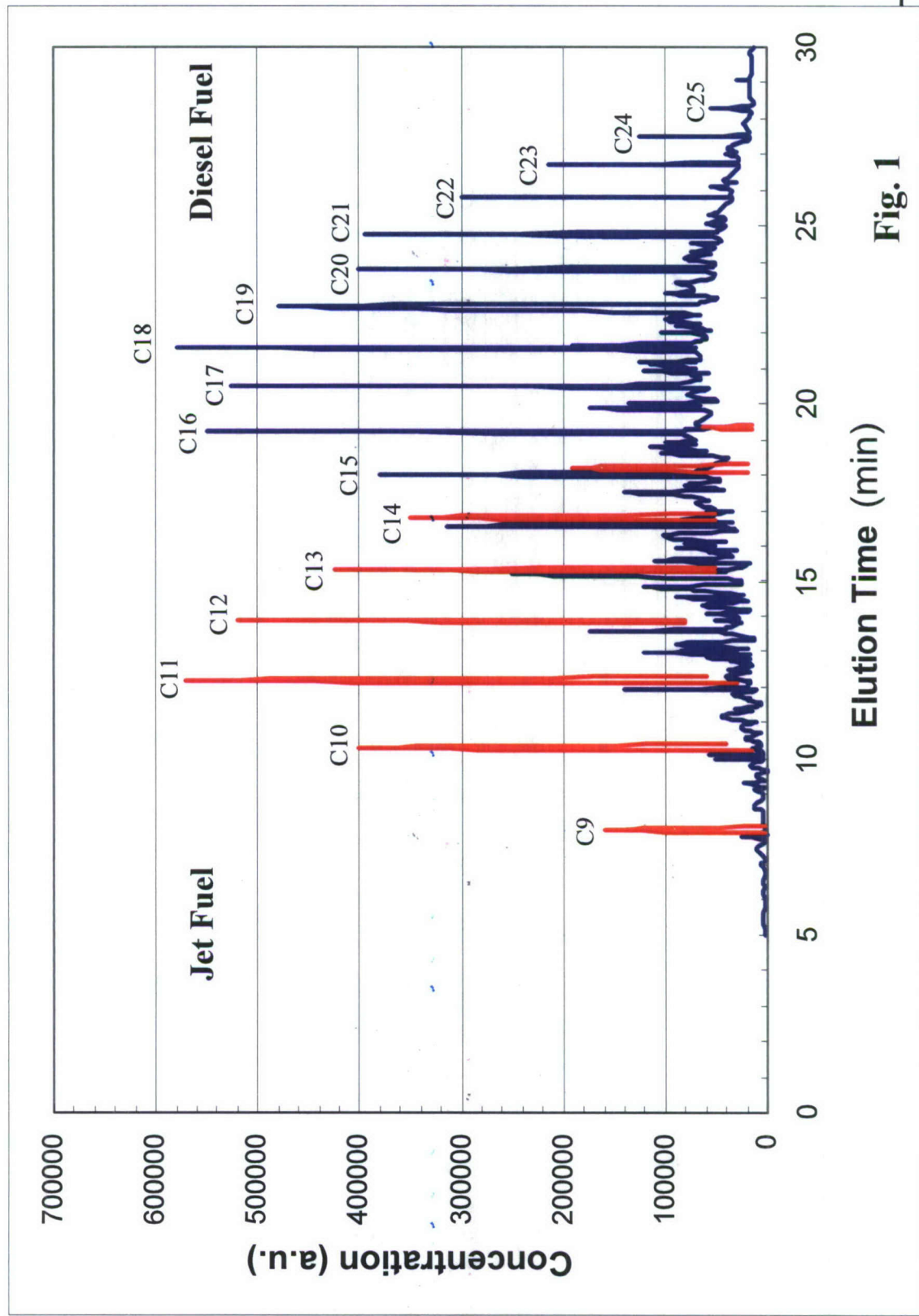


Fig. 1

Fuel: Diesel with 315 ppm S at 720°C
O₂/C: 0.28, H₂O/C: 3.3

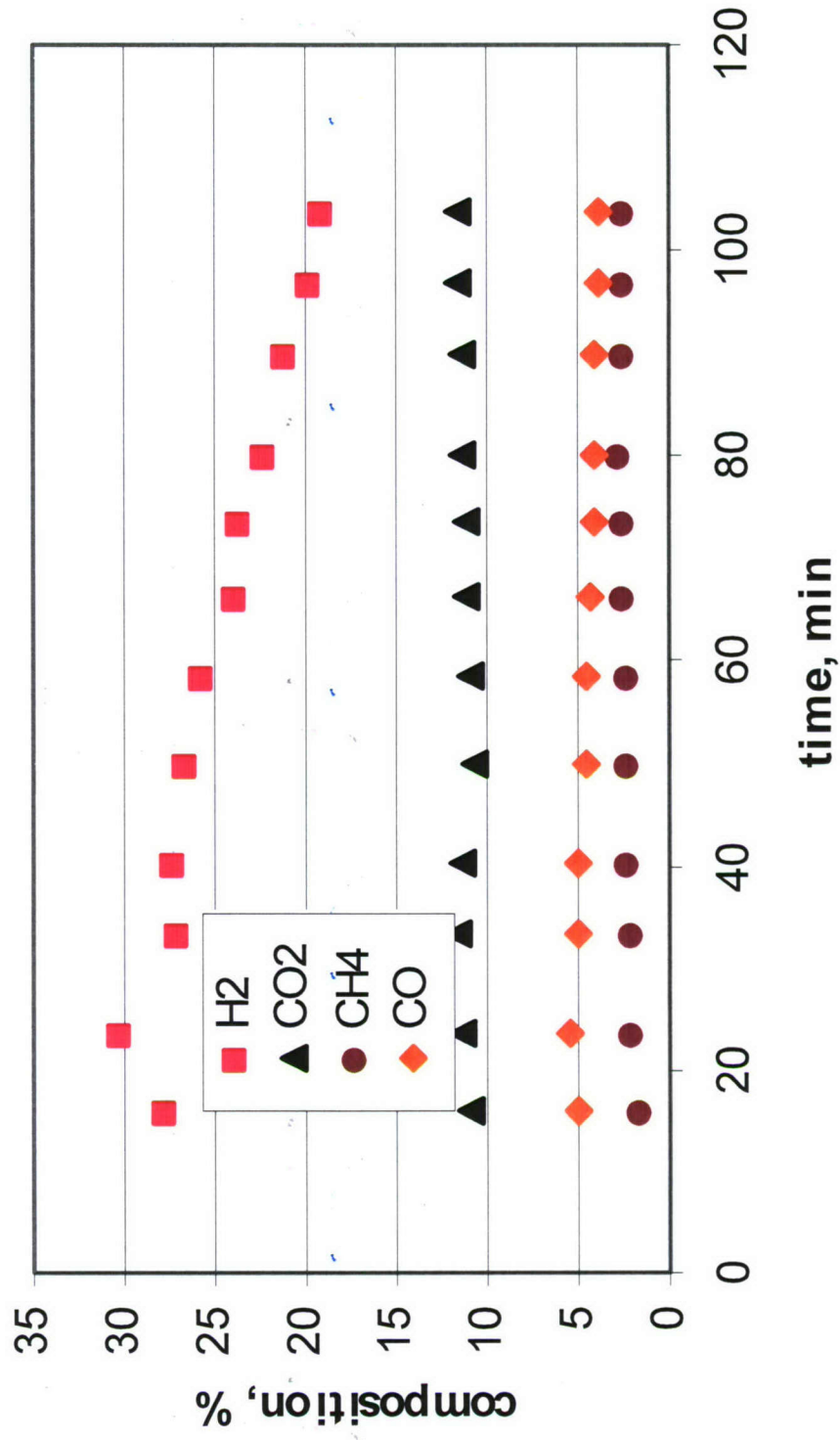


Fig. 2

Fuel: Diesel with 315 ppm S at 820°C
 $O_2/C: 0.28, H_2O/C: 3.3$

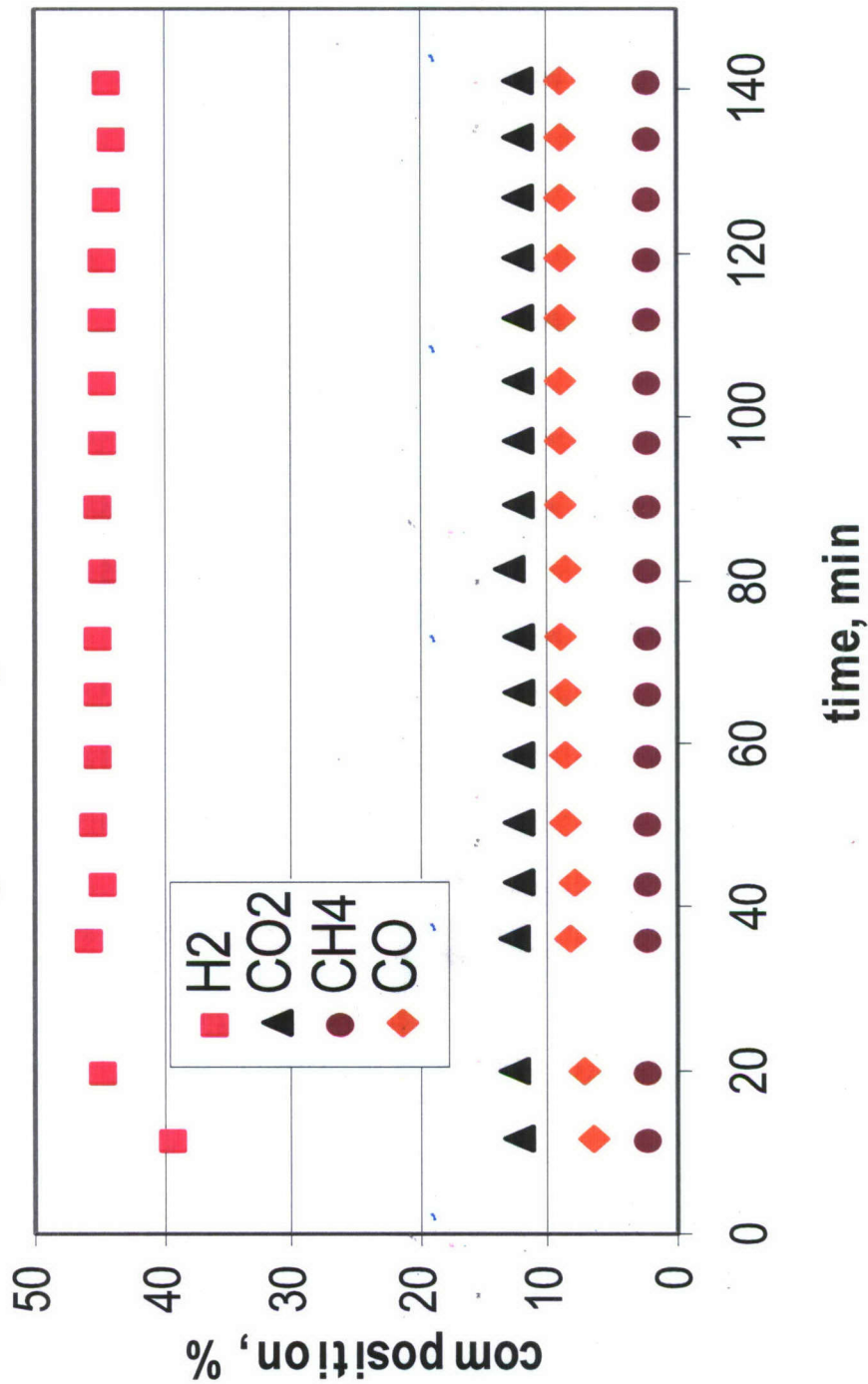


Fig. 3

Temperature Profile of ESSO Diesel (15ppm S) Plasma Reforming

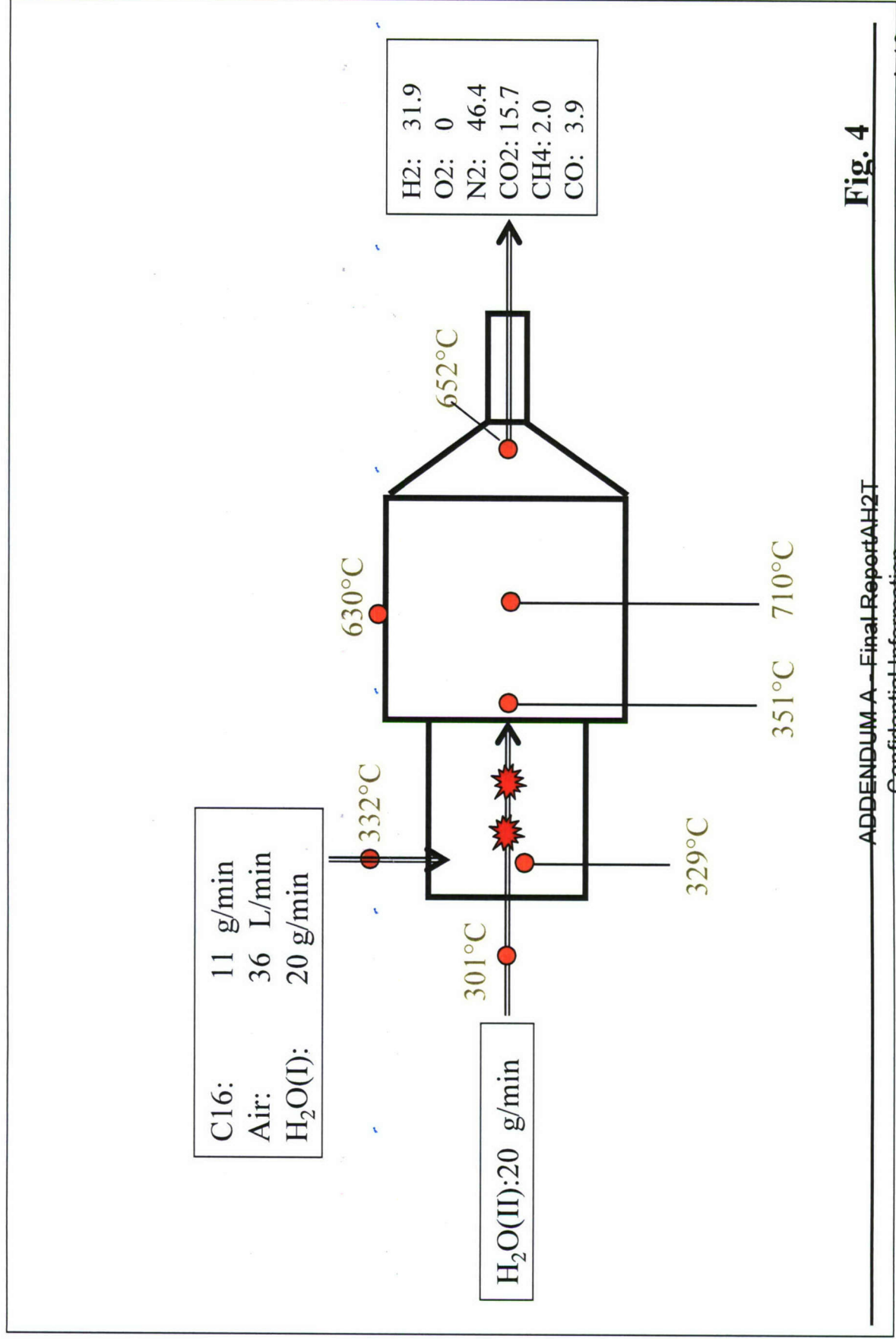
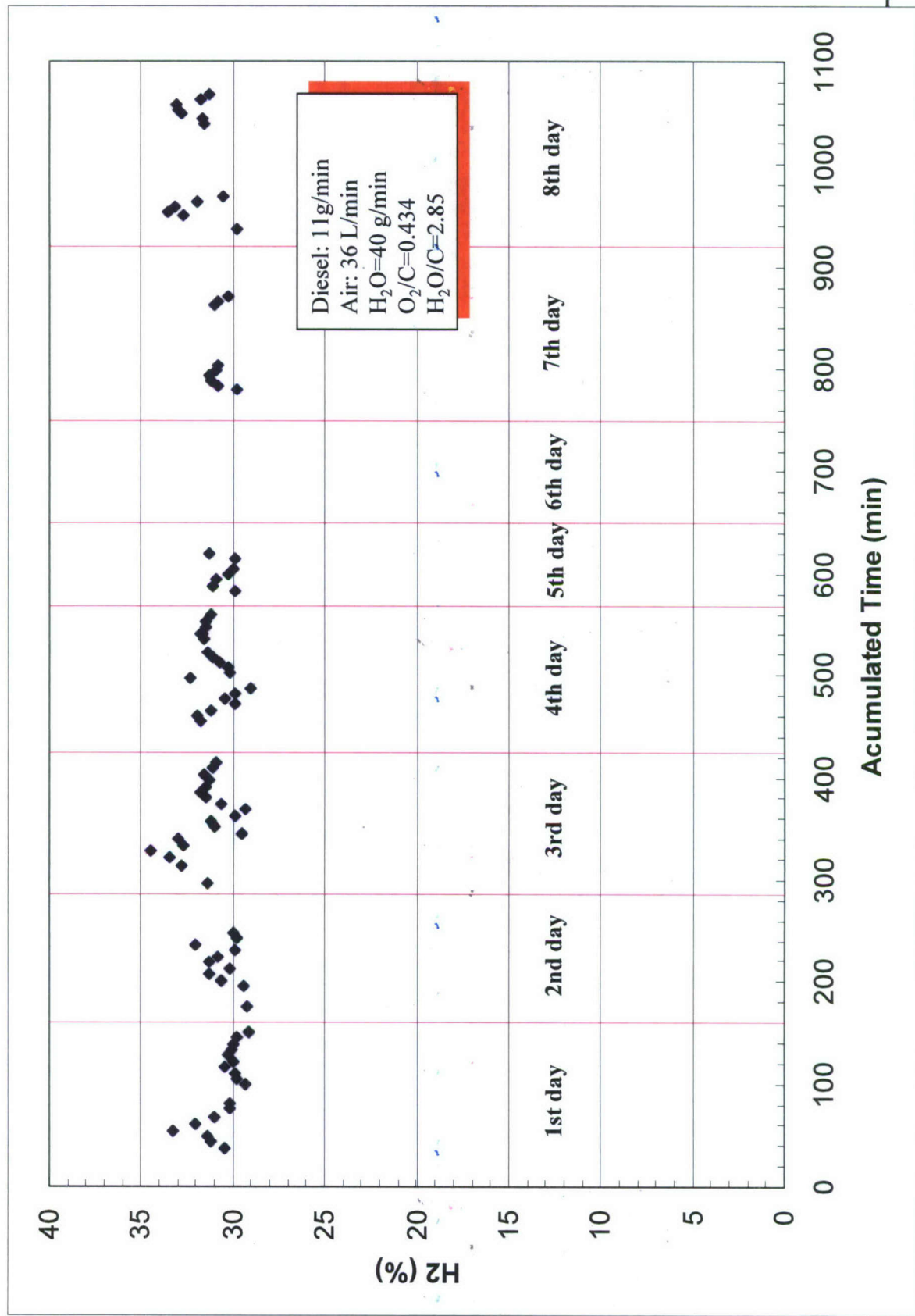


Fig. 4

ADDENDUM A - Final Report AH2T

Confidential Information

Fig. 5
Catalyst Stability Experiments for ESSO Diesel (15ppm S) Plasma Reforming



Temperature Profile of ESSO Diesel (15ppm S + 300 ppm S) Plasma Reforming

March 15, 2007

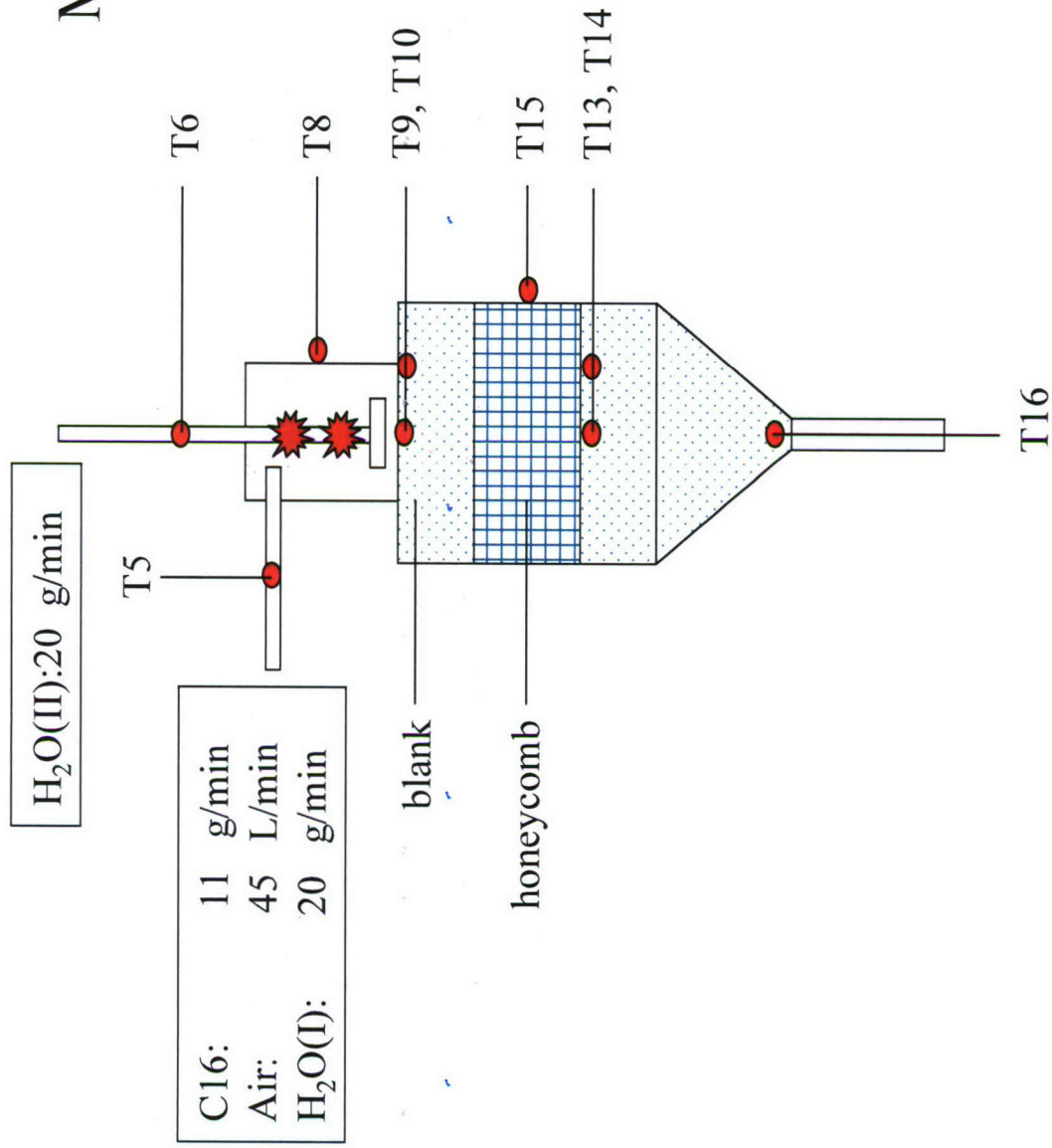


Fig. 6

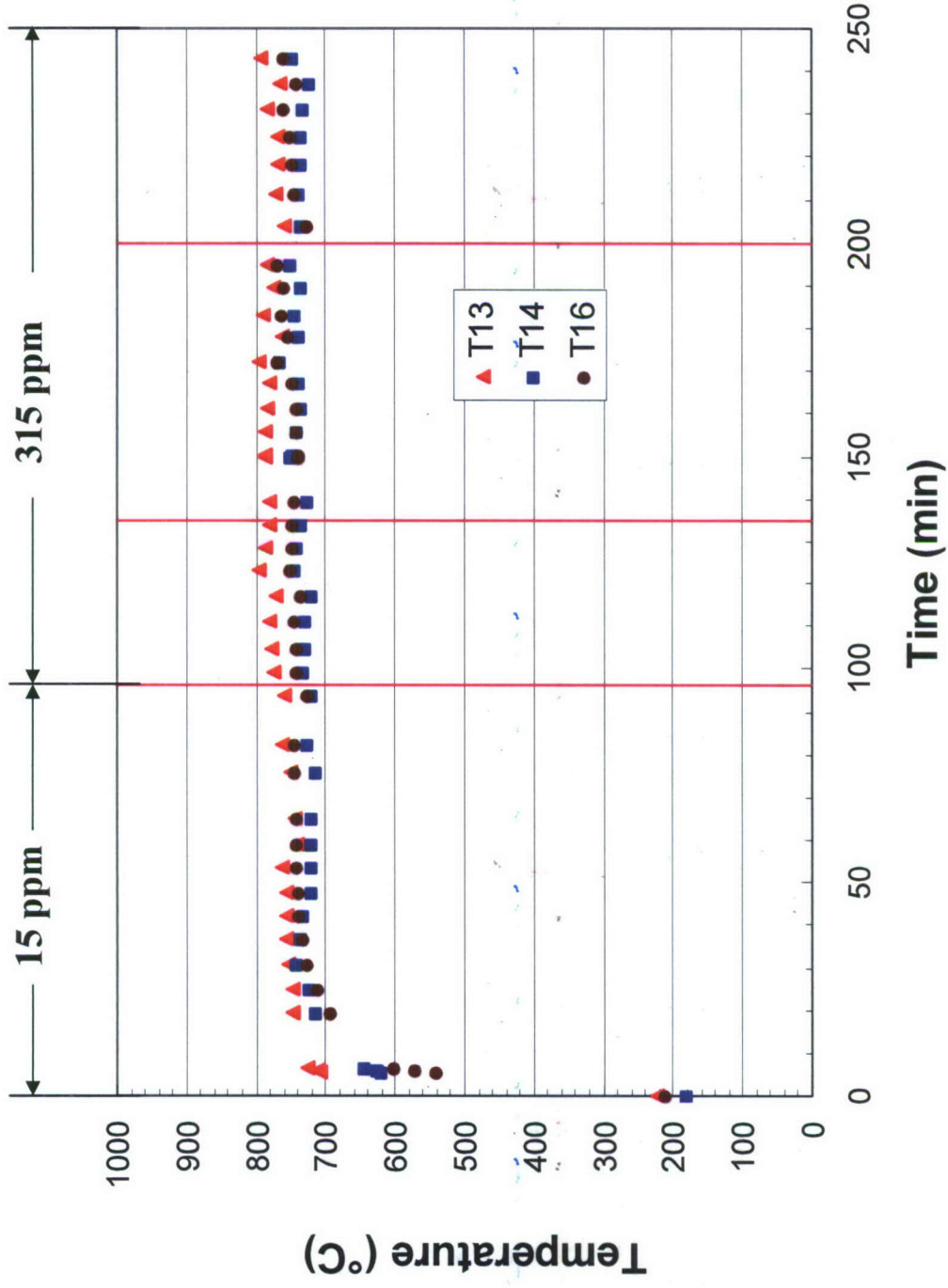


Fig. 7

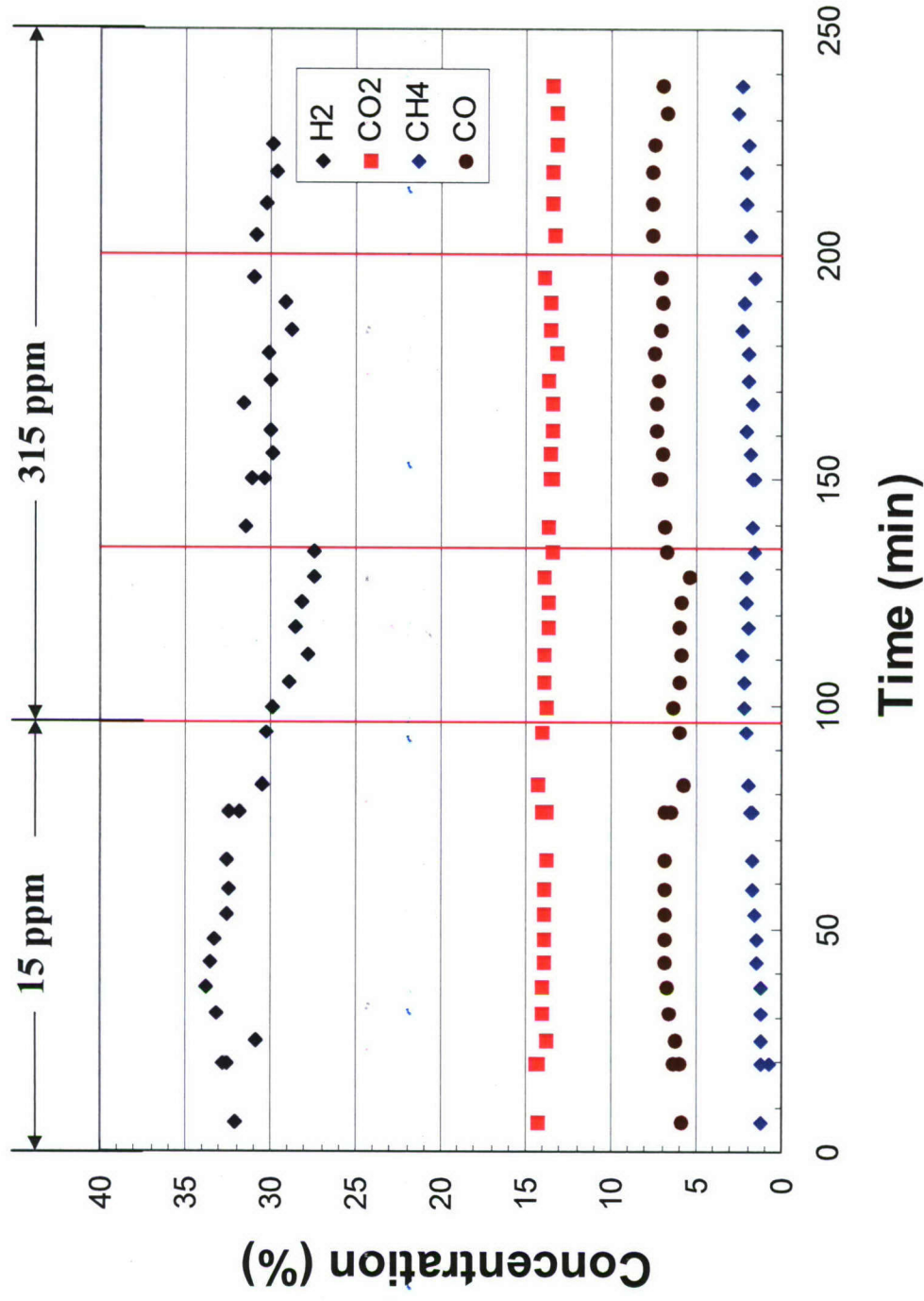


Fig. 8

Fig. 9

ESSO diesel plasma ATK mass balance 2007-03-15 Sampling NO.41

Reactants in		Formula	C	H	MW
Diesel	C ₁₆ H ₃₄	16	34	226	

Product out		H ₂	O ₂	N ₂	CO ₂	CH ₄	CO
		30.3	0	46.8	13.4	2	7.5

Reactants in		g/min	L/min	moles/min
Diesel		11		0.049
C				0.779
H ₂				0.827
Air			45	2.009
O ₂			9.45	0.422
N ₂			35.55	1.587
H ₂ O		40		2.222
H ₂				2.222
O ₂				1.111

O ₂ /C	0.542		
S/C	2.854		
(O ₂ +S)/C	3.395		

		L/min	moles/min	Carbon moles/min
Total Out		72		
CO ₂		9.648	0.431	
C				0.431
O ₂			0.431	
CO		5.4	0.241	
C				0.241
O ₂			0.121	
CH ₄		1.44		
C				0.064
H ₂			0.129	
H ₂		21.816		
O ₂		0		
N ₂		33.696	1.504	
Total		72		0.736
Carbon conversion (%)				94.518

The product dry gas is measured at 25°C, 1 atm condition

S ---- steam

ADDENDUM A - Final Report AH2T

Confidential Information

Fuel: Diesel with 315 ppm S

March 20, 2007

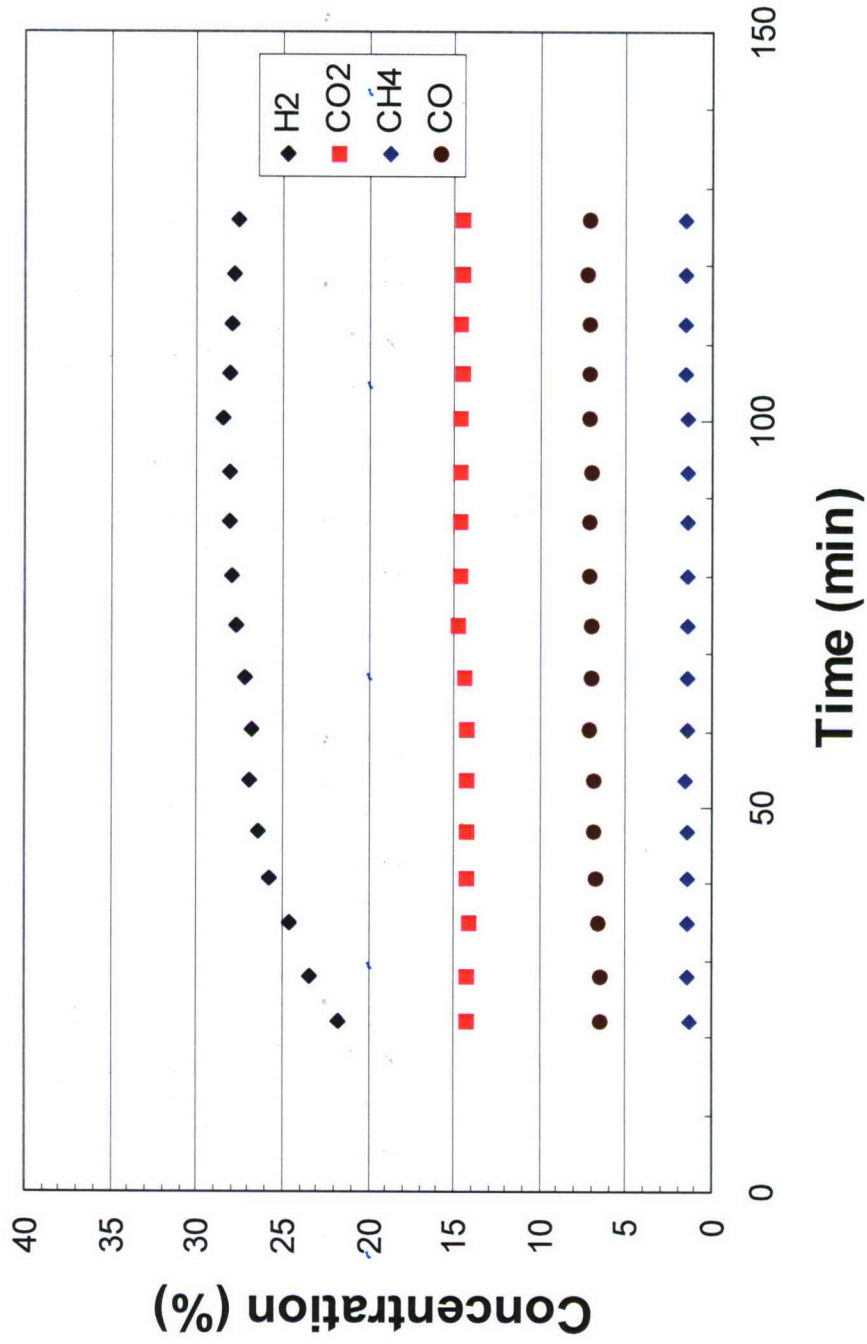


Fig 10

Fuel: Diesel with 315 ppm S

March 20, 2007

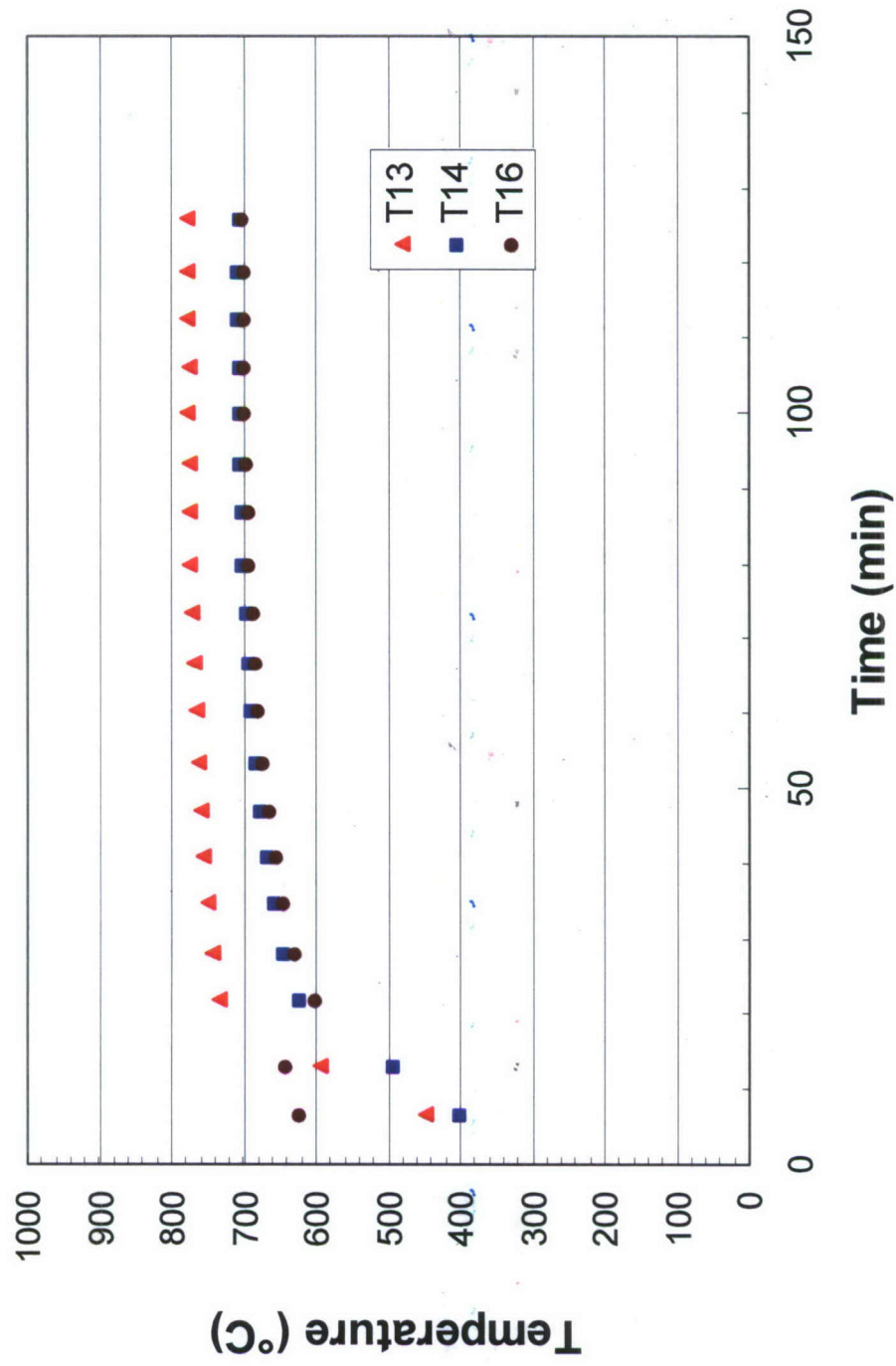


Fig. 11

Fig. 12

ESSO diesel plasma ATR mass balance 2007-03-20 Sampling NO.28

Reactants in		Formula	C	H	MW
Diesel	C ₁₆ H ₃₄	16	34	226	

Product out		H ₂	O ₂	N ₂	CO ₂	CH ₄	CO
		28.1	0	48.9	14.6	1.4	7

Reactants in		g/min	L/min	moles/min
Diesel		5.5		0.024
C				0.389
H ₂				0.414
Air			23	1.027
O ₂			9.45	0.216
N ₂			35.55	0.811
H ₂ O		20		1.111
H ₂				1.111
O ₂				0.556

		L/min	moles/min	Carbon moles/min
Total Out		37		
CO ₂		5.402	0.241	
C				0.241
O ₂			0.241	
CO		2.59	0.116	0.116
C			0.058	
O ₂				
CH ₄		0.518		
C				0.023
H ₂			0.046	
H ₂		10.397		
O ₂		0		
N ₂		18.093	0.808	
Total		37		0.380
Carbon conversion (%)				97.568

O ₂ /C	0.554		
S/C	2.854		
(O ₂ +S)/C	3.407		

The product dry gas is measured at 25°C , 1 atm condition
S ---- steam

Fuel: Diesel with 315 ppm S

March 21, 2007

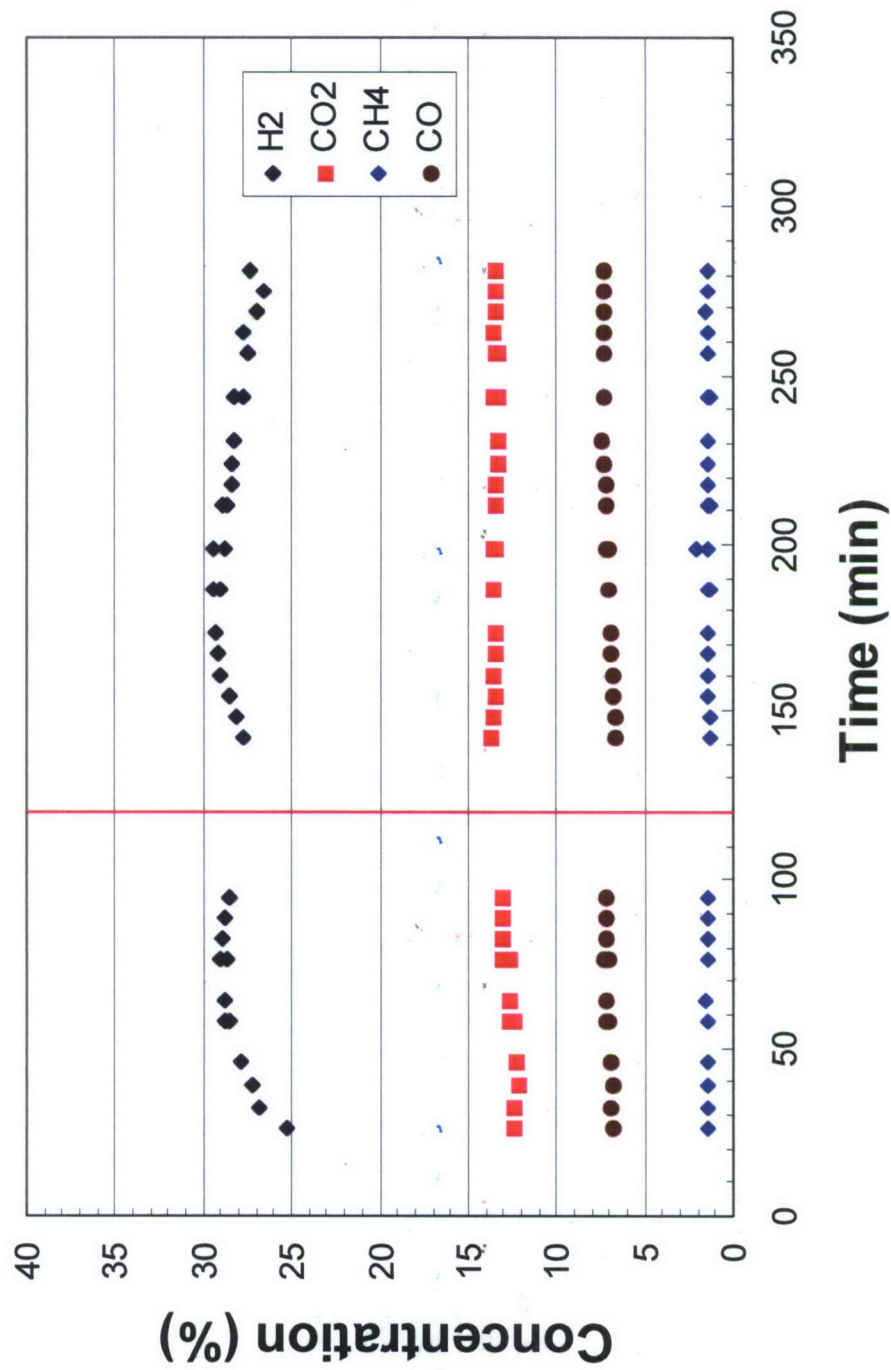


Fig. 13

Fuel: Diesel with 315 ppm S

March 21, 2007

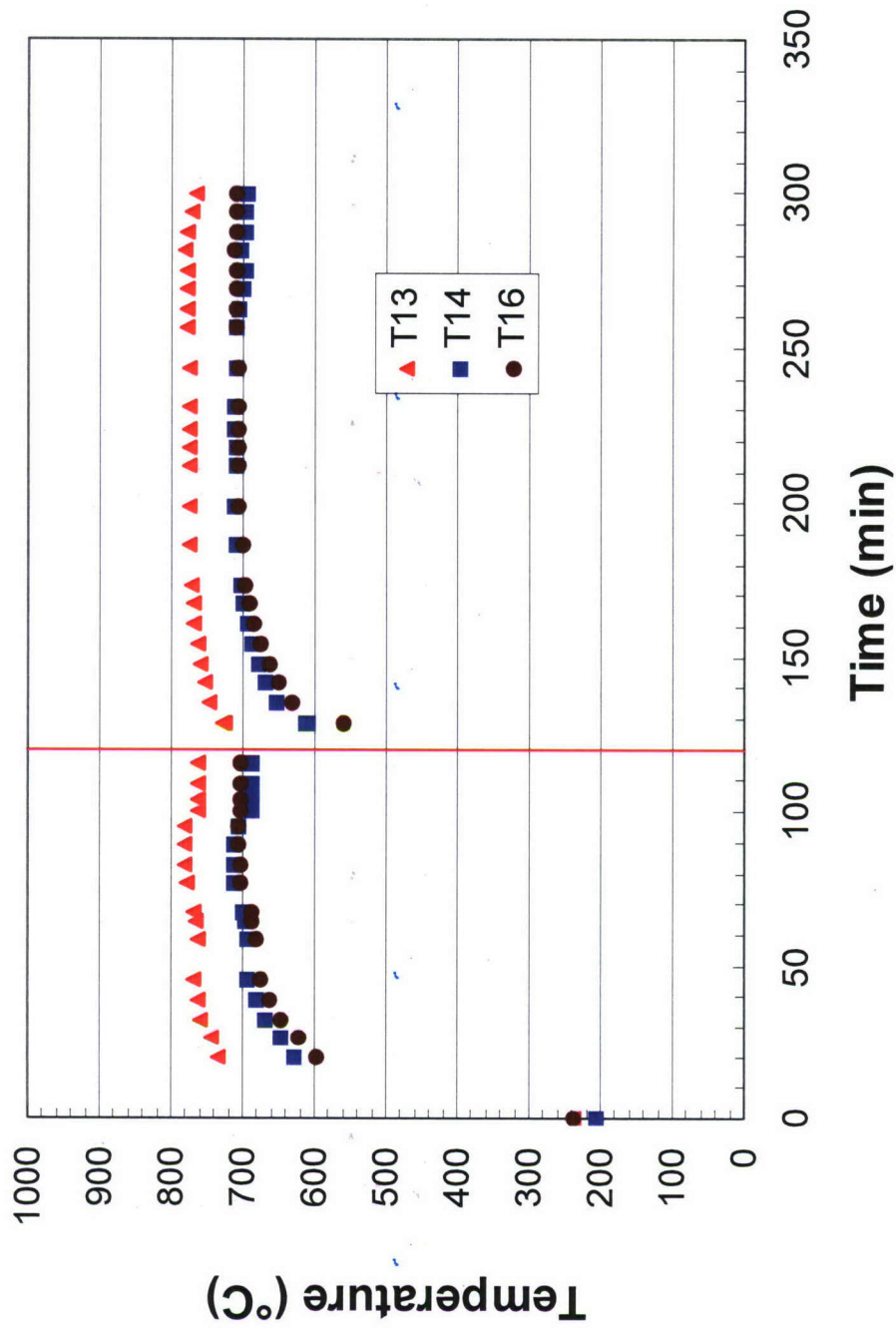


Fig. 14

Fig. 15

ESSO diesel plasma ATR mass balance 2007-03-21 Sampling NO.28

Reactants in		Formula	C	H	MW
Diesel	C ₁₆ H ₃₄	16	34	226	

Product out		H ₂	O ₂	N ₂	CO ₂	CH ₄	CO
		29.2	0	49.1	13.5	1.4	6.9

Reactants in		g/min	L/min	moles/min
Diesel		5.5		0.024
C				0.389
H ₂				0.414
Air			24	1.071
O ₂			9.45	0.225
N ₂			35.55	0.846
H ₂ O		20		1.111
H ₂				1.111
O ₂				0.556

		L/min	moles/min	Carbon moles/min
Total Out		39		
CO ₂		5.265	0.235	
C				0.235
O ₂			0.235	
CO		2.691	0.120	
C				0.120
O ₂			0.060	
CH ₄				
C		0.546		0.024
H ₂			0.049	
H ₂		11.388		
O ₂		0		
N ₂		19.149	0.855	
Total		39.039		0.380
Carbon conversion (%)				97.476

O ₂ /C	0.578		
S/C	2.854		
(O ₂ +S)/C	3.431		

The product dry gas is measured at 25°C, 1 atm condition
S ---- steam

ADDENDUM A - Final Report AH2T

Confidential Information

Selective Membrane Purification of Hydrogen for Fuel Cells

Jin Huang, Jian Zou and W.S. Winston Ho
Department of Chemical and Biomolecular Engineering
Department of Materials Science and Engineering
The Ohio State University
2041 College Road
Columbus, OH 43210-1178

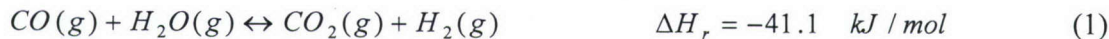
Phone: (614) 292-9970; Fax: (614) 292-3769; E-mail: ho@chbmeng.ohio-state.edu

Abstract

This report summarizes the status and results on selective membranes for hydrogen purification for proton-exchange membrane (PEM) fuel cells. We have synthesized novel CO₂-selective membranes with high CO₂ permeability and high CO₂/H₂ and CO₂/CO selectivities by incorporating amino groups in polymer networks. We have also developed a one-dimensional non-isothermal model for the countercurrent water-gas-shift (WGS) membrane reactor. The modeling results have shown that H₂ enhancement via CO₂ removal and CO reduction to 10 ppm or lower are achievable for synthesis gas from autothermal reforming. With this model, we have elucidated the effects of system parameters, including CO₂/H₂ selectivity, CO₂ permeability, sweep/feed flow rate ratio, feed temperature, sweep temperature, feed pressure, catalyst activity, and feed CO concentration, on the membrane reactor performance. Based on the modeling study using the membrane data obtained, we showed the feasibility of achieving H₂ enhancement via CO₂ removal, CO reduction to ≤ 10 ppm, and high H₂ recovery. Using the membrane synthesized, we have obtained < 10 ppm CO in the H₂ product in WGS membrane reactor experiments. From the experiments, we have verified the model developed. In addition, the membranes have also shown high H₂S permeability and selectivity vs. H₂. Our initial experiments demonstrated < 10 ppb H₂S in the H₂ product using the membrane synthesized.

Introduction

A water gas shift (WGS) reactor for the conversion of carbon monoxide (CO) and water to hydrogen (H₂) and carbon dioxide (CO₂) is widely used in chemical and petroleum industries. The reactor is also critically needed for the conversion of fuels, including gasoline, diesel, methanol, ethanol, natural gas, biomass, and coal, to H₂ for fuel cells. Since the WGS reaction is reversible, it is not efficient, resulting in a high concentration of unconverted CO ($\sim 1\%$) in the H₂ product and a bulky, heavy reactor. The reversible, exothermic WGS reaction is as follows:



where ΔH_r is the heat of reaction. This reaction can be enhanced significantly through a CO₂-selective or H₂-selective membrane, which removes one of the reaction products, CO₂ or H₂, respectively, to beat the reaction equilibrium and shift the reaction towards the product side.

Using a CO₂-selective membrane [1-7] with the continuous removal of CO₂, a CO₂-selective WGS membrane reactor is a promising approach to enhance CO conversion and increase the purity of H₂ under relatively low temperatures (~150°C). In comparison with the H₂-selective membrane reactor, the CO₂-selective WGS membrane reactor is more advantageous because (1) a high-purity H₂ product is recovered at the high pressure (feed gas pressure) and (2) air or an inert gas can be used as the sweep gas to remove the permeate, CO₂, on the low-pressure side of the membrane to have a high driving force for the separation. These advantages are especially important for fuel cell vehicles. The first advantage eliminates the need for an unwanted compressor. With the second advantage, the high driving force created by the sweep gas can result in low CO concentration and high H₂ purity and recovery. Several studies have been done on H₂-selective membrane reactors, mainly based on palladium membranes and using high-temperature WGS catalysts [8-13].

We have synthesized novel CO₂-selective polymer membranes containing amino groups with high CO₂ permeability and high CO₂/H₂ and CO₂/CO selectivities [6, 7, 14-16]. We have also developed a mathematical model [3, 14, 15] to predict the performance of the WGS membrane reactor and to guide and minimize experimental efforts on the reactor. With the modeling and experimental efforts, we have obtained < 10 ppm CO in the H₂ product from the WGS membrane reactor using CO₂-selective membrane we have synthesized. In addition, the membranes have also shown high H₂S permeability and selectivity vs. H₂. Our initial experiments showed < 10 ppb H₂S in the H₂ product using the membrane synthesized.

Approach

We have synthesized novel CO₂-selective membranes with high CO₂ permeability and high CO₂/H₂ and CO₂/CO selectivities by incorporating amino groups in polymer networks [6, 7, 14-16]. We incorporated the membrane synthesized in the WGS membrane reactors to show CO reduction to 10 ppm or lower in the H₂ product in reactor experiments using the synthesis gas feed with 1% CO. We have developed a mathematical model [3, 14, 15] to predict the performance of the WGS membrane reactor and to guide and minimize experimental efforts on the reactor. In the model, the low-temperature WGS reaction kinetics for the commercial catalyst (Cu/ZnO/Al₂O₃) reported by Moe [17] and Keiski et al. [18] was used. We have verified the model for the prediction of the performance of the "Big Cell" WGS membrane reactor. As the membranes have also shown high H₂S permeability and selectivity vs. H₂, we also used the "Big Cell" without containing catalyst particles to demonstrate H₂S removal to 10 ppb.

Results and Discussion

We have synthesized novel CO₂-selective membranes by incorporating amino groups in polymer networks [6, 7, 14-16]. Figure 1 gives the CO₂ permeability and CO₂/H₂ selectivity results as a function of temperature from 100°C to 180°C for the feed gas pressure of 2.1 atm and the sweep gas (air or nitrogen) of atmospheric pressure. As shown in this figure, the CO₂ permeability was about 4000 Barrers (1 Barrer = 10⁻¹⁰ cm³ (STP)-cm/cm²-s-cmHg) or higher for the temperatures ranging from 100°C to 150°C. However, the permeability reduced to about 2000 Barrers as the temperature increased to 180°C. This was due to the reduction of water retention in the membrane as the temperature increased. Also shown in this figure, the CO₂/H₂ selectivity was

about 100 or higher for the temperatures ranging from 100°C to 150°C. However, the selectivity reduced slightly as the temperature increased to 170°C. This was a result of CO₂ permeability decrease due to the reduction of water retention in the membrane described above. At 180°C, the selectivity reduced significantly to slightly greater than 10 due to the significant swelling of this membrane at this high temperature. Nonetheless, the selectivity of 10 is still good enough to give a reasonably high H₂ recovery of about 90%, which will be described in the following modeling work.

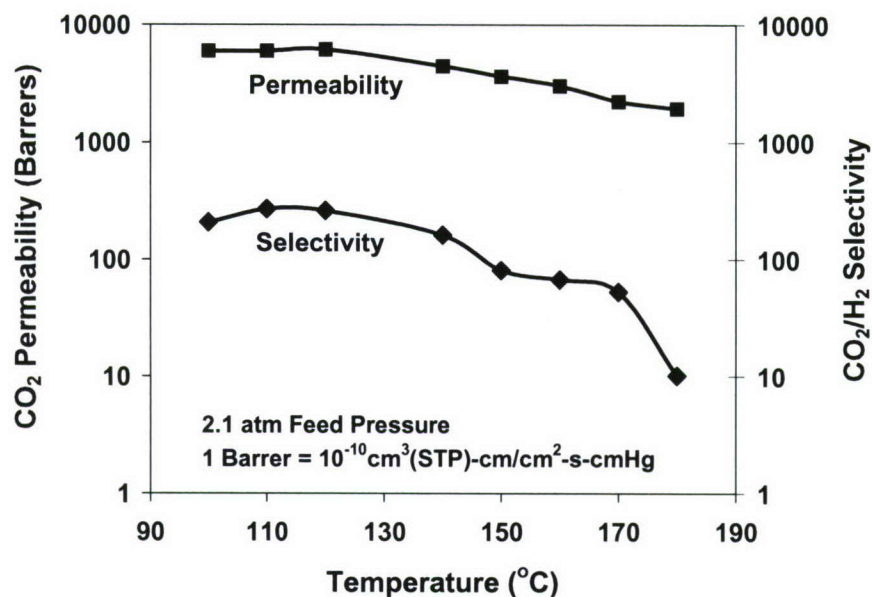


Figure 1. CO₂ permeability and CO₂/H₂ selectivity results as a function of temperature.

Figure 2 gives the CO₂ permeability results as a function of feed pressure from about 2 atm to about 4 atm at 150°C. As shown in this figure, the permeability did not change significantly with the feed pressures investigated.

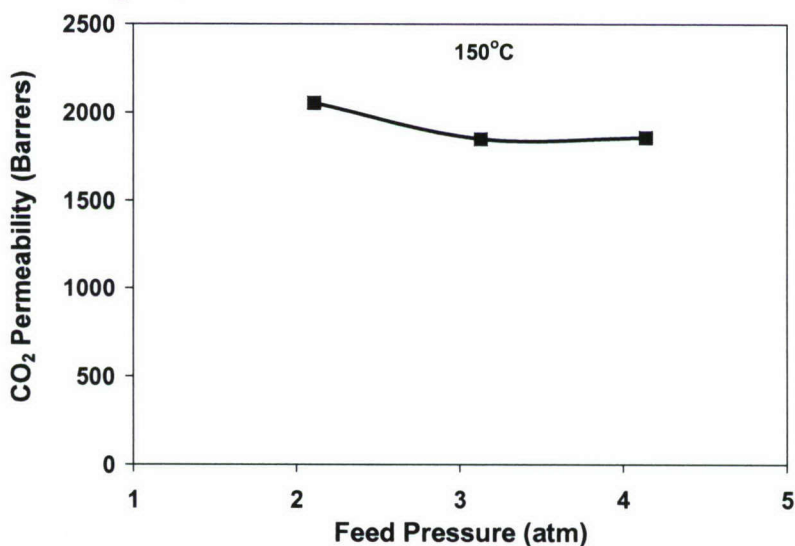


Figure 2. CO₂ permeability results as a function of feed pressure at 150°C.

Figure 3 depicts the CO_2/CO selectivity results as a function of temperature from 100°C to 170°C for the feed gas pressure of 2.1 atm. As depicted in this figure, the selectivity reduced as the temperature increased. This was a result of CO_2 permeability decrease due to the reduction of water retention in the membrane described above. However, the CO_2/CO selectivity results for this temperature range were greater than about 160, which is very good.

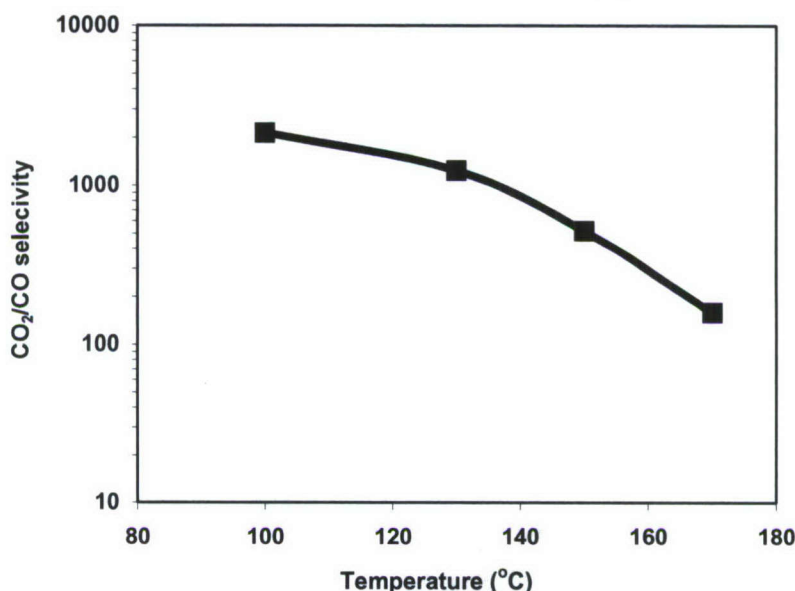


Figure 3. CO_2/CO selectivity results as a function of temperature.

Modeling of Membrane Reactor

Model Development

As one of the two main types of commercialized membrane modules, the hollow fiber membrane module has shown excellent mass transfer performance because of its large surface area per unit volume (about $3000 \text{ ft}^2/\text{ft}^3$ for gas separation) [19]. In this modeling work, the WGS membrane reactor was configured to be a hollow fiber membrane module with catalyst particles packed inside the fibers. The following assumptions were made in the model:

- (1) The hollow fiber module is composed of CO_2 -selective facilitated transport membrane;
- (2) CO_2 and H_2 are the only two gases permeating through the membrane;
- (3) Membrane permeability is fixed and does not change with temperature variation in the module;
- (4) There is no temperature variation in the radial direction inside a hollow fiber due to its small dimension;
- (5) The module is adiabatic and operating at a steady state;
- (6) There is no axial mixing;
- (7) The pressure drops on both lumen and shell sides are negligible.

As shown in Figure 1, the CO₂ permeability of the membrane was in the range of 1000 to 8000 Barrers (1 Barrer = 10⁻¹⁰ cm³ (STP)-cm/cm²-s-cm Hg), and the CO₂/H₂ selectivity, expressed in Eq. (2) [19], was in the range of 10 to 80.

$$\alpha = \frac{y_{CO_2}/y_{H_2}}{x_{CO_2}/x_{H_2}} \quad (2)$$

The catalyst packed was assumed to be the commercial Cu/ZnO catalyst for lower-temperature WGS reaction. A number of studies on the reaction kinetics of the commercial WGS catalyst, CuO/ZnO/Al₂O₃, have been published [17, 18, 20-23]. Above 200°C, Campbell's [20] rate equation is pore-diffusion limited, not chemical-reaction limited. Campbell stated that his reaction rate fitted poorly with experimental data obtained for temperatures less than 200°C. Fiolitakis et al. [21] gave an activation energy of 46 kJ/mol but did not give a reaction rate constant. Salmi and Hakkarainen [22] only had data for temperatures greater than 200°C. Based on the experimental data of the commercial catalyst (ICI 52-1), Keiski et al. [18] gave two reaction rates for the low-temperature WGS reaction over a range of 160 – 250°C. The first was dependent only on CO concentration and gave an activation energy of 46.2 kJ/mol. The second reaction rate was dependent on CO and steam concentrations with a lower activation energy of 42.6 kJ/mol. Because of the proximity of our operation conditions to theirs and the fact that steam is in excess in most of the membrane reactors, Keiski et al.'s first reaction rate expression was chosen for this work. The reaction rate is given by Eq. (3).

$$r_i = 1.0 \times 10^{-3} \frac{\rho_b P_f}{n_i R T_f} \exp\left(13.39 - \frac{5557}{T_f}\right) n_{CO} \left(1 - \frac{n_{f,H_2} n_{f,CO_2}}{K_T n_{f,CO} n_{f,H_2O}}\right) \quad (3)$$

where the expression for K_T [17, 18] is as follows:

$$K_T = \exp\left(-4.33 + \frac{4577.8}{T_f}\right) \quad (4)$$

The temperatures of both feed (lumen) and sweep (shell) sides are affected by the heat of the reaction and the heat transfer through the membrane. The overall heat transfer coefficient U_i was derived via the series resistance method to include both convective and conductive heat transfer.

$$U_i = \frac{1}{\frac{1}{h_f} + \frac{d_{in}}{2k_m} \ln\left(\frac{d_{in} + 2\ell}{d_{in}}\right) + \frac{d_{in}}{2[(1-\varepsilon)k_m + \varepsilon k_a]} \ln\left(\frac{d_{out}}{d_{in} + 2\ell}\right) + \frac{d_{in}}{d_{out}} \frac{1}{h_s}} \quad (5)$$

where h_f is the feed (lumen) side heat transfer coefficient, h_s is the sweep (shell) side heat transfer coefficient, ℓ is the effective thickness of the selective membrane layer (on the inside of the hollow fiber), k_m and k_a are the thermal conductivities of the membrane and the gas, respectively, ε is the porosity of the support layer of the hollow fiber, and d_{in} and d_{out} are the inside and outside diameters of the hollow fiber, respectively. In Eq. (5), the thermal conductivities of the selective membrane layer and the hollow-fiber support layer were assumed to be the same, i.e., k_m , which is true for an integrally skinned membrane [19].

The convective heat transfer for the feed (lumen) side can be considered to be that on the inside wall of a packed bed. Due to the small dimension of the lumen, we assumed that the inside heat transfer resistance was negligible and then there was no temperature difference in the radial direction inside the fiber. Many researchers have studied the shell side mass transfer of hollow fiber modules based on either empirical or fundamental work [24-28]. According to the analogy between heat and mass transfer, similar equations can be used for the calculation of heat transfer coefficients by changing Sh to Nu and Sc to Pr, respectively. Yang and Cussler's correlation equation [24] was chosen because the module configuration and operation parameters they used were similar to those in this work.

$$h_s = 1.25 \frac{k_a}{d_h^{0.07}} \left(\frac{Re}{L} \right)^{0.93} Pr^{0.33} \quad (6)$$

where d_h is the hydraulic diameter, L is the hollow fiber length, Re is the Reynolds number, and Pr is the Prandtl number. In addition, because mass transfer and heat transfer occurred simultaneously in the membrane reactor, the energy carried by permeating gases was also taken into account in the model.

Based on the schematic diagram of the WGS hollow-fiber membrane reactor illustrated in Figure 4, the molar and energy balances were performed on both feed (lumen) and sweep (shell) sides, respectively.

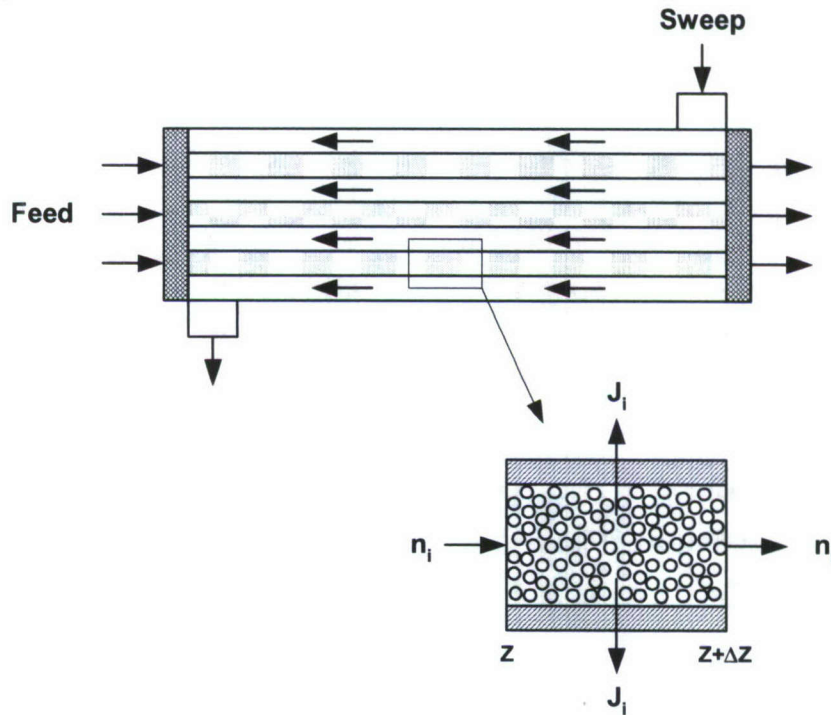


Figure 4. Schematic diagram of water-gas-shift hollow-fiber membrane reactor.

Molar Balance

Based on the volume element from z to $z + \Delta z$, the molar balance on the feed or lumen side for gas species i can be expressed as:

In - Out + Generation = Accumulation
or

$$n_{fi}|_z - n_{fi}|_{z+\Delta z} - \pi d \Delta z J_i + \frac{1}{4} \pi d^2 \Delta z r_i = 0 \quad (7)$$

where n_i , J_i and r_i are the molar flow rate, permeation flux and reaction rate of gas species i , respectively; and

$$J_i = P_i \frac{\Delta p_i}{\ell} \quad (8)$$

where P_i and Δp_i are the membrane permeability and transmembrane partial pressure difference of gas species i , respectively.

Dividing both sides of equation (7) by Δz and taking the limit as $\Delta z \rightarrow 0$ give:

$$\frac{dn_{fi}}{dz} = \frac{1}{4} \pi d_m^2 r_i - \pi d_{in} J_i \quad (9)$$

Similarly, the molar balance on the sweep or shell side is carried out, and the resulting equation is:

$$\frac{dn_{si}}{dz} = -\pi d_{in} J_i \quad (10)$$

In addition, the H_2 recovery is defined as the ratio of the exit H_2 molar flow rate to the combination of the inlet H_2 and CO molar flow rates. All these flow rates are on the feed, lumen side.

Energy balance

Considering the heat of the reaction, the heat transfer through the membrane, and the energy carried by permeating gases, we carried out the energy balance on the volume element of the membrane reactor from z to $z + \Delta z$. Differential equations were obtained by taking the limit as $\Delta z \rightarrow 0$. The differential equation for the feed or lumen side is:

$$\frac{d\sum(n_{fi} c_{pfi} T_f)}{dz} = \frac{1}{4} \pi d_m^2 r_i \Delta H_r T_f - \pi d_{in} (U_i + c_{pCO_2} J_{CO_2} + c_{pH_2} J_{H_2}) \Delta T \quad (11)$$

where ΔH_r is the heat of reaction, and c_p is the heat capacity of the individual gas species in the gas mixture.

The differential equation for the sweep or shell side is:

$$\frac{d\sum(n_{si} c_{psi} T_s)}{dz} = -\pi d_{in} (U_i + c_{pCO_2} J_{CO_2} + c_{pH_2} J_{H_2}) \Delta T \quad (12)$$

The boundary conditions of above differential equations are listed as follows:

At $z = 0$:

$$T_f = 140^\circ\text{C}, \quad n_{f,CO} = x_{CO} n_{t0}, \quad n_{f,H_2O} = x_{H_2O} n_{t0}, \\ n_{f,H_2} = x_{H_2} n_{t0}, \quad n_{f,CO_2} = x_{CO_2} n_{t0}$$

At $z = L$:

$$T_s = 140^\circ\text{C}, \quad n_{s,CO} = 0, \quad n_{s,H_2O} = 0, \\ n_{s,H_2} = 5 \times 10^{-7} n_{t0} \gamma, \quad n_{s,CO_2} = 370 \times 10^{-6} n_{t0} \gamma$$

where n_{t0} is the feed molar flow rate, x is the molar fraction of the individual gas species in the gas mixture, and γ is the inlet sweep-to-feed molar flow rate ratio or sweep-to-feed ratio in the following paragraphs.

Although pure hydrogen is a superior fuel-cell fuel, currently there are issues on its storage and distribution [29]. As a more practical way, hydrogen used in an automotive fuel cell is suggested to be produced by reforming reactions of the available fuels, such as methanol, natural gas, gasoline and diesel. Steam reforming (SR), partial oxidation (POX) and autothermal reforming (ATR) are three major reforming processes. In SR, steam reacts with hydrocarbon over a catalyst to form H_2 , CO and CO_2 at around $750 - 800^\circ\text{C}$ since this reaction is strongly endothermic. In POX, the hydrocarbon reacts with a deficient amount of oxygen or air to produce H_2 , CO and CO_2 while a large amount of heat is generated. ATR integrates these two processes together by feeding the hydrocarbon, water, and air together into the reactor at the same time. The SR reaction absorbs most of the heat generated by the POX reaction, and an overall process takes place slightly exothermally. Since the steam reforming reaction is strongly endothermic, a large and heavy reactor is needed to meet the heat exchange requirement. With smaller and lighter hardware, the autothermal reforming process is generally considered to be more attractive for on-board hydrogen generation for the automotive fuel cell system [30].

In this work, n_{t0} was 1 mol/s for autothermal reforming synthesis gas. With the composition of the synthesis gas given in Table 1, the flow rate was chosen because a sufficient H_2 molar flow rate would hence be provided to generate a power of 50 kW via the fuel cell for a five-passenger car [29]. Heated air was used as the sweep gas. The concentrations of hydrogen and carbon dioxide in the inlet air were set as 0.5 ppm and 370 ppm, respectively.

Table 1. The compositions of autothermal reforming synthesis gas.

	CO	H ₂ O	H ₂	CO ₂	N ₂	CH ₄
Autothermal reforming	1%	9.5%	41%	15%	33.5%	0%

The bvp4c solver in Matlab[®] was used to solve the above differential equations of the boundary value problem with the given boundary conditions. During the calculation, the hollow fiber number was adjusted to satisfy the constraint of feed exit CO concentration, i.e., <10 ppm.

Reference Case

A reference case for the autothermal reforming synthesis gas was chosen with the CO₂/H₂ selectivity of 40, the CO₂ permeability of 4000 Barrers (1 Barrer = 10⁻¹⁰ cm³ (STP)-cm/cm²-s-cm Hg), the inlet sweep-to-feed molar flow rate ratio of 1, the membrane thickness of 5 μm, 52,500 hollow fibers (a length of 61 cm, an inner diameter of 0.1 cm, and a porous support with a porosity of 50% and a thickness of 30 μm), both inlet feed and sweep temperatures of 140°C, and the feed and sweep pressures of 3 and 1 atm, respectively. With respect to this case, the effects of CO₂/H₂ selectivity, CO₂ permeability, sweep-to-feed ratio, inlet feed temperature, inlet sweep temperature, feed pressure, and catalyst activity on the reactor behavior were then investigated.

Figure 5 shows the profiles of the feed-side mole fractions of CO and CO₂ along the length of the countercurrent membrane reactor. The modeling results demonstrated that this membrane reactor could decrease CO concentration from 1% to 9.82 ppm along with the removal of almost all the CO₂.

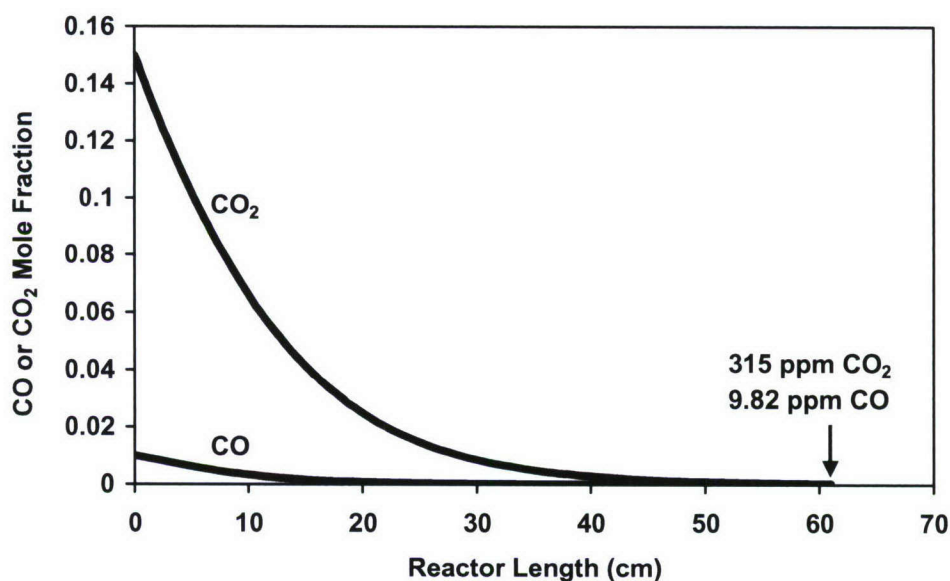


Figure 5. Feed-side CO and CO₂ mole fraction profiles along the length of membrane reactor for autothermal reforming syngas.

Figure 6 depicts the profiles of feed-side H_2 concentrations on the dry and wet bases. As depicted in this figure, the membrane reactor could enhance H_2 concentration from 45.30% to 54.95% (on the dry basis), i.e., from 41% to 49.32% (on the wet basis). In this case, the H_2 recovery calculated from the model was 97.38%. With the advancement of the high temperature proton-exchange-membrane fuel cell ($120 - 180^\circ\text{C}$), it is expected that the constraint of CO concentration can be relaxed to about 50 ppm in the near future. Then, the required hollow fiber number could be reduced significantly to 39,000 based on the modeling results.

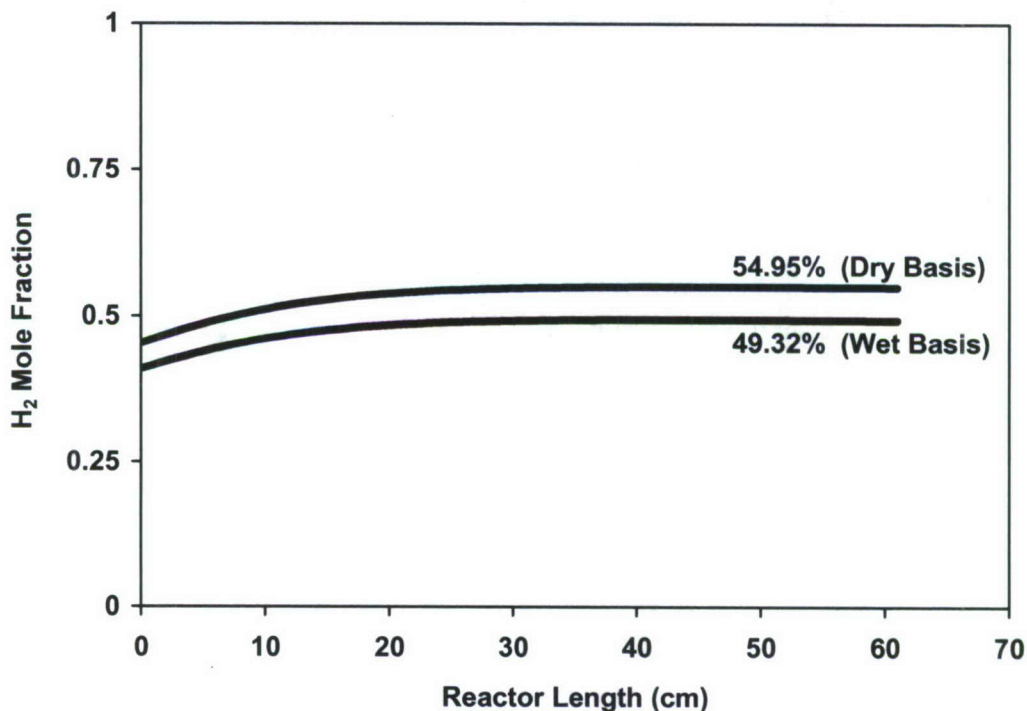


Figure 6. Feed-side H_2 mole fraction profiles along the length of membrane reactor for autothermal reforming syngas.

The temperature profiles for both feed and sweep sides are shown in Figure 7 with a maximum for each profile. Since the overall module was adiabatic, the feed gas was heated by the exothermic WGS reaction. The highest feed-side temperature was 158°C at about $z = 15$ cm. Beyond that, the feed-side temperature reduced, and it became very close to the sweep-side temperature at the end of membrane reactor. This was due to the efficient heat transfer provided by the hollow fiber configuration. Higher temperatures enhance WGS reaction rates but are unfavorable for CO conversion. Thus, it is important to use air with appropriate temperature, i.e., 140°C as the sweep gas to keep the feed gas within $150 \pm 10^\circ\text{C}$.

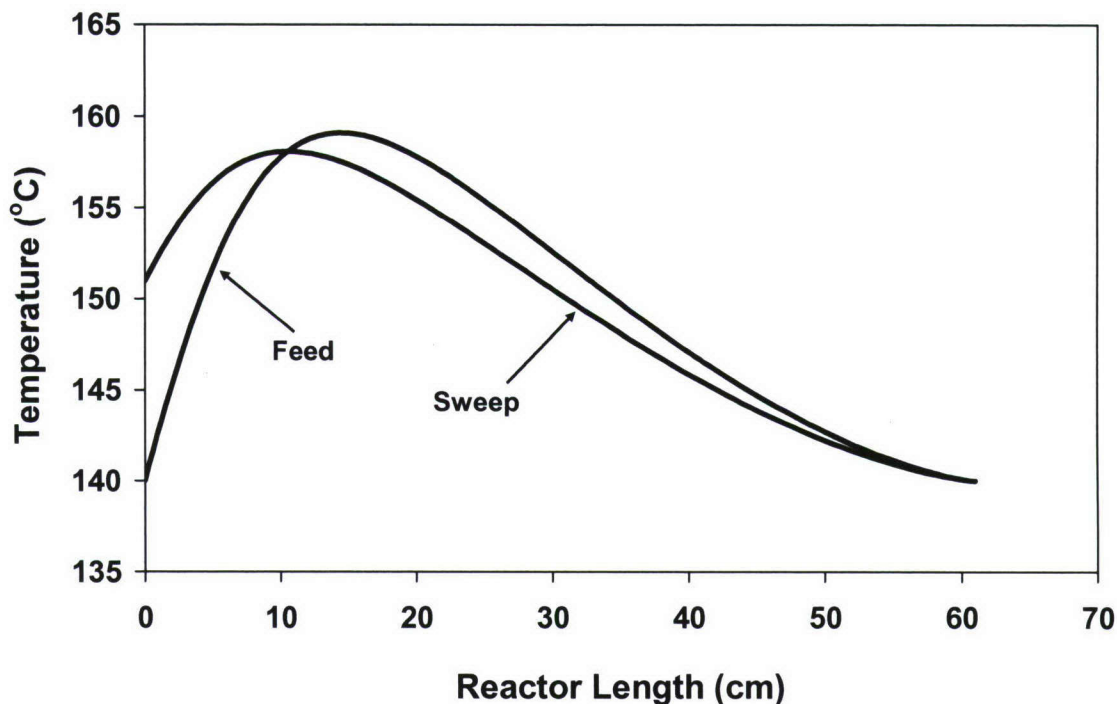


Figure 7. Feed-side and sweep-side temperature profiles along the length of membrane reactor for autothermal reforming syngas.

Effect of CO_2/H_2 Selectivity

In order to study the impact of CO_2/H_2 selectivity on the membrane reactor performance, $\alpha = 10, 20, 40, 60$ and 80 were applied in the model while the other parameters for the reference case were kept constant. As shown in Figure 8, the feed-side exit CO concentration increased slightly as the CO_2/H_2 selectivity increased. This was due to the fact that higher selectivity caused lower H_2 permeability and thus a lower H_2 permeation rate or higher H_2 concentration on the feed side, which was unfavorable for the WGS reaction rate. Also shown in this figure, the H_2 recovery increased from 89.85% to 98.68% as the CO_2/H_2 selectivity increased from 10 to 80. This indicated that the higher selectivity decreased the H_2 loss because of the reduction in H_2 permeation through the membrane. In addition, the modeling results showed that a CO_2/H_2 selectivity of 10 was the minimum value required for a H_2 recovery of about 90%.

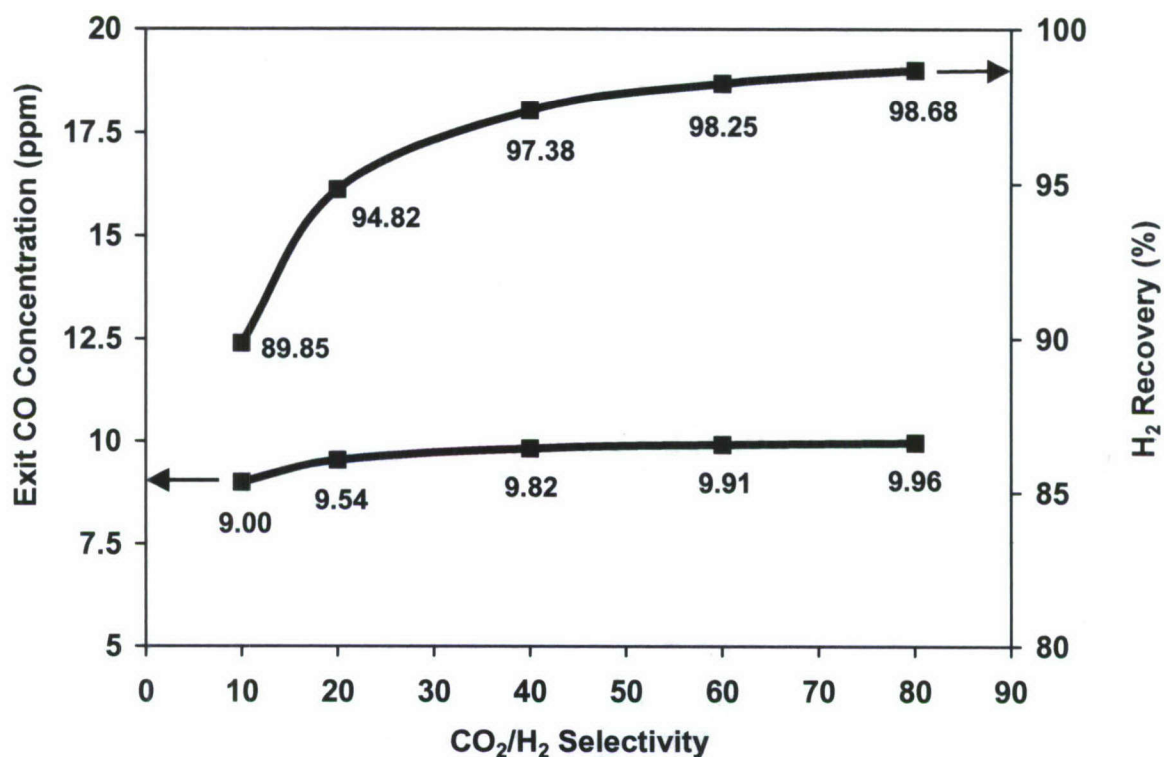


Figure 8. The effects of CO₂/H₂ selectivity on feed-side exit CO concentration and H₂ recovery for autothermal reforming syngas.

Effect of CO₂ Permeability

The membrane areas required for the exit feed CO concentration of <10 ppm in the H₂ product were calculated with five different CO₂ permeabilities ranging from 1000 to 8000 Barrers while the other parameters for the reference case were kept constant. As demonstrated in Figure 9, the required membrane area or hollow fiber number dropped rapidly as permeability increased from 1000 Barrers to 4000 Barrers. Beyond that, it approached an asymptotic value gradually. Increasing CO₂ permeability increased the CO₂ permeation rate and enhanced the CO₂ removal, which shifted the WGS reaction towards the product side. However, after the permeability exceeded about 6000 Barrers, the overall system became reaction controlled. Hence, the influence of the permeability became less significant.

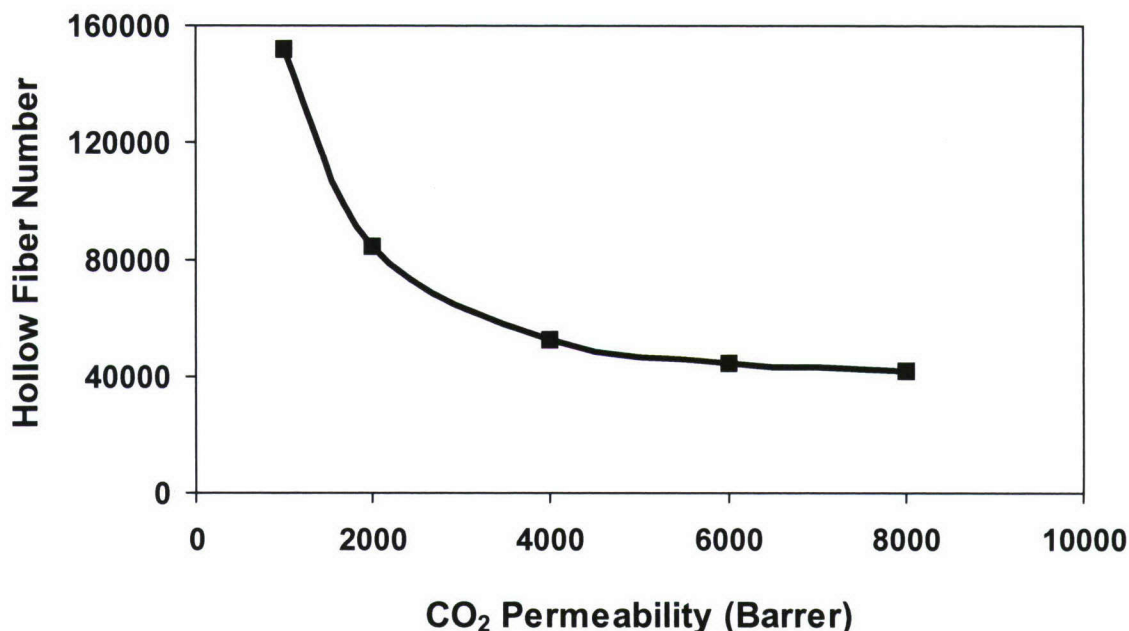


Figure 9. The effect of CO₂ permeability on required membrane area for autothermal reforming syngas.

Effect of Sweep-to-Feed Ratio

The inlet sweep-to-feed molar flow rate ratios of 0, 0.25, 0.5, 1, 1.5, 2 and 2.5 were used in the calculation while the other parameters for the reference case were kept constant. Figure 10 illustrates the effect of sweep-to-feed ratio on feed-side exit CO concentration. As illustrated in this figure, increasing the sweep-to-feed ratio decreased the exit CO concentration first and then increased it slightly. A higher sweep-to-feed ratio resulted in a lower CO₂ concentration on the sweep side and then a higher CO₂ permeation driving force. However, it also enhanced heat transfer and then decreased the feed-side temperature, which was unfavorable to the WGS reaction rate. Therefore, an optimal sweep-to-feed ratio of about 1 existed as a result of the tradeoff between the effects on the CO₂ permeation rate and the WGS reaction rate. Also illustrated in this figure is the effect of sweep-to-feed ratio on H₂ recovery. The sweep-to-feed ratio, particularly for $\gamma = 0.25$ or greater, did not have a significant effect on the H₂ recovery. This was due to the fact that the resulting CO concentrations were very low (< 240 ppm for $\gamma = 0.25$ or greater) and did not affect the H₂ recovery.

For the extreme case with zero sweep flow, the exit CO concentration increased drastically to 1168 ppm, and the H₂ recovery became 98.15%. Lowering a sweep-to-feed ratio (to 0.25 or lower) decreased the CO₂ removal and the H₂ permeation by reducing their driving forces. This

resulted in a lower CO conversion accompanied with a higher CO concentration in the H_2 product and a slightly higher H_2 recovery. The effect of sweep flow on membrane reactor performance was investigated experimentally and theoretically by some researchers [31-33]. Giessler et al. showed a similar trend and maximum CO conversion for their molecular sieve silica membrane reactor [31].

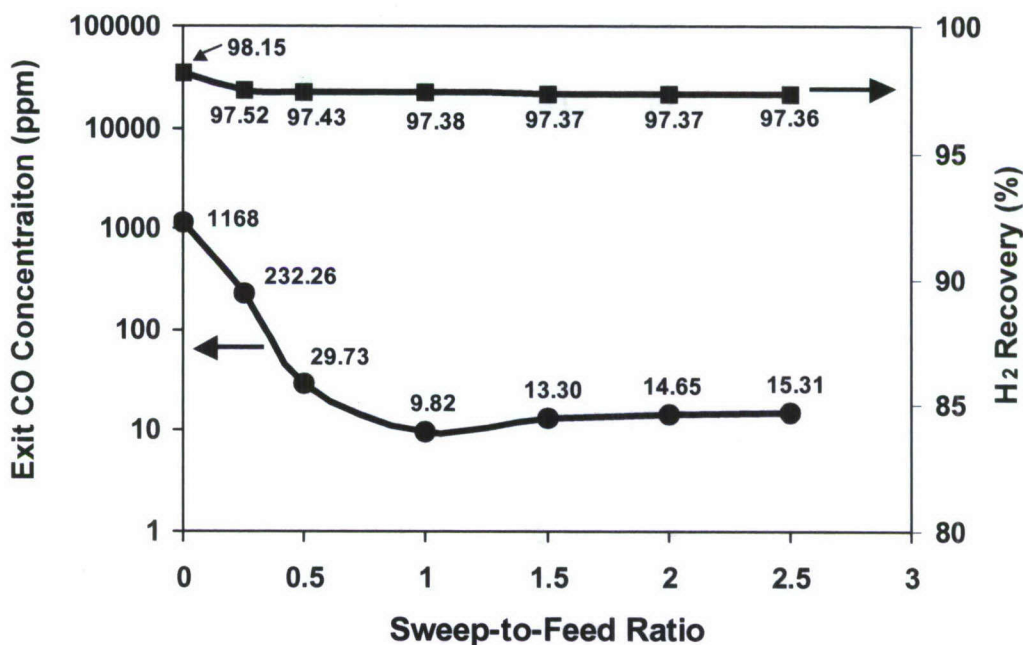


Figure 10. The effects of sweep-to-feed ratio on feed-side exit CO concentration and H_2 recovery for autothermal reforming syngas.

Effect of Inlet Feed Temperature

In order to study the impact of inlet feed temperature on the membrane reactor performance, $T_{f0} = 80, 100, 120, 140, 160, 180$ and 200°C were applied in the model while the other parameters for the reference case were kept constant. As shown in Figure 11, the required membrane area or hollow fiber number decreased as the inlet feed temperature increased. It approached an asymptotic value gradually. The feed side temperature profiles for different feed inlet temperatures are presented in Figure 12. The feed side temperature increased as the inlet feed temperature increased especially at the entrance section. The higher feed side temperature gave a higher WGS reaction rate, and thus a less reactor or catalyst volume, i.e., a lower membrane area, was required. The unfavorable WGS equilibrium at high temperatures was compensated by the simultaneous CO_2 removal.

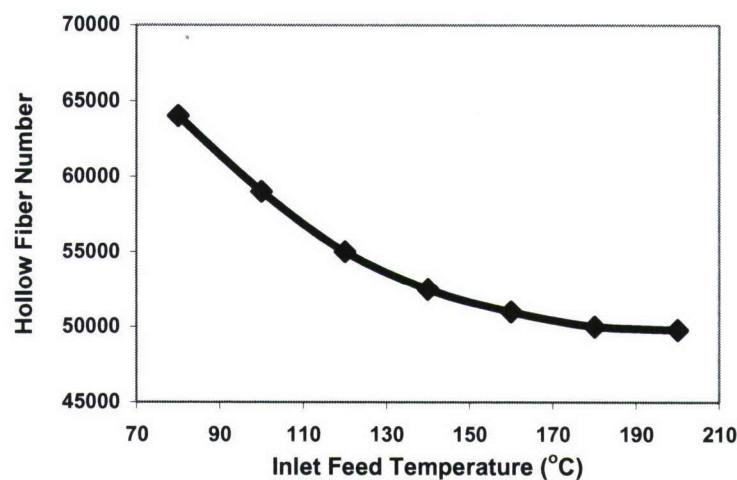


Figure 11. The effect of inlet feed temperature on required membrane area for autothermal reforming syngas.

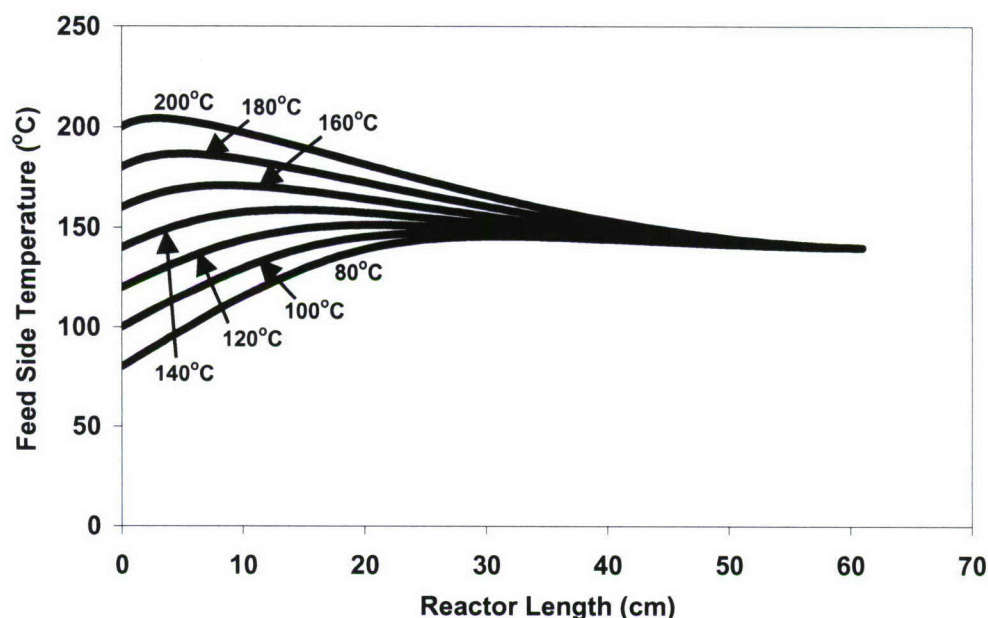


Figure 12. Feed-side temperature profiles along the length of membrane reactor for autothermal reforming syngas with different inlet feed temperatures.

Effect of Inlet Sweep Temperature

The membrane areas required for the exit feed CO concentration of <10 ppm in the H₂ product were calculated with seven different inlet sweep temperatures ranging from 80 to 200°C, while the other parameters for the reference case were kept constant. As demonstrated in Figure 13, the required membrane area or hollow fiber number dropped rapidly as the inlet sweep temperature increased from 80°C to 160°C. Beyond 160°C, it increased slightly. Figure 14

depicts the feed side temperature profiles along the membrane reactor with different inlet sweep temperatures. Increasing the inlet sweep temperature increased the feed side temperature significantly over a longer reactor length in comparison with increasing the inlet feed temperature as shown in Figure 12. A higher feed side temperature resulted in a higher WGS reaction rate and thus a lower membrane area as described earlier. When the inlet sweep temperature exceeded about 160°C, the WGS reaction equilibrium became less favorable, and the overall system became more mass transfer controlled. Hence, more membrane area was needed to remove the generated CO₂ to achieve < 10 ppm CO in the H₂ product.

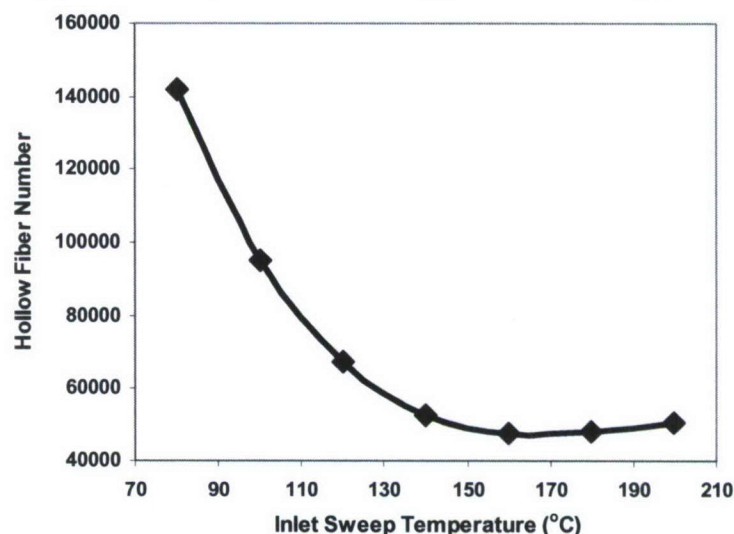


Figure 13. The effect of inlet sweep temperature on required membrane area for autothermal reforming syngas.

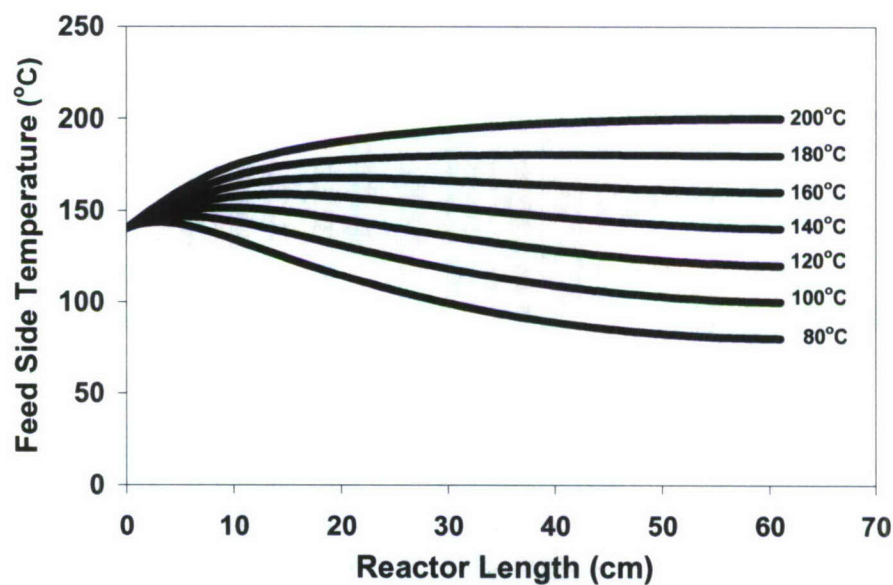


Figure 14. Feed-side temperature profiles along the length of membrane reactor for autothermal reforming syngas with different inlet sweep temperatures.

Effect of Feed Pressure

Six different feed pressures ranging from 1 to 6 atm were used in the calculation while other parameters for the reference case were kept constant. The effect of feed pressure on the required membrane area for the exit feed CO concentration of <10 ppm is depicted in Figure 15. As depicted in this figure, increasing feed pressure decreased the required membrane area significantly, particularly from 1 to 2 atm. Beyond that, the hollow fiber number continued gradually decreasing. Obviously, the increasing feed-side pressure brought a higher CO₂ permeation driving force, but the pressure of 1 atm would be too small to provide enough driving force. In addition, for a gas phase reaction, the WGS reaction rate is proportional to the feed-side pressure, p_f , which is evidenced by Equation (3). Therefore, higher feed-side pressure would not only increase the mass transfer driving force, but also enhance the reaction rate.

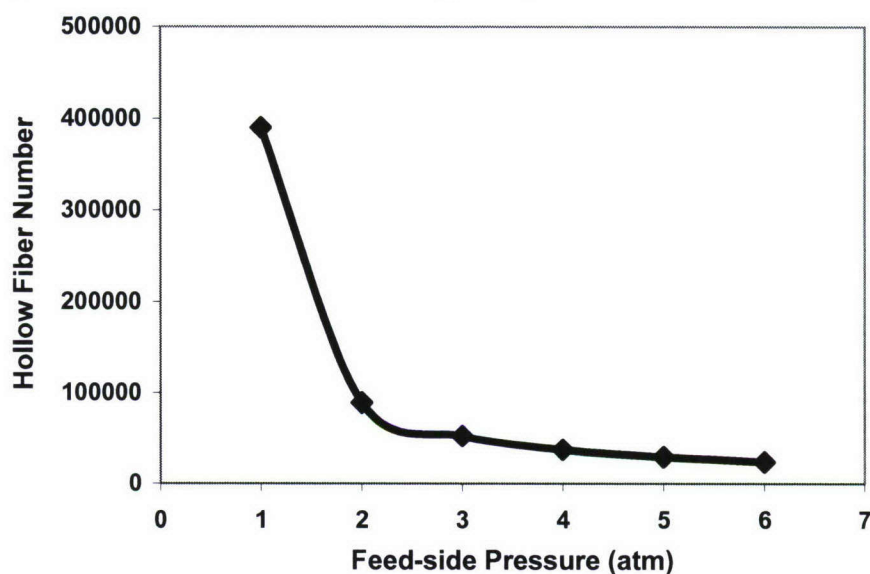


Figure 15. The effect of feed pressure on required membrane area for autothermal reforming syngas.

Effect of Catalyst Activity

The effect of catalyst activity on the required membrane area was studied by assuming several WGS reaction kinetics based on the Cu/ZnO kinetics equation proposed by Keiski et al. [18]. In Figure 16, the number on the horizontal x axis indicates the reaction kinetic rate in terms of the times of the Cu/ZnO kinetics, e.g., 1 represents the Cu/ZnO kinetics, 2 represents a kinetics of 2 times the Cu/ZnO kinetics, etc. As illustrated in this figure, increasing catalyst activity reduced the required membrane area significantly. The higher catalyst activity resulted in a higher reaction rate, which also increased the CO₂ permeation rate because of a higher CO₂ partial pressure on the feed side and thus a higher driving force across the membrane. Hence, with the advancement of a more active WGS catalyst, the membrane reactor would become more compact.

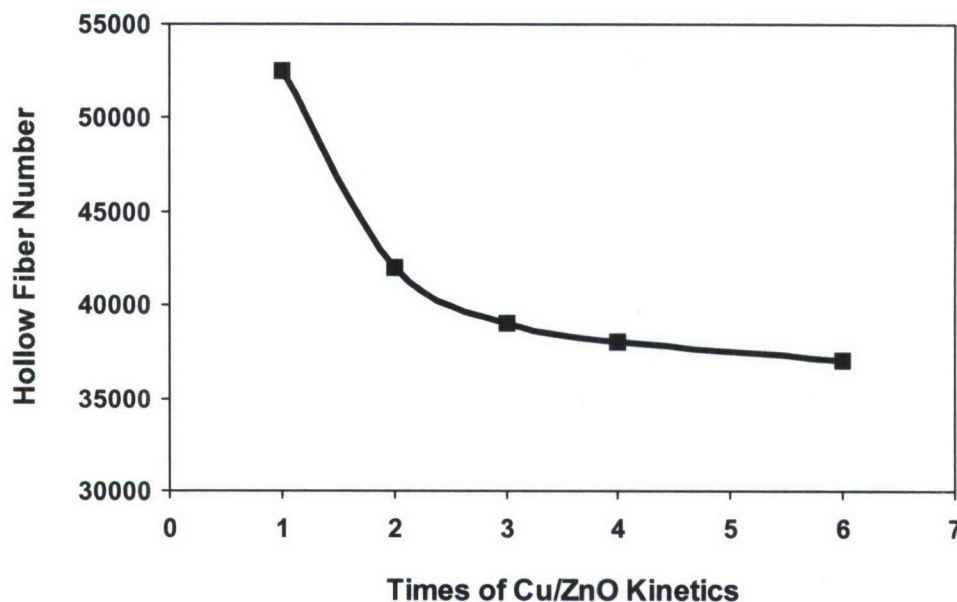


Figure 16. The effect of catalyst activity on required membrane area for autothermal reforming syngas.

Modeling of Membrane Reactor Using Membrane Data Obtained

We used the selectivity and flux data obtained as the input to the mathematical model developed [3, 14, 15] to show the feasibility of achieving H_2 enhancement, CO reduction to ≤ 10 ppm, and high H_2 recovery, to study the effects of system parameters on the reactor, and to guide / minimize experimental work. The CO_2/H_2 selectivity of 40 and the CO_2 permeability of 4000 Barrers were used again in the modeling work. We have investigated the performance of the countercurrent membrane reactor for the synthesis gases from the autothermal reforming of gasoline with air. The three synthesis gases investigated at 3 atm contained CO at concentrations of 10%, 5%, and 1%. Figure 17 illustrates the profiles of the CO concentration in the H_2 product for a total reactor length of 61 cm for these three feed CO concentrations. As shown in this figure, a H_2 product with less than 10 ppm CO was obtained from each of these synthesis gases. In the membrane reactor for each of these synthesis gases, the syngas flow with an inlet temperature of $140^\circ C$ was countercurrent to the flow of hot air sweep with an inlet temperature of $140^\circ C$, the molar flow rate ratio of the air sweep to the syngas (γ) was 1, and the catalyst was the commercial Cu/ZnO supported on alumina.

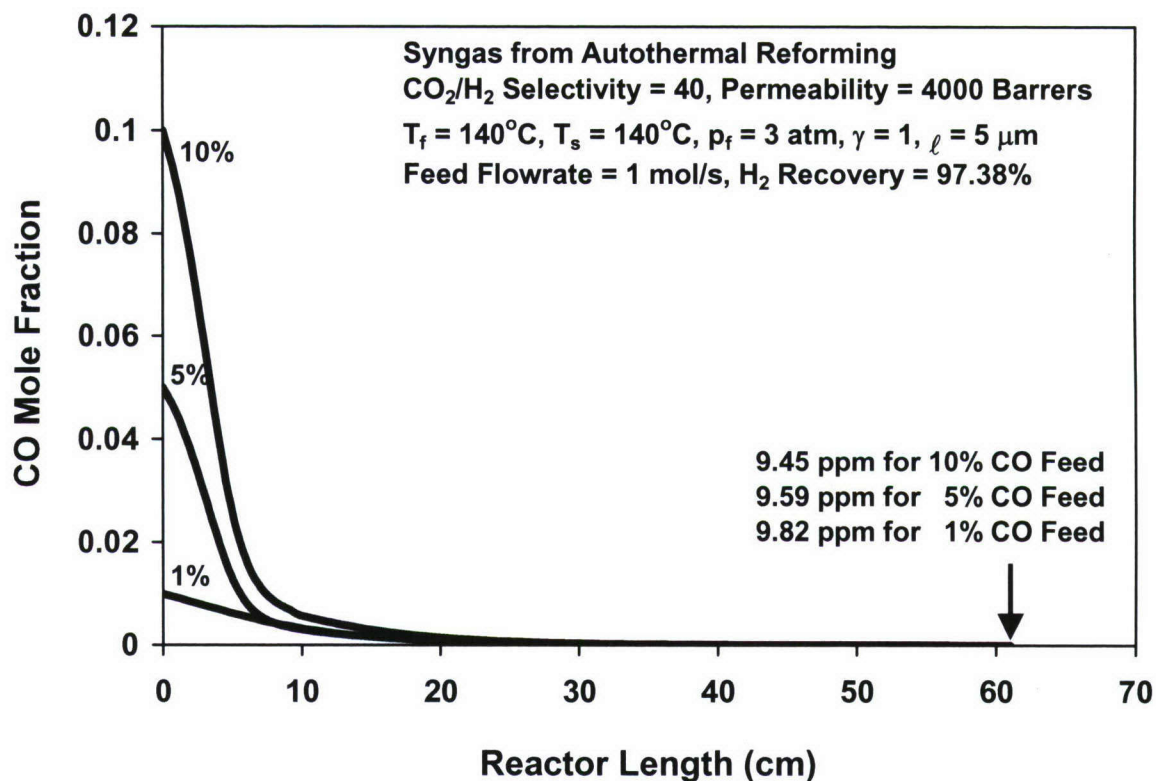


Figure 17. Feed-side CO mole fraction profiles along the length of membrane reactor for autothermal reforming syngases with 10%, 5%, and 1% CO.

For each of these synthesis gases, significant H_2 enhancement was achieved via CO_2 removal. For example, the H_2 concentration was increased from 41% in the inlet 1% CO feed gas to 49.3% in the outlet H_2 product on the wet basis including water (from 45.3% to 55.0% on the dry basis). Similar significant H_2 enhancement was also achieved for the 5% and 10% CO feed gases. In addition, a high H_2 recovery of greater than 97.3% was obtained for these synthesis gases as indicated in Figure 17.

We also investigated the effects of CO_2/H_2 selectivity on exit CO concentration and H_2 recovery for these synthesis gases through the modeling. For the CO_2/H_2 selectivity ranging from 10 to 80, the exit CO concentration of less than 10 ppm was achievable. A lower selectivity actually resulted in a slightly lower exit CO concentration as a lower selectivity (higher H_2 loss) enhanced the WGS reaction. However, the selectivity had a significant effect on H_2 recovery as shown earlier in Figure 8 for the 1% CO feed gas. A selectivity of 10 gave a H_2 recovery of about 90%, which is still quite good. As the selectivity increased, the H_2 recovery increased significantly. At the selectivity of 40, the H_2 recovery was greater than 97.3% as mentioned earlier. For the selectivity of 60 or greater, the H_2 recovery was greater than 98.2%.

"Big Cell" Membrane Reactor Experiments

We constructed and set up a "Big Cell" membrane reactor for studying the scale-up of WGS membrane reactor. The "Big Cell" membrane reactor was a rectangular cell with a well-defined gas flow and velocity both for the feed and sweep sides. Thus, this membrane reactor is suitable for modeling and scale-up work. That is, the data from this membrane reactor can be used for comparison with modeling results and for scale-up. Figure 18 shows the schematic of this membrane reactor.

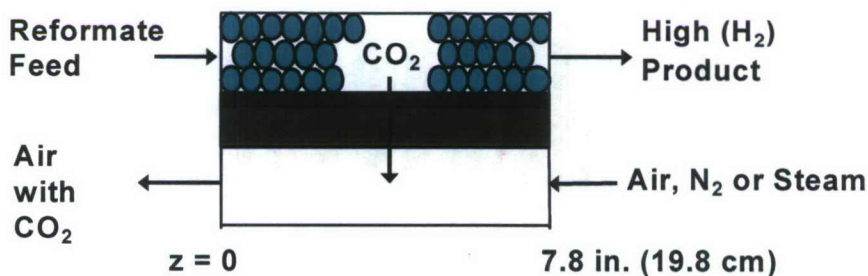


Figure 18. The schematic of the rectangular "Big Cell" water-gas-shift membrane reactor.

In the membrane reactor experiments using the "Big Cell", the synthesis gas feed containing 1% CO, 17% CO₂, 45% H₂, 37% N₂ (on the dry basis) entered into the membrane reactor after the catalyst activation. The operating temperature was 150°C, and the feed pressure of the synthesis gas was 2 atm. Figure 19 shows the results obtained from this "Big Cell" WGS membrane reactor. As shown in this figure, the CO concentration in the exit stream, i.e., the H₂ product, was <10 ppm (on the dry basis) for the various feed flow rates of the syngas from 20 to 70 cc/min. The data agreed reasonably with the prediction by the non-isothermal mathematical model that we have developed [3, 14, 15] based on the material and energy balances, membrane permeation, and the low-temperature WGS reaction kinetics for the commercial catalyst (Cu/ZnO/Al₂O₃) reported by Moe [17] and Keiski et al. [18] as described earlier.

As indicated from Figure 15, if the feed pressure of the synthesis gas was higher than 2 atm, a higher feed gas rate could be processed to obtain <10 ppm CO in the H₂ product for the given membrane area of the "Big Cell" reactor.

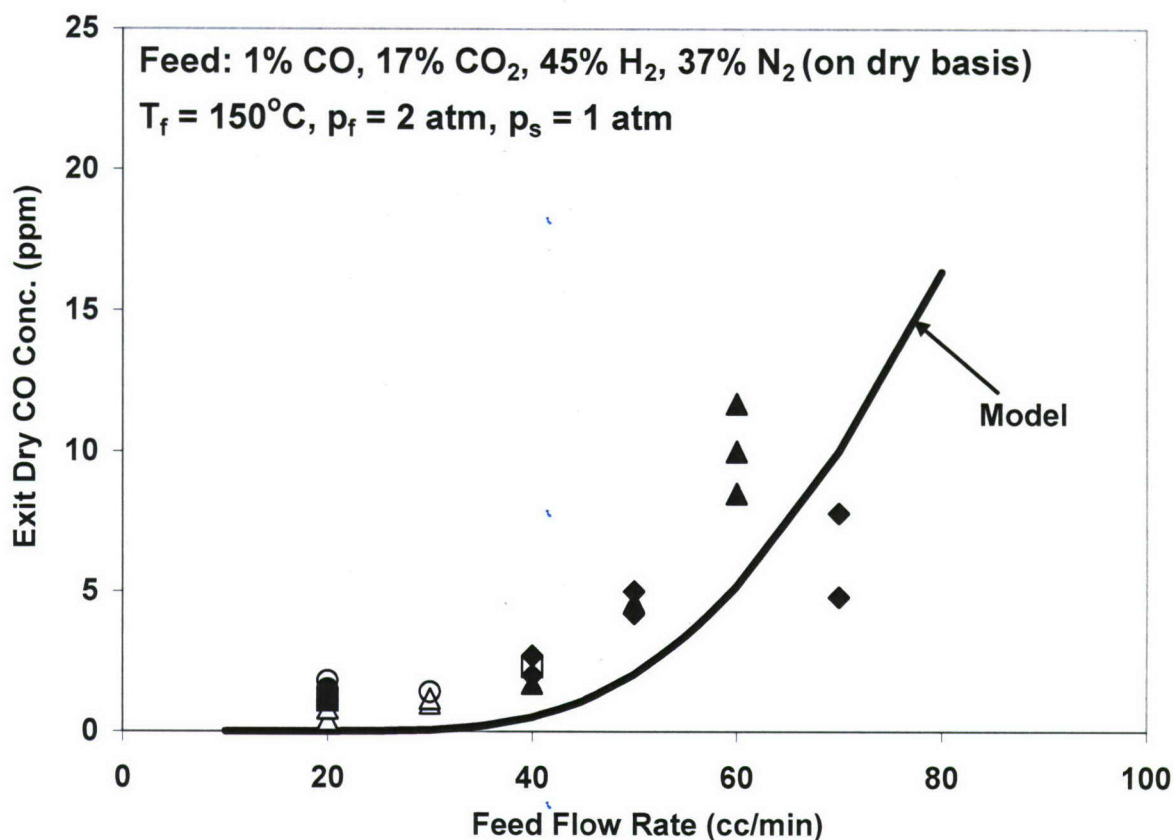


Figure 19. The results of CO in the exit H₂ product for the inlet 1% CO feed gas at various flow rates from the “Big Cell” water-gas-shift membrane reactor.

Gas hourly space velocity (GHSV) is defined in the following equation:

$$GHSV = \frac{\text{Gas Flow Rate (L/h)}}{\text{Reactor Volume (L)}} \quad (13)$$

Thus, the units of GHSV are hr^{-1} . The GHSV values for the data shown in Figure 19 were calculated according to this equation by taking into account the membrane thickness and packing density. The calculated GHSV results corresponding to the experimental data given in Figure 19 are shown in Figure 20. As shown in Figure 20, a high GHSV of about 4600 hr^{-1} is achievable. As mentioned earlier, if the feed pressure of the synthesis gas was higher than 2 atm, a higher feed gas rate could be processed, i.e., a higher GHSV would be achievable.

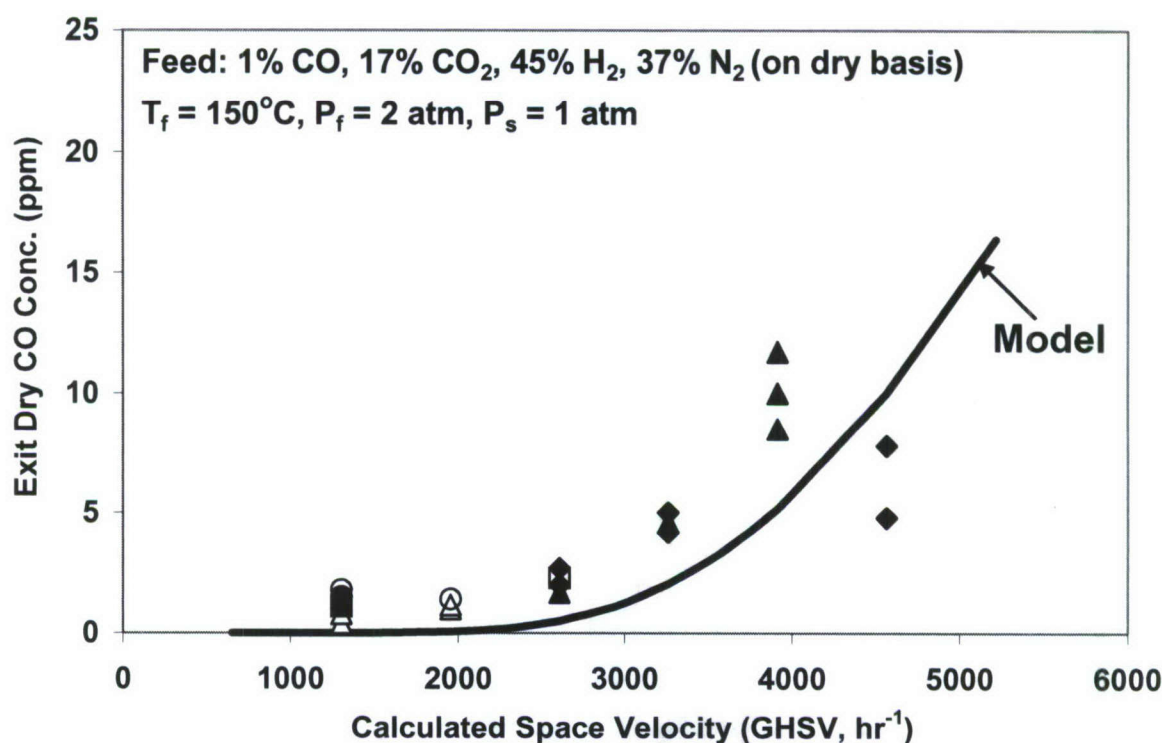


Figure 20. The calculated GHSV results for the data shown in Figure 19 at various flow rates from the “Big Cell” water-gas-shift membrane reactor.

H₂S Transport Properties

The synthesized CO₂-selective membranes containing amino groups are stable to H₂S. However, H₂S has much higher reaction rate with the amine than CO₂ as the former reacts with the amine via proton transfer and the latter reacts with the amine via carbamate formation primarily. Thus, H₂S can permeate through the membrane much faster than CO₂, and H₂S can be completely removed in the front section of the WGS membrane reactor. In the absorption of H₂S and CO₂ into aqueous amine solutions, the H₂S/CO₂ selectivity is about 3 [34-40]. Our initial membrane data (2 atm) in Figure 21 have also shown H₂S with about 3 times permeability of CO₂. A very high permeability of greater than about 20000 Barrers was obtained at 110 – 130°C.

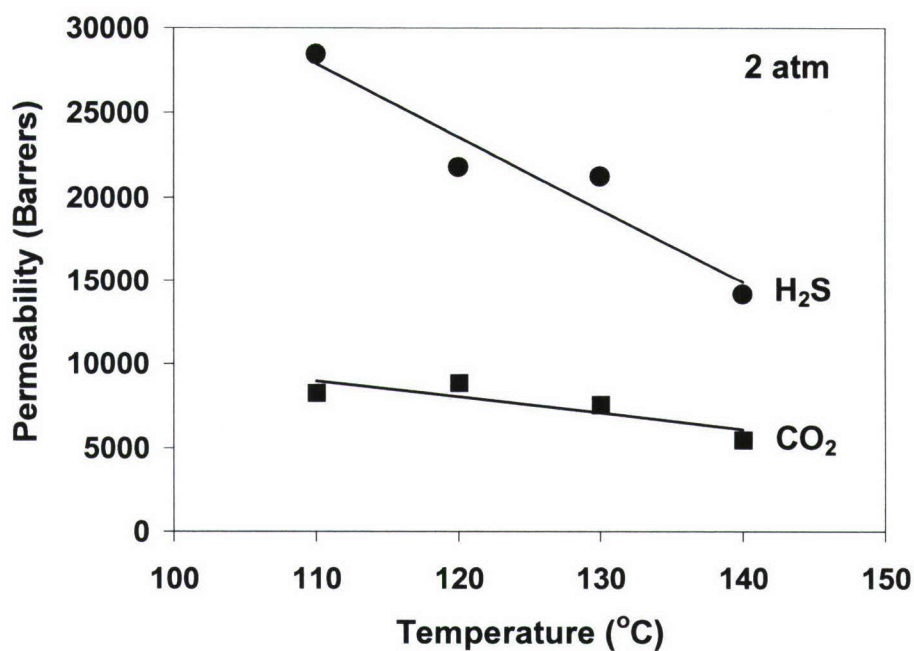


Figure 21. H₂S and CO₂ permeabilities as a function of temperature

Figure 22 depicts the corresponding H₂S and CO₂ selectivities vs. H₂. As depicted in this figure, the H₂S and CO₂ selectivities vs. H₂ were very high, i.e., about 600 and 200, respectively. The CO₂ permeability/selectivity results were consistent with those shown in Figure 1.

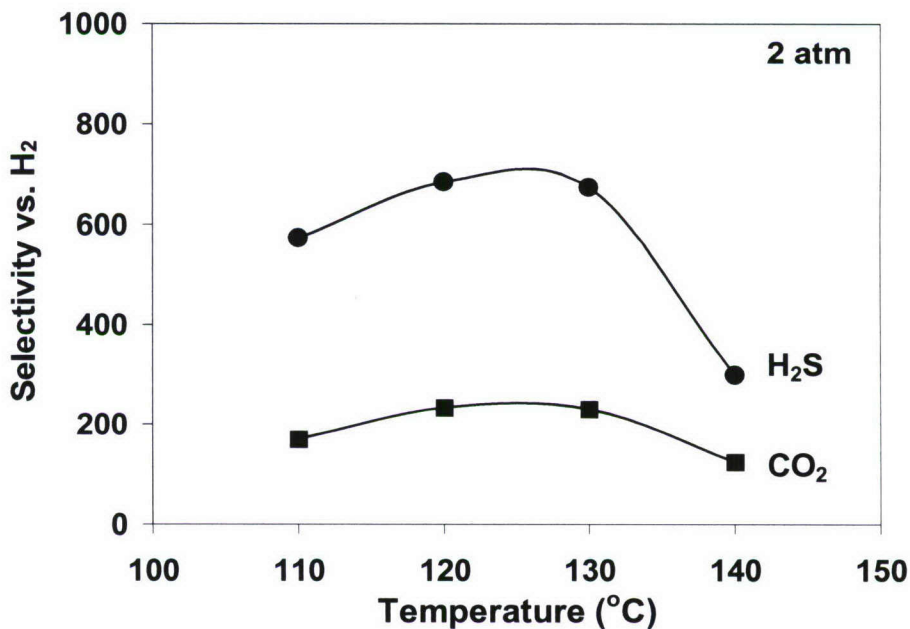


Figure 22. H₂S and CO₂ selectivities vs. H₂ as a function of temperature.

Effective Removal of H_2S from Syngas

We have recently shown effective removal of H_2S with the CO_2 -selective membrane we have synthesized. Figure 23 shows the schematic of the H_2S removal as well as CO_2 removal using the "Big Cell" as an example. In the experiments, Argon was used as the sweep gas for the ease of gas chromatography analysis.

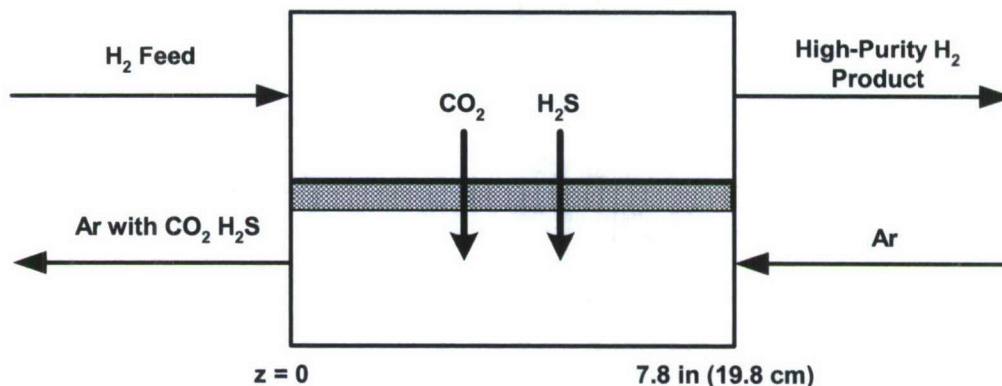


Figure 23. The schematic of the "Big Cell" without containing catalyst particles for H_2S removal.

In our initial experiments, we used a small circular membrane cell with an active membrane area of 45.6 cm^2 . Figure 24 shows the results using the syngas feed containing 50 ppm H_2S , 1% CO , 17% CO_2 , 45% H_2 , and 37% N_2 (on the dry basis) at 120°C and 2 atm from autothermal reforming with air. As shown in this figure, H_2S was removed from 50 ppm to about 0.08 ppm (80 ppb) at a feed flow rate of 10 cc/min.

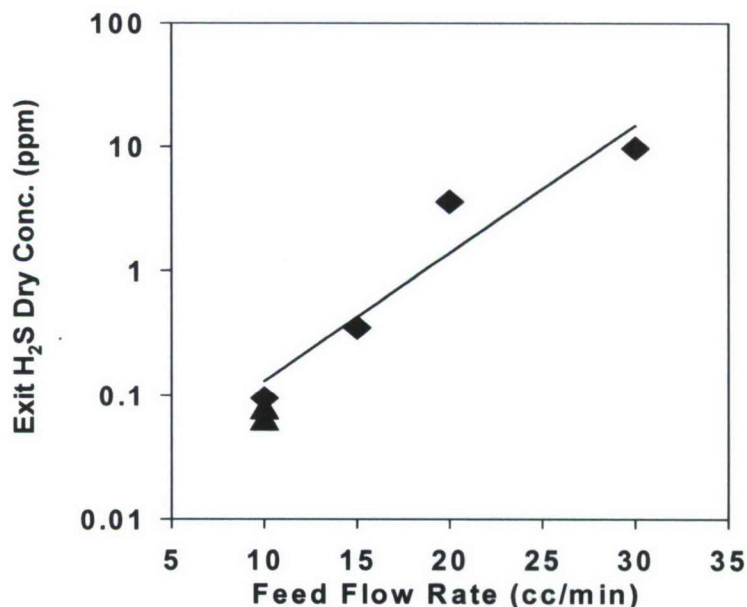


Figure 24. The results of H_2S in the exit H_2 product from the small cell at various feed rates for the syngas feed containing 50 ppm H_2S and 1% CO .

Figure 25 depicts the H₂S results using the synthesis gas containing 100 ppb H₂S (on the dry basis) at 120°C and 2 atm. Approximately 5 ppb H₂S in the treated syngas was obtained with a feed flow rate of 10 cc/min.

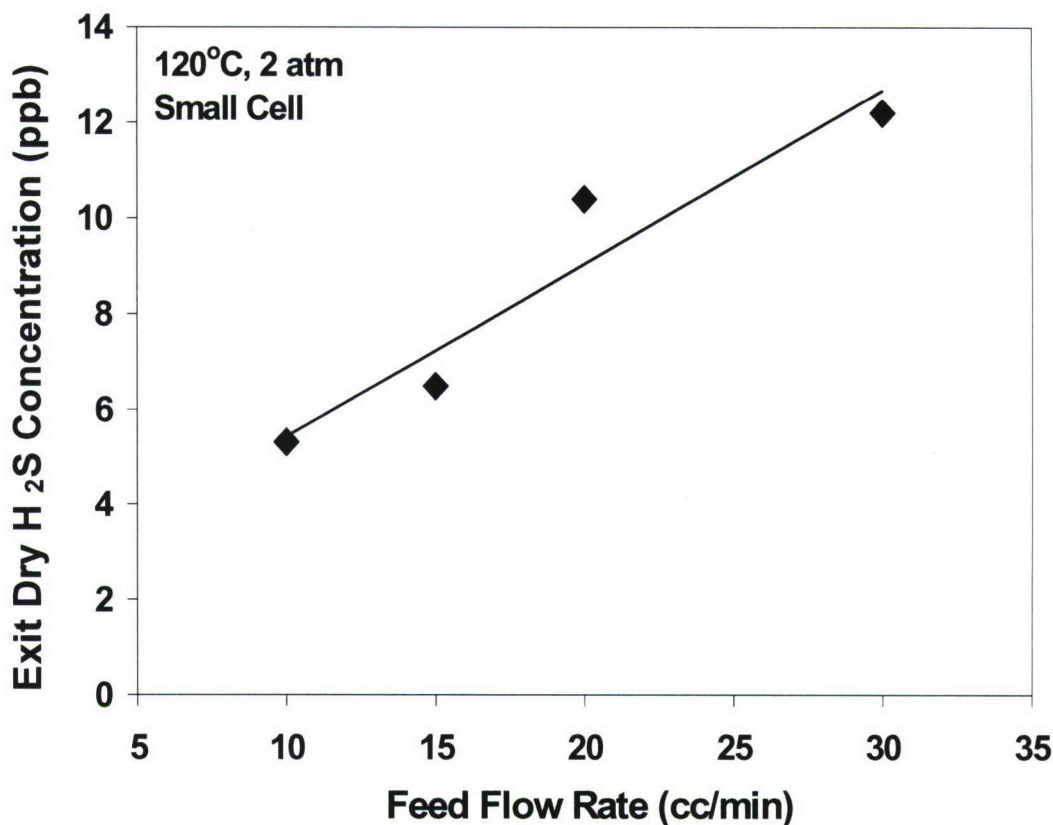


Figure 25. The results of H₂S in the exit H₂ product from the small cell at various feed rates for the syngas feed containing 100 ppb H₂S.

The “Big Cell” without containing catalyst particles was also used for the removal of H₂S from the syngas containing 50 ppm H₂S, 6.5% CO, 12% CO₂, 40% H₂, 40% N₂ (on the dry basis). Figure 26 shows the results of H₂S concentration (on the dry basis) in the exit stream (the H₂ product) at 120°C and 2.5 atm from the rectangular membrane cell at various feed flow rates. As shown in this figure, a low H₂S concentration of about 10 ppb was obtained for a feed flow rate of about 5 cc/min, indicating a nearly complete removal of H₂S from the syngas. Even at the high feed rate of 60 cc/min, the H₂S concentration in the exit stream was less than 1000 ppb (1 ppm).

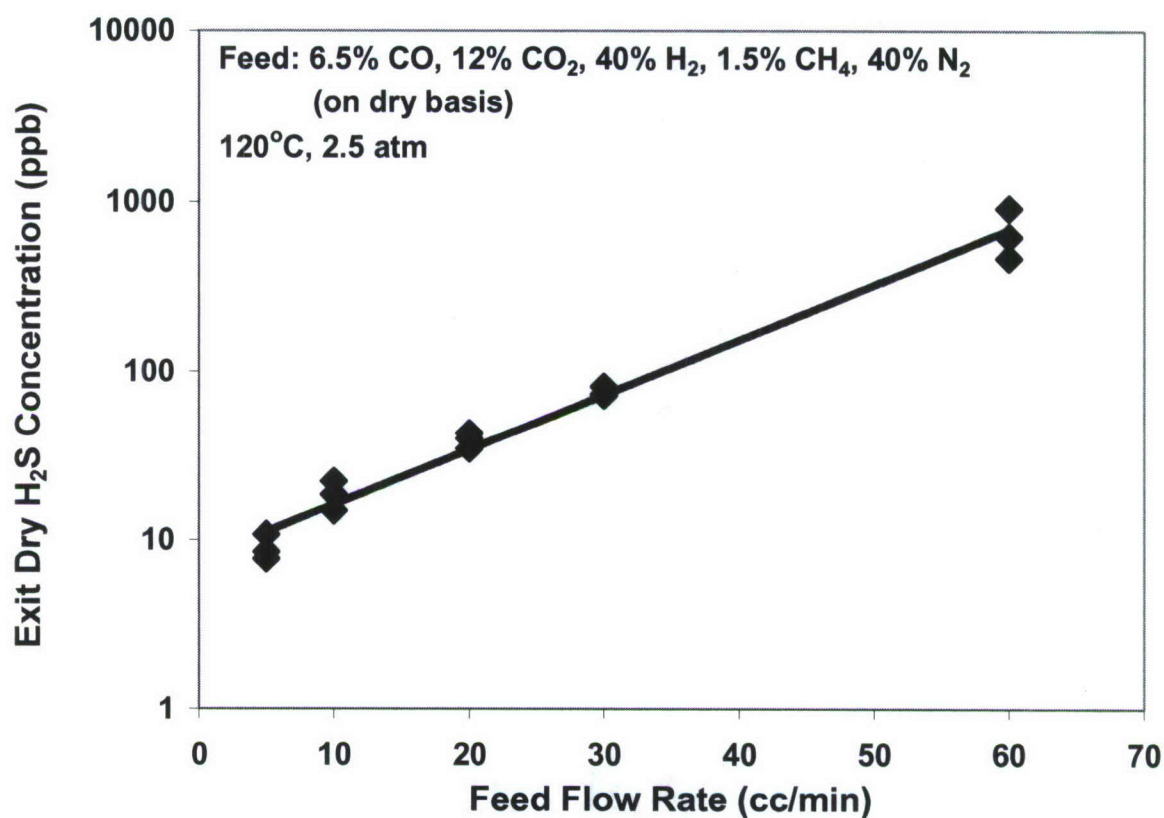


Figure 26. The results of H₂S in the exit H₂ product from the “Big Cell” (without containing catalyst particles) at various flow rates for the syngas feed containing 50 ppm H₂S and 6.5% CO.

The GHSV values for the data shown in Figure 26 were calculated in the same way described earlier. The calculated GHSV results corresponding to the experimental data given in this figure are shown in Figure 27. As shown in this figure, a high GHSV of about 2500 hr⁻¹ is achievable for an exit H₂S concentration of 100 ppb.

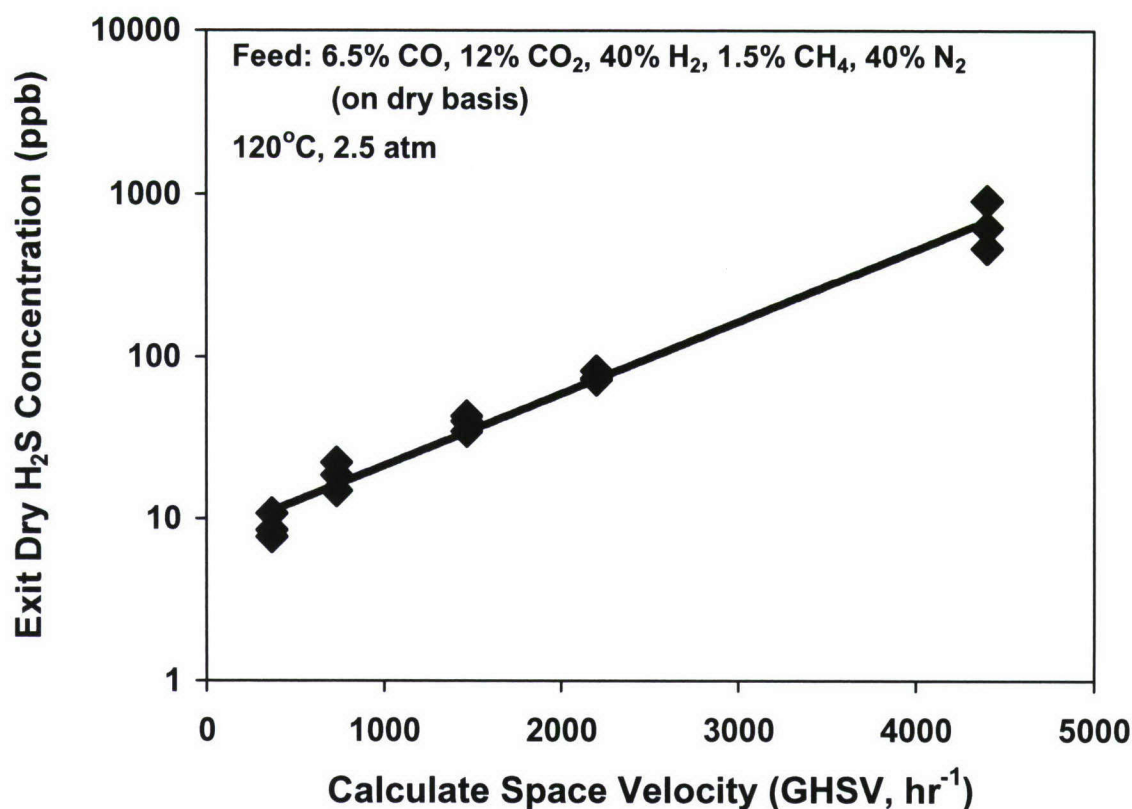


Figure 27. The calculated GHSV results for the data shown in Figure 26 from the “Big Cell” (without containing catalyst particles) at various flow rates for the syngas feed containing 50 ppm H₂S and 6.5% CO.

Conclusions

We have synthesized membranes containing amino groups with high CO₂ permeability and high CO₂/H₂ and CO₂/CO selectivities. The membranes showed a high CO₂ permeability of about 4000 Barrers, a high CO₂/H₂ selectivity of greater than 40, and a high CO₂/CO selectivity of greater than 160 at 100 – 170°C. These membranes could be operated to about 180°C.

A one-dimensional non-isothermal model was developed to predict the performance of the novel water-gas-shift (WGS) membrane reactor. The modeling results have shown that H₂ enhancement via CO₂ removal and CO reduction to 10 ppm or lower are achievable for synthesis gas from the autothermal reforming of gasoline with air. With this model, we have elucidated the effects of system parameters, including CO₂/H₂ selectivity, CO₂ permeability, sweep/feed flow rate ratio, feed temperature, sweep temperature, feed pressure, catalyst activity, and feed CO concentration, on the membrane reactor performance. As the CO₂/H₂ selectivity increased, the recovery of H₂ increased, without affecting the membrane area requirement and the low CO attainment significantly. Higher membrane permeability resulted in the reduction of the required membrane area. Increasing sweep-to-feed ratio enhanced the permeation driving force but

decreased the feed side temperature and thus the reaction rate, resulting in a net effect balanced between them and an optimal ratio of about 1. As either of the inlet feed and sweep temperatures increased, the membrane area requirement decreased. However, the temperatures greater than about 170°C would be unfavorable to the exothermic, reversible WGS reaction. Increasing feed pressure decreased the required membrane area significantly, particularly from 1 to 2 atm. Increasing catalyst activity enhanced WGS reaction and CO₂ permeation. The modeling study showed that both WGS reaction and CO₂ permeation played an important role on the overall reactor performance and that the reactor was effective for the syngas with a wide range of CO concentration (from 1% to at least 10%).

Based on the modeling study using the membrane data obtained, we have shown the feasibility of achieving H₂ enhancement via CO₂ removal, CO reduction to ≤ 10 ppm, and high H₂ recovery. We have obtained <10 ppm CO in the H₂ product in WGS membrane reactor experiments using the "Big Cell" WGS membrane reactor with well-defined flows. The data from the "Big Cell" WGS membrane reactor have agreed well with the mathematical model developed, which can be used for scale-up.

In addition, the membranes have also shown high H₂S permeability and selectivity vs. H₂. A very high H₂S permeability of greater than about 20000 Barrers was obtained at 110 – 130°C. At this temperature range, the H₂S / H₂ selectivity was very high, i.e., about 600. Initial H₂S removal experiments were carried out using the small cell and the "Big Cell" without containing catalyst particles. From the experiments, the H₂ product containing less than 10 ppb H₂S was successfully achieved.

Nomenclature

c_p	heat capacity (J/mol/K)
d	hollow fiber diameter (cm)
d_h	hydraulic diameter (cm)
h	convective heat transfer coefficient (W/cm ² /s)
ΔH_r	heat of reaction (J/mol)
J	permeation flux (mol/cm ² /s)
k_a	gas thermal conductivity (W/cm/s)
k_m	membrane thermal conductivity (W/cm/s)
K_T	reaction equilibrium constant (atm ⁻²)
ℓ	membrane thickness (cm)
L	length of reactor or hollow fiber (cm)
n	molar flow rate (mol/s)
Nu	Nusselt number
p	pressure (atm)
P	permeability (Barrer)
Pr	Prandtl number
r	volumetric reaction rate (mol/cm ³ /s)
R	ideal gas constant (atm • cm ³ /mol/K)
Re	Reynolds number

Sc	Schmidt number
Sh	Sherwood number
T	temperature ($^{\circ}\text{C}$)
U_i	overall heat transfer coefficient ($\text{W}/\text{cm}^2/\text{K}$)
x	feed side molar fraction
y	sweep side molar fraction
z	axial position along the length of reactor (cm)

Greek Letters

α	CO_2/H_2 selectivity
γ	inlet sweep-to-feed molar flow rate ratio
ε	porosity of the support layer in the hollow fiber
ρ_b	catalyst bulk density (g/cm^3)

Subscripts

0	initial
f	feed side
i	species
in	inside of the hollow fiber
out	outside of the hollow fiber
s	sweep side
t	total

References

1. W. S. W. Ho, "Membranes Comprising Salts of Aminoacids in Hydrophilic Polymers," U. S. Patent 5,611,843 (1997).
2. W. S. W. Ho, "Membranes Comprising Aminoacid Salts in Polyamine Polymers and Blends," U. S. Patent 6,099,621 (2000).
3. J. Huang, L. El-Azzami, and W. S. W. Ho, "Modeling of CO_2 -Selective Water-Gas-Shift Membrane Reactor for Fuel Cell," *J. Membr. Sci.*, **261** (1-2), 67-75 (2005).
4. Y.-H. Tee, J. Zou, and W. S. W. Ho, " CO_2 -Selective Membranes Containing Dimethylglycine Mobile Carriers and Polyethylenimine Fixed Carrier," *J. Chin. Inst. Chem. Engrs.*, **37** (1), 37-47 (2006).
5. G. Shil and W. S. W. Ho, "Synthesis and Characterization of Interfacially Polymerized Membranes for CO_2 Separation," *J. Environ. Eng. Mgmt.*, **16** (4), 233-241 (2006).
6. J. Zou and W. S. W. Ho, " CO_2 -Selective Polymeric Membranes Containing Amines in Crosslinked Poly(vinyl alcohol)," *J. Membr. Sci.*, **286**, 310-321 (2006).
7. J. Zou, J. Huang, and W. S. W. Ho, " CO_2 -Selective Membranes with Water Gas Shift Reaction for H_2 Purification," *Proceedings of International Workshop on Process Intensification in Fluid and Particle Engineering*, Kobe, Japan, October 15-18, 2006, Invited Keynote Lecture, Paper No. K201, pp.12-13.

8. D. Lee, P. Hacırlıoğlu, and S. T. Oyama, "The Effect of Pressure in Membrane Reactors: Trade-off in Permeability and Equilibrium Conversion in the Catalytic Reforming of CH₄ with CO₂ at High Pressure," Topics in Catal., **29**, 45-57 (2004).
9. A. Basile, L. Paturzo, and F. Gallucci, "Cocurrent and Countercurrent Modes for Water Gas Shift Membrane Reactor," Catal. Today, **82**, 275-281 (2003).
10. D. Ma and C. R. F. Lund, "Assessing High-Temperature Water-Gas Shift Membrane Reactors," Ind. Eng. Chem. Res., **42**, 711-717 (2003).
11. A. Criscuoli, A. Basile, and E. Drioli, "An Analysis of the Performance of Membrane Reactors for the Water-Gas Shift Reaction Using Gas Feed Mixtures," Catal. Today, **56**, 53-64 (2000).
12. A. Basile, A. Criscuoli, F. Santella, and E. Drioli, "Membrane Reactor for Water Gas Shift Reaction," Gas Sep. Purif., **10**, 243-254 (1996).
13. S. Uemiyama, N. Sato, H. Ando, and E. Kikuchi, "The Water Gas Shift Reaction Assisted by a Palladium Membrane Reactor," Ind. Eng. Chem. Res., **30**, 585-589 (1991).
14. W. S. W. Ho, "Development of Novel CO₂-Selective Membrane for H₂ Purification," Proceedings of DOE Hydrogen, Fuel Cells & Infrastructure Technologies 2004 Program Review, Philadelphia, PA, Project No. 107, Paper FC-P3 (2004).
15. W. S. W. Ho, "Development of Novel Water-Gas-Shift Membrane Reactor," DOE Hydrogen, Fuel Cells & Infrastructure Technologies Project Report, Project No. 107 (2005).
16. W. S. W. Ho, "Membranes, Methods of Making Membranes, and Methods of Separating Gases Using Membranes," PCT Appl. US 2005/40420 (2005); PCT Int. Appl. WO 2006/050531 (May 11, 2006).
17. J. M. Moe, "Design of Water-Gas-Shift Reactors," Chem. Eng. Progr., **58**, 33 (1962).
18. R. L. Keiski, O. Desponds, Y. F. Chang, and G. A. Somorjai, "Kinetics of the Water-Gas-Shift Reaction over Several Alkane Activation and Water-Gas-Shift Catalysts," Applied Catalysis A: General, **101**, 317-338 (1993).
19. W. S. W. Ho and K. K. Sirkar, eds., Membrane Handbook, Chapman & Hall, New York (1992).
20. J. S. Campbell, "Influences of Catalyst Formulation and Poisoning on the Activity and Die-off of Low Temperature Shift Catalysts," Ind. Eng. Chem. Proc. Des. Develop., **9**, 588-595 (1977).
21. E. Fiolitis, U. Hoffmann, and H. Hoffmann, "Application of Wavefront Analysis for Kinetic Investigation of Water-Gas Shift Reaction," Chem. Eng. Sci., **35**, 1021-1030 (1980).
22. T. Salmi and R. Hakkarainen, "Kinetic Study of Low-Temperature Water-Gas Shift Reactor over a Copper-Zinc Oxide Catalyst," Appl. Catal., **49**, 285-306 (1989).
23. N. Amadeo and M. Laborde, "Hydrogen Production from the Low Temperature Water-Gas Shift Reaction: Kinetics and Simulation of the Industrial Reactor," Int. J. Hydrogen Energy, **20**, 949-956 (1995).
24. M.-C. Yang and E. L. Cussler, "Designing Hollow-Fiber Contactors," AIChE J., **32**, 1910-1916 (1986).
25. L. Dahuron and E. L. Cussler, "Protein Extractions with Hollow Fibers," AIChE J., **34**, 130-136 (1988).
26. M. J. Costello, A. G. Fane, P. A. Hogan, and R. W. Schofield, "The Effect of Shell Side Hydrodynamics on the Performance of Axial Flow Hollow Fiber Modules," J. Membr. Sci., **80**, 1-11 (1993).

27. J. Wu and V. Chen, "Shell-Side Mass Transfer Performance of Randomly Packed Hollow Fiber Modules," J. Membr. Sci., **172**, 59-74 (2000).
28. F. Lipnizki and R. W. Field, "Mass Transfer Performance for Hollow Fiber Modules with Shell-Side Axial Feed Flow: Using an Engineering Approach to Develop a Framework," J. Membr. Sci., **193**, 195-208 (2001).
29. L. F. Brown, "A Comparative Study of Fuels for On-Board Hydrogen Production for Fuel-Cell-Powered Automobiles," Int. J. Hydrogen Energy, **26**, 381-397 (2001).
30. S. Ahmed and M. Krumpelt, "Hydrogen from Hydrocarbon Fuels for Fuel Cells," Int. J. Hydrogen Energy, **26**, 291-301 (2001).
31. S. Giessler, L. Jordan, J. C. Diniz da Costa, and G. Q. Lu, "Performance of Hydrophobic and Hydrophilic Silica Membrane Reactors for the Water Gas Shift Reaction," Sep. Purif. Technol., **32**, 255 (2003).
32. F. Gallucci, L. Paturzo, and A. Basile, "A Simulation Study of the Steam Reforming of Methane in a Dense Membrane Reactor," Int. J. Hydrogen Energy, **29**, 611 (2004).
33. F. Gallucci, L. Paturzo, A. Fama, and A. Basile, "Experimental Study of the Methane Steam Reforming Reaction in a Dense Pd/Ag Membrane Reactor," Ind. Eng. Chem. Res., **43**, 928 (2004).
34. W. S. W. Ho and G. Sartori, "Advances in Gas Treating and Membrane Separation", Proceedings of the Second Joint China/USA Chemical Engineering Conference, Beijing, China, pp. 593-598 (1997).
35. G. Sartori, W. S. W. Ho, D. W. Savage, G. R. Chludzinski, and S. Wiechert, "Sterically-Hindered Amines for Acid Gas Absorption", Separ. Purif. Methods, **16**, 171-200 (1987).
36. G. Sartori, W. S. W. Ho, W. A. Thaler, G. R. Chludzinski, and J. C. Wilbur, "Sterically-hindered Amines for Acid Gas Absorption", Spec. Publ.-R. Soc. Chem., **153**, 205 (1994).
37. W. S. W. Ho, E. L. Stogryn, and G. Sartori, "Absorbent Composition Containing a Severely-Hindered Amine Mixture for the Absorption of H₂S", U. S. Patent 4,894,178 (1990).
38. W. S. W. Ho, G. Sartori, and E. L. Stogryn, "Absorbent Composition Containing a Severely-Hindered Amine Mixture with Amine Salts and/or Aminoacid Additives for the Absorption of H₂S", U. S. Patent 4,961,873 (1990).
39. L. J. Shulik, G. Sartori, W. S. W. Ho, W. A. Thaler, G. E. Milliman, and J. C. Wilbur, "A Novel, V⁺⁵ Stable K₂CO₃ Promoter for CO₂ Absorption", Separ. Sci. Technol., **31**, 1663 (1996).
40. P. C. Tseng, W. S. W. Ho, and D. W. Savage, "Carbon Dioxide Absorption into Promoted Carbonate Solutions", AIChE J., **34**, 922-931 (1988).

ADDENDUM C

Design of Integrated Plasma Reformer

to the

Hawaii Natural Energy Institute

Fuels Processing and Purity Studies

Purchase Order # Z774282

Prepared by
DJW TECHNOLOGY, LLC
June, 2007

Design of Integrated Plasma Reformer

The objective of the systems integration design activity is to identify the physical and chemical interfaces between the plasma reformer and the selective membrane purification system. Analysis of the interface requirements will define the balance of plant components for the integrated system. Table 1 provides the input parameters for the plasma reformer. Table 2 identifies the temperature, pressure and flow rates for the reformat product from the plasma reformer.

<u>Table 1: Plasma fuel processor input parameters: proposed solutions</u>		
Fuel inlet temperature	330 - 370°C	Pre-heat fuel: heater or heat exchanger
Fuel inlet flow rate	5.5 g/minute	Flow regulator
Fuel inlet pressure	3 atm	Liquid pump
Air inlet temperature	330 – 370°C	Pre- heat air: heater or heat exchanger
Air inlet flow rate	23 L/minute	Flow regulator
Air inlet pressure	3 atm	Compressor
Water inlet flow rate	20 g/minute	Flow regulator
Water inlet temperature	300 – 350°C	Pre- heat water: heater or heat exchanger
Water inlet pressure	3 atm	Liquid pump

Table 2: Plasma fuel processor reformat	
Reformat temperature	650°C
Reformat pressure	3 atm
Reformat flow rate	37 L/min
Reformat composition: 28.1% H ₂ , 48.9% N ₂ , 14.6%CO ₂ , 1.4%CH ₄	

Two Stage Purification Concept:

The design of a two stage purification unit with the first stage to remove H₂S appears a tractable solution for H₂S and CO₂ reductions. The design may require an initial reduction of the reformat input to the purifier to 120°C to eliminate the H₂S.

Subsequent heating of the partially purified reformat to ~ 150°C would then permit optimum reduction of the CO₂. The concept is shown in Figure 1.

The sweep gas for the selective membrane purification system is considered to be air. A mismatch exists in the temperatures of the exiting reformat and the input requirements for the selective membrane purification system.

The first stage input parameters for the selective membrane purification system are given in Table 3 where the H₂S concentration will be reduced to < 10 ppb. Table 4 identifies the input parameters for the CO₂ removal in the second stage. Preheating of the H₂S scrubbed reformat is required prior to stage 2. Water gas shift catalyst is used in stage 2 to promote the conversion of CO to CO₂. The enriched hydrogen for the PEM fuel cell exits stage 2. The complete system is schematically given in Figure 2.

Table 3: Input parameters for H ₂ S selective membrane purification: proposed BOP solutions		
Feed temperature	120°C	Exit from heat exchanger #1
Feed pressure	3 atm	Delivered from reformer
Feed flow rates	2,000 hr ⁻¹ – 2,500 hr ⁻¹	(reformat at 37L/min)
Sweep temperature	120°C	Pre-heat air: heater – heat exchanger
Sweep pressure	1 atm	Blower
Sweep flow to feed flow ratio	1	Flow regulators on sweep

Table 4: Input parameters for CO ₂ selective membrane purification: proposed BOP solutions		
Feed temperature	150°C	Exit from heat exchanger #2
Feed pressure	2 - 3 atm	Delivered from H ₂ S clean up
Feed flow rates	4,000 hr ⁻¹ – 4,500 hr ⁻¹	
Sweep temperature	140°C	Preheat air heater – heat exchanger
Sweep pressure	1 atm	Blower
Sweep flow to feed flow ratio	1	Flow regulators on sweep

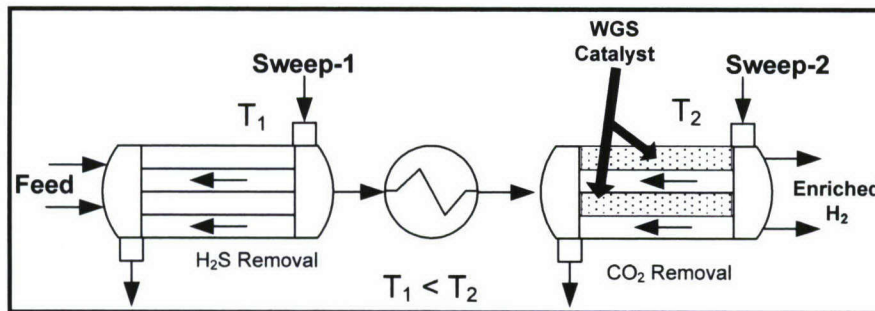


Figure 1: Two stage hydrogen purification system

The integrated design in Figure 2 provides the basis for the construction of a breadboard system. Balance of plant components exist for the construction of the system. The plasma reformer is not optimized. Additional experiments to optimize the plasma power into the reformer and to demonstrate long term, continuous operation are needed prior to the design and construction of the next generation plasma reformer.

The selective membrane purification system was demonstrated using laboratory cells. Full size flow reactors need to be built and tested to translate the results identified here to a full scale device.

The design presented here represents the first iteration in the development of a full scale device. The design will provide the basis for a laboratory, breadboard test facility.

System components:

Parker Hannifin was contacted and the availability of balance-of-plant components reviewed. The heat exchangers, gas pre-heaters, and flow control components (not shown in Figure 11. Parker Hannifin identified that off-the-shelf components could be used based on the data provide in Tables 1, 2, 3 and 4.

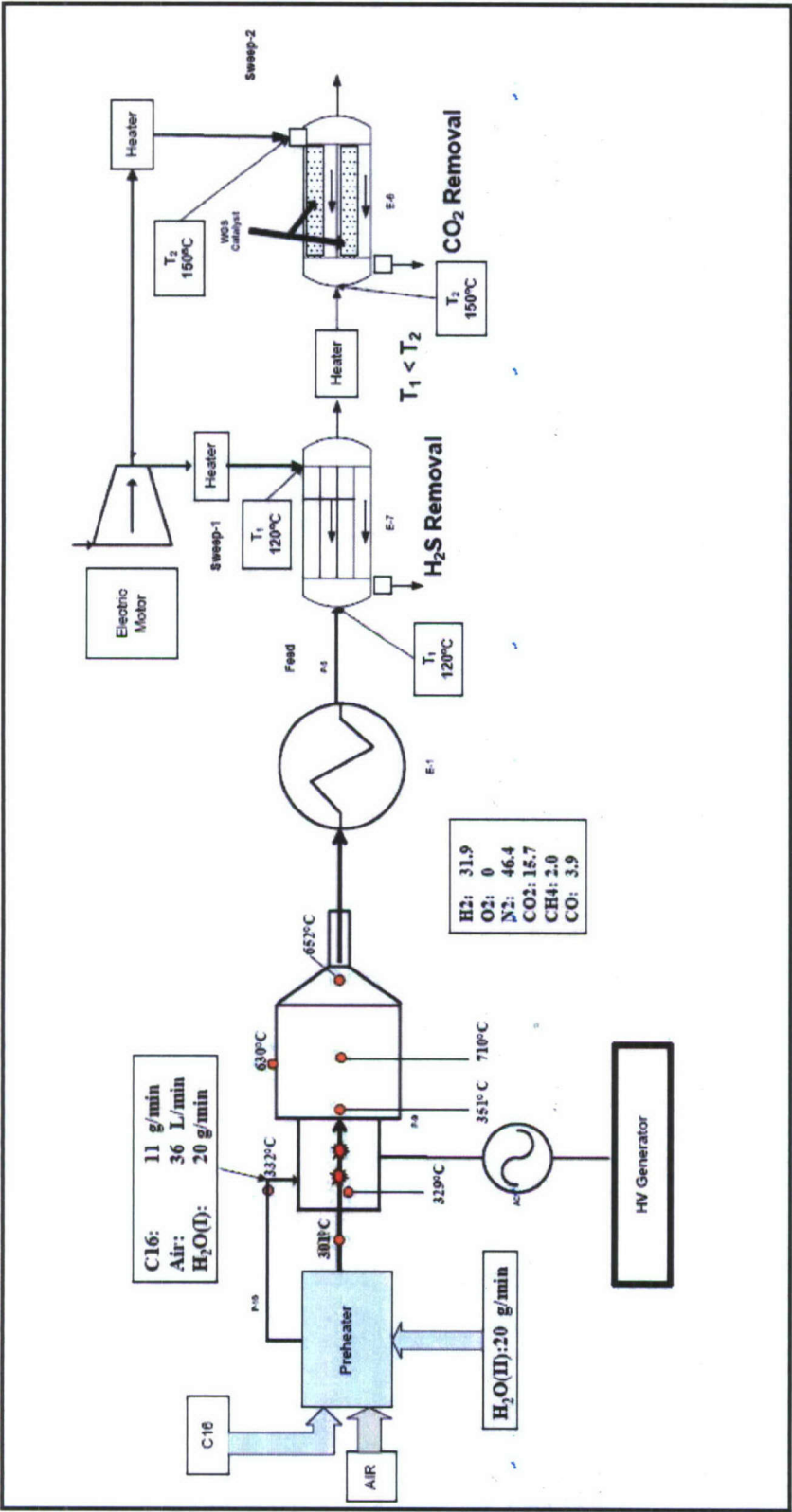


Figure 1: System diagram for plasma reformer interfaced with selective membrane purification system